Numerical studies of vortices and dark solitons in atomic Bose-Einstein condensates

Nicholas Parker

Numerical Studies of Vortices and Dark Solitons in Atomic Bose-Einstein Condensates

Nicholas Parker

A thesis submitted in partial fulfilment
of the requirements for the degree of
Doctor of Philosophy

Department of Physics
University of Durham
October 2004

Numerical Studies of Vortices and Dark Solitons in Atomic Bose-Einstein Condensates

Nicholas Parker

Abstract

Dilute atomic Bose-Einstein condensates support intriguing macroscopic excitations in the form of quantized vortices and dark solitons. In this thesis we present extensive quantitative studies of the dynamics of these phenomena in the limit of zero temperature, performed by numerical simulation of the Gross-Pitaevskii equation. We show that vortices and dark solitons are inherently unstable to acceleration through the condensate, leading to the emission of sound waves. Indeed, for a single vortex/soliton, the power emitted is proportional to the square of the local acceleration. However, due to the finite size of the condensate, the vortex/soliton reinteracts with the emitted sound. This coupling has an important effect on the ensuing dynamics, and we illustrate how it can be engineered to induce net decay, stabilise, or even drive energy into the vortex/soliton.

Under the harmonic confinement typically employed to trap the condensates, the acceleration-induced decay is stabilised by reabsorption of the emitted sound. However, by modifying the trap geometry, e.g. by adding an inner dimple in which the soliton resides or an optical lattice potential, it is possible to break this equilibrium and so induce a net decay of the vortex/soliton in a controllable manner. The decay rate can be considerable and should be observable under current experimental conditions. The dynamical stability of quantized vortices is also relevant to the field of turbulence in superfluid Helium, where the motion of the vortices is induced by the surrounding distribution of vortices rather than density. We extend these results to this field, and additionally consider the interactions between two and three vortices, which are also found to involve sound emission.

By exciting the sound field of the condensate it is possible to drive parametrically energy into a dark soliton. In a real dissipative environment, this can be used to stabilise the soliton decay. Finally, we illustrate the links between dark solitons and vortices: a dark soliton embedded in a three-dimensional system is prone to decay into vortex rings, while a vortex in a quasi-one-dimensional geometry cannot be supported and exists as a hybrid between a vortex and dark soliton, known as a solitonic vortex.

Dedicated to Mum and Dad,
for all their love, friendship, and support.

Declaration

I confirm that no part of the material offered has previously been submitted by myself for a degree in this or any other University. Where material has been generated through joint work, the work of others has been indicated.

Nicholas Parker
Durham, 7th October 2004

Acknowledgements

I'm very grateful to Charles Adams for his support, enthusiasm, endless ideas, and motivational meetings throughout the three years. Many thanks to Nick Proukakis for his day-to-day help and guidance, and for the thorough proof-reading of this thesis, and to Mark Leadbeater for getting me up and running with the numerics and his insight into the field. Thanks also to Carlo Barenghi for stimulating discussions.

Thanks to all the regular coffee-timers, especially Cip for being a great office-mate from day one, Dave for amusing discussions, and Ifan Hughes for words of wisdom and cheerful chats. Outside of work, I'd like to say a big cheers to Griff(man) and Pete(man) for being such great housemates throughout. Rich, Kate and Jo, thanks for keeping me entertained with parties and summer holidays. Thanks to all the Parker family for the friendship and laughter. Last but certainly not least, I'd like to say a big thank you to Claire for her constant love and support.

Contents

List of Figures

List of Tables

Chapter 1

Introduction

The story of Bose-Einstein condensation began with a hypothesis in the 1920s, and ended the century in a hive of striking experimental discovery, following the realization of this state in the clean and pure form of dilute atomic Bose-Einstein condensates.

In nature, particles can be divided into two categories: bosons are particles with integer spin (e.g. photons) and fermions have half-integer spin (e.g. electrons). A key difference is that fermions are limited to only one particle per state by the Pauli exclusion principle, while bosons can occupy the same state in any number.

Bose-Einstein condensation was first predicted in 1924 after Albert Einstein [1] generalised the Bose's photon distribution law [2] to an ideal gas of non-interacting bosons. Under these Bose-Einstein statistics, the occupation of the ground state of the system diverges in the limit of zero temperature, leading to macroscopic population of this single state. This is the phenomenon of Bose-Einstein condensation.

The effect is inherently quantum mechanical. Consider an ensemble of particles in thermal equilibrium at temperature T. In the quantum world, each particle is represented by a localised wavepacket, with its spatial extent being characterised by the de Broglie wavelength $\lambda_{\mathrm{dB}} = \sqrt{2\pi\hbar^2/mk_{\mathrm{B}}T}$, where m is the mass of the particle, $\hbar$ is equal to Planck's constant divided by 2π, and k_{B} is Boltzmann's constant. At low temperatures and/or high particle densities, this wavelength can become comparable to the average distance between the particles. In this

regime, the individual wavepackets overlap and a quantum degenerate gas is formed. In the ideal Bose gas, this criterion is fulfilled when $n\lambda_{\mathrm{dB}}^3 \approx 2.612$, where n is the particle density [3]. A key feature of Bose-Einstein condensation is macroscopic coherence across the system.

At first Bose-Einstein condensation was not expected to occur in real non-ideal systems due to the interactions between particles. However, it is now known that Bose-Einstein condensation is a generic phenomenon occurring in diverse areas, from astrophysics and particle physics to condensed matter and atomic physics [4]. Its most famous consequences are superfluidity and superconductivity [5]. The latter case can be considered as the Bose-Einstein condensation of electrons, made possible by BCS pairing of the fermionic electrons into composite bosons.

1.1 Superfluid Helium

In 1938 Kapitza [6] and Allen and Misener [7] observed inviscid flow in liquid ^{4}He below a critical temperature, and the phrase 'superfluidity' was coined. This phase of ^{4}He is known as Helium II. This effect was controversially interpreted by London [8] as a manifestation of the Bose-Einstein condensation of a macroscopic fraction of Helium atoms, even though this strongly-interacting liquid is far from Einstein's ideal gas. This idea did not gain acceptance until much later, and the first successful model was instead provided by Landau's two-fluid theory [9], where a superfluid component with zero viscosity is assumed to exist alongside a normal fluid component.

Landau additionally showed that superfluid behaviour could be accounted for by a dispersion relation which is linear at low momenta [9]. Later, Bogoliubov showed that the weakly-interacting Bose gas supported such a dispersion law [10], and subsequently this gained credit as a model of superfluidity in Helium II. Importantly, it was a strong indication that Bose-Einstein condensation was responsible for superfluidity. However, due to the strong interactions in liquid Helium, the weakly-interacting Bose gas is restricted to a qualitative model.

Onsager [11] and Feynman [12] advanced London's quantum mechanical description to predict the existence of quantized circulation in a superfluid. Unlike a classical fluid, which rotates smoothly as a solid body, a superfluid is constrained

by quantum theory to be irrotational. Any rotation in the system is manifested in singularities, or quantized vortices, with the circulation quantized in units of $\kappa = h/m$. This behaviour was confirmed by Vinen's experiment on rotating Helium II in 1961 [13], although direct observation of quantized vortices was not made until 1979 [14].

1.2 Dilute Bose-Einstein condensates

The topic of Bose-Einstein condensation was revolutionized in 1995 when a dilute weakly-interacting Bose-Einstein condensate (BEC) was realized in a confined ultracold gas of alkali atoms [15, 16]. This was made possible by advancements in atom cooling and trapping techniques [17, 18], which enabled a phase-space density $n\lambda_{\mathrm{dB}}^3$ of the order of unity (predicted to be necessary for condensation) to be reached. This realization followed the earlier work on cooling spin-polarized atomic hydrogen towards degeneracy [19, 20, 21]. However, Bose-Einstein condensation of hydrogen was not acheived until 1998 [22] due to complications, such as the tendency of the atoms to flip spin and form molecules.

The basic method of creating a dilute BEC is as follows [23, 24, 25, 26]. Typically around 10^9 atoms are confined in a magneto-optical trap formed by a combination of laser beams and magnetic fields. These atoms have a temperature and density of the order of $T \sim 10^{-5}\mathrm{K}$ and $n \sim 10^{10}\mathrm{cm}^{-3}$, but the phase-space density is still around five orders of magnitude lower than the threshold for condensation. The cloud is then transferred to a separate magnetic trap giving three-dimensional harmonic confinement, while radio-frequency pulses are employed to evaporate selectively high-energy atoms, such that the cloud rethermalises to lower temperatures. At a temperature and density of the order of $T \sim 10^{-6}\mathrm{K}$ and $n \sim 10^{14}\mathrm{cm}^{-3}$, a Bose-Einstein condensate emerges with starkly contrasting characteristics to the thermal component, e.g. a narrow velocity distribution rather than a broad thermal distribution.

The particle interactions in these gases are dominated by low-energy two-body collisions, which can be characterised by the atomic s-wave scattering length a. The equality $n^{1/3}a \ll 1$ is satisfied, which implies that the interactions

are weak. From a geometric point of view, the scattering cross-section in this regime is much less than the average distance between particles. Due to these weak interactions, it is expected that over 99% of atoms can condense in the limit of zero temperature. This is stark contrast to Helium II, where strong interactions limit the condensed fraction to less than 10% [27]. Consequently, dilute BECs represent the purest example of Bose-Einstein condensation, and a close representation of Einstein's ideal quantum gas. In particular, at low enough temperature, the macroscopic coherence of the condensed state extends across the whole sample [28]. Furthermore, the dilute nature of these gases implies that their lengthscales and timescales are typically a factor of three larger than in their condensed matter counterparts (Helium II and superconductors), therefore bringing BEC phenomena into the regime where they can be easily observed and probed.

To date, dilute BEC's have been created with Rubidium [15], Sodium [16], Lithium [29], spin-polarized Hydrogen [22], metastable Helium [30], Potassium [31], Caesium [32] and, most recently, Ytterbium [33]. These highly-pure degenerate gases enable ultra-precision measurements of fundamental physical phenomena, and a test-bed for quantum theory. A key feature is that they are readily controlled and manipulated by electromagnetic and optical means. Beams of coherent atoms, the 'atom lasers', have been out-coupled from a BEC [34, 35, 36], while, in suitable trap geometries, BECs can be engineered with reduced dimensionality [37, 38, 39, 40]. This has lead to the prospect of performing coherent atom optics [41] in effectively one-dimensional (1D) waveguides, for example, on atom chips [42, 43, 44, 45]. Optical lattice potentials can be employed to bridge the gap to periodically-structured condensed matter [46, 47], such as the observation of band structure in the form of Bloch waves [48] and the demonstration of the quantum Mott insulator transition [49]. The atomic interactions can be tuned from attractive to repulsive, and in magnitude, by the molecular Feshbach resonance [50, 51, 52, 53]. Molecular condensates have been produced from fermionic atoms [54, 55, 56], and similarly the BCS pairing of fermionic atoms is being probed [57, 58], in analogy to the pairing of electrons in conventional superconductors. The characteristic signatures of superfluidity, e.g. critical velocities [59, 60], quantized vortices [61, 62, 63, 64] and the scissors mode [65, 66], have been verified to exist. An important feature of

Bose condensed gases is their inherent nonlinearity. Analogs of nonlinear optical phenomena such as four-wave mixing of matter waves [67], superradiance and matter-wave amplification [68, 69, 70], and bright [71, 72, 73] and dark [74, 75, 76, 77] solitary matter waves, have all been observed.

From a theoretical point of view, dilute BECs are an attractive topic due to the fact that the many-body system can be characterised, to first order, by a mean-field macroscopic order parameter, or *wavefunction*. Furthermore, this macroscopic wavefunction is well-described by a nonlinear Schrödinger-type equation called the Gross-Pitaevskii equation [23, 24, 78, 79].

1.3 Macroscopic (nonlinear) excitations

1.3.1 Vortices

Vortices are diverse in nature, representing the breakdown of ordered fluid flow and playing a key role in turbulence. The amount of fluid rotation associated with a vortex can be parameterised in terms of the circulation $\Gamma = \oint d\mathbf{r}.\mathbf{v}(\mathbf{r})$ about the vortex, where $\mathbf{v}(\mathbf{r})$ is the fluid velocity field at point $\mathbf{r}$. Classical vortices can represent any degree of fluid rotation, i.e. the circulation about the vortex can take any value. Superfluid vortices represent the dissipation of superfluidity, and feature quantized circulation, making them well-defined objects. Superfluid vorticity is not only interesting in its own right, but represents a simplified platform to study vortex dynamics and turbulence in general. Due to the lack of fluid viscosity, very high Reynolds numbers, i.e. intense turbulence, can be generated on microscopic length scales [80], and this has led to the idea of modelling the universe within a Helium droplet [81].

The standard method of generating quantized vortices in a superfluid is by rotation of the system about a fixed axis. At low rotation frequencies the fluid remains stationary. However, above some critical rotation frequency, the presence of one or more vortices lowers the free energy of the system [64, 82], and one or more vortices become nucleated into the system. Multiple vortices tend to crystallise into a lattice formation, with each vortex being singly-charged and contributing one quantum of circulation κ to the total circulation. The

lattice typically has the triangular Abrikosov form due to the mutual repulsion of the vortices, first predicted for quantized magnetic flux lines in type-II superconductors [83], and observed in Helium II [14] and dilute BECs [84].

In optics, vortices can also occur in modes characterised by a helical phase structure and a central dark singularity, with the photons featuring quantized orbital angular momentum. Optical vortices have been shown to exhibit dynamics which are analogous to vortices in superfluids [85].

Vortices and turbulence in liquid Helium

Ordered vortex lattices in liquid Helium can be achieved by mechanical rotation of the container about the central axis. However, direct observation of the vortices is hampered by the presence of the large normal fluid component and the nanometre size of the cores. For example, the clearest observation of a vortex lattice in rotating Helium II employed a complicated ion-imaging technique and resolved only 11 vortices [14].

Turbulence in Helium II has been probed experimentally and theoretically since the 1950's [27], and is typically generated by thermal counterflow or mechanical means, e.g. oscillating grids. The superfluid component is expected to involve a disordered array of vortex lines, known as a vortex tangle. At finite temperatures, mutual friction between the normal and superfluid component leads to a dissipation of the superfluid vorticity [27]. However questions remain over the behaviour of quantum turbulence in the limit of very low temperature where mutual friction becomes effectively nonexistent. For example, the decay of vortex tangles in Helium II at temperatures less than 70mK has been shown to be independent of temperature [86], suggesting the occurrence of purely dynamical dissipation mechanisms. Vortex reconnections [87] and Kelvin wave excitations [88, 89] lead to the decay of vorticity via the emission of sound waves. However, these mechanisms cannot alone account for the total observed decay [90].

The conventional method in modelling large-scale vortex dynamics is to employ the classical vortex model whereby the dynamics of the vortex filaments are described by the Biot-Savart law [80]. Here, the motion of an element of vortex line is induced by the velocity field of the surrounding elements, whether they be on the same or a different vortex line [27]. A limitation of this approach is

that is does not describe phenomena occurring on the length-scale of the vortex core, e.g. reconnections between vortices and the process of sound emission, and so is only valid when the average vortex separation is large. However, such effects can be introduced 'by hand' [80], once they have been characterised on a microscopic level.

The Gross-Pitaevskii model, on the other hand, provides a useful microscopic model of Helium II. It includes the core structure of vortices, and is capable of modelling microscopic effects, such as vortex nucleation, reconnections between vortices [91, 92], the interaction with rarefaction pulses [89], and sound emission from reconnections [87] and Kelvin wave excitations [88, 89]. However, it fails to describe the full physics of dense, strongly-interacting Helium II, e.g. the presence of high momentum roton excitations. Consequently, the GPE is mainly limited to giving qualitative information regarding vortex dynamics in Helium II.

Vortices in dilute BEC

In recent years, the topic of superfluid vorticity has been revolutionized with the realisation of dilute BECs. Their negligible non-condensed component and micron-sized cores have enabled clear observation of vortex structures.

Creation of quantized vortices in dilute BECs involves transferring angular momentum to the cloud. This has been achieved in a two-component condensate using a dynamical phase-imprinting technique [61], and in single-component BECs by rotation of the cloud using an anis0tropic perturbation [62, 63, 84, 93] and by optical phase-imprinting [94, 95]. Providing the rotation is greater than a critical value, one or more vortices become nucleated at the edge and enter the condensate [96, 97].

Single vortices with one quantum of circulation have been generated with lifetimes of up to 10s [61, 62, 98]. Thermal dissipation between the vortex and the thermal cloud is expected to be responsible for limiting the vortex lifetime [99]. Multiply-quantized vortices have also been created [94, 95]. The dynamics of a vortex line have been experimentally probed, including their precessional motion in traps [100], bending [98], Kelvin wave excitation [101], gyroscopic oscillations [102], and splitting of multi-charged vortices [95]. Highly regular

vortex lattices, ranging from a few vortices [62] to several hundred vortices [84, 103], have been clearly imaged, along with their excited states in the form of Tkachenko modes [104] and 'giant' vortices [103]. Vortex rings have been generated in the decay of dark solitary waves [76, 77], and by the motion of a laser beam through a condensate above a critical velocity [60, 105]. The vast majority of these vortex dynamics have been shown to be in good qualitative, and often quantitative, agreement with simulations of the GPE [64].

The size of the vortex core (of the order of a micron) is under the resolution limit of current imaging techniques (of the order of ten microns), and so observation of the vortices involves releasing the BEC from the trap, allowing it to expand, and taking an optical absorption image. This is a destructive effect and so must be repeated in order to obtain time-dependent information.

Experimental results indicate that the crystallisation of vortex lattices is temperature-independent at sufficiently low temperature [106]. Initial attempts to model this formation process using the GPE in two-dimensions found it necessary to include a damping term to allow relaxation to the lattice configuration [96, 107, 108, 109, 110]. However, Lobo *et al.* [97] recently modelled the lattice crystallisation using the GPE in three-dimensions without any damping terms. Here the onset of crystallisation is probably enabled due to 3D effects, such as the bending and Kelvin wave excitation of the vortex line. In particular, this is further evidence for the importance of the purely dynamical dissipation of vortices.

1.3.2 Solitons

The inherent nonlinearity of dilute BEC's means that they support a family of nonlinear excitations known as solitons. These structures are localised one-dimensional wavepackets that propagate without dispersion, due to a delicate balance between the natural tendency of a wave to disperse and the nonlinearity within the medium. In addition, solitons travel with finite and constant speed in a homogeneous system, and emerge unchanged from collisions. Although a soliton technically takes the form of a solitary wave when embedded in a three-dimensional system, we will generally refer to both forms as a soliton.

Solitons occur in diverse fields of physics [111, 112], with optical solitons in

particular being an area of much theoretical and experimental research. While matter wave solitons are relatively under-developed, possible applications may include matter wave interferometry, quantum entanglement, and quantum information processing. Consequently, the dynamics and stability of solitary waves in dilute BECs is an area of much interest. Solitary waves come in bright and dark forms depending on whether the medium is effectively attractive/focussing or repulsive/defocussing, respectively.

Bright solitons

Bright solitary waves are the more common of the two soliton species. The classic example is the propagating solitonic hump in shallow water [113], first reported by John Scott Russell in 1845 [114]. Bright solitons also arise in optical fibres [115, 116], plasma systems [117, 118], macromolecules [119], acoustics [120], and excitonic systems [4]. Due to their non-dispersive properties, optical bright solitons have found important applications in optical communications [121] and photonics [122].

Bright solitary matter waves are supported for effectively attractive interactions [123] and have been generated in attractive condensates [71, 72]. A form of bright soliton, known as a gap soliton, was recently produced in a repulsive condensate in an optical lattice, due to the modification of the dispersion properties of the system by the band-like structure [73].

Dark solitons

Dark solitary waves are supported for effectively repulsive interactions [124]. They feature a dip in the ambient density and a phase slip, and are often referred to as the 1D analogs of vortices. They are rare in comparison to their bright counterparts, and have been realised in a handful of systems. Dark solitons were first realized in 1987 in nonlinear optics [125], where the wave was observed as a dark region (absence of light), and this is the origin of the name. This was followed by the creation of non-propagating kink modes in a parametrically-driven shallow liquid [126], dark soliton standing waves in a discrete mechanical system [127], and magnetic-envelope dark solitons in thin magnetic films [128]. Dark solitons are most well-known in the field of optics [129], where potential

applications include the formation of zero cross-talk optical junctions [130].

More recently, dark solitary waves have been created in repulsive atomic BECs by phase-imprinting [74, 75, 76] and perturbing the atomic density [77]. In the former case, a portion of the condensate was illuminated by a far-detuned laser beam for a short period of time such that it instantaneously acquired a phase shift, but generated no significant density perturbation. Following this, a dark solitary wave evolved, plus sound waves as by-products. The size of dark solitons is less than the resolution limit of optical imaging so the condensate is expanded before absorption imaging. Another experiment involved the sudden removal of a disk-shaped region of atoms from the condensate via a slow-light technique, which generated counter-propagating dark solitary waves [77]. In two of these experiments [76, 77], the dark solitary wave was observed to decay into vortex rings due to their inherent instability to transverse excitations.

Dark solitons are also predicted to be formed by the collision of two condensates [131, 132], the Bragg reflection of a condensate in an optical lattice [133], and a time-dependent obstacle [134, 135, 136]. More advanced methods of selectively preparing a dark soliton state have been proposed [137, 138], including the combination of phase imprinting and density engineering [139, 140]. Dark solitons are also predicted to be supported in two-component repulsive BECs [141], and in attractive condensates under optical lattice and/or harmonic confinement if embedded in a broader bright soliton [142].

1.4 Instabilities of vortices and dark solitary waves in dilute BECs

Vortices and dark solitary waves represent macroscopically excited states of the system and so are prone to instabilities. These effects typically come in three forms: thermal, quantum, and dynamical.

1.4.1 Vortices

In a rotating condensate, the presence of vortices lowers the free energy of the system, and therfore becomes energetically favourable, above a certain critical

rotation frequency [64, 143, 144]. However, in a non-rotating condensate, the ground state is vortex-free. The presence of a vortex in a non-rotating system constitutes an excited state, and this implies that the vortex state is thermodynamically unstable.

An off-centre vortex in a trapped dilute BEC is expected to follow a path of constant potential, which amounts to precession about the trap centre [145, 146]. Fedichev *et al.* [99] have considered the thermal instability of a precessing straight-line vortex in a dilute BEC, and predict that the relative motion of the vortex through the thermal cloud induces dissipation via scattering of thermal excitations off the vortex core. This induces a motion towards a local minimum of the energy, which in a harmonically-confined BEC amounts to a drift of the vortex away from the trap centre, such that the vortex spirals outwards [145]. Since the vortex is a topological defect it can only disappear at the condensate boundary, where it is thought to decay into elementary excitations. A central vortex line is stationary, and so is not directly prone to this thermal frictional dissipation. However, in a real environment thermal and quantum fluctuations are expected to nudge such a vortex off-centre, where it becomes susceptible to this mechanism and therefore has a finite lifetime [147]. The thermodynamic lifetime of a vortex in a confined BEC is predicted to be of the order of seconds [99], which is consistent with vortex experiments [61, 62, 98].

Quantum depletion of the condensate is thought to lead to the vortex core becoming partially filled up with non-condensed, non-rotating atoms [148].

Dynamical instabilities of vortices in superfluids come in many forms. A vortex is expected to be inherently unstable to acceleration. For example, corotating vortex pairs [149, 150, 151] and single vortices performing circular motion in homogeneous 2D superfluids [152, 153] are expected to decay via the emission of sound waves. However, this is thought to be prohibited in finite-sized BECs due to the wavelength of the radiation being larger than the system itself [152, 64]. The vortex line can become excited with long-wavelength oscillatory modes [101, 154], known from classical fluid dynamics as Kelvin waves [155], and these waves are predicted to slowly dissipate their energy via the emission of sound waves [88]. In the context of vortices in Helium II [27], vortex lines can cross, causing a dislocation and reconnection of the vortex lines, and this is thought to induce a burst of sound emission [87].

1.4.2 Dark solitary waves

Unlike a vortex, a dark solitary wave is not a topological defect and can disappear anywhere in the condensate in the presence of dissipation. A dark solitary wave tends to undergo oscillatory motion in a confined dilute BEC, and its relative motion with thermal cloud is predicted to cause dissipation via the scattering of thermal excitations off the density node [156]. This leads to a decrease in the density contrast and an increase in the oscillation amplitude [157, 158]. The solitary wave ultimately becomes so fast and shallow that it merges into the background fluid. Although this is a motional effect, one might expect a stationary soliton at the trap centre to become 'kicked' off-centre by fluctuations and so become prone to this dissipation mechanism. The rate of thermal dissipation depends strongly on the transverse size of the wave. In the experiment of Burger *et al.* [74], the soliton density contrast was observed to decay by around 50% in 10 ms. Here the trap geometry was relatively wide, and this timescale is consistent with the predicted thermodynamic lifetime [158]. However, in quasi-1D geometries, the thermodynamic lifetime is expected to be greatly enhanced, and to be of the order of seconds.

Quantum depletion of the condensate is expected to cause the soliton density notch to fill up with incoherent atoms [159]. This has also been proposed for the observed decrease in the soliton density contrast, and the predicted timescale for this process agrees with the experimental observation [74].

The dark soliton is also prone to dynamical instabilities. Firstly, since the dark soliton is strictly a *one-dimensional* solution, it is prone to a *transverse* instability when embedded in a 3D system as a dark solitary wave. For weak transverse confinement, the solitary wave plane can become torn into more stable 3D excitations, such as vortex rings and sound waves. This decay has been experimentally observed [76, 77], and is analogous to the *snake instability* of dark solitary waves in 2D or 3D optical media [160, 161, 162]. We will discuss the snake instability later in this thesis. However, under tight transverse confinement, i.e. in quasi-1D geometries, this decay route is expected to be heavily suppressed [157]. In geometries where the solitary wave is transversely unstable but the transverse width of the system is too small to support vortex rings, an excitation with soliton and vortex properties, known as a solitonic

vortex, is predicted to occur [163, 164].

Secondly, since the dark soliton is a solution within a *homogeneous* system, it is prone to a *longitudinal* dynamical instability when the density is inhomogeneous, as in the case of confined dilute BECs. Busch *et al.* [165] have considered the longitudinal motion of a dark soliton in a harmonically-confined BEC. They predict the soliton to be dynamically stable when the trap is purely harmonic, but when confined within an additional microtrap, the soliton decays gradually via the emission of sound waves. Furthermore, Huang *et al.* [166] have considered the motion of a dark soliton over a potential step in a condensate, and predict the emission of radiation from the soliton, and under certain conditions, disintegration into multiple dark solitons.

In nonlinear optics, the background on which the soliton propagates is generally homogeneous. However, an analogous longitudinal instability arises from modifications in the nonlinearity of the optical medium [129]. Such effects lead to the decay of the soliton via the emission of radiation [167].

Other forms of dynamical instability arise for dark solitons in atomic condensates. For example, in periodic optical lattice geometries the soliton is prone to an oscillatory instability [168, 169].

1.4.3 Effects in a finite-sized system

Dynamical instabilities in vortices and dark solitons generally induce the emission of sound waves. Dilute BECs are confined by traps, making them finite-sized, and this additionally confines the excitations to the system. From our point of view, a vortex or dark soliton in a confined BEC will typically co-exist with other excitations within the system, such as collective excitations and sound waves. The vortex/soliton is then not technically a vortex/soliton in the pure, unperturbed (mathematical) sense, but represents a region of space which includes a vortex/soliton and other excitations. It is not possible for us to resolve numerically the vortex/soliton from these co-existing excitations within the Gross-Pitaevskii formalism. However, this is not a significant problem since it is precisely the behaviour of this 'vortex/soliton region', including local excitations, which is probed experimentally.

1.5 Overview

This thesis explores the dynamics of quantized vortices and dark solitary waves in trapped dilute BECs, and in particular, their dynamical stability. Our motivation for studying quantized vortices is partly from a fundamental point of view, but also due to two experimental results. Both the decay of vortex tangles in liquid Helium [86] and the crystallisation of vortex lattices in dilute BECs [106] appear to be temperature-independent at sufficiently low temperatures where thermal dissipation is negligible. This suggests the occurence of dynamical dissipation mechanisms, but the nature of these processes is not well understood. The dynamical stability of dark solitary waves in trapped dilute BECs is interesting from a fundamental point of view. In addition, dark solitary waves are often considered as the 1D analogs of quantized vortices, and so may shed light on the dynamical stability of vortices.

To explore these dynamical instabilities we perform extensive numerical simulations using the time-dependent Gross-Pitaevskii equation. This model ignores thermal effects and so is well-suited for focussing on purely dynamical phenomena.

In chapter 2 we introduce the Gross-Pitaevskii equation, some basic properties of trapped dilute BECs, and their vortex and dark soliton solutions. Chapter 3 discusses the transverse dynamical instability of dark solitary waves, while chapters 4 and 5 consider the effect of longitudinal inhomogeneity on a dark solitary wave in both infinite-sized and harmonically-confined systems, respectively. The possibility of parametrically driving a dark solitary wave in a harmonically-confined condensate is presented in chapter 6. We then turn our attention to vortices in exploring the dynamics of vortices induced by inhomogeneous densities in chapter 7, and due to the presence of other vortices in homogeneous systems in chapter 8. In Chapter 9 we consider the dynamics of vortices in elongated geometries, and explore analogies to dark solitary waves. Chapter 10 presents some ideas for future work, and finally, chapter 11 presents the conclusions of this work.

The work in this thesis has been partially covered in the following publications:

- *Soliton-sound interactions in dilute Bose-Einstein condensates*,

N. G. Parker, N. P. Proukakis, M. Leadbeater and C. S. Adams,
Phys. Rev. Lett. **90**, 220401 (2003).

- *Deformation of dark solitons in inhomogeneous Bose-Einstein condensates*,
  N. G. Parker, N. P. Proukakis, M. Leadbeater and C. S. Adams,
  J. Phys. B **36**, 2891 (2003).

- *Coupling between topological excitations and the background sound field in atomic Bose-Einstein condensates*,
  N. P. Proukakis, N. G. Parker, C. F. Barenghi and C. S. Adams,
  Laser Physics **14**, 284 (2004).

- *Dynamical instability of a dark soliton in a quasi-one-dimensional Bose-Einstein condensate perturbed by an optical lattice*,
  N. G. Parker, N. P. Proukakis, C. F. Barenghi and C. S. Adams,
  J. Phys. B **37**, S175 (2004). Proceedings for "Theory of quantum gases and quantum coherence" (Levico, Italy, June 2003).

- *Analogies between dark solitons in atomic Bose-Einstein condensates and optical systems*,
  N. P. Proukakis, N. G. Parker, D. J. Frantzeskakis and C. S. Adams,
  J. Opt. B: Quantum Semiclass. Opt. **6**, S380 (2004).

- *Controlled vortex-sound interactions in atomic Bose-Einstein condensates*,
  N. G. Parker, N. P. Proukakis, C. F. Barenghi and C. S. Adams,
  Phys. Rev. Lett. **92**, 160403 (2004).

- *Parametric driving of dark solitons in atomic Bose-Einstein condensates*,
  N. P. Proukakis, N. G. Parker, C. F. Barenghi and C. S. Adams,
  Phys. Rev. Lett. **93**, 130408 (2004).

- *Decay of quantised vorticity by sound emission*,
  C. F. Barenghi, N. G. Parker, N. P. Proukakis and C. S. Adams,
  J. Low. Temp. Phys. accepted, cond-mat/0405635.

- *Dark soliton dynamics in confined Bose-Einstein condensates*,
  N. G. Parker, N. P. Proukakis and C. S. Adams,

Invited chapter for book *Progress in Soliton Research*, Nova Publishing (New York), expected in print in 2005.

Chapter 2

Theoretical Framework

An important feature of dilute Bose-Einstein condensates is that their zero-temperature dynamics can be parameterised by a macroscopic order parameter which satisfies a nonlinear Schrödinger equation, called the Gross-Pitaevskii equation. This versatile model has proven to give a good description of many static and dynamic properties of dilute Bose-Einstein condensates at low temperature [23, 24, 78, 79], and will form the basis of the numerical results presented in this thesis. In this chapter, we introduce the Gross-Pitaevskii equation, and discuss its solutions, including vortices and solitons.

2.1 The Gross-Pitaevskii equation

The theoretical work on confined Bose gases of weakly-interacting particles was pioneered by Gross [170] and Pitaevskii [171] in the late 1950's. This lead to the formulation of the Gross-Pitaevskii equation, which forms the basis of this work. Here we outline the origin of this important equation, while the full mathematical derivation is given in appendix A.

We consider a gas of N bosons. The many-body problem can be described within the framework of second quantization, where the second-quantized Hamiltonian for the Bose field operator $\hat{\Psi}$ is given by,

$$\hat{H} = \int \mathrm{d}^3\mathbf{r}\hat{\Psi}^\dagger(\mathbf{r})H_0\hat{\Psi}(\mathbf{r}) + \frac{1}{2}\int \mathrm{d}^3\mathbf{r}\int \mathrm{d}^3\mathbf{r}'\hat{\Psi}^\dagger(\mathbf{r})\hat{\Psi}^\dagger(\mathbf{r}')V_{\mathrm{int}}(\mathbf{r},\mathbf{r}')\hat{\Psi}(\mathbf{r}')\hat{\Psi}(\mathbf{r}). \quad (2.1)$$

Here, $V_{\mathrm{int}}(\mathbf{r},\mathbf{r}')$ is the two-body interaction potential, and $H_0 = -(\hbar^2/2m)\nabla^2 +$

V_{ext} is the single particle hamiltonian, where $V_{\text{ext}}(\mathbf{r})$ is the external potential. The operators $\hat{\Psi}^\dagger(\mathbf{r})$ and $\hat{\Psi}(\mathbf{r})$ represent the creation and annihilation of a particle at position $\mathbf{r}$, and satisfy the following equal-time commutation relations,

$$\left[\hat{\Psi}(\mathbf{r}), \hat{\Psi}^\dagger(\mathbf{r}')\right] = \delta(\mathbf{r} - \mathbf{r}'), \tag{2.2}$$

and,

$$\left[\hat{\Psi}(\mathbf{r}), \hat{\Psi}(\mathbf{r}')\right] = \left[\hat{\Psi}^\dagger(\mathbf{r}), \hat{\Psi}^\dagger(\mathbf{r}')\right] = 0. \tag{2.3}$$

Using Heisenberg's relation $i\hbar\partial\hat{\Psi}/\partial t = \left[\hat{\Psi}, \hat{H}\right]$ and the commutation relations for the field operators, we obtain the equation of motion,

$$i\hbar\frac{\partial\hat{\Psi}(\mathbf{r},t)}{\partial t} = H_0\hat{\Psi}(\mathbf{r},t) + \int \mathrm{d}^3\mathbf{r}'\hat{\Psi}^\dagger(\mathbf{r}',t)V_{\text{int}}(\mathbf{r},\mathbf{r}')\hat{\Psi}(\mathbf{r}',t)\hat{\Psi}(\mathbf{r},t). \tag{2.4}$$

Since Bose-Einstein condensation involves the macroscopic population of a single quantum state, it is appropriate to consider a mean-field approach. The Bose field operator is decomposed as,

$$\hat{\Psi}(\mathbf{r},t) = \psi(\mathbf{r},t) + \hat{\Psi}'(\mathbf{r},t), \tag{2.5}$$

where $\psi(\mathbf{r},t) \equiv \langle\hat{\Psi}(\mathbf{r},t)\rangle$ is the classical field (expectation value) of $\hat{\Psi}(\mathbf{r},t)$, and $\hat{\Psi}'(\mathbf{r},t)$ represents fluctuations about this value. In the context of BECs, the former quantity is a mean-field order parameter representing the condensed atoms, and is generally referred to as a macroscopic *wavefunction*. The latter quantity is associated with the non-condensed atoms, induced by thermal and quantum effects. A Bose-Einstein condensate is therefore a classical state of the atomic field, in a similar manner to the laser being a classical state of the electromagnetic field.

We assume the limit of zero temperature, such that the thermal component of the system is non-existent. Furthermore, due to the weakly-interacting nature ($a \ll \lambda_{\text{dB}}$) of the condensate, quantum depletion at zero temperature is expected to be minimal. It is then reasonable to neglect the non-condensed atoms $\hat{\Psi}'(\mathbf{r},t) \to 0$, and consider only the classical field $\hat{\Psi}(\mathbf{r},t) \to \psi(\mathbf{r},t)$. Note that the assumption of zero temperature is generally satisfied in reality for temperatures much less than the transition temperature for condensation.

If the gas is sufficiently dilute, the atomic interactions are dominated by low energy, two-body s-wave collisions. These collisions are characterised by a single

parameter, known as the s-wave scattering length a, and can be represented by a pseudo-potential of the form,

$$V_{\text{int}}(\mathbf{r}, \mathbf{r}') = g\delta(\mathbf{r} - \mathbf{r}'), \tag{2.6}$$

known as the *contact potential*. The scattering coefficient is given by,

$$g = \frac{4\pi\hbar^2 Na}{m}, \tag{2.7}$$

where m is the atomic mass. This condition is valid for $na^3 \ll 1$, where n is the atomic density, and this is typically fulfilled in current dilute BECs. Note that for $g < 0$ the interactions are effectively attractive, whereas for $g > 0$ they are effectively repulsive. Insertion of the pseudo-potential into equation (2.4) leads to the equation of motion in terms of the macroscopic mean-field wavefunction,

$$i\hbar\frac{\partial\psi(\mathbf{r}, t)}{\partial t} = \left(-\frac{\hbar^2}{2m}\nabla^2 + V_{\text{ext}}(\mathbf{r}, t) + g|\psi(\mathbf{r}, t)|^2\right)\psi(\mathbf{r}, t). \tag{2.8}$$

This time-dependent equation is known as the Gross-Pitaevskii equation (GPE) [79] after independent derivations by Gross [170] and Pitaevskii [171]. The GPE resembles the time-dependent Schrödinger equation apart from the nonlinear $|\psi|^2$ term, which arises due to the atomic interactions and has important effects on the properties of the system. The GPE is analogous to the cubic nonlinear Schrödinger equation (NLSE) employed in nonlinear optics to describe media with Kerr nonlinearity [172].

The chemical potential μ, that is, the energy associated with removing a particle from the system, characterises the ground state energy of the condensate. Time-independent solutions to the GPE may be written in the form $\psi(\mathbf{r}, t) = \phi(\mathbf{r})\exp[-i\mu t/\hbar]$, and the resulting time-independent equation is given by,

$$\left(-\frac{\hbar^2}{2m}\nabla^2 + V_{\text{ext}}(\mathbf{r}) + g|\phi(\mathbf{r})|^2\right)\phi(\mathbf{r}) = \mu\phi(\mathbf{r}). \tag{2.9}$$

The GPE has proven to give an excellent qualitative and quantitative description of many static and dynamic properties in dilute BECs at temperature much less than the transition temperature. Examples include the condensate density profile, dynamics under expansion, inteference effects, collective excitations and sound (see [79] for a review), vortices [64, 97, 100], and bright [71, 72, 173, 174, 175, 176] and dark solitary waves [74, 75, 76, 77]. Although

the GPE is a zero temperature model, it can be modified to include finite temperature and quantum effects (see for example [79]).

In this thesis, we employ the GPE to investigate the dynamics of dilute BECs. Due to the presence of the nonlinear term in the GPE, it is generally necessary to solve the equation by numerical means (although analytic solutions exist in certain limits). This is performed using the Crank-Nicholson numerical method [177]. The full details of our numerical methods are outlined in appendix B.

2.1.1 Integrals of motion

The integrals of motion of the Gross-Pitaevskii model are the total energy, number of particles, and momentum. We will only consider the two former quantities. The energy E of the system can be derived using the variational relation,

$$i\hbar\frac{\partial\psi}{\partial t} = \frac{\delta\varepsilon}{\delta\psi^*}, \tag{2.10}$$

where ε is the energy density, or energy functional, of the system. Using the Gross-Pitaevskii equation of equation (2.8) to evaluate the left-hand side of equation (2.10) and integrating over ψ^* leads to,

$$\varepsilon[\psi] = \left(\frac{\hbar^2}{2m}|\nabla\psi|^2 + V_{\text{ext}}|\psi|^2 + \frac{g}{2}|\psi|^4\right). \tag{2.11}$$

The total energy is then the integral of the energy functional over all space,

$$E = \int \mathrm{d}^3\mathbf{r}\ \varepsilon[\psi]. \tag{2.12}$$

The total number of particles in the system is defined to be,

$$N = \int \mathrm{d}^3\mathbf{r}|\psi|^2. \tag{2.13}$$

For a non-dissipative system and a time-independent potential, these integrals of motion are conserved.

2.1.2 Hydrodynamic equations

The GPE may be conveniently represented in terms of classical fluid dynamics by employing the Madelung transformation [178],

$$\psi(\mathbf{r},t) = \sqrt{n(\mathbf{r},t)}\exp[iS(\mathbf{r},t)], \tag{2.14}$$

where $n(\mathbf{r},t)$ is the fluid density and $S(\mathbf{r},t)$ represents a macroscopic phase factor. The gradient of the phase defines a fluid velocity via,

$$\mathbf{v}(\mathbf{r},t) = \frac{\hbar}{m}\nabla S(\mathbf{r},t). \tag{2.15}$$

The GPE is a fluid model which encapsulates equations familiar from classical hydrodynamics. Substituting equations (2.14) and (2.15) into the GPE and equating imaginary terms leads to a continuity equation,

$$\frac{\partial n}{\partial t} + \nabla(n\mathbf{v}) = 0. \tag{2.16}$$

Similarly, the real components lead to,

$$m\frac{\partial \mathbf{v}}{\partial t} + \nabla\left(V + ng + \frac{1}{2}mv^2 - \frac{\hbar^2}{2m\sqrt{n}}\nabla^2\sqrt{n}\right) = 0 \tag{2.17}$$

which resembles the classical Euler equation describing a inviscid compressible fluid. The only difference in the case of a quantum fluid is the last term on the left hand side, which represents the *quantum pressure* (see [179] for further discussion).

2.2 Time-independent solutions

An important feature of dilute BECs is the three-dimensional (3D) trapping used to confine spatially the atoms. This induces an inhomogeneous background density and a finite size to the system. The confinement is most commonly harmonic, formed by magnetic fields. However, other shapes of potential, including gaussian, quartic, step-like, and periodic lattice potentials, can be generated by magnetic and/or optical means.

2.2.1 Non-interacting regime

In the case of a non-interacting ($g = 0$) ideal gas confined by a 3D harmonic potential $V_{\text{ext}} = (m/2)(\omega_x^2x^2 + \omega_y^2y^2 + \omega_z^2z^2)$, the excitation states are the standard harmonic oscillator states. For example, the ground state has a gaussian density profile, as shown in figure 2.1 (dot-dashed line). For an interacting gas with sufficiently weak interactions, such that $Na/\bar{l} \ll 1$, where $\bar{l} = \sqrt{\hbar/(m\bar{\omega})}$ is the mean harmonic oscillator length and $\bar{\omega} = (\omega_x\omega_y\omega_z)^{1/3}$, the states are similar to the non-interacting case [79].

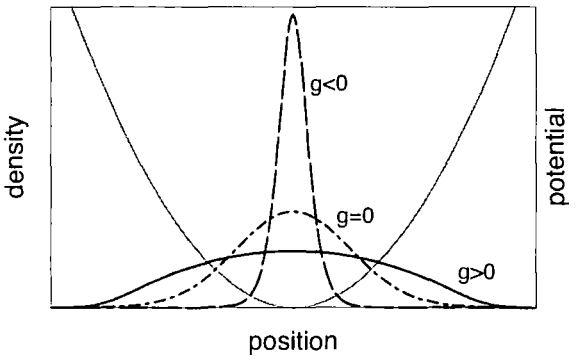

Figure 2.1: Schematic of the radial density profile (left axis) of a dilute BEC within a spherically symmetric harmonic trap, for repulsive interactions (solid line), attractive interactions (dashed line), and the non-interacting gas (dot-dashed line). The harmonic potential is illustrated (right axis, grey line). The area under the curves, representing the number of atoms, is the same in all three cases.

2.2.2 Interacting regime

Current dilute Bose-Einstein condensates reside in the opposing limit where $N|a|/\bar{l} \gg 1$ [79]. This is the regime of relatively strong interactions and/or large number of particles. Here, the atomic interactions tend to have a significant effect on the condensate density. For attractive interactions ($g < 0$) the density profile becomes narrower than the corresponding ground harmonic oscillator state, tending towards a sharp peak located at the trap centre, as illustrated in figure 2.1 (dashed line). For a large number of atoms and/or strong attractive interactions, the attraction dominates to the point that the condensate is prone to a catastrophic collapse [24, 50, 52, 180, 181].

Thomas-Fermi solution

For the case of repulsive interactions ($g > 0$), the density profile in a harmonic trap becomes broader than the corresponding ground harmonic oscillator state, as indicated in figure 2.1(solid line). In the limit of relatively strong interactions ($Na/\bar{l} \gg 1$), the kinetic energy term in the GPE can be neglected in comparison to the dominant interaction and potential terms. Then, the density profile can

be approximated by the Thomas-Fermi (TF) solution, which corresponds to,

$$n(\mathbf{r}) = \begin{cases} (\mu - V(\mathbf{r}))/g & \text{for} \quad \mu \geq V(\mathbf{r}) \\ 0 & \text{elsewhere.} \end{cases} \tag{2.18}$$

This provides a very useful analytic tool in the theoretical description of a condensate. The TF profile can be used to define an approximate perimeter to the condensate, which occurs where $V(\mathbf{r}) = \mu$. For example, in a spherically-symmetric harmonic trap of frequency ω_r, the Thomas-Fermi radius of the cloud is $R_{\mathrm{TF}} = \sqrt{2\mu/m\omega_r^2}$.

Healing at a hard wall

In a homogeneous ($V_{\mathrm{ext}} = 0$) system with repulsive interactions ($g > 0$), the GP hamiltonian consists of two terms: the kinetic energy $-(\hbar^2/2m)\nabla^2$ and the self-interaction energy ng. On dimensional grounds, the balance of these terms occurs on a length-scale given by,

$$\xi = \frac{\hbar}{\sqrt{mng}} = \frac{1}{\sqrt{4\pi na}}. \tag{2.19}$$

This distance defines the *healing* length of the fluid, which characterises the lengthscale over which the fluid density can respond to perturbations. For example, at a hard-wall boundary the fluid density becomes pinned to zero, and this transition region has a width of the order of ξ. For a boundary at $z = 0$, the solution in the z-direction has the form,

$$\psi(z) = \sqrt{n}\tanh(z/\xi), \tag{2.20}$$

where n is the peak (bulk) density.

2.3 Reduced dimensionality

By employing highly-anisotropic trap geometries it is possible to engineer the effective dimensionality of the condensate. Quasi-one-dimensional [37, 38, 39] and quasi-two dimensional [37, 40] condensates have been realized in elongated and flattened geometries, respectively. The reduced dimensionality leads to strong quantum fluctuations, which tend to destroy the macroscopic coherence

across the sample, creating a quasi-condensate [182, 183]. However, this effect becomes suppressed in the limit of very low temperature [184, 185].

Note that in Helium, effectively 2D superfluid systems have been achieved using atomically thin films of Helium II [27].

Quasi-1D regime

Consider a cylindrically-symmetric trap geometry $V(\mathbf{r}) = (m/2)(\omega_z^2 z^2 + \omega_r^2 r^2)$, where ω_z and ω_r are the longitudinal and radial trap frequencies, respectively. For $\omega_r \gg \omega_z$ and $\hbar\omega_r \gg \mu$, the condensate adopts a highly-elongated 'cigar'-shape, and the transverse high-energy modes of excitation become heavily suppressed. In this regime, the longitudinal dynamics, which are of relatively low energy, dominate the system and a quasi-1D condensate is formed. Note that at finite temperature, the equality $\hbar\omega_r \gg k_B T$ must also be satisfied to suppress thermal excitation of transverse modes.

In the quasi-1D limit, the heavily-suppressed radial component of the wavefunction tends towards the static harmonic oscillator ground state. It is then reasonable to decouple the wavefunction into the product of a time-dependent axial component and a time-independent transverse component, via $\psi(r, z, t) = \psi_r(r)\psi_z(z, t)$. Here, $\psi_r(r) = \sqrt{m\omega_r/\hbar\pi}\exp[-(m\omega_r r^2/2\hbar]$, where the prefactor is derived from the normalisation condition $\int |\psi(r)|^2 2\pi r \mathrm{d}r = 1$. Substituting these approximations into equation (2.12) for the system energy, and integrating out the dependence on r, we arrive at an effective 1D energy,

$$E_z = \int_z \left\{ \frac{\hbar^2}{2m}\left|\frac{\partial\psi_z}{\partial z}\right|^2 + \hbar\omega_r|\psi_z|^2 + V|\psi_z|^2 + \frac{g}{4\pi l_r^2}|\psi_z|^4 \right\} \mathrm{d}z. \tag{2.21}$$

The second term arises from an energy contribution of $\hbar\omega_r/2$ from each of the x- and y-components of the transverse harmonic oscillator ground state. The interaction term features a modified 1D coupling constant $g_{1D} = g/(2\pi l_r^2)$, where $l_r = \sqrt{\hbar/m\omega_r}$ is the transverse harmonic oscillator length [186].

Using the variational relation of equation (2.10) we arrive at a 1D time-dependent GPE,

$$i\hbar\frac{\partial\psi_z}{\partial t} = \left(-\frac{\hbar^2}{2m}\frac{\partial^2}{\partial z^2} + V + g_{1D}|\psi_z|^2 + \hbar\omega_r\right)\psi_z, \tag{2.22}$$

where the z-subscript on the longitudinal wavefunction has been dropped. The

$\hbar\omega_r$ term in equation (2.22) can be absorbed into the 1D chemical potential, which is then related to its 3D counterpart by $\mu_{1D} = \mu - \hbar\omega_r$. A 1D description of a highly-elongated quasi-1D condensate has been considered in [157, 158, 166, 187]. In the limit of no external potential term, the 1D GPE is identical in form to the integrable NLSE, and so will support the soliton solutions derived for the NLSE in the 1970's [188, 189].

Quasi-2D regime

For $\omega_z \gg \omega_r$ and $\hbar\omega_z \gg \mu$ (and $\hbar\omega_z \gg k_B T$ at finite temperatures), the condensate takes the form of a highly-flattened 'pancake'-shape. The tight confinement in the z-direction suppresses this degree of freedom, and the dynamics become effectively planar (in the radial plane). In this quasi-2D limit, the 3D system can be approximated by a 2D GPE. The 2D interaction coefficient is $g_{2D} = g/(\sqrt{2\pi}l_z)$, and the 2D chemical potential $\mu_{2D} = \mu - \hbar\omega_z/2$, where $\hbar\omega_z/2$ is the energy associated with the ground harmonic oscillator state in the z-dimension.

2.4 Excitations in BECs

2.4.1 Collective excitations

Homogeneous systems

The elementary excitations of the Bose gas can be analysed in terms of the Bogoliubov spectrum [10]. Weak perturbations of the wavefunction from its steady state solution are investigated by considering a trial wavefunction of the form,

$$\psi(\mathbf{r}, t) = e^{-i\mu t/\hbar}\left[\phi_0(\mathbf{r}) + u(\mathbf{r})e^{-i\omega t} + v^*(\mathbf{r})e^{i\omega t}\right], \tag{2.23}$$

where $\phi_0(\mathbf{r})$ is the time-independent background state, and $u(\mathbf{r})$ and $v(\mathbf{r})$ are complex amplitude functions. Insertion of this trial wavefunction into the GPE, and keeping terms linear in $u(\mathbf{r})$ and $v(\mathbf{r})$, leads to a set of coupled equations in terms of the excitation frequency ω,

$$\left[H_0 - \mu + 2g|\phi_0(\mathbf{r})|^2\right]u(\mathbf{r}) + g\phi_0(\mathbf{r})^2 v(\mathbf{r}) = \hbar\omega u(\mathbf{r}) \tag{2.24}$$

$$\left[H_0 - \mu + 2g|\phi_0(\mathbf{r})|^2\right] v(\mathbf{r}) + g\phi_0^*(\mathbf{r})^2 u(\mathbf{r}) \;=\; -\hbar\omega v(\mathbf{r}), \tag{2.25}$$

where H_0 is the single-particle hamiltonian. The full derivation of these equations is outlined in appendix C.

In a uniform system, u and v represent plane waves, and we find the Bogoliubov relation,

$$\hbar\omega = \sqrt{\frac{\hbar^2 k^2}{2m}\left(\frac{\hbar^2 k^2}{2m} + 2ng\right)}, \tag{2.26}$$

where k is the wavevector of the excitation. For small wavelengths ($\lambda < \xi$), the spectrum approaches that of a free particle, with $\hbar\omega = \hbar^2 k^2/(2m)$. For large wavelengths ($\lambda > \xi$), the dispersion relation is linear and phonon-like, with the form $\omega = ck$, where $c = \sqrt{ng/m}$. This is the regime of sound waves, and the parameter c represents the speed of sound.

Harmonically-confined systems

Due to the finite size of the condensate, *collective* excitations have two regimes depending on the wavelength of the excitation λ relative to the size of the condensate R. For $\lambda \ll R$, the excitations represent the sound waves known from uniform systems (providing $\lambda > \xi$ such that free particle excitations are not populated). The propagation of sound has been observed in a dilute BEC [190], with the speed of sound found to be consistent with the Bogoliubov prediction. For $\lambda \sim R$, the excitations are large-scale oscillations of the fluid. The lowest energy modes, representing standing phonon waves, come in the form of monopolar breathing oscillations, dipolar centre of mass oscillations, and quadrupolar oscillations of the atomic cloud. The dispersion law for these modes predicted using the Bogoliubov approach [191] is found to be in excellent agreement with experimental observations [192, 193, 194].

2.4.2 Vortices

Topological excitations in superfluids come in the form of vortex structures featuring quantized circulation. They are topological in the sense that they can only decay at the boundary of the system or under collision. In dilute BECs,

vortex structures have been observed in several forms, including single vortices [61, 62, 100, 102], vortex lattices [62, 84, 103] and vortex rings [76, 77].

Quantization of circulation

Under the Madelung transformation (equation (2.14)) the macroscopic wavefunction can be expressed in terms of a fluid density and a macroscopic phase. In order that the wavefunction remains single-valued, the phase around any closed contour C must be an integer multiple of 2π,

$$\int_C \nabla S \cdot d\mathbf{l} = 2\pi q, \tag{2.27}$$

where $q = 0, \pm 1, \pm 2, ...$ Since the gradient of the phase defines the local velocity flow via equation (2.15), this condition implies that the circulation about the contour C is given by,

$$\int_C \mathbf{v} \cdot d\mathbf{l} = q\left(\frac{h}{m}\right). \tag{2.28}$$

In other words, the circulation of fluid is quantized in units of $\kappa = h/m$. This constraint comes from the quantum mechanics associated with the macroscopic population of a single state. Any rotation of the fluid must be contained in the form of vortex lines featuring quantized circulation. Indeed, one finds that as a superfluid is rotated, the presence of vortices becomes energetically favourable above a critical rotation frequency [64, 82].

A quantized vortex can be represented by the form,

$$\psi(r) = \sqrt{n_v(r)}\exp(2\pi q i) \tag{2.29}$$

where r is the distance from the vortex centre and q is the topological charge of the vortex. The vortex density profile n_v, for which there is no analytic solution, is shown in figure 2.2 (black line) for a singly-quantized vortex. This profile is calculated numerically by propagating the 2D GPE in imaginary time subject to an azimuthal 2π-phase slip, as outlined in appendix B.

The circulating fluid velocity is given by $v = q\hbar/(mr)$. At the centre of the vortex, the phase singularity corresponds to infinite fluid rotation speed. In order to maintain a finite energy density, the fluid density is pinned to zero, and recovers to the bulk background density n_0 at a distance of the order of

several healing lengths. For comparison, the density profile obtained by simply pinning the density to zero (equation 2.20)) is also shown (grey line). The centrifugal effect of the rotating fluid leads to a slight expansion of the singly-quantized vortex profile in relation to the corresponding non-rotating profile. Although the density in the region of a vortex rapidly recovers to the bulk

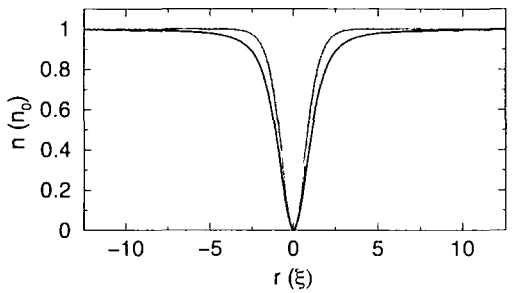

Figure 2.2: Density profile of a singly-quantized ($q = 1$) vortex (black line), and for the non-rotating case where the density is simply pinned to zero (grey line).

value with distance, the topological phase profile technically extends up to the boundary of the system. The vortex energy therefore depends strongly on the size of the system. In terms of classical hydrodynamics the vortex energy per unit line length is approximated by,

$$E_{\mathrm{V}} = \int_a^b \frac{1}{2} mnv^2 d\mathbf{r}^2 = \frac{mn\kappa^2}{4\pi} \ln\left(\frac{b}{a}\right), \tag{2.30}$$

where the lower cutoff is set by the vortex core size $a \sim \xi$ and the upper cutoff is the size of the system $b = L$ [27].

This work is concerned with the dynamical stability of vortices, and so it is useful to have a *local* indication of the vortex energy, e.g. to measure any transfer of energy between the vortex and the background condensate. In 2D we achieve this by numerical integration of the GP energy functional (equation (2.11)) in the region of the vortex, taken to be a circle of radius 5ξ about the vortex centre, and subtracting from this the corresponding contribution of the time-independent background density n_{TI}, i.e.

$$E_{\mathrm{V}} = \int_0^{5\xi} \varepsilon[\psi] 2\pi r \mathrm{d}r - \int_0^{5\xi} \varepsilon[\sqrt{n_{\mathrm{TI}}}] 2\pi r \mathrm{d}r. \tag{2.31}$$

This method of evaluating the vortex energy is described in appendix B. In the context of finite-sized BECs, the vortex region will typically contain sound

excitations. However, providing the energy of the vortex is not too small, these contributions to the energy will be small enough to be neglected.

2.4.3 Dark solitons

Due to their nonlinear nature, dilute BECs can support localised non-dispersive wavepackets known as bright [123] and dark solitons [124]. These nonlinear excitations have recently been observed in dilute BECs [71, 72, 73, 74, 75, 76, 77].

Soliton solutions of the integrable NLSE were first derived by Zakharov and Shabat in the 1970's [188, 189]. Physically, they represent localised 1D wavepackets that propagate without spreading due to a balance between dispersion and nonlinearity in the system, and for this reason they are often analogised to particles. Another characteristic property is that they emerge from collisions with their original shape and direction of propagation. Depending on whether the nonlinearity of the medium is attractive or repulsive, solitons come on bright and dark forms. Due to the instability of attractive condensates, repulsive condensates are most common, and so we are interested in the latter case.

Dark Solitons

Dark solitons are characterised by a notch in the ambient density and a non-trivial phase slip across their centre, and occur in repulsive (or defocussing) nonlinear media [124]. On a homogeneous background of density n, the wavefunction of a dark soliton with speed v and position $(z - vt)$ has the 1D form,

$$\begin{aligned} \psi_{\rm s}(z,t) &= \sqrt{n}\exp\left(-\frac{i\mu}{\hbar}t\right) \\ &\times \left\{\sqrt{1-\left(\frac{v}{c}\right)^2}\tanh\left[\sqrt{1-\left(\frac{v}{c}\right)^2}\frac{(z-vt)}{\xi}\right] + i\left(\frac{v}{c}\right)\right\}. \end{aligned} \tag{2.32}$$

The density and phase profile of a dark soliton for various speeds is illustrated in figure 2.3. The spatial extent of a dark soliton is characterised by the healing length ξ, with the soliton becoming slightly wider for higher speed. The soliton speed is intimately dependent on both the depth of the density depression $n_{\rm d}$ and the phase slip S across its centre via $v/c = \sqrt{1-(n_{\rm d}/n)} = \cos(S/2)$, where the maximum value is set by the Bogoliubov speed of sound $c = \sqrt{ng/m}$. In

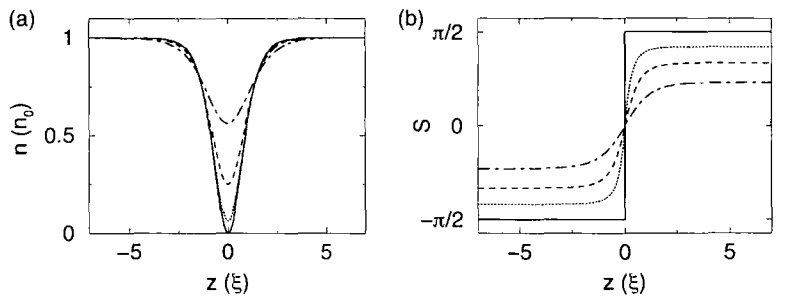

Figure 2.3: (a) Density n and (b) phase S profile of a dark soliton with speed $v/c = 0$ (solid line), 0.25 (dotted line), 0.5 (dashed line), and 0.75 (dot-dashed line).

the two limiting cases, a stationary *black* soliton has a node of zero density and a phase slip of π, whereas a soliton at speed c has no phase or density contrast and is indistinguishable from the background field.

Since a dark soliton represents an absence of particles, it has a negative effective mass. Note that, for weak forces and to first order, a dark soliton is predicted to behave like an effective classical particle of negative mass [131, 195, 196, 197].

Dark soliton integrals of motion

The dark soliton is an integrable solution of the 1D GPE in an infinite, homogeneous system, and has an infinite number of integrals of motion. The three integrals with clear physical meaning are the energy, linear momentum, and number of particles displaced by the soliton. We are only interested in the energy and number of particles. We can derive these soliton integrals using the GP integrals of motion given by equations (2.12) and (2.13). Although the GP integrals of the system will be infinite, we can subtract the contributions of the background field such that only the soliton part contributes. These renormalised soliton integrals of motion then become finite quantities given by [129],

$$E_{\mathrm{s}} = \frac{4}{3}\hbar n c \left[1 - \left(\frac{v}{c}\right)^2\right]^{\frac{3}{2}}, \tag{2.33}$$

and

$$N_{\mathrm{s}} = \left(\frac{2\hbar}{\sqrt{mg}}\right)\sqrt{1 - \left(\frac{v}{c}\right)^2}. \tag{2.34}$$

An important point is that a stationary soliton has maximum energy, while the $v = c$ soliton has essentially zero energy. This is consistent with the idea of a dark soliton having a negative effective mass.

Equation (2.33) is only valid in a homogeneous system. An alternative method to calculate the soliton energy is to integrate numerically the energy functional (equation (2.11)) across the soliton region, defined to be 5ξ either side of the soliton centre, and subtract from this the contribution of the background fluid, i.e.

$$E_{\rm s} = \int_{z_{\rm s}-5\xi}^{z_{\rm s}+5\xi} \varepsilon[\psi]{\rm d}z - \int_{z_{\rm s}-5\xi}^{z_{\rm s}+5\xi} \varepsilon[\sqrt{n_{\rm TI}}]{\rm d}z. \tag{2.35}$$

This method is valid for dark solitons in inhomogeneous systems, and is outlined in appendix B. In finite-sized BECs, the soliton region will in general contain additional excitations, e.g. sound waves. However, their contribution to this energy is expected to be small, providing the soliton is not of too low energy itself, and does not affect the results in this work.

2.5 Units

The atomic species with positive scattering length (repulsive interactions) which have been Bose condensed are listed in table 2.1, along with their mass, s-wave scattering length, and 3D scattering coefficient. Typically, dilute BECs contain around $N \sim 10^3 - 10^7$ atoms and have a peak density of $n \sim 10^{20}{\rm m}^{-3}$. The frequency of the harmonic traps used to confine the atoms range from several Hz up to several kHz. These numbers relate to a healing length of the order of a micron, and a speed of sound of the order of a millimeter-per-second. For example, in the ^{23}Na BEC experiment of Andrews *et al.* [190], the speed of sound was directly measured to be $c \sim 5{\rm mm\ s}^{-1}$, and the healing length inferred to be $\xi \sim 0.2\mu{\rm m}$.

Out of the fifty or so condensate experiments worldwide, the majority are formed with ^{87}Rb and ^{23}Na atoms. Additionally, vortices and dark solitons have only been realized with these atoms. Therefore, we will concentrate on parameters relating to these two atomic species.

Atom	m (10^{-27}kg)	a (nm)	g (10^{-50})
^{1}H	1.67	0.1 [198, 199]	0.55
^{4}He	6.64	16.0 [30]	33.60
^{23}Na	38.18	2.8 [200, 201]	1.03
^{41}K	68.06	4.0 [31]	0.82
^{87}Rb	144.42	5.8 [202]	0.56
^{133}Cs	220.78	23.3 [32]	1.48
^{174}Yb	288.84	~2 [33]	~0.1

Table 2.1: Table of the mass m, s-wave scattering length a, and 3D scattering coefficient g for the atomic species that have been Bose condensed with positive scattering length (repulsive interactions). Note that these cases apply in the absence of a static magnetic field. The presence of static magnetic fields can greatly modify the scattering length via the molecular Feshbach resonance. For example, a condensate of ^{85}Rb has been formed with positive scattering length in the range $a \sim 0 - 80$nm [51], although in zero field ^{85}Rb has negative scattering length.

2.5.1 Natural units

In a *homogeneous* system, the natural unit of length x is the healing length ξ. Energy ε is then expressed in units of the chemical potential μ, and speed v in terms of the speed of sound c. We call these *natural* units. Importantly, they can also be applied to trapped systems. The rescaled quantities, denoted by tildes, are expressed as,

$$\tilde{x} = x/\xi \qquad \tilde{\varepsilon} = \varepsilon/\mu \qquad \tilde{v} = v/c. \tag{2.36}$$

It follows that time t and frequency ω are rescaled as,

$$\tilde{t} = t/(\xi/c) \qquad \tilde{\omega} = \omega/(c/\xi). \tag{2.37}$$

Furthermore, the density is expressed in units of the homogeneous density n, such that the wavefunction becomes rescaled via $\tilde{\psi} = \psi/\sqrt{n}$. In these units, the GPE of equation (2.8) reduces to the dimensionless form,

$$i\frac{\partial\tilde{\psi}}{\partial\tilde{t}} = \left(-\frac{1}{2}\nabla^2 + \tilde{V}_{\text{ext}} + |\tilde{\psi}|^2\right)\tilde{\psi}. \tag{2.38}$$

In a homogeneous system, the quantities ξ, μ and c are fixed to the homogeneous values, while, in a confined system the peak values are taken. For a 3D dilute

BEC of ^{23}Na (^{87}Rb) atoms, with typical density $n \sim 10^{20}$ m^{-3} and scattering coefficient $g \sim 10^{-50}$ Jm^{-3}, these quantities correspond to $\xi = 0.54$ (0.28) μm, $\mu = 10^{-30}$ J and $c = 5.1$ (2.6) mm s^{-1}. The time parameter is $(\xi/c) = 10^{-4}$ s.

For comparison, in Helium II the values of the atomic density, healing length and speed of sound are measured to be $n = 2.18 \times 10^{28}$ m^{-3}, $\xi = 0.18$nm, and $c = 238$ms^{-1}, respectively. Then, the chemical potential is $\mu = 7.4 \times 10^{-21}$J and time parameter is $(\xi/c) = 7.5 \times 10^{-10}$s.

2.5.2 Harmonic oscillator units

In the context of harmonically-confined BECs, harmonic oscillator units are most commonly used. Here, energy is expressed in terms of the harmonic oscillator energy $\hbar\omega$, where ω is the trap strength, length in units of the harmonic oscillator length $l = \sqrt{\hbar/m\omega}$, and time in terms of ω^{-1}, such that,

$$\tilde{\varepsilon}_{\mathrm{HO}} = \varepsilon/(\hbar\omega) \qquad \tilde{x}_{\mathrm{HO}} = x/l \qquad \tilde{t}_{\mathrm{HO}} = t\omega. \tag{2.39}$$

Furthermore, the wavefunction is rescaled such that its norm is equal to unity.

To make our quantities meaningful to a BEC experimentalist, we outline the inter-conversion between natural and harmonic oscillator quantities. It is trivial to show that energy, length and time in harmonic oscillator form are related to the natural quantities via,

$$\tilde{\varepsilon}_{\mathrm{HO}} = \tilde{\varepsilon}/\tilde{\omega} \qquad \tilde{l}_{\mathrm{HO}} = \sqrt{\tilde{\omega}}\tilde{l} \qquad \tilde{t}_{\mathrm{HO}} = \tilde{\omega}\tilde{t}, \tag{2.40}$$

where $\tilde{\omega}$ is the trap frequency in natural units.

2.5.3 Natural units in reduced dimensions

In this thesis we employ the 1D and 2D GPE to describe the dynamics of quasi-1D and quasi-2D condensates, since they are much less demanding computationally than a full 3D description. Here we outline how to relate 1D and 2D parameters to physical 3D quantities.

Natural units in one-dimension

The 1D parameters in the 1D GPE, e.g. chemical potential and healing length, are specified by the 1D density n_{1D} and scattering coefficient g_{1D}. As outlined in section 2.3, the 1D GPE arises from assuming an elongated quasi-1D condensate with tight radial harmonic trapping ω_r. The 1D scattering coefficient is given by $g_{1D} = g/(2\pi l_r^2)$ where $l_r = \sqrt{\hbar/(m\omega_r)}$. For a chosen atomic species, g is known (see table 2.1), while ω_r is a free parameter (within the bounds of realistic trap frequencies). The 1D density in elongated condensates is typically $n_{1D} \sim 10^8 \mathrm{m}^{-1}$ [37].

Once n_{1D} and g_{1D} are known all other quantities can be evaluated, e.g. the natural longitudinal trap frequency $\tilde{\omega}_z$ relates to a real frequency of,

$$\omega_z = \frac{n_{1D} g_{1D}}{\hbar} \tilde{\omega}_z = \frac{m n_{1D} g}{2\pi\hbar^2} \tilde{\omega}_z \omega_r. \tag{2.41}$$

Table 2.2 shows how the natural quantities used in the 1D simulations relate to realistic quantities for ^{23}Na and ^{87}Rb quasi-1D condensates. We consider several different transverse frequencies, and for each case show how some typical values of $\tilde{\omega}_z$ used in this work relate to real longitudinal frequencies. Similarly, the corresponding values of the healing length ξ, speed of sound c, time unit (ξ/c), harmonic oscillator length l_z and 1D chemical potential μ_{1D} are listed.

ω_r (Hz/2π)	$\tilde{\omega}_z$	ω_z (Hz/2π)	ξ (μm)	c (mm s^{-1})	ξ/c (10^{-5}s)	l_z (μm)	μ_{1D} (10^{-30}J)
5000	$\sqrt{2}\times10^{-2}$	38 (73)	0.4 (0.2)	6.7 (5.0)	6 (3)	3.4 (1.8)	1.8 (3.4)
	$\sqrt{2}\times10^{-1}$	380 (730)	0.4 (0.2)	6.7 (5.0)	6 (3)	1.1 (0.6)	1.8 (3.4)
2500	$\sqrt{2}\times10^{-2}$	19 (38)	0.6 (0.2)	4.8 (3.5)	12 (6)	4.8 (2.5)	0.9 (1.7)
	$\sqrt{2}\times10^{-1}$	190 (370)	0.6 (0.2)	4.8 (3.5)	12 (6)	1.5 (0.8)	0.9 (1.7)
1000	$\sqrt{2}\times10^{-2}$	8 (15)	0.9 (0.3)	3.0 (2.2)	30 (16)	7.6 (3.9)	0.4 (0.7)
	$\sqrt{2}\times10^{-1}$	76 (150)	0.9 (0.3)	3.0 (2.2)	30 (16)	2.41(1.23)	0.4 (0.7)

Table 2.2: Typical conversion of 1D natural quantities to real quantities, for a ^{23}Na (^{87}Rb) quasi-1D condensate, for three values of the transverse trap frequency ω_r. The linear 1D density is taken to be $n_{1D} = 10^8 \mathrm{m}^{-1}$.

ω_z (Hz/2π)	$\tilde{\omega}_r$	ω_r (Hz/2π)	ξ (μm)	c (mm s^{-1})	$\xi/c(10^{-5}$s)	$l_r(\mu$m)	$\mu_{2D}(10^{-30}$J)
5000	$\sqrt{2}\times10^{-2}$	72 (140)	0.5 (0.2)	5.9 (4.3)	7.9 (4.0)	2.5 (0.9)	1.3 (2.6)
	$\sqrt{2}\times10^{-1}$	720 (1400)	0.5 (0.2)	5.9 (4.3)	7.9 (4.0)	0.8 (0.3)	1.3 (2.6)
	$2\sqrt{2}\times10^{-1}$	1440 (2800)	0.5 (0.2)	5.9 (4.3)	7.9 (4.0)	0.6 (0.2)	1.3 (2.6)
2500	$\sqrt{2}\times10^{-2}$	51 (99)	0.6 (0.2)	4.9 (3.7)	11.2 (5.7)	2.9 (1.1)	1.0 (1.8)
	$\sqrt{2}\times10^{-1}$	510 (990)	0.6 (0.2)	4.9 (3.7)	11.2 (5.7)	0.9 (0.3)	1.0 (1.8)
	$2\sqrt{2}\times10^{-1}$	1020 (1980)	0.6 (0.2)	4.9 (3.7)	11.2 (5.7)	0.7 (0.2)	1.0 (1.8)
1000	$\sqrt{2}\times10^{-2}$	32 (63)	0.7 (0.3)	4.0 (2.9)	17.7 (8.9)	3.7 (1.4)	0.6 (1.2)
	$\sqrt{2}\times10^{-1}$	32 (630)	0.7 (0.3)	4.0 (2.9)	17.7 (8.9)	3.7 (1.4)	1.2 (0.4)
	$2\sqrt{2}\times10^{-1}$	640 (890)	0.7 (0.3)	4.0 (2.9)	17.7 (8.9)	0.8 (0.3)	1.2 (0.4)

Table 2.3: Typical conversions between 2D natural quantities and their physical counterparts for a ^{23}Na (^{87}Rb) quasi-2D condensate, for three values of ω_z. The 2D density is taken to be $n_{2D} = 10^{14}\mathrm{m}^{-2}$.

Natural units in two-dimensions

Similarly, for the 2D GPE, the relevant parameters to evaluate are the 2D density n_{2D} and the 2D scattering coefficient g_{2D}. Assuming a quasi-2D condensate, with tight transverse harmonic trapping ω_z, the 2D scattering coefficient is given by $g_{2D} = g/\sqrt{2\pi}l_z$, which is known once an atomic species and transverse frequency ω_z are chosen. The 2D density for dilute BECs is typically $n_{2D} \sim 10^{14}\text{m}^{-2}$. All other quantities can now be derived from n_{2D} and g_{2D}. For example, for a cylindrically-symmetric pancake BEC, the planar frequency ω_r is given by,

$$\omega_r = \frac{n_{2D}g_{2D}}{\hbar}\tilde{\omega}_r = \frac{mn_{2D}g}{\sqrt{2\pi\hbar^3}}\sqrt{\tilde{\omega}_z}\tilde{\omega}_r, \tag{2.42}$$

where $\tilde{\omega}_r$ is the radial planar frequency in natural units. Table 2.3 shows how typical 2D natural parameters relate to physical quantities for a ^{23}Na (^{87}Rb) quasi-2D condensate.

2.6 Summary

In this chapter we have presented the theoretical framework for this thesis. We have derived the Gross-Pitaevskii equation for describing a dilute Bose-Einstein condensate at zero temperature. By employing restricted trap geometries, the effective dimensionality of the system can be engineered to create quasi-one-dimensional and quasi-two-dimensional condensates. Under such geometries, we have shown how the three-dimensional Gross-Pitaevskii equation can be reduced to its one-dimensional and two-dimensional forms. The work in this thesis is based on the numerical simulation of the Gross-Pitaevskii equation, from one to three dimensions, with the numerical methods described in Appendix B. Furthermore we have introduced vortex and dark soliton solutions, and described their basic properties.

Chapter 3

Transverse instability of a dark solitary wave

Dark solitons are strictly 1D objects and feature an instability when embedded in a 2D or 3D systems as dark solitary waves. This phenomenon, known as the *snake-instability*, was first observed in the field of nonlinear optics [160, 161, 162]. Here, in planar waveguides or bulk media, where the optical system is effectively 2D or 3D, the rectilinear dark soliton stripe is subject to a long-wavelength transverse instability. This leads to the break-up of the soliton stripe and creation of optical vortex solitons with alternate charge. More recently, the matter-wave analog of this instability has been verified in atomic BECs [76, 77]. In these experiments, the dark solitary wave, initially in the form of a linear stripe in the 3D system, was observed to bend and contort as it moved through the atomic fluid. The wave was ultimately and catastrophically torn into moving vortex rings and sound waves, which represent stable 3D excitations.

The dynamical stability of a dark solitary wave in a trapped BEC due to transverse effects has been the subject of much theoretical discussion. Using linear stability analysis of the Bogoliubov equations to probe the transerve stability of stationary dark solitary waves in BEC, Muryshev *et al.* [157] and Feder *et al.* [203] identify a regime of stability in elongated traps at low density or high aspect ratio, i.e. the quasi-1D regime. Outside this regime, the transverse instability is predicted to occur by means of decay into more stable vortex structures. This decay channel is due to the existence of a mode in the system

with imaginary frequency components [163, 203]. At first, the decay products were predicted to be pairs of vortices with opposing charge [157], in analogy to the snake instability in nonlinear optics [162], but this was corrected to three-dimensional vortex rings [203]. Soon after, the decay of an atomic dark solitary wave into vortex rings was observed experimentally [76, 77]. Note that simulations of the GPE are shown to give good agreement with the observed decay.

In a later paper, Muryshev *et al.* extended their earlier results to consider the transverse stability of *moving* dark solitary waves in elongated BECs. They showed that the stability is dependent on the speed of the wave, with slow solitons being most prone and fast solitons having enhanced stability [158]. Several theoretical works have considered the form of dark soliton-like excitations in waveguide geometries. Brand *et al.* [163, 164] have shown that departure from the quasi-1D regime leads to the emergence of a stationary state with lower energy than the corresponding stationary dark soliton. This state, known as a solitonic vortex, is a single deformed vortex with solitonic properties, and represents the smallest possible decay product. Less restrictive transverse confinement opens further decay channels involving the formation of vortex rings and/or solitonic vortices [204, 205]. Note that we consider the relation between vortices, dark solitary waves and solitonic vortices in chapter 9.

In this chapter we aim to illustrate the effect of the transverse degree of freedom on a dark solitary wave in a 3D BEC, showing the snake instability of the wave under weak transverse confinement, and demonstrate how this decay mechanism can become suppressed under tight transverse confinement. The majority of this work has been covered in [206, 207].

3.1 Snake instability of a dark solitary wave

The transverse instability of a dark solitary wave in a trapped BEC can be studied by monitoring the evolution of a dark solitary wave in a 3D harmonic trap. We consider a cylindrically-symmetric harmonic trap, with frequencies ω_z and ω_r, where z and r denote the longitudinal and radial directions respectively. This enables us to use the cylindrically-symmetric GPE (in the z-r plane) to

describe the 3D system, which is computationally less demanding than the full 3D GPE. The cylindrically-symmetric GPE is outlined in appendix B. Note that the ensuing dynamics are not strictly 3D since they are constrained by the cylindrical-symmetry.

Under a 1D description, using the 1D GPE of equation (2.22), the initial soliton state can be introduced using the analytic soliton solution of equation (2.33). However, in a 3D condensate the nonlinearity becomes a function of the transverse trap frequency, and so the corresponding soliton solution deviates from equation (2.33) by non-trivial scalings. Therefore, we generate our initial dark solitary wave by propagating the GPE in imaginary subject to an enforced axially-symmetric π-phase step. This generates an axially-symmetric dark solitary wave which is initially stationary.

Although this chapter deals with the effect of a transverse degree of freedom on the dark solitary wave in a harmonically-confined BEC, we must briefly mention the longitudinal dynamics. Due to its particle-like behaviour, a dark soliton in 1D is predicted to follow, to first order, a classical trajectory [131, 195, 196, 197]. In particular, a dark soliton under harmonic confinement is expected to oscillate back and forth in the trap [131, 165]. If a stationary dark soliton is initially created off-centre in the trap it will experience a force causing it to accelerate towards the trap centre. The depth of the soliton density depression stays, to first order, constant, such that, as the soliton accelerates towards the trap centre, the density of the soliton minimum increases. After the soliton has passed through the trap centre, it becomes decelerated, and accordingly the density of the soliton minimum decreases. At the point where the soliton touches zero density, the soliton reverses direction. Note that, at the trap centre the density and potential are locally homogeneous. Here, a stationary black soliton represents a time-independent solution to the GPE and will remain fixed.

Figure 3.1 illustrates the density and phase of a dark solitary wave in a dilute BEC under slightly-elongated harmonic confinement, $\omega_r > \omega_z$. The plots are shown in the $r-z$ plane. Note that, although the radial coordinate r technically extends from 0 to some maximum value $r_{\max}$, we have plotted the radial axis from $-r_{\max}$ to $+r_{\max}$ (rather than 0 to $r_{\max}$) as a visual aid, i.e. included the mirror image about the z-axis.

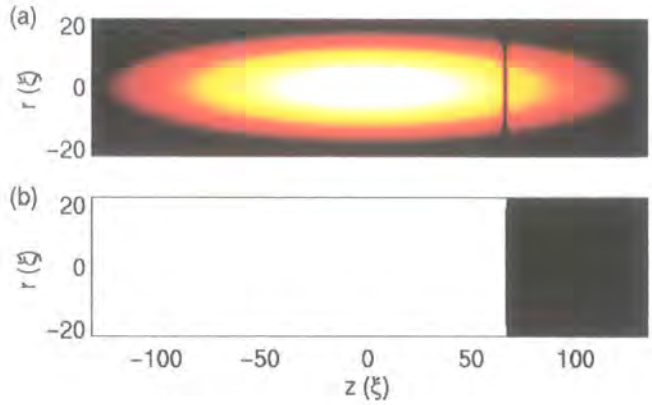

Figure 3.1: Planar view of (a) density and (b) phase of a stationary off-centre dark solitary wave in a condensate confined in a cylindrically-symmetric 3D harmonic trap. Here z denotes the longitudinal and r the transverse directions. The dark soliton plane is rectilinear, oriented along the r-direction, and located at the longitudinal position $z = 66\xi$. It appears as a notch of zero density and a longitudinal phase step of π. The trap frequencies are $\omega_z = \sqrt{2} \times 10^{-2}(c/\xi)$ and $\omega_r = 7\omega_z$. Note that, in the density (phase) scale, white represents maximum density n_0 $(\pi/2)$ and black represents zero $(-\pi/2)$. Also note that the radial axis is plotted from $-r_{\max}$ to $+r_{\max}$ (rather than 0 to $r_{\max}$) as a visual aid, i.e. included the mirror image about the z-axis.

The first point to note is that the cylindrically-symmetric harmonic confinement induces an elliptical shape and an inhomogeneous density distribution, with the density reaching a peak value n_0 at the trap centre (z=r=0) and decreasing with distance from the origin. The solitary wave is stationary, located off-centre in the longitudinal direction, and appears as a plane of zero density (figure 3.1(a)) and an abrupt phase slip of π (figure 3.1(b)).

The geometry of the system in figure 3.1 is weakly elongated, featuring a trap aspect ratio of $\omega_r/\omega_z = 7$, but the system is still 3D in character. The evolution of this dark solitary wave from its initial state is illustrated in figure 3.2 by consecutive snapshots of the soliton density (figure 3.2(a)) and phase (figure 3.2(b)). As the soliton starts to move towards the trap centre, the soliton plane, which is initially linear, becomes excited transversely. This begins as a gradual bending of the soliton plane, as shown in figures 3.2(i)-(ii). This bending arises from the inhomogeneous transverse density profile of the condensate. Since the

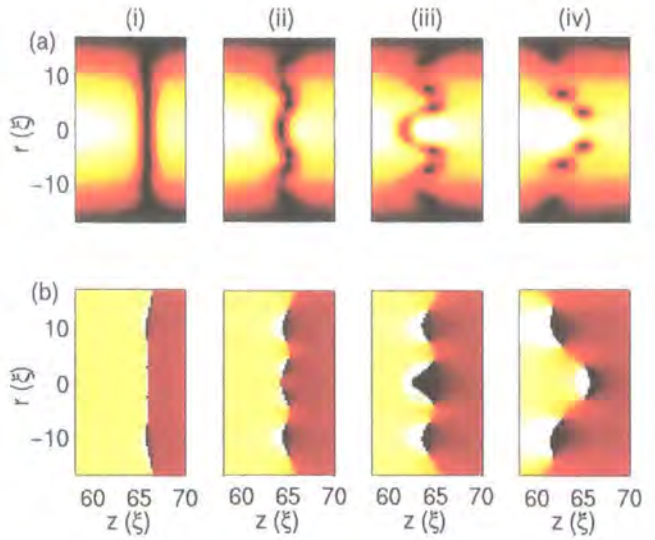

Figure 3.2: Close-up snapshots of (a) density and (b) phase profiles for the initial soliton configuration shown in figure 3.1, showing the evolution of the snake instability. Successive images correspond to $t \approx$ (i) 15, (ii) 23, (iii) 27 and (iv) 39 (ξ/c). In (iv), the dark soliton has already decayed into three concentric vortex rings, evident from the corresponding phase profile.

speed of sound is related to the density, via $c = \sqrt{ng/m}$, and the transverse density is at a maximum at $r = 0$ and decreases with r, the solitary wave propagates fastest along the $r = 0$ axis and slower away from the centre. The soliton plane therefore tends to become slightly curved as it propagates, and this was observed experimentally in [75]. Subsequently, the soliton plane becomes torn apart, creating vortex rings and a burst of sound waves. By the final snapshot of figure 3.2(iv), three concentric vortex rings are produced. Since figure 3.1 represents a density cross-section in the r-z plane, each vortex ring appears as a 2D vortex-antivortex pair, located symmetrically about the $r = 0$ axis. Each vortex is characterised by a node in the density and an azimuthal 2π-phase slip, representing the circulating velocity field. Note that the density and phase profile of an isolated vortex-antivortex pair in a 2D homogeneous system is shown in figure 8.4. Following the soliton decay in figure 3.2 the adjacent vortex rings have opposite polarity and initially propagate in opposing directions. The inner ring in figure 3.2(iv) propagates to the left, the middle ring to the right, and the outer ring to the left, with all three rings propagating

with different speeds due to their varying radii and background densities. In this 3D system, vortex rings represent stable excitations [208, 209], in contrast to the unstable solitary wave. Similarly, in nonlinear optics, the snake instability results in the decay of the solitary wave into optical vortex solitons of opposing charge [162].

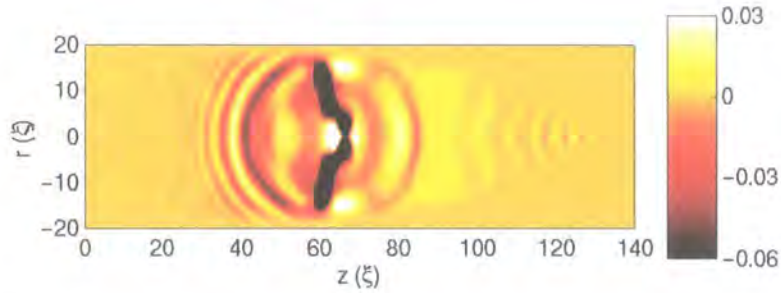

Figure 3.3: Density plot of renormalised density (actual density minus the time-independent background density) for the case corresponding to figure 3.2(iv). A burst of sound waves is radiated during the transverse decay of the solitary wave. The vortex rings are represented by the darkest region in the plot.

The sound emission from the decay of the solitary wave is not visible on the scale of figure 3.2. In order to visualise these low amplitude excitations we consider the *renormalised* condensate density, that is, the actual density minus the time-independent background. Figure 3.3 shows the renormalised density following the decay of the solitary wave, and corresponds to the case of figure 3.2(iv). On this expanded density scale, the three vortex rings appear as a black band of low density located around $z \approx 65\xi$. We clearly observe the sound waves that were emitted during the decay of the solitary wave into rings. These waves propagate outwards at the speed of sound, and have an amplitude of around $0.05n_0$. Due to the radial dependence of the speed of sound, the sound waves become bow-shaped. At a later time the sound waves will reflect off the condensate edge and reinteract with vortex rings. However, the solitary wave does not reform, and the sound waves only have a minor backaction on the motion of the vortex rings.

Due to the axial-symmetry of the initial solitary wave, and the lack of a symmetry-breaking process in the GPE, the transverse decay remains axially-symmetric at all times in both the density and phase. For example, the vortex rings

that are produced are always cylindrically-symmetric. Brand's solitonic vortex [163, 164], and the combinations of solitonic vortices and vortex rings discussed in [204, 205, 210] are not cylindrically-symmetric, and therefore cannot be produced in the decay of a cylindrically-symmetric dark solitary wave under the zero temperature description of the GPE. Where Brand *et al.* simulated the decay of a dark solitary wave into a solitonic vortex using the GPE, the system was seeded with white noise which serves to break the symmetry [163]. In a real system symmetry-breaking processes do occur, for example, thermal and quantum fluctuations, trap imperfections, etc, and this will open such decay channels.

3.2 Effect of transverse confinement

If the transverse trap frequency is large, the transverse modes of excitation in the system will require a large amount of energy to be excited, and the snake instability will become suppressed. In such a quasi-1D condensate, a dark solitary wave is expected to become stable to the transverse decay mechanism [157]. Similarly, in the context of nonlinear optics, the use of finite-size beams and narrow waveguides can heavily suppress transverse effects. An alternative method of suppressing the snake instability is to bend the soliton plane into a ring-shape. Such 'ring dark solitons' have recently been observed in optics [211] and are expected to be supported in BECs [212].

To highlight the crucial dependence of the soliton stability on the transverse confinement, we consider the evolution of an initially off-centre dark solitary wave under various transverse trap strengths. Figure 3.4(a) shows the density of the condensate when the solitary wave or its main decay product (the highest energy vortex ring) reach the centre of the trap. In addition, figure 3.4(b) shows the close-up phase profile in the region of the solitary wave or vortex ring, allowing us to discriminate between the two states. Note that the vortex rings and solitary waves in general travel at different speeds, and so the cases (i)-(iii) correspond to different times.

The topmost case (figure 3.4(i)) corresponds to the unstable 3D case examined in figures 3.1-3.2, with a weak aspect ratio of $\omega_r/\omega_z = 7$. Here the solitary wave

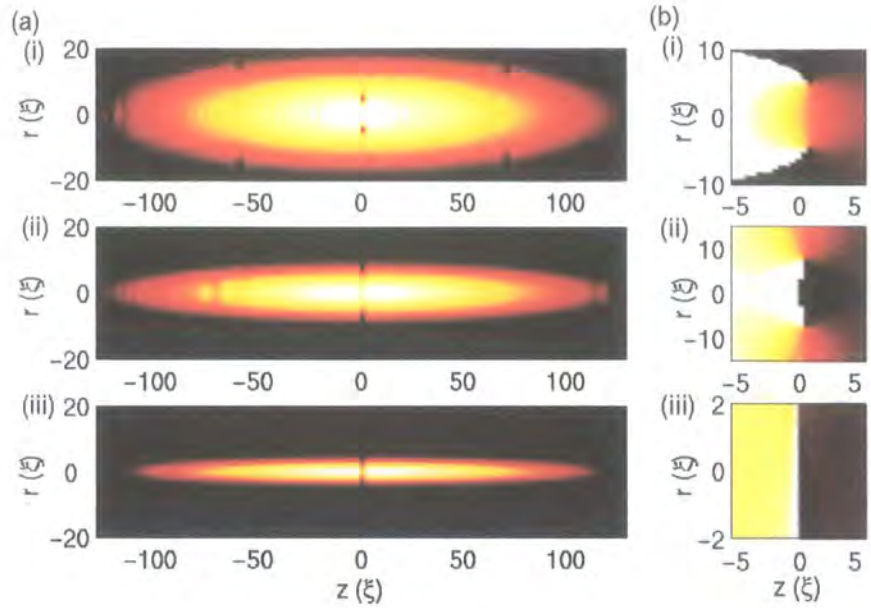

Figure 3.4: (a) Density and (b) close-up phase profiles showing the evolution of an initially stationary off-centre dark solitary wave under different transverse confinement. Each simulation starts with the solitary wave located at $z = 66\xi$, while the images shown correspond to when the solitary wave, or its main decay product, reach the centre of the trap, at times of (i) 279, (ii) 193 and (iii) 160 (ξ/c). The longitudinal trap frequency is kept constant at $\omega_z = \sqrt{2} \times 10^{-2}(c/\xi)$. (i) $\omega_r/\omega_z = 7$: soliton decays into three vortex rings. (ii) $\omega_r/\omega_z = 14$: soliton decays into one vortex ring. (iii) $\omega_r/\omega_z = 35.5$: the soliton is stable to the snake-instability and remains effectively 1D in character.

decays into three vortex rings, with the central vortex ring evident in figure 3.4(b)(i) by the 2π phase singularities locate symmetrically about the central axis. Tightening the transverse confinement leads to a decrease in the bending of the soliton plane and suppresses the snake instability. This reduces the number of vortex rings produced. For an intermediate aspect ratio of $\omega_r/\omega_z = 14$, the wave has evolved into only one vortex ring, as shown in figure 3.4(b)(ii), with the characteristic vortex phase shown in figure 3.4(b)(ii). However, for a sufficiently large aspect ratio of $\omega_r/\omega_z = 35.5$, the solitary wave stays intact after the fixed evolution time (figure 3.4(c)) and remains 1D in nature. This is confirmed by the phase of the object, shown in figure 3.4(b)(iii), which remains step-like. Even after very long evolution times, involving many oscillations of

the solitary wave in the trap, we observe no overall decay of the solitary wave, implying that, in this regime, the transverse decay is completely suppressed.

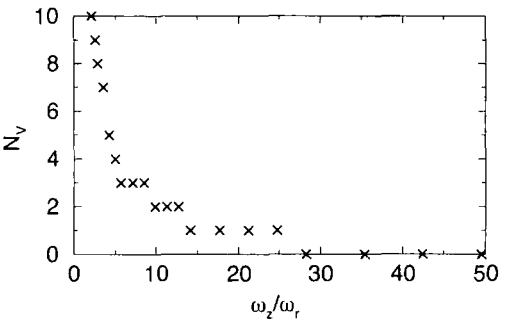

Figure 3.5: Number of vortex rings N_V formed in the decay of a dark solitary wave as a function of the trap ratio ω_r/ω_z. The stationary dark solitary wave is initially created off-centre at $z = 66\xi$, and the longitudinal trap frequency is kept fixed at $\omega_z = \sqrt{2} \times 10^{-2}(c/\xi)$.

The effect of the transverse confinement on the solitary wave is further exhibited in figure 3.5 which shows the number of vortex rings produced over a range of trap aspect ratios. This plot corresponds to a particular longitudinal trap frequency and initial soliton state, with the solitary wave formed at a fixed distance from the trap centre. Note that a wave initially formed at a different point in the trap, or in a trap with different longitudinal frequency, will have a different energy, and so will tend to produce a different number of vortex rings. However, the qualitative dependence will be the same for all initial configurations. For $\omega_r/\omega_z > 30$, the solitary wave remains intact. For $\omega_r/\omega_z < 30$, we observe the production of vortex rings, with the number of vortex rings increasing in a step-like manner as ω_r is decreased. Decreasing ω_r leads to an increase in the transverse extent of the condensate, and increases the total energy associated with the initial solitary wave. This enables more vortex rings to be generated.

Note that the snake instability of the wave is induced by its motion. A dark solitary wave which remains stationary, e.g. if created at the trap centre, will not decay via this instability. However, in a real environment, thermal fluctuations will cause small displacements of the wave, nudging it away from the trap centre, thereby giving it a velocity and making it prone to the snake instability. This is analogous to the effect of thermal fluctuations on an initially stationary vortex in the centre of a BEC [147], which give it a finite thermodynamic lifetime.

3.3 Relating quasi-1D to pure 1D

In the quasi-1D regime, where the transverse instability is suppressed, the 1D GPE is expected to provide a good description of the solitary wave dynamics. We now address this issue.

We consider first the pure 1D system under harmonic confinement. The ground state density profile is shown in figure 3.6(a) (solid grey line) for a trap strength of $\omega_z = \sqrt{2} \times 10^{-2}(c/\xi)$. This somewhat awkward value for the trap frequency is used because is gives sensible values for the coefficient of the harmonic potential, e.g. $\omega_z^2/2 = 10^{-4}(c^2/\xi^2)$, and Thomas-Fermi radius, e.g. $R_{\rm TF} = 100\xi$. This system has, in natural units, a peak density $n_{\rm 1D} = 1$, a scattering coefficient $g_{\rm 1D} = 1$, and chemical potential $\mu_{\rm 1D} = 1$.

We now aim to identify the cylindrically-symmetric quasi-1D system to which the 1D system corresponds. Essentially this means that the wavefunction along the central $r = 0$ axis of the quasi-1D system should match the pure 1D wavefunction. In order to achieve this mapping, we expect from section 2.3 that:

- the quasi-1D geometry is highly-elongated $\omega_r \gg \omega_z$;
- the radial component of the wavefunction resembles the harmonic oscillator ground state;
- the 3D scattering coefficient is related to the 1D value by $g_{\rm 3D} = 2\pi l_r^2 g_{\rm 1D}$, where $l_r = \sqrt{\hbar/m\omega_r}$;
- the 3D chemical potential is related to the 1D value by $\mu = \mu_{\rm 1D} + \hbar\omega_r$.

By varying the only remaining free parameter ω_r, we find numerically that the respective ground state wavefunctions are matched closest when $\omega_r \approx 3.52(\xi/c)$.

Figure 3.6(a) plots the ground state density profiles in the pure 1D system and along the $r = 0$ axis in the corresponding quasi-1D system. The density profiles are practically identical. The radial density profile along the $z = 0$ axis in the quasi-1D system is shown in figure 3.6(b) (solid line), along with the ground harmonic oscillator profile (dotted line). The radial profile is reasonably close to, but slightly more relaxed than, the harmonic oscillator profile. For tighter radial

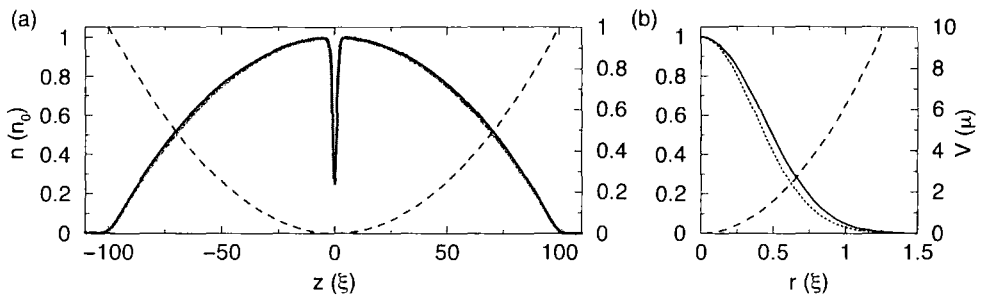

Figure 3.6: Density (left axis, dashed line) and potential (right axis) under harmonic confinement for pure 1D and quasi-1D systems. (a) Longitudinal density profile under longitudinal harmonic confinement $\omega_z = \sqrt{2}\times 10^{-2}(c/\xi)$ for a pure 1D (grey line) and quasi-1D (black line). (b) Radial density profile for the quasi-1D system (solid line), and the ground harmonic oscillator solution $n_r^{\rm HO} = \exp[-\omega_r r^2]$ (dotted line). The quasi-1D system has transverse confinement $\omega_r = 3.52(c/\xi)$ and chemical potential $\mu_{\rm 3D} \approx 4.5\mu_{\rm 1D}$.

confinement, the radial density profile tends towards the harmonic oscillator state, but the longitudinal density profile deviates from the 1D profile.

Here we have mapped a cylindrically-symmetric quasi-1D condensate under the 3D GPE to a purely 1D condensate under the 1D GPE, in a time-independent manner. The comparison of the soliton dynamics under the two descriptions will be considered in chapter 5.

3.4 Summary

We have demonstrated the crucial effect of transverse confinement on the stability of a dark solitary wave in a harmonically-confined condensate. For weak transverse confinement, a moving solitary wave is subject to a transverse *snake instability* known from nonlinear optics. This begins with bending of the soliton plane and ends with the solitary wave being catastrophically torn into one or more vortex rings. However, for sufficiently tight transverse confinement, the solitary wave becomes stable to the snake instability, and retains its 1D nature throughout its motion. Indeed, in this quasi-1D regime, we have shown that the 3D GPE can be mapped onto the 1D GPE.

Chapter 4

Longitudinal dynamics of a dark soliton in an infinite system

A soliton is strictly a solution to a *homogeneous* system, i.e. the 1D GPE with $V_{\text{ext}} = 0$, and so, even in the 1D limit, is expected to become dynamically unstable when the longitudinal density is inhomogeneous. Since an inhomogeneous background density is a general feature of dilute BECs (due to the trapping potential used to confine the gas), the motion of dark solitons through an inhomogeneous density is an important consideration.

In the limit of zero temperature, a dark soliton in a 1D system under harmonic confinement is expected to oscillate back and forth in the trap [131, 157, 165]. By considering a dark soliton in a shallow microtrap located within harmonic trap, Busch *et al.* [165] have illustrated the emission of sound waves from the soliton, while Huang *et al.* [166] predict that a dark soliton incident on a potential step in a 1D homogeneous system will emit radiation. However, the resulting soliton decay is expected to be a small effect.

In the previous chapter we illustrated the crucial effect of transverse confinement on the stability of the solitary wave. In 3D geometries, the transverse decay of the solitary wave into vortex rings is the dominant dynamical decay mechanism. However, in the limit of a quasi-1D geometry, this snake instability is heavily suppressed and the solitary wave behaves like a 1D object. In this regime one would expect the instability induced by the longitudinal inhomogeneity to become the dominant *dynamical* decay mechanism.

If the change in the background potential is weak, then, to first order, the soliton dynamics are similar to those of an effective particle of constant (negative) mass [131, 195, 197]. Any decay of the soliton during its motion leads to a change in the soliton *effective mass*, and hence a change in its subsequent trajectory [156, 165, 166, 213]. To monitor this change, one can apply a perturbative approach [214, 215], which will be valid as long as the potential does not vary significantly over the size of the soliton. However, if the density perturbation is substantial, the total emitted energy can be a significant fraction of the initial soliton energy, and, consequently, the *net* change in the soliton dynamics can be significant.

In this chapter we study the longitudinal dynamics of a dark solitary wave through various forms of inhomogeneous density. In particular we explore the resulting soliton instability and sound emission. For simplicity, we consider a system which is longitudinally unbounded. In addition, we assume a highly-elongated quasi-1D condensate. In this regime, the 1D GPE is expected to give good agreement with a full 3D description, and so we progress with the 1D GPE. This work has formed the basis of the following publications [207, 216].

4.1 Dark soliton incident on a potential step

In order to investigate the motion of a dark soliton through an inhomogeneous background density, we first consider the simplest case of a dark soliton incident on an infinitely-long potential step of the form,

$$V(z) = \begin{cases} 0 & \text{for} \quad z \leq 0 \\ V_0 & \quad\quad\; z > 0 \end{cases} \tag{4.1}$$

where V_0 is the height of the step. This system essentially represents two adjacent homogeneous regions (here named regions I and II) of different background density. For a positive step $V_0 > 0$ (figure 4.1), the density in region II becomes reduced in relation to the unperturbed density, while for a negative step $V_0 < 0$ (figure 4.5) the density is enhanced. Away from the step boundary, region I has the unperturbed density $n_{\mathrm{I}} = 1$, while in region II the density reaches the TF value $n_{\mathrm{II}} = (1 - V_0)$. However, in the local region of the step there is a *tanh*-like healing of the fluid density between the two limiting values. This is

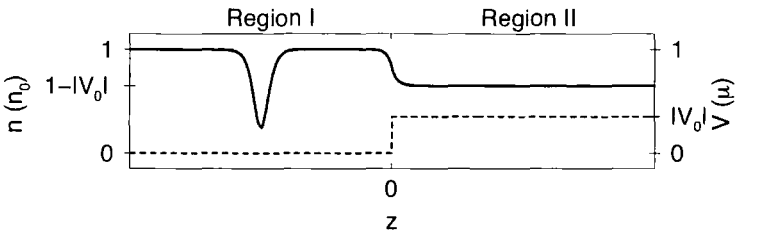

Figure 4.1: Schematic of the atomic density (left axis, solid line), plus an incident dark soliton, at the boundary of an infinitely-long *positive* potential step of height V_0, where $V_0 > 0$ (right axis, dashed line).

due to the finite length scale over which the fluid can adjust to perturbations, and consequently this transition region has a width of the order of the fluid healing length.

Since the local speed of sound is related to the local fluid density, this system represents two adjacent regions with different speed characteristics. The atomic system is therefore analogous to the boundary between two dielectric regions of different refractive index in a nonlinear optical fibre. The propagation of *bright* spatial solitons across such a boundary has been considered in terms of the so-called *effective particle theory*. Here the soliton is treated as a particle of constant effective mass interacting with an effective step-like potential induced by the interface [217]. This approach ignores radiative effects, which have however been included, to lowest order, in a perturbative treatment [218]. Bright solitons incident on potential steps have been studied numerically using the NLSE [219], with no observed soliton decay.

Huang *et al.* [220] have analytically considered the interaction of a dark soliton with a step-like potential in a BEC. They predict the emission of radiation from the soliton, and, where the step is downward, that the soliton is prone to decay into a train of multiple solitons. The interaction of a dark soliton with an impurity (i.e. a localised potential) has been investigated in [221, 222], with no direct observation of sound emission.

4.1.1 Positive step ($V_0 > 0$)

For a positive $V_0 > 0$ step the density, and therefore speed of sound, become reduced in region II, as shown in figure 4.1. Following the collision of the dark soliton with the step, we observe three distinct regimes depending on the height of the step. These regimes are illustrated in figure 4.2. For low step heights the soliton has sufficient energy to ascend the boundary, and is transmitted into region II (case(i), solid line). Once in region II the soliton propagates with a reduced, constant speed due to the lower ambient speed of sound.

One observes the emission of two asymmetric counter-propagating sound pulses as the soliton passes over the step. The forward-travelling pulse is a positive-density perturbation, and the opposing pulse is a negative-density perturbation, with both pulses having an amplitude of the order of $0.01n_0$. Note that in general the amplitude of the emitted sound depends on the step height and incident soliton speed. The pulses propagate away from the soliton at the local speed of sound and slowly disperse into a train of waves, confirming that they are indeed sound excitations. The shape of the emitted sound pulse reflects the nature of the interaction. The interaction is a short-lived perturbation on the soliton dynamics, and correspondingly, the pulse is a sharp burst of sound.

As the soliton passes over the step into the region of reduced speed of sound it becomes *decelerated*, but the simultaneous sound emission from the soliton reduces its energy and tends to *accelerate* it. However, the latter effect is small in relation to the former, and overall the soliton is decelerated.

In the limit of very large step heights $V_0 \gg \mu$, the soliton sees a hard wall (there is no fluid in region II) and is reflected elastically with no decay (case(iii), dashed line). Here, the soliton changes direction before its centre of mass has actually reached the boundary. This effect is analogous to the head-on collisions of dark solitons, whereby they transfer momentum before their centres cross [220]. Indeed, the reflection of the soliton from the hard wall can be interpreted as a virtual collision with its mirror image.

There is an intermediate regime where the step height is large enough to reflect the soliton but is far from the hard-wall limit, i.e. fluid exists in region II. In this regime (case(ii), dot-dashed line) the soliton reflection is accompanied by the emission of sound waves. Following reflection, the soliton propagates with

a slightly increased speed, i.e. lower energy, due to the sound emission at the step.

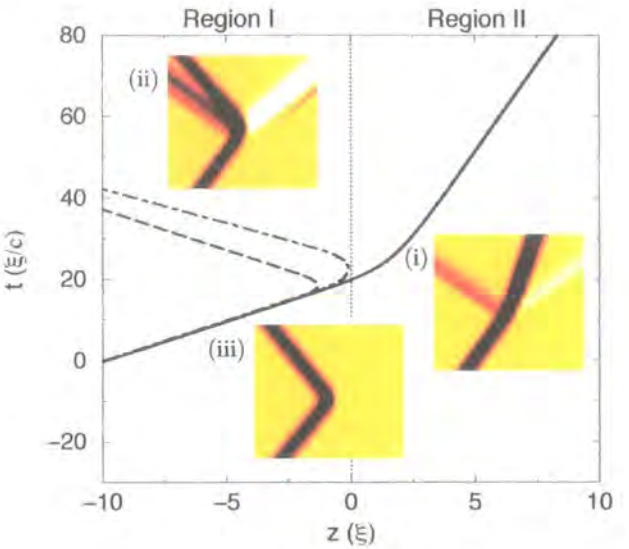

Figure 4.2: Path of a soliton, initially in region I with speed $v_{\mathrm{I}} = 0.5c$, incident on a positive potential step of amplitude V_0 (region II). Insets show the corresponding space-time carpet plots of renormalised density (actual density minus background density). (i) $V_0 = 0.2\mu$ (solid line): soliton transmits into region II, emitting sound waves with amplitude $\sim 0.005 n_0$. (ii) $V_0 = 0.55\mu$ (dot-dashed line): soliton reflects at step, emitting sound waves with amplitude $\sim 0.02 n_0$. (iii) $V_0 \gg \mu$ (dashed line): soliton sees a hard-wall and reflects elastically (no sound emission).

To estimate the critical point between soliton transmission and reflection at the step, we will assume that both the soliton depth and energy remain conserved. A soliton in region I with speed v_{I} features a density depression of size $(1 - v_{\mathrm{I}}^2)$. In region II, which has a background density $(1 - V_0)$, this soliton will propagate with a reduced speed of $v_{\mathrm{II}} = \sqrt{v_{\mathrm{I}}^2 - V_0}$, providing the soliton depth remains constant as it passes over the boundary. We therefore expect the critical point between transmission and reflection to be when $V_0 = v_{\mathrm{I}}^2$. This corresponds to when the density in region II is identical to the soliton depth, i.e. it can *just* support the soliton. Figure 4.3(a) shows the final speed of the *transmitted* soliton as a function of step height (solid line), for a fixed initial soliton speed. The dependence agrees well with the constant energy prediction

of $v_{\rm II} = \sqrt{v_{\rm I}^2 - V_0}$ (dashed line) for low step heights but deviates at higher values. The deviation is due to the effects of sound emission from the soliton as it traverses the step, which become more considerable as the step height increases. This decay decreases the energy and depth of the soliton, and so the critical point between transmission and reflection occurs at a slightly greater step height than the prediction based on a constant soliton energy/depth. This can be seen in figure 4.3(a) in the limit of $v_{\rm II} \to 0$. Here, for a soliton with initial speed $v_{\rm I} = 0.5c$ (solid line), we observe transmission for step heights up to $V_0 = 0.26658\mu$ (to 5 decimal places), while reflection is already observed for $V_0 = 0.26660\mu$. The constant energy prediction (dashed line) leads to a critical step height of $V_0 = 0.25\mu$. Similarly, for initial soliton speeds of $v = 0.25c$ and $0.75c$, the transmission/reflection crossover occurs at $V_0 \approx 0.067\mu$ and 0.63μ, respectively, while the non-radiative predictions are 0.0625μ and 0.5625μ.

The soliton dynamics at the positive potential step are somewhat analogous to the propagation of light from one medium to another of lower refractive index. An interesting question is whether, at the critical step height, the soliton becomes permanently fixed on the boundary, in analogy to the critical angle of incidence in optics. In order to investigate this possibility, figure 4.3(b) plots the time spent by the soliton in the region of the step $t_{\rm step}$ (arbitrarily defined to be the region $[-6\xi, 6\xi]$) as a function of the step height, for a soliton with initial speed $v_{\rm I} = 0.5c$. We observe a clear resonance in $t_{\rm step}$, centred around the step height $V_0 \simeq 0.26660\mu$, with the soliton remaining in the region of the step for times of over $1200(\xi/c)$. This *quasi-trapping* of the soliton by a potential has been predicted elsewhere for potential steps [221] and localised impurities [222]. Figure 4.3(c)-(d) shows the evolution of the soliton for step heights which are marginally either side of the resonance. For $V_0 = 0.26658\mu$ (figure 4.3(c)) the soliton transmits into region II with a very low final speed of around $v_{\rm II} = 0.003c$. The soliton takes a long time to traverse the step and, while doing so, emits a single large burst of sound. For $V_0 = 0.26660\mu$ (figure 4.3(d)) the soliton spends a time of around $1200(\xi/c)$ in the region of the step before reflecting back into region II. During this time the soliton almost completely traverses the step region, passing into region II by a substantial distance of the order of 5ξ. However, the smoothing of the fluid in the region of the step means that there is an effective retarding force on the soliton even several healing lengths

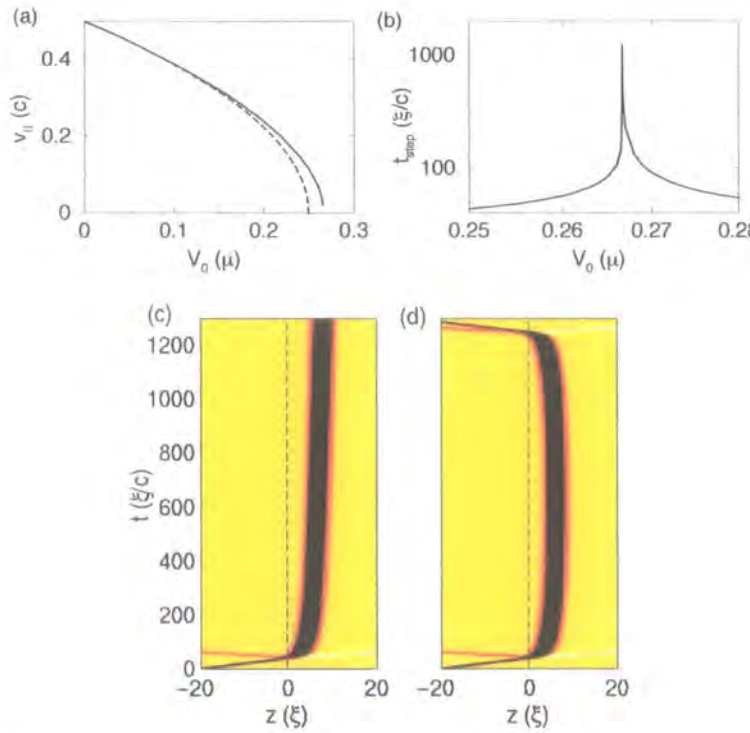

Figure 4.3: (a) Speed of the transmitted soliton v_{II} as a function of step height V_0 (solid line), for fixed initial soliton speed $v_{\mathrm{I}} = 0.5c$, and the prediction assuming constant soliton energy/depth $v_{\mathrm{II}} = \sqrt{v_{\mathrm{I}}^2 - V_0}$ (dashed line). (b) Time t_{step} which the soliton spends in the step region $[-6\xi, 6\xi]$ as a function of step height, with the y-axis plotted on a logarithmic scale. Space-time plot of renormalised density showing the evolution of the soliton for a step height of (c) $V_0 = 0.26658\mu$ (transmittive quasi-trapping) and (d) $V_0 = 0.26660\mu$ (reflective quasi-trapping).

away from the actual boundary. Consequently, the soliton eventually reverses direction and returns back down the step into region I. An analogous effect is observed for bright solitons incident on potential steps [219]. We observe the emission of two large bursts of sound, one as it ascends the step and another as it finally descends. However, sound emission also occurs in the intervening time as the soliton gradually reverses direction, albeit on a very small-scale (not visible in figure 4.3(d)). Undoubtedly we will observe longer quasi-trapping times if we go to greater precision/resolution in locating the critical step height. However, as illustrated here, the soliton at the step is a constantly-evolving entity and can never reach a steady state on the boundary. The ultimate fate of the soliton

is therefore to transmit or reflect at the step, although the quasi-trapping time may be extremely large.

We now consider the *energetics* of the dark soliton incident on the infinitely-long potential step. The soliton energy is evaluated numerically in accordance with equation (2.35) and as outlined in Appendix B. The sound energy emitted by the soliton, i.e. the change in the soliton energy following its interaction with the step, is shown in figure 4.4 as a function of step height. Three initial soliton speeds are considered, with all showing a similar qualitative behaviour. The behaviour is a result of the interplay between the magnitude of the density gradient experienced by the soliton and the reduced density in region II, which tends to suppress sound emission. For low step heights the soliton has sufficient energy to transmit into region II, emitting a single burst of sound energy as it passes over the boundary. As the step height increases, so does the depth and gradient of the background density perturbation, and, as a result, the emitted sound energy initially increases with V_0. This increase is monotonic and smooth up to the threshold for reflection (corresponding to $V_0 \approx 0.067\mu$, 0.267μ and 0.63μ for $v_I = 0.25c$, $0.5c$ and $0.75c$, respectively).

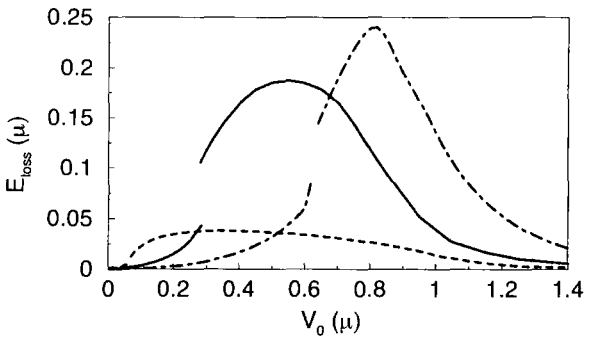

Figure 4.4: Emitted sound energy E_{loss} as a function of step height V_0, for a soliton with initial speed $v_I/c = 0.25$ (dashed line), 0.5 (solid line), and 0.75 (dot-dashed line).

From this point onwards the soliton effectively interacts twice with the step, both as it *ascends* and *descends* the step (ignoring the small-scale sound emission in the intervening time). We therefore see a discontinuous increase in the emitted sound energy at this point, as it approximately doubles in magnitude. Past this point the sound energy initially increases with V_0, as the density gra-

dient and depth associated with the step increase. However, in this reflective regime, the soliton only probes a proportion of the density inhomogeneity before it ultimately changes direction. Although the absolute density gradient and depth increase further with V_0, a point is reached where the density gradient/depth *seen by the soliton* saturates. The sound energy emitted by the soliton then begins to decrease. Furthermore, as the density in region II becomes very small, sound emission becomes suppressed, and in the limit of a hard wall, where no density exists in region II, the soliton reflects elastically. Note that the sound emission at the step can be considerable: the $v_I = 0.75c$ soliton (figure 4.4, dot-dashed line) radiates up to around 70% of its initial energy with one interaction with the step.

4.1.2 Negative step ($V_0 < 0$)

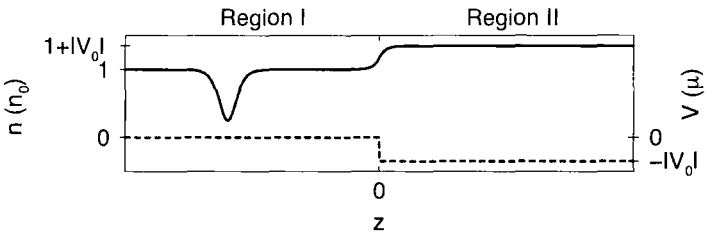

Figure 4.5: Schematic of the atomic density (left axis, solid line), including an incident dark soliton, at the boundary of an infinitely-long *negative* potential step of height V_0, where $V_0 < 0$ (right axis, dashed line).

For a negative $V_0 < 0$ step, the density in region II is higher than in region I, as illustrated in figure 4.5. The incident soliton will therefore always be supported in region II, and transmit over the step. Figure 4.6(a) shows the final speed of a $v_I = 0.5c$ soliton after passing down the step, as a function of V_0. The final soliton speed (solid line) increases with V_0, mainly due to the increased speed of sound in region II (dot-dashed line). In addition, the final soliton speed is slightly larger than the constant energy prediction $v_{II} = \sqrt{v_I^2 - V_0}$ (dashed line), indicating that the soliton has undergone dissipation during its interaction with the step. This is confirmed in figure 4.6(b), which illustrates the energy loss from the soliton as it accelerates over the boundary, for various initial speeds. The energy emission increases monotonically with step height. Also plotted in

figure 4.6(a), alongside the final soliton speed, is the speed of sound in region II (dot-dashed line). Since these quantities have a different dependence on V_0, the ratio of the two $v_{\rm II}/c_{\rm II}$ increases with $|V_0|$ and tends towards unity in the limit $|V_0| \to \infty$.

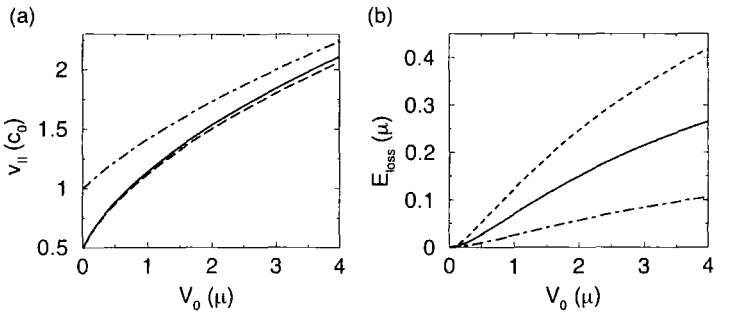

Figure 4.6: (a) Final soliton speed in region II, $v_{\rm II}$ (solid line), as a function of V_0, for a soliton with initial speed $v_{\rm I} = 0.5c$, along with the corresponding constant mass prediction (dashed line), and the speed of sound in region II (dot-dashed line). (b) The corresponding energy loss $E_{\rm loss}$ from the soliton, for initial soliton speeds of $v_{\rm I}/c = 0.25$ (dashed line), 0.5 (solid line), and 0.75 (dot-dashed line).

We now address the issue of what form the dissipation takes. Huang *et al.* [166] have investigated the interaction of a dark soliton with a downward step and predict that the soliton will disintegrate into a train of dark solitons, plus some residual sound waves, with the number of solitons in the train increasing with the size of the step.

Figure 4.7 illustrates the decay of a $v_{\rm I} = 0.5c$ soliton as it interacts with a downward step. For a shallow negative step with $V_0 = -0.25\mu$ (figure 4.7(i)), the soliton accelerates over the boundary, clearly emitting counter-propagating sound waves. The final soliton speed is around $0.54c_{\rm II}$, such that the transmitted soliton and emitted sound rapidly separate in space. For a deeper step of $V_0 = -2\mu$, the soliton undergoes a greater acceleration at the boundary, and emits waves of much larger amplitude. Here, the transmitted soliton has a speed of around $0.9c_{\rm II}$, and only slowly separates from the emitted waves. Figure 4.7(iii) shows the original soliton (top-most line) and its forward-propagating decay products after a long time. Over this time, the decay products appear to have slowly separated into a train of sound waves and a dark density notch

travelling at very close to the local speed of sound, i.e. a very fast dark soliton. This would seem to agree with the prediction of Huang *et al.* [166]. They also predict that the number of additional solitons generated during the interaction increases with the size of the step. However, for further increases of $|V_0|$ (up to a magnitude of 10μ), only one additional soliton appears to be generated.

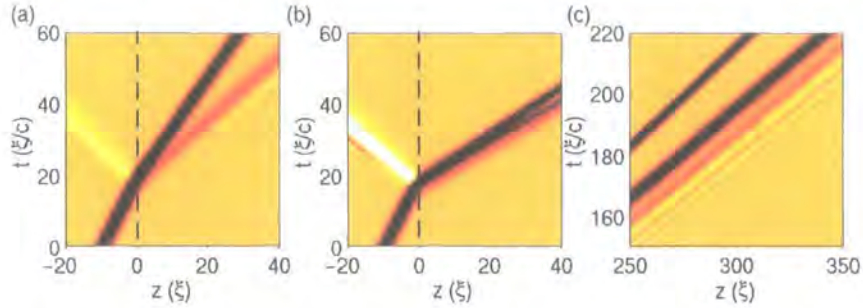

Figure 4.7: Space-time plots of renormalised fluid density showing a dark soliton, with initial speed $v_I = 0.5c$, passing down a potential step (dashed line) of height (a) $V_0 = -0.25\mu$ and (b) $V_0 = -2\mu$. (c) shows the decay products of case (b) after a long time.

By considering the sudden interaction of a dark soliton with an infinitely-long potential step we have illustrated the basic instability of a dark soliton to motion through an inhomogeneous longitudinal density. We have mapped the soliton decay in terms of the step height. Furthermore, in Appendix D we consider the interaction of a dark soliton with a square potential barrier of finite length. These dynamics bear qualitative links to the infinitely-long step. Indeed, for a sufficiently long barrier, the soliton dynamics can be resolved into separate interactions at both ends of the barrier. However, for sufficiently narrow barriers (where the width is of the order of the healing length) the healing of the fluid becomes heavily restricted, and the dynamics become strongly dependent on the barrier length. Here we have mapped the decay of the soliton in terms of both the step height and length.

However, due to the sudden nature of the soliton-step interaction and the rapid burst of sound generated, it is difficult to infer the dependence of the decay on more general soliton parameters, such as the soliton speed, acceleration, and its local background density. We therefore employ next a more gentle and controllable potential to perturb the soliton from its stable homogeneous state.

4.2 Dark soliton traversing a linear ramp

We now consider a dark soliton traversing a linear potential ramp of the form

$$V(z) = \begin{cases} 0 & z \leq 0 \\ \alpha z \quad \text{for} & 0 < z < z_0 \\ \alpha z_0 & z \geq z_0 \end{cases} \tag{4.2}$$

where α is the gradient of the ramp, taken to be positive. This set-up is

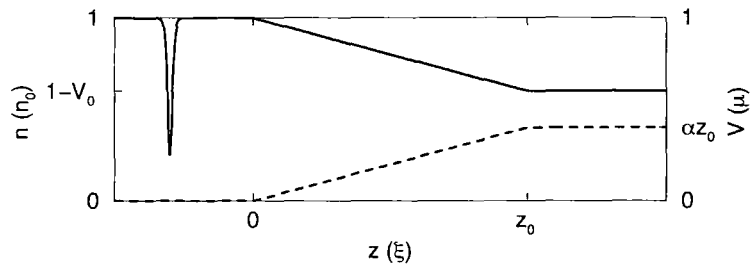

Figure 4.8: Schematic of the density (solid line), featuring a dark soliton, in the region of a finite-length linear ramp (dashed line) with *positive* gradient α, which terminates at position z_0.

illustrated in figure 4.8. The linear potential provides a simple way of imparting a controlled and constant force to the soliton, and can represent, for example, the force of gravity. Providing the gradient is not too steep, the fluid density in the presence of the ramp should closely match the TF profile $n_{\mathrm{TF}} = (1 - \alpha z)$, and decrease linearly with z. The incident soliton will start to pass up the ramp, experiencing a reducing local density, and slow down. If the maximum ramp height αz_0 is sufficiently low in relation to the soliton speed the soliton can traverse the ramp fully and enter the second homogeneous region at a reduced speed. Otherwise, at the point where the soliton density depression touches zero density, i.e. when the soliton depth equals the local density, the soliton becomes stationary, changes direction, and proceeds to pass back down the ramp.

We explore the dynamics of a dark soliton with initial speed $v = 0.5c$ incident on a linear ramp with gradient $\alpha = 4 \times 10^{-3}(\mu/\xi)$ and length $z_0 = 100\xi$. The parabolic trajectory of the soliton on a ramp is evident in figure 4.9(a), which shows the space-time density plot of the system. In addition, we clearly observe the continuous emission of asymmetric sound waves from the soliton while on

the ramp. This soliton decay causes a reduction in the energy and depth of the soliton, and by analogy to a classical particle, we can interpret this as a reduction in the effective mass of the soliton. Such a decrease implies that the soliton acceleration should increase over time, and the path should deviate from the corresponding constant mass trajectory. However for the weak ramp considered here the soliton acceleration (figure 4.9(b)) remains approximately constant while on the ramp.

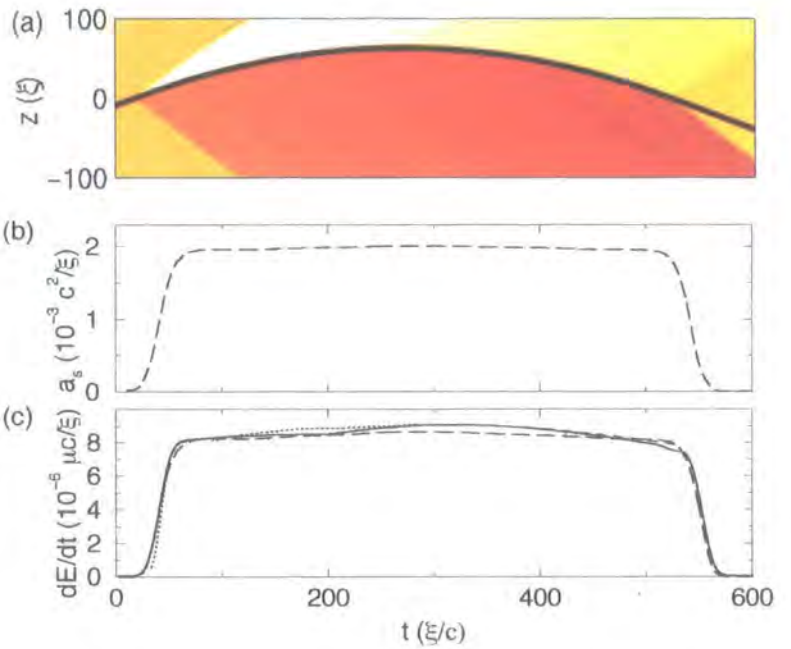

Figure 4.9: (a) Space-time carpet of renormalised fluid density showing a soliton (black line), with initial speed $v = 0.5c$, ascending a linear ramp with gradient $\alpha = 4\times10^{-3}(\mu/\xi)$ and length z_0, and emitting counter-propagating sound waves of amplitude $\sim 0.01n_0$. (b) Soliton acceleration as a function of time. (c) Power emitted by the soliton computed from the GP energy functional (solid line), equation (4.3) $\kappa = 2.14\ (\mu\xi/c^3)$ (dashed line), and the prediction of equation (4.4) (dotted line).

Figure 4.9(c) shows the power radiated from the soliton due to sound emission. The first thing to notice is that it bears a similar step-like functional form to the soliton acceleration. In order to investigate the dependence of the power emission on the soliton acceleration, figure 4.10 plots the average power radi-

ated by the soliton on the ramp against the average acceleration it experiences, repeated over a range of potential gradients. This suggests a behaviour of the form,

$$\frac{dE_{\mathrm{s}}}{dt} = -\kappa a^2, \tag{4.3}$$

where a is the soliton acceleration and κ is a constant coefficient. Figure 4.10 plotted on a logarithmic scale (see inset) shows, to a good approximation, that the power is indeed proportional to the square of the acceleration. However, there is slight deviation in the limit of very small accelerations (for $\ln(a_{\mathrm{s}}) < -7$), which may arise due to numerical errors associated with the small values of the emitted power. In figure 4.9(c), we also plot equation (4.3) (dashed line) with scaling coefficient $\kappa = 2.14(\mu\xi/c^3)$, which is empirically chosen to fit the data. This step-like function agrees well with the emission derived from the GP energy functional (solid line). Note that, while equation (4.3) predicts a roughly constant power emission while on the ramp, the actual power emission is slightly bowed, being marginally higher when the soliton is close to its turning point.

Overall, this result suggests that the power radiated by the soliton is proportional to the soliton acceleration squared. This is analogous to the electromagnetic Larmor radiation from an accelerating charge in electrodynamics [223]. It is important to note that the soliton acceleration we refer to here is the acceleration of the soliton with respect to the background fluid. Acceleration of the whole fluid induces no additional sound emission from the soliton.

The instability investigated here arises from the inhomogeneous longitudinal density, induced by the longitudinal potential, which breaks the integrability of the atomic system. In nonlinear optical waveguides an analogous breakdown of integrability can arise due to modifications of the nonlinearity within the *homogeneous* optical medium, e.g. due to saturation effects. By employing multiscale asymptotic techniques, it has been shown that a dark soliton in such a system is unstable, and prone to decay by the emission of radiation [167]. In particular, the soliton energy is predicted to decay at a rate,

$$\frac{\mathrm{d}E_{\mathrm{s}}}{\mathrm{d}t} = -L_{\mathrm{s}}(v,n)\left(\frac{\mathrm{d}v}{\mathrm{d}t}\right)^2, \tag{4.4}$$

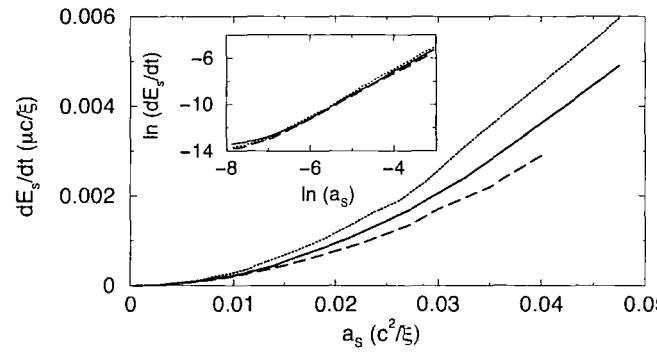

Figure 4.10: Power radiated dE_s/dt versus soliton acceleration a_s, for a dark soliton traversing a linear ramp. Each point corresponds to the average power emission and average acceleration for a particular ramp, with gradients considered in the range $(10^{-3} - 10^{-1})(\mu/\xi)$. Three initial soliton speeds are plotted: $v = 0.3c$ (dashed line), $0.5c$ (solid line) and $0.7c$ (dotted line). Inset: Same data plotted on a ln-ln scale has a gradient of approximately 2.

where

$$L_s(v,n) = \frac{c}{c^2 - v^2}\left[\frac{2c^2}{n}\left(\frac{\partial N_s}{\partial v}\right)^2 + 2v\left(\frac{\partial N_s}{\partial v}\right)\left(\frac{\partial S_s}{\partial v}\right) + \frac{n}{2}\left(\frac{\partial S_s}{\partial v}\right)^2\right]. \quad (4.5)$$

Here n is the local background density, S_s the total phase slip across the moving soliton, and $N_s = \int (n - |\psi|^2)\,\mathrm{d}z$ is the number of particles displaced by the soliton.

In equation (4.3) we assumed for simplicity that the coefficient κ is constant, and we obtained its value by empirically matching the acceleration-squared power law with our numerical results. However, this coefficient will in general depend on time-varying quantities such as the local soliton speed and background density. The decay law of equation (4.4) has the same acceleration-squared dependence as found for equation (4.3) but additionally features an analytically-obtained coefficient $L_s(v,n)$ which depends on local soliton quantities. The power radiated according to this prediction is shown in figure 4.9(c) (dotted line). Despite the fundamentally different physical system and nature of the instability, the agreement with the result from the GP energy functional is excellent for this simple system. Due to the presence of the time-dependent coefficient $L_s(v,n)$, this prediction gives almost perfect agreement with the power emission evaluated numerically. In particular, the slightly bowed shape of the

power emission curve is correctly described by the coefficient $L_s(v, n)$, in contrast to the case of a constant coefficient in equation (4.3). Nonetheless, it is remarkable that even the oversimplified assumption of a constant coefficient yields such good values for the rate of sound emission.

4.3 Summary

In this chapter we have demonstrated the dynamical instability of a dark soliton to motion through an inhomogeneous background density in a system of infinite extent. The instability induces the emission of sound waves from the soliton. We introduce this effect by first considering the simple case of a dark soliton interacting with an infinitely-long potential step, and mapped the resulting soliton decay in terms of the height of the step. The sudden interaction of the soliton with the step induces a sharp acceleration. Dissipation occurs via the emission of sound waves, and when the step is negative, we have observed the generation of an additional soliton. The exception to these dissipative dynamics arises when the step is sufficiently high that it acts like a hard wall: the soliton then reflects elastically. Furthermore, in Appendix D, we extended this to consider a dark soliton incident on a potential step of finite length, i.e. a potential barrier, and mapped the soliton decay in terms of the barrier height and length.

The sudden nature of the soliton-step interaction restricts us from interpreting the decay in terms of general soliton parameters, such as speed, acceleration, local density, etc. A linear ramp, on the other hand, can be employed to induce a constant and controllable acceleration to the soliton over a significant period of time. Using this scenario, we have shown that the rate of sound emission from the soliton is proportional to the square of its acceleration. Furthermore, this soliton decay is shown to agree with a result from nonlinear optics for solitons destabilised by modifications in the optical nonlinearity.

In addition to potential steps and ramps, we have also considered a dark soliton passing over a gaussian-shaped bump and oscillating within a microtrap formed by two gaussian bumps. These results are presented in Appendix D. In the former case, the gaussian bump represents a smoothed-out version of the

square barrier potential, with the qualitative behaviour of the interaction being similar, e.g. the threshold for reflection/transmission, and sound emission. However, the soliton dynamics at the gaussian bump are less abrupt that at the square barrier, and this allows us to analyse the power emission in terms of the soliton acceleration. In the case of the gaussian microtrap, the oscillating soliton radiates sound waves which propagate away to infinity, but the soliton remains confined to the microtrap. This allows us to observe continuous sound emission over a prolonged time. The radiative acceleration of the soliton causes its oscillation amplitude to increase over time, in agreement with the anti-damping observed by Busch *et al.* [165] for a soliton in a microtrap within an ambient harmonic trap. In particular, in both the single and double bump cases, we find that the power emission from the soliton is consistent with the acceleration-squared behaviour of equations (4.3) and (4.4).

This investigation has given us insight into the instability of a dark soliton under acceleration. However, the infinitely-long system we have considered is not realistic in the context of dilute BECs. Experimental BECs are generally confined by harmonic traps, which tend to dominate their static and dynamic properties. We do point of however that in the limit of weak longitudinal harmonic confinement, BECs can be almost homogeneous on certain length scales, and by turning off the longitudinal harmonic confinement, the regime of BEC in homogeneous waveguides [42, 43, 44, 45] has been probed in recent experiments [71, 72].

Chapter 5

Longitudinal instability of a dark soliton in confined systems

In the previous chapter we considered the interaction of a dark soliton with simple potentials, including potential steps and ramps, in an otherwise unbounded homogeneous system. We thereby illustrated the instability of a dark soliton to acceleration through an inhomogeneous density, and the emission of sound waves. However, a real condensate features global confinement in all three dimensions, generally in the form of magnetically-induced harmonic traps (although optically-generated gaussian traps are also used). In this chapter we investigate the longitudinal dynamics of dark solitons in condensates under such confinement. The condensate is now finite in extent, and excitations, e.g. solitons and sound waves, are confined to the same region of space. Any sound generated by the motion of the soliton will therefore be forced to reinteract with the soliton. We will see that the reinteraction of the sound with the soliton has a significant effect in stabilising the soliton against decay. However, by modifying the harmonic trap, e.g. introducing an outer region into which the emitted sound can escape, or additional dynamical instability by means of a perturbing potential, e.g. an optical lattice, soliton decay can be induced in a controllable manner. Some of this work has been covered in the following publications [224, 225, 226].

As in the previous chapter, we assume a quasi-1D condensate and proceed in general using the 1D GPE to describe the longitudinal dynamics of the sys-

tem. However, in section 5.1.1 we compare the 1D description to the full 3D description of the system, and confirm the validity of the 1D approach.

5.1 Dark soliton dynamics in a harmonic trap

We first consider the longitudinal dynamics of a soliton in a condensate under longitudinal harmonic confinement given by,

$$V(z) = \frac{1}{2}\omega_z^2 z^2. \tag{5.1}$$

An important feature is that the system is now finite in extent. The TF density profile has the form of an inverted parabola $n_{\rm TF} = (1 - \omega_z^2 z^2/2)$, and the TF width of the condensate is given by $R_{\rm TF} = \sqrt{2/\omega_z^2}$. The TF approximation is valid when the kinetic energy in the system becomes negligible in comparison to the interaction energy, which typically occurs for a large number of particles. In our numerical method, where the peak density is kept fixed, this is valid for relatively weak harmonic traps.

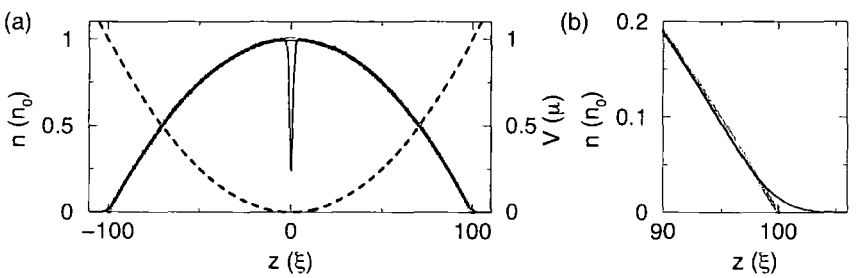

Figure 5.1: (a) Longitudinal density (left axis, solid line) of a condensate under harmonic trapping $\omega_z = \sqrt{2} \times 10^{-2}(c/\xi)$ (right axis, dashed line), featuring a dark soliton with speed $v_0 = 0.5c$ at the origin. The TF density profile in the absence of the soliton is also shown (grey line). (b) Close-up of the density at the edge of the condensate.

Figure 5.1(a) illustrates the longitudinal density profile (black line) of a condensate under harmonic trapping (dashed line) with frequency $\omega_z = \sqrt{2}\times 10^{-2}(c/\xi)$, and a dark soliton positioned at the trap centre with initial speed $v = 0.5c$. The trap is relatively weak and so the TF density profile (grey line in figure 5.1(a)) matches the actual profile very well. The only deviation occurs at the edge of

the cloud, as shown in figure 5.1, where the small kinetic energy contribution leads to the presence of 'tails' of low density. Consequently, the actual extent of the BEC is marginally larger than the TF radius of $R_{\mathrm{TF}} = 100\xi$.

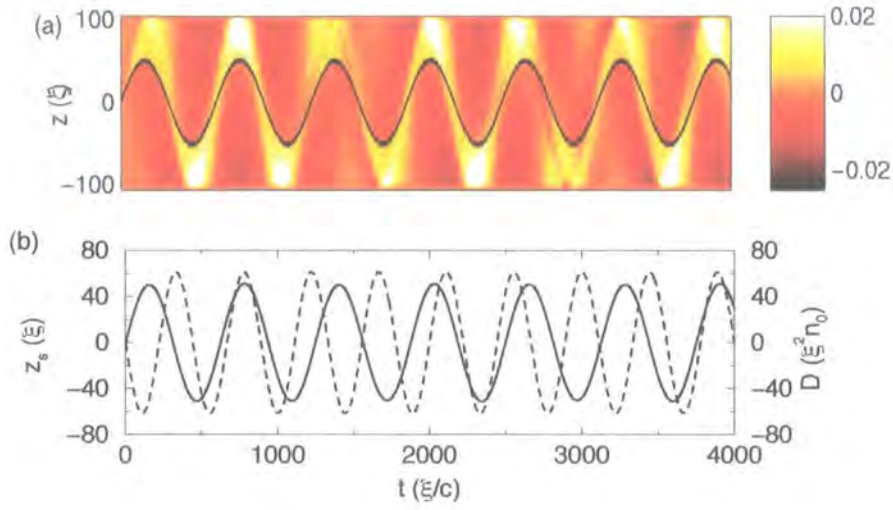

Figure 5.2: (a) Space-time plot of renormalised condensate density showing the evolution of the initial state shown in figure 5.1. (b) Soliton position z_{s} (solid line, left axis) and dipole moment of the condensate D (dashed line, right axis).

The time evolution of the atomic density in this system is shown in figure 5.2(a). The soliton, appearing as a localised dip in the density, decelerates as it moves up the trap walls, and eventually reaches a turning point when the density notch touches zero density. In other words, the ratio of the soliton speed to the speed of sound, v/c, decreases from its initial value to zero. It then accelerates back towards the trap centre, and passes through it in the opposing direction at $-v/c$. Since the the ratio v/c changes throughout the soliton motion, we specify the soliton in terms of its speed at the trap centre v_0. Although not shown, the phase slip across the soliton increases as it moves away from the trap centre, and reaches a π-phase step at the maximum amplitude. The phase step then flips to $-\pi$ (due to the 2π phase cycle) as the soliton reverses its trajectory, and subsequently decreases in magnitude as the soliton accelerates back towards the trap centre.

The oscillation frequency of a dark soliton in a harmonic trap is predicted to be $\omega_{\mathrm{s}}^0 = \omega_z/\sqrt{2}$ [156, 157, 165, 166, 222]. This has been derived analytically assum-

ing a TF condensate density, and has been confirmed by numerical simulations close to the TF regime [213, 222]. In the case of figure 5.2, the soliton oscillation period features a modulation over time, and is given by $T_s = 625 \pm 20(\xi/c)$, which corresponds to a frequency of $\omega_s = 0.0101 \pm 0.0003(c/\xi)$. Given that the trap frequency is $\omega_z = \sqrt{2} \times 10^{-2}(\xi/c)$, the theoretical prediction lies within the bounds of the numerically-observed oscillation frequency.

Assuming the soliton form is preserved, a soliton with speed v maintains a density depth of $(1-v^2)$, and therefore probes the condensate out to background densities equal to this value before reversing direction. For a TF density profile, this leads to an estimate for the soliton oscillation amplitude, given by,

$$z_s^0 = \sqrt{2} v_0 / \omega_z. \tag{5.2}$$

For the system in figure 5.2, this corresponds to an oscillation amplitude of $z_s^0 = 50\xi$, which is consistent with the observed amplitude.

As evident in figure 5.2(a), the motion of the soliton generates an oscillation of the background fluid with a density amplitude of around $0.02 n_0$. This fluid excitation oscillates in the trap in an asymmetrical manner, i.e. a dipolar oscillation. We can follow its evolution in terms of the dipole moment D of the condensate, defined as,

$$D = \int_{-\infty}^{+\infty} z |\psi(z)|^2 \mathrm{d}z. \tag{5.3}$$

The dipole moment D of the condensate and the soliton path z_s are shown in figure 5.2(b). The soliton (solid line) oscillates at $\omega_s = \omega_z/\sqrt{2}$, while the condensate dipole moment (dashed line) oscillates at the trap frequency ω_z. This corresponds to the fundamental dipole mode of a 1D condensate in a harmonic trap [191, 227, 228].

The results of chapter 4 indicate that an accelerating soliton is dynamically unstable and prone to sound emission. This would suggest that the soliton oscillating in the harmonic trap will radiate sound waves and decay. In that case the soliton would become shallower and faster, causing it to probe further up the trap walls over time. However, we do not see any net change in the amplitude of the soliton motion which would infer decay.

We observe that soliton trajectory is not perfectly sinusoidal, but features small periodic modulations. This is not visible on the scale of the soliton path shown

in figure 5.1(c). However, figure 5.3(a) plots the absolute distance of the soliton from the trap centre, and zooms up on the region around the soliton turning point. The oscillation amplitude remains close to, but not equal to, the TF prediction of 50ξ. The modulation of the soliton motion is evident from the small-scale periodic variations in the soliton oscillation amplitude.

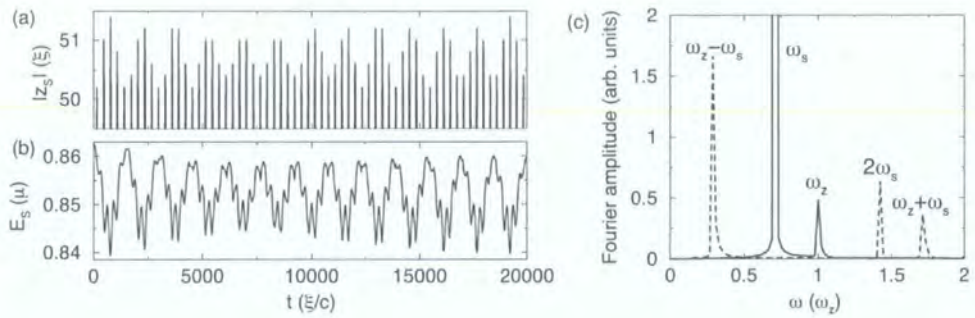

Figure 5.3: (a) Absolute value of the amplitude of the soliton oscillations $|z_s|$ zoomed around the soliton turning point, and (b) soliton energy E_s, for the system in figure 5.1. (c) Fourier spectrum of soliton position (solid line) and energy (dashed line) as a function of frequency, where frequency is scaled in terms of the trap frequency ω_z. Here we consider the magnitude of the Fourier transform.

Further light is shed on this effect by analysing the frequency components of the soliton position $z_s(t)$ by means of the Fourier spectrum. The frequency Fourier transform $F(\omega)$ acting on a time-dependent function $f(t)$ is given by,

$$F[f(t)](\omega) = 2\pi \int_{-\infty}^{\infty} f(t) \exp(-i\omega t) dt. \tag{5.4}$$

We will consider only the magnitude of the complex Fourier transform, i.e. $|F[f(t)](\omega)|$.

The Fourier spectrum of the soliton position is shown in figure 5.3(c)(solid line). We observe two main peaks in the spectrum: a dominant, large amplitude peak located at $\omega_s = \omega_z/\sqrt{2}$, corresponding to the (unperturbed) soliton oscillation in the trap, and a lower-amplitude peak exists at ω_z, corresponding to the dipolar motion of the background fluid in the trap. The origin of this modulation is now clear: the dipolar fluid mode, set up by the soliton motion, has a periodic back-action on the oscillating soliton. In other words, the soliton propagates through a background density which is weakly time-varying.

Similarly, the soliton energy, shown in figure 5.3(b), remains on average constant, but is modulated by small-amplitude oscillations. The frequency Fourier spectrum of the soliton energy is shown in figure 5.3(c). Whereas the soliton position depends on the *displacement* from the trap centre, with frequency ω_s, the soliton energy depends on the *distance* from the trap centre, which has frequency $2\omega_s$. Furthermore, the spectrum is heavily dominated by beat frequencies between the soliton and dipole, e.g. $(\omega_z - \omega_s)$, $(\omega_z + \omega_s)$, plus higher order combinations.

5.1.1 Comparison with 3D results

We now present the basic dynamics of a soliton in a harmonic trap as described by a full 3D description of a highly-elongated quasi-1D condensate, and compare to the 1D results. For the 3D description, we assume a cylindrically-symmetric system, and proceed using the cylindrically-symmetric 3D GPE in the $r - z$ plane. In section 3.3 we numerically mapped an elongated quasi-1D condensate onto a 1D condensate, and found that this requires a transverse trap frequency $\omega_r \approx 3.52(\xi/c)$. The 3D equivalent of the 1D system in figure 5.1, with longitudinal frequency $\omega_z = \sqrt{2} \times 10^{-2}(\xi/c)$, therefore has a trap ratio of $\omega_r/\omega_z \approx 250$. Under these scalings, the longitudinal density profile of the system is virtually identical under both the 1D GPE and cylindrically-symmetric 3D GPE (see figure 3.6).

Figure 5.4 shows the path and energy relating to a solitary wave oscillating in this harmonically-confined quasi-1D condensate as derived from the cylindrically-symmetric 3D GPE and the 1D GPE. Since the quasi-1D system has been mapped onto the 1D system, it has the same longitudinal scalings as the pure 1D case, and so we can introduce a solitary wave with arbitrary speed using the analytic dark soliton solution. Here the solitary wave is initially located at the origin with speed $v_0 = 0.5c$. The soliton energy is evaluated numerically according to equation (2.35). This is a 1D energy, and so in the 3D system, this is evaluated along the central $r = 0$ axis.

The solitary wave oscillates back and forth in the trap, as shown in figure 5.4(a), and is virtually identical under the 1D and 3D descriptions. The evolution of the 1D soliton energy is shown in figure 5.4(b). The soliton energy from the

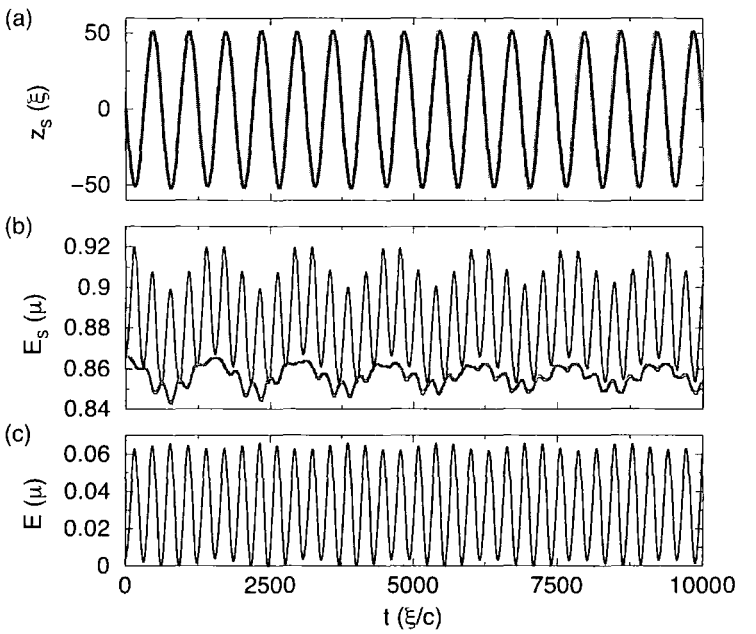

Figure 5.4: (a) Path and (b) energy of a dark solitary wave, initially at the origin with speed $v_0 = 0.5c$, in a quasi-1D BEC under harmonic confinement. The results are obtained using the 1D GPE (grey lines) and the corresponding cylindrically-symmetric $z - r$ GPE (black lines). (c) shows the additional modulation in the soliton energy in the 3D system due to the coupling to transverse modes. The trap frequencies are $\omega_z = \sqrt{2} \times 10^{-2}(c/\xi)$ and $\omega_r = 3.52(c/\xi)$.

1D and cylindrically-symmetric 3D GPE each maintain, on average, a constant value but are modulated by oscillations. In the case of the 1D GPE (grey line), we have shown previously that these oscillations come from the longitudinal interaction of the oscillating soliton with a dipolar fluid mode. The soliton energy from the cylindrically-symmetric 3D GPE (black line) includes similar oscillations due to this longitudinal effect, but also an additional energy modulation. This additional modulation, which is shown in figure 5.4(c), arises due to the coupling of longitudinal and transverse modes. This coupling induces a transverse oscillation which periodically reduces the density along the $r = 0$ axis, and therefore directly affects the soliton energy, which is calculated along this axis. This oscillation is set up by, and subsequently driven by, the oscillating solitary wave and has a frequency of twice the soliton oscillation frequency. This is confirmed by the absence of these energy modulations when the solitary wave is stationary at the trap centre.

Despite these transverse oscillations, we observe no decay of the solitary wave. Subtracting the 3D transverse energy modulations gives essentially perfect agreement with the 1D results. Indeed, if ω_r is decreased, these transverse energy oscillations increase in magnitude but we still do not observe a net soliton decay due to this effect. We only observe soliton decay when the transverse confinement is sufficiently weak to allow the solitary wave to decay into vortex rings (this effect in discussed in chapter 3).

Due to the excellent agreement between the 1D and 3D descriptions of the soliton dynamics, we proceed in general using the 1D GPE, although key results will be verified with the 3D GPE.

5.1.2 Variation with soliton speed

The path of a soliton in a fixed harmonic trap for various initial speeds is shown in figure 5.5(a). The main effect of increasing the soliton speed is that the soliton oscillation amplitude increases. The soliton oscillation frequency remains around the expected value of $\omega_s^0 = \omega_z/\sqrt{2}$ for speeds up to $v_0 = 0.7c$. However for a very fast $v_0 = 0.9c$ soliton (green dot-dashed line) it is evident that the oscillation frequency is slightly higher than this. This is likely to be because this fast shallow soliton probes the edge of the condensate, where the density deviates from the TF profile (recall that the $\omega_s^0 = \omega_z/\sqrt{2}$ prediction assumes a TF density profile). In contrast, slower solitons are confined to oscillate in the centre of the system where the density essentially corresponds to the TF profile.

From equation (5.2) we know that the soliton oscillation amplitude in a harmonic trap is, to first order, approximately proportional to the initial soliton speed. Using this proportionality we can renormalise the soliton position for different soliton speeds, as shown in figure 5.5(b). The modulation in the soliton trajectory due to the back action of the dipole mode is present for all speeds, and increases in magnitude with soliton speed. This effect is also observed in the oscillatory evolution of the soliton energies, shown in figure 5.5(c). For a fast $v_0 = 0.9c$ soliton (green dot-dashed line) the energy modulations are substantial, extending down to around 0.4 of the initial energy.

We saw earlier that these position and energy modulations are generated by interaction of the dipole mode (set up by the soliton) with the oscillating soliton.

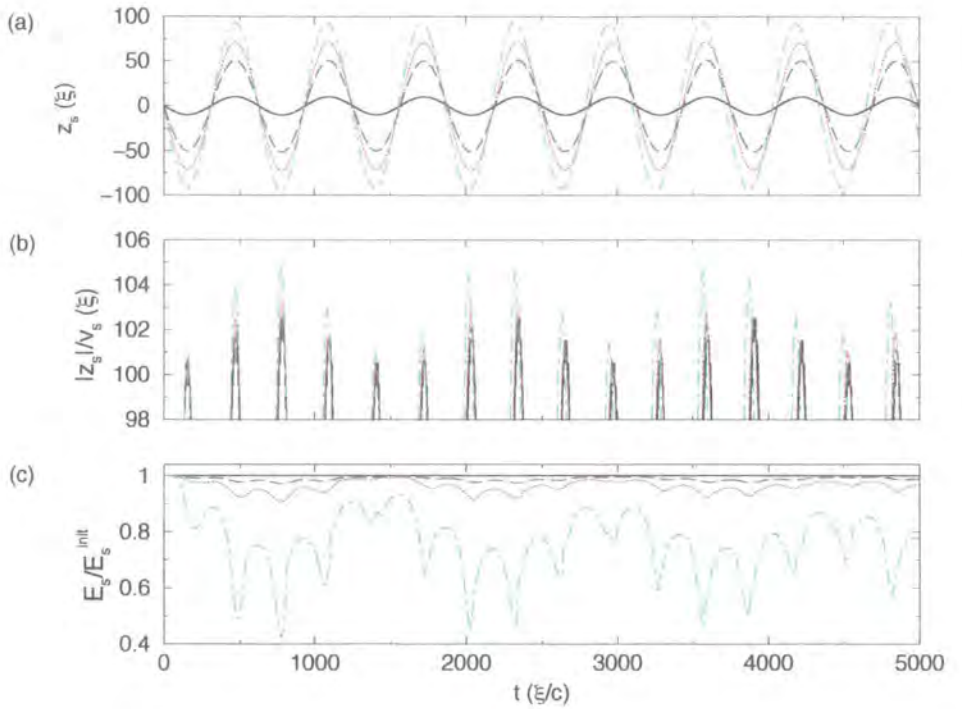

Figure 5.5: (a) Soliton position in an infinite harmonic trap $\omega_z = \sqrt{2}\times 10^{-2}(c/\xi)$, for initial speeds of $v_0/c = 0.1$ (black solid), 0.5 (blue dashed), 0.7 (red dotted), and 0.9 (green dot-dashed). (b) Absolute value of the amplitude of the soliton oscillations, renormalised by the initial soliton speed, and zoomed up around the soliton turning point. (c) Soliton energies E_s, renormalised by initial soliton energy E_s^{init}.

Fast shallow solitons have low energy and are comparable in amplitude to the dipolar motion of the background fluid. This interaction therefore has a large back action on fast solitons, and induces large position and energy modulations.

5.1.3 Variation with trap strength

Increasing the longitudinal trap strength (while maintaining the peak density) reduces the spatial extent of the condensate. For fixed initial speed, the soliton oscillation amplitude decreases, while remaining an approximately constant fraction of the TF radius, and the oscillation frequency increases. Figure 5.6(a) shows the soliton trajectory for various trap strengths. In order to allow direct comparison of the soliton dynamics in the different traps, position is rescaled

in terms of the TF radius $R_{\rm TF}$ and time in units of the inverse trap strength ω_z^{-1}. For low trap frequencies, e.g. $\omega_z = \sqrt{2} \times 10^{-2}(c/\xi)$ (black solid line), the soliton oscillates at the analytic prediction of $\omega_{\rm s}^0 = \omega_z/\sqrt{2}$. However, for higher trap frequencies, e.g. $\omega_z = 6\sqrt{2} \times 10^{-2}(c/\xi)$ (green dot-dashed line), the soliton oscillation frequency is clearly larger than this value.

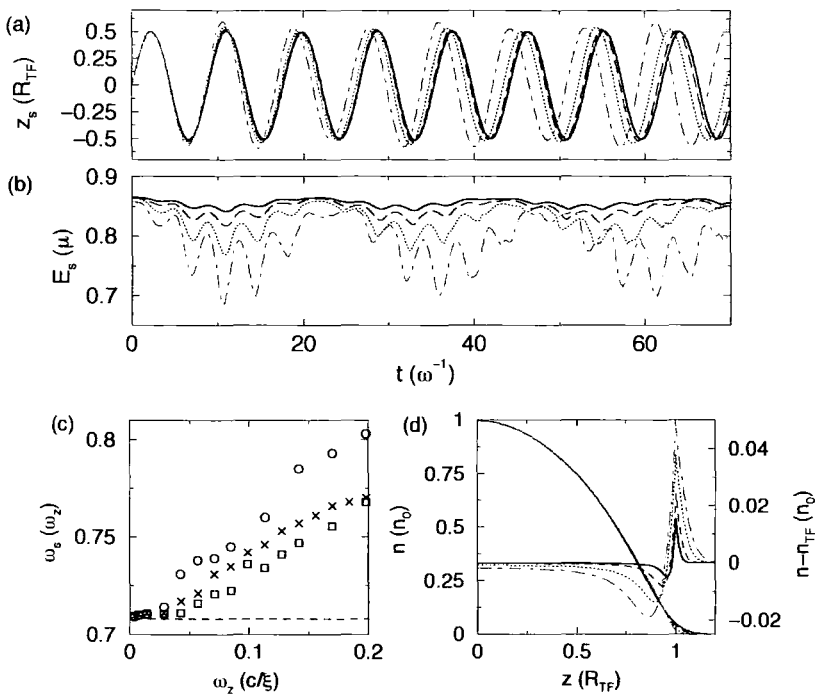

Figure 5.6: (a) Soliton position $z_{\rm s}$ as a fraction of the TF radius $R_{\rm TF}$ for trap strengths of $\omega_z = \omega_0 = \sqrt{2} \times 10^{-2}(c/\xi)$ (black solid line), $2\omega_0$ (blue dashed line), $4\omega_0$ (red dotted line), and $6\omega_0$ (green dot-dashed line).(b) Corresponding soliton energies $E_{\rm s}$. In order to allow direct comparison of the dynamics in different traps, time is expressed in units of the inverse trap frequency ω_z^{-1}. (c) Soliton oscillation frequency $\omega_{\rm S}$ as a function of trap frequency ω_z, for initial soliton speeds of $v_0/c = 0.25$ (squares), 0.5 (crosses), and 0.75 (circles). The analytic prediction of $\omega_{\rm s}^0 = \omega_z/\sqrt{2}$ is shown (dashed line). (d) Condensate density n (left axis) and deviation from the TF density $(n - n_{\rm TF})$ (right axis), for the trap frequencies considered in (a).

Figure 5.6(c) plots the soliton oscillation frequency as a function of the trap frequency, for various initial soliton speeds. For weak traps we see that $\omega_{\rm s}/\omega_z \approx 1/\sqrt{2}$, in agreement with the analytic prediction (dashed line). However, for in-

creasing trap strength, the ratio ω_s/ω_z increases monotonically from this value. This deviation can be considerable, being up to around 10% for the trap frequencies considered here.

The reason for this deviation is that, as the trap frequency is increased, the system moves further away from the TF limit. This effect is illustrated in figure 5.6(d), which plots the density profile across the condensate (left axis) for various trap frequencies. As the trap frequency is increased, the density increasingly deviates from the TF profile of an inverted parabola. This deviation is most prevalent towards the edge of the cloud, where it is observed as the formation of a 'tail' of low density extending past the TF radius. In order to highlight this deviation, we also plot the difference between the actual density and TF density in the same figure (right axis).

The modulations of the soliton position (figure 5.6(a)) and energy (figure 5.6(b)) due to interaction with the dipole mode increase in amplitude as the trap strength is increased. Here, the condensate is decreasing in size, reducing its effective mass, while the soliton remains fixed in size and effective mass. The oscillating soliton therefore induces a greater relative disturbance on the background fluid, which subsequently induces larger modulations on the soliton dynamics.

5.2 Dark soliton dynamics in a dimple trap

As described in chapter 4, the longitudinal acceleration of a dark soliton through an inhomogeneous density induces decay of the soliton via the emission of sound waves. However, it is evident that a soliton oscillating in an infinite harmonic trap does *not* decay over time. In order to investigate this apparent contradiction, we introduce the idea of a cutoff in the harmonic trap. From an experimental perspective the atoms still require global confinement, and so we consider a dimple trap geometry of the form,

$$V_{\text{ext}} = \begin{cases} \frac{1}{2}\omega_z^2 z^2 & \text{for} \quad |z| \leq z_0 \\ V_0 + \frac{1}{2}\omega_\zeta^2(|z| - z_0)^2 & \text{for} \quad |z| > z_0 \end{cases} \tag{5.5}$$

This consists of a tight harmonic with frequency ω_z and depth V_0, embedded in the centre of a much weaker harmonic trap of frequency ω_ζ, as illustrated

in figure 5.7. Although a harmonic *dimple* may not be experimentally possible, we will consider it here in order to gain information on the behaviour of dark solitons under harmonic confinement in general. A gaussian dimple, on the other hand, can be created experimentally, and naturally includes a cutoff. We will consider the case of a gaussian dimple trap later.

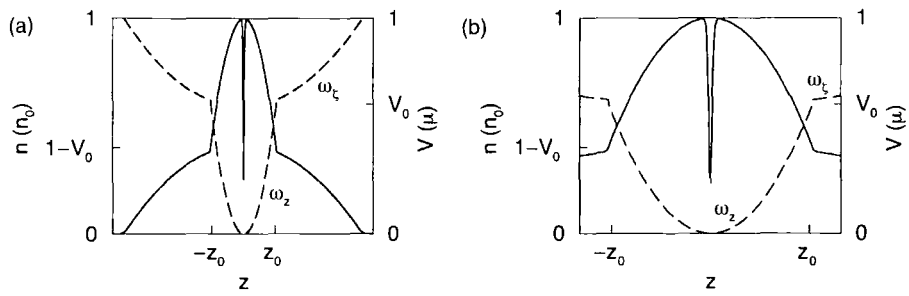

Figure 5.7: (a) Schematic of a condensate confined by a tight harmonic dimple of frequency ω_z, embedded within a weaker harmonic trap of frequency ω_ζ. The condensate density (left axis, solid line) and potential (right axis, dashed line) are shown. The density includes a non-stationary soliton centred at the origin. (b) Enlarged image of central region.

The soliton is confined to oscillate in the inner dimple, where it is expected to generate sound waves [166, 165]. These sound excitations have an energy of the order of the chemical potential μ. The depth of the inner trap V_0 therefore provides a sensitive handle on the containment of sound waves within the inner trap, and leads to two limiting regimes:

- For $V_0 > \mu$, the sound emitted will become reflected before it can escape to the outer trap, thus remaining confined to the inner region and forced to re-interact with the soliton. In this regime, the inner trap effectively represents a single harmonic trap.

- For $V_0 < \mu$, the sound emitted by the soliton can escape to the outer trap. The sound will eventually become reflected at the boundary of the BEC and return back to the inner trap, but the time for this to occur is now much longer. In essence, the aim of the dimple trap is that the soliton sees a tight harmonic potential and undergoes rapid oscillation, but the boundary that the sound waves experience, is large. This allows

us to probe, for a considerable time, the soliton dynamics in the absence of sound reinteraction, i.e. pure sound emission.

5.2.1 Homogeneous outer region

For a sufficiently weak outer trap $\omega_z \gg \omega_\zeta$ the density in the outer region can become almost homogeneous on the length-scale of the inner dimple. This is illustrated in figure 5.7(b), which shows an enlarged image of the central region of the dimple trap geometry. As a first approximation, we will assume the outer region to be homogeneous $\omega_\zeta = 0$. This means that any sound waves which escape to the outer region will propagate away indefinitely. This will allow us to investigate qualitatively the effect of the emitted sound escaping, without being limited to short measurement times. We will return later to the experimentally relevant case of $\omega_\zeta \neq 0$.

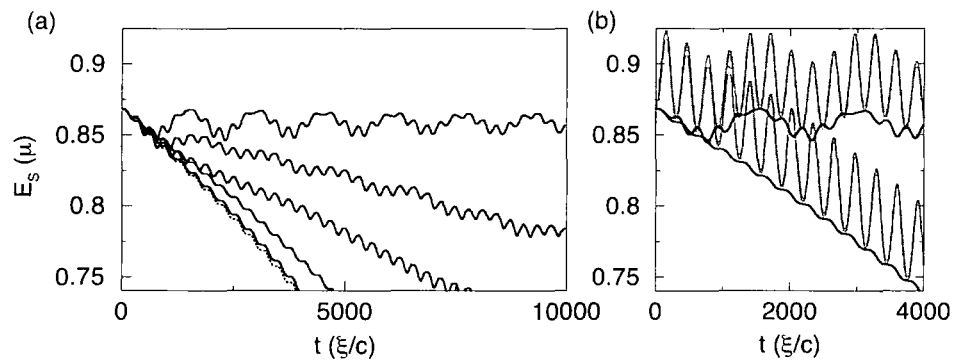

Figure 5.8: (a) Soliton energy as a function of time for a soliton with initial speed $v_0 = 0.5c$ and position $z = 0$ in a harmonic trap $\omega_z = \sqrt{2} \times 10^{-2}(c/\xi)$ for various potential cutoffs V_0/μ of (from bottom to top) 0.4, 0.8, 1, 1.02 and 1.1. The energy loss predicted by the nonlinear prediction of equation (4.4), valid in the limit of no sound reinteraction, is shown by the dotted line. (b) Soliton energy in the two extreme cases of $V_0/\mu = 0.4$ (lower lines) and 1.1 (upper lines) derived from the 1D GPE (black lines) and cylindrically-symmetric 3D GPE (grey lines).

We consider a harmonic dimple with frequency $\omega_z = \sqrt{2} \times 10^{-2}(c/\xi)$ and a homogeneous outer region $\omega_\zeta = 0$. A dark soliton is initially positioned at the trap centre with speed $v_0 = 0.5c$. Figure 5.8(a) shows the evolution of the soliton

energy for varying depths of the inner trap V_0. For $V_0 < \mu$ (figure 5.8(a), lowest line), the sound can escape the dimple and the soliton energy decays almost monotonically over time. This energy decrease has a step-like pattern with a periodicity of twice the soliton oscillation frequency (this behaviour will be explained later). For dimple depths of the order of the chemical potential, a significant fraction of the emitted sound becomes confined to the inner dimple. This leads to partial reabsorption of the emitted sound by the soliton, and a slowing of the decay. For $V_0 = 1.1\mu$ (figure 5.8(a), top line), the soliton energy features modulations but remains on average constant, and is essentially identical to the evolution of the soliton energy in a single harmonic trap (figure 5.3(b)). Here, the sound remains confined to the inner region. The soliton does not decay overall and so the emitted sound must be fully reabsorbed by the soliton. The periodic modulations in the energy can then be interpreted as arising from the continuous sound emission/reabsorption process.

The soliton energy from the 1D GPE and 3D GPE are compared in figure 5.8(b) for the two extreme cases of $V_0 = 0.4\mu$ and 1.1μ. As seen in section 5.1.1, the energy from the 3D GPE (grey lines) features an additional modulation due to the coupling to transverse modes. However, this effect induces no additional decay in the soliton, and subtracting these modulations leads to perfect agreement with the 1D results (black lines).

Low cutoff $V_0 < \mu$

Figure 5.9(a) illustrates the excitations in the fluid for a soliton oscillating in a dimple trap with a low cut-off, $V_0 < \mu$. The dark soliton (appearing as a black line) oscillates back and forth in the dimple, emitting counter-propagating sound waves (light/dark bands) which propagate out of the dimple. This decay causes a gradual reduction in the soliton depth, an increase in speed, and an increase in the oscillation amplitude. This is in direct contrast to a classical damped harmonic oscillator, where the speed and amplitude of oscillation decreases with time, and has led to the term *anti-damping* [165]. By $t \approx 1200(\xi/c)$, the soliton has anti-damped sufficiently to escape the inner trap into the outer homogeneous region. Here it propagates with constant speed and experiences no further sound emission. The path which would be expected for a non-dissipative

soliton is shown by the white dashed line.

The soliton energy (figure 5.9(b), solid line) decreases in a step-like manner until the soliton escapes the dimple, following which it maintains a constant value. Also shown on the same plot is the analytic renormalised soliton energy of equation (2.33) (dot-dashed line). This equation applies to an unperturbed soliton and gives the same result as the numerically integrated energy at the trap centre, where the density is locally homogeneous, but differs elsewhere.

The soliton acceleration (figure 5.9(c), left axis, dashed line) oscillates in time, while the power emission from the soliton (figure 5.9(d)) consists of a series of peaks, with both becoming fixed at zero when the soliton escapes to the outer homogeneous region. When the soliton is at the trap centre, where the potential is zero and background density is locally homogeneous, the soliton essentially represents a local solution to the 1D GPE and does not radiate sound waves. As the soliton passes up the trap walls, it experiences an inhomogeneous background density and an acceleration, which induces it to radiate sound waves. Both the acceleration and power emission increase with the soliton amplitude, and reach a maximum when the soliton is at its extrema. The soliton then changes direction and propagates towards the trap centre, with the soliton acceleration and power emission decreasing to zero at the trap centre. This cycle repeats itself, generating several power peaks, until the point when the soliton escapes into the outer region (where the soliton is stable).

The amplitudes of the power and acceleration peaks increase over time. The soliton decay has an accelerative effect, causing it to climb slightly further up the trap wall with each oscillation, and therefore the peak soliton acceleration and power emission increase over time. At the edges of the inner trap, fluid healing leads to a smoothing of the effective potential. When the soliton enters this crossover region, it experiences reduced acceleration, and this causes the small intermediate dips in the power emission at $t \approx 900$ and $1050(\xi/c)$. When the soliton escapes the inner trap and enters the outer homogeneous region it no longer experiences acceleration or sound emission.

In section 4.2 we studied a dark soliton accelerating on a linear ramp, and showed that the rate of sound emission from the soliton is proportional to the soliton acceleration squared. In figure 5.9 we see that the empirical acceleration-

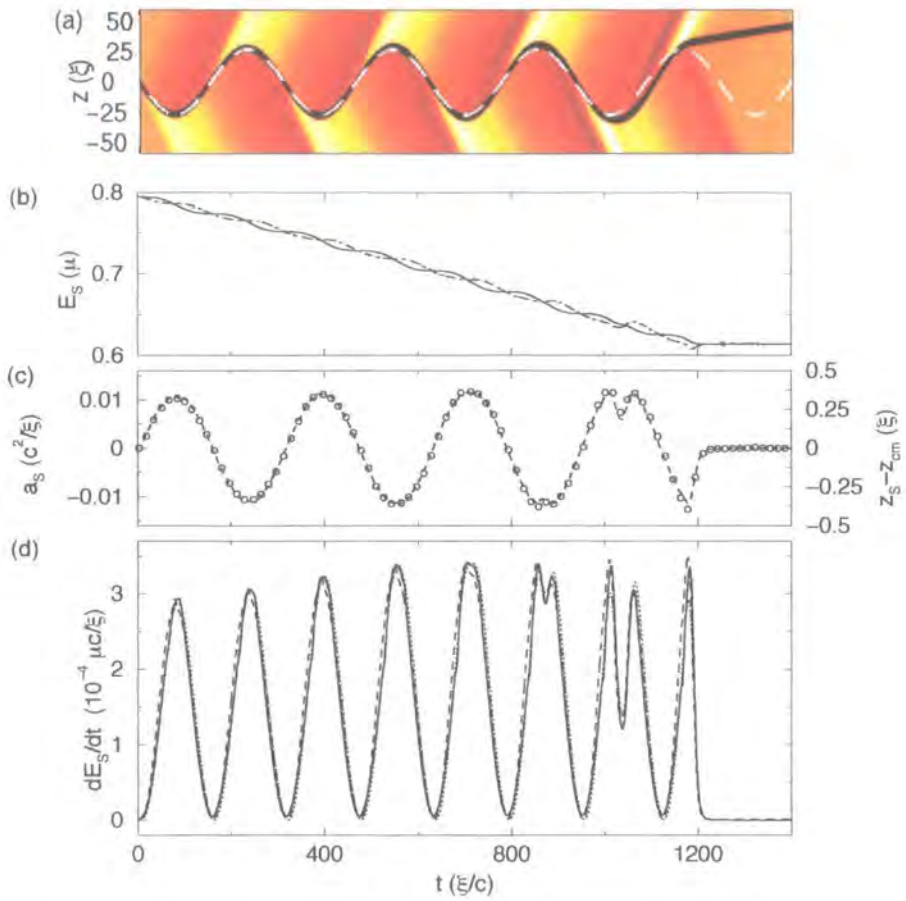

Figure 5.9: Soliton dynamics in a dimple trap $\omega_z = \sqrt{2} \times 10^{-2}(c/\xi)$ with low cutoff $V_0 = 0.4\mu$ and homogeneous outer region $\omega_\zeta = 0$. The soliton is initially at the trap centre with speed $v_0 = 0.5c$. (a) Space-time carpet plot of the renormalised density (actual density minus background density). Sound emission is evident (bright/dark bands), with an amplitude of $\sim 2\% n_0$. (b) Soliton energy E_S from the GP energy functional (solid line) and homogeneous soliton energy of equation (2.33) (dot-dashed line). The dotted line corresponds to the theoretical prediction of equation (4.4). (c) Soliton acceleration a_S (left axis, dashed line) and the deformation parameter $(z_s - z_{cm})$ (right axis, circles). (d) Power radiated from the oscillating soliton dE_s/dt, calculated from the GP energy functional (solid line), the acceleration-squared law of equation (4.3) with $\kappa = 2.3(\mu\xi/c^3)$ (dashed line), and the prediction from nonlinear optics of equation (4.4) (dotted line).

squared law of equation (4.3) (dashed line) gives good agreement with the power emission derived numerically (solid line). Furthermore, we also consider the applicability of the acceleration-squared law of equation (4.4) for unstable dark solitons in nonlinear optics. This equation is derived by assuming a homogeneous system of infinite extent. Firstly, it can only be valid in double trap structures if the dimple trap is sufficiently shallow that it essentially allows complete escape of sound to the outer trap. Even then, it will only hold until the emitted sound returns to the dimple region after reflection from the outer trap. In these limits the asymptotic conditions become practically indistinguishable from the homogeneous ones, thus justifying the use of the nonlinear optics result. The validity of equation (4.4) is not dependent on the origin of the instability, but rather on the fact that the emitted sound escapes from the soliton region. Figure 5.9(d) confirms the applicability of equation (4.4) (dotted line) in the regime $V_0 < \mu$ by direct comparison to the results from the GP energy functional (solid line). Further evidence is provided in figure 5.8 which shows clearly that as the cutoff is decreased, the variation of energy with time (solid lines) approaches this analytic result in the limit of no reabsorption (dotted line). We stress that equation (4.4) will *not* hold in the usual infinite harmonic traps, where multiscale asymptotic techniques must be combined with boundary layer theory [165].

The process of sound emission causes an apparent deformation of the soliton density profile from its unperturbed state. Huang *et al.* [166] have predicted soliton deformation for a dark soliton interacting with a potential step in a condensate. Figure 5.10(a) illustrates the actual density (solid line) and background density (dotted line) in the soliton region, at (i) the first turning point $t \approx 80(\xi/c)$, (ii) first passage through trap centre $t \approx 160(\xi/c)$, and (iii) second turning point $t \approx 240(\xi/c)$. Subtracting the background density from the actual density in the soliton region allows us to view the deformation without the overall background modulation. This renormalised (perturbed) soliton profile (solid line) is shown in figure 5.10(b). We have also included the corresponding unperturbed soliton profile (dashed line), which has the same density depth as the actual soliton. At the trap centre, where the sound emission is locally zero, the soliton profile is essentially unperturbed. However, when the soliton is off-centre, the asymmetric nature of the emitted sound waves results in a

lop-sided deformation of the apparent soliton profile. This means that during sound emission the soliton centre of mass deviates from the density minimum [213].

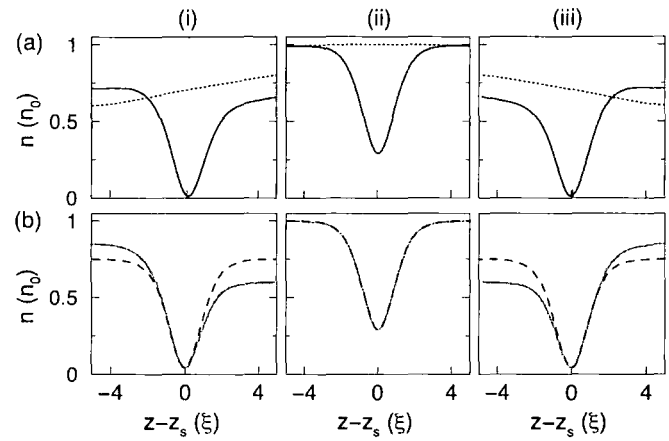

Figure 5.10: (a) Actual density (solid line) and background density (dotted line) in the soliton region, for snapshots of the soliton motion shown in figure 5.9(a): (i) first turning point, (ii) first passage though the trap centre, and (iii) second turning point. (b) Renormalised density in the soliton region (grey line) and the correspondng unperturbed soliton profile of equation (3) (dashed line). Note that, for clearer illustration, the sound densities in (a) and (b) have been amplified by a factor of 10. (The sound density has been obtained by subtracting from the actual perturbed soliton profile the corresponding unperturbed soliton profile.)

A convenient quantity to parameterise the soliton deformation is the displacement of the soliton centre of mass $z_{\rm cm}$ from the soliton density minimum $z_{\rm s}$, with the former being defined as

$$z_{\rm cm} = \frac{\int_{z_{\rm s}-5\xi}^{z_{\rm s}+5\xi} z\,(|\psi|^2 - n)\,{\rm d}z}{\int_{z_{\rm s}-5\xi}^{z_{\rm s}+5\xi} (|\psi|^2 - n)\,{\rm d}z}. \tag{5.6}$$

The evolution of the deformation parameter $(z_{\rm s} - z_{\rm cm})$ is shown in figure 5.9(c) (right axis, circles). The quantity oscillates in time with the soliton motion, being zero when the soliton is at the trap centre and at a maximum when the soliton is at the zenith of its trajectory. The shift can be substantial; in this case, it reaches up to around half a healing length, and will be larger for

tighter traps. Importantly, we find that the shift is proportional to the soliton acceleration, and is thus an alternative quantity with which to parameterise the power emission from the soliton.

5.2.2 Harmonic outer region

In a real BEC experiment there is no direct method by which to measure the soliton energy, and the emitted sound waves are too low in amplitude to be observed with current techniques. In fact, the only soliton quantities which can be directly tracked are its position and density contrast. The experimental signatures of a decaying soliton in a harmonic trap would therefore be an increase in the oscillation amplitude, a reduction in the soliton density contrast, and a change in the oscillation frequency. The harmonic dimple considered in section 5.2.1 is relatively weak, and the soliton oscillation amplitude is slow to evolve. We will now consider a tighter inner dimple, in which the soliton dynamics are expected to evolve at a much faster rate. In addition, we now explicitly include an ambient harmonic trap, as would be required in the corresponding experiment.

We take the inner trap frequency to be $\omega_z = \sqrt{2} \times 10^{-1}(c/\xi)$, which is ten times larger than we have considered so far, and the outer frequency $\omega_\zeta = \omega_z/10$. The potential cutoff is $V_0 = \mu$, which *just* allows sound to escape to the outer region. The evolution of this system, featuring a soliton with initial speed $v_0 = 0.2c$, is shown in figure 5.11(a), while the corresponding case featuring a large potential cutoff $V_0 > \mu$ is shown in figure 5.11(b). Figure 5.11(c) shows the path of the soliton for low (dashed line) and high (solid line) cutoff. For $V_0 > \mu$, the soliton oscillates in the fluid, inducing density excitations, but features no net decay. For $V_0 = \mu$, however, the sound waves generated by the oscillating soliton can escape the inner dimple for a short time. The soliton decays rapidly, resulting in a visible increase in the oscillation amplitude and decrease in frequency. At a time of around $t \approx 200(\xi/c)$ the escaped sound begins to return back to the dimple. However, the re-interaction of the soliton with the emitted sound does *not* lead to the stabilisation of the soliton decay. The motion of the sound through the different outer trap modifies it, or 'dephases' it, with respect to the soliton, such that it does not become fully reabsorbed. By around $t \approx 300(\xi/c)$,

the density dip is extremely shallow and oscillates almost up to the edge of the dimple. This suggests that the soliton may have completely decayed by this point, and left behind a 'ghost soliton' in the form of a dark (negative amplitude) sound excitation.

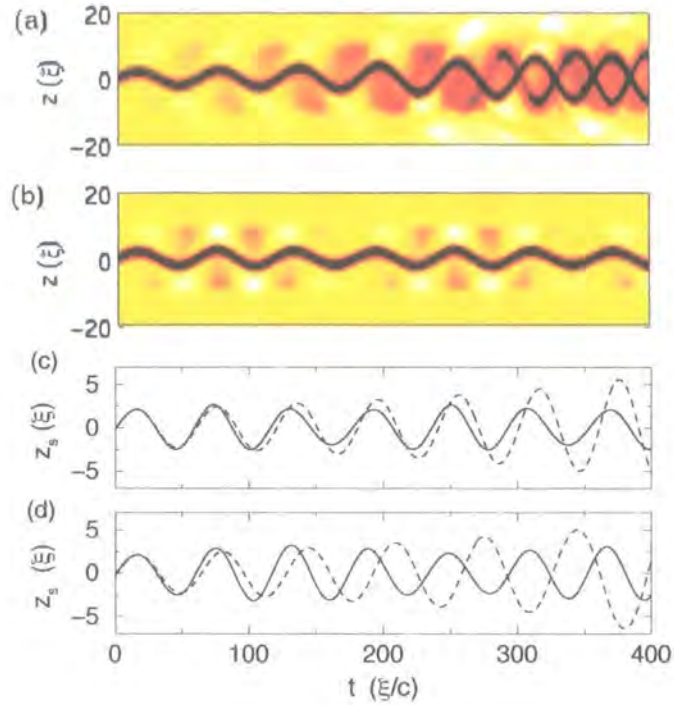

Figure 5.11: (a)-(b) Space-time plots of the renormalised density showing a soliton, with initial speed $v_0 = 0.2c$, oscillating in a double trap with frequencies $\omega_z = \sqrt{2} \times 10^{-1}(c/\xi)$, $\omega_\zeta = \omega_z/10$, and a potential cutoff (a) $V_0 = 1\mu$ and (b) $V_0 = 5\mu$. The density scale has an amplitude of $2\%n_0$. (c) Path of the soliton in (a) (dashed line) and (b) (solid line). (d) Path of the soliton for the case of a gaussian inner dimple, featuring the same effective trap frequency as the harmonic dimple, for potential cutoffs of $V_0 = 5\mu$ (solid line) and $V_0 = \mu$ (dashed line).

So far we have considered the motion of a dark soliton in harmonic dimple. However, a more experimentally realistic scenario is that of a gaussian dimple. Such a potential can be experimentally induced by the presence of a far-off-resonant red-detuned laser beam [32, 229]. The gaussian potential has the form $V(z) = V_0[1 - \exp(-\omega_z^2 z^2/2V_0)]$, such that for small z the trap yields the same

oscillation frequency as a harmonic dimple of frequency ω_z. Figure 5.11(d) shows the soliton paths for the case of a gaussian dimple. Here, the soliton dynamics for low and high potential cutoff are qualitatively similar to the case for a harmonic dimple. However, the change in the soliton dynamics due to sound emission is more rapid and noticeable in the gaussian dimple. This is due to the fact that, as the soliton anti-damps to the edge of the trap, the potential that it experiences tails off, decreasing its oscillation frequency.

In section 3.3 we showed that a condensate under the 1D GPE corresponds to a cylindrically-symmetric quasi-1D condensate with transverse confinement $\omega_r = 3.52(c/\xi)$. The trap parameters in figure 5.11 therefore correspond to a quasi-1D condensate with $\omega_z = \omega_r/25$ and $\omega_\zeta = \omega_r/250$. Choosing $\omega_r = 2\pi \times 1000$ Hz, we find that the time unit for ^{23}Na atoms corresponds to $(\xi/c) \approx 3 \times 10^{-4}$s, which implies that the timescale of figure 5.11 is of the order of a few hundred milliseconds. This lies within the expected soliton lifetime for a quasi-1D system [156, 158, 165], and implies that soliton decay due to sound emission is an experimentally observable phenomena.

5.3 Dark soliton dynamics in a harmonic trap perturbed by an optical lattice

Optical lattices represent highly-tunable periodic geometries in which to confine BECs, and enable atomic systems to probe the regime of crystalline condensed matter. Recent BEC experiments involving optical lattices have led to the atomic realisation of the quantum Mott insulator transition [49], arrays of Josephson junctions [47], gap solitons [73, 230, 231, 232], number squeezed states [46], and Bloch oscillations [48]. Following the multitude of current optical lattice experiments, we will consider the longitudinal dynamics of a dark soliton in a quasi-1D optical lattice geometry. Note that the transition radiation by bright matter wave solitons in an optical lattice potential has been predicted in [233]. An optical lattice is formed by the standing wave set up by two counter-propagating laser beams. If these beams are off-resonant, then the standing wave interacts with the atoms via the optical dipole force to induce a periodic potential which is proportional to the intensity of the light field. Global

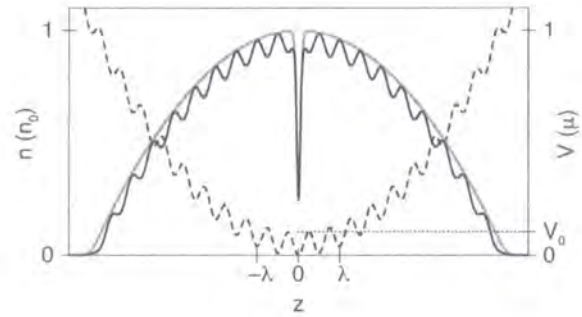

Figure 5.12: Schematic of the condensate density (left axis, solid line) under the confinement of a harmonic trap and optical lattice (right axis, dashed line), with a non-stationary soliton located at the origin. The optical lattice has height V_0 and periodicity $\lambda/2$. The corresponding density in the absence of the optical lattice is also illustrated (grey line).

confinement of the atoms is still necessary, and so the optical lattice generally acts in addition to an overall harmonic trap. The combined potential of a 1D optical lattice and harmonic trap is given by,

$$V(z) = \frac{1}{2}\omega_z^2 z^2 + V_0 \sin^2(2\pi z/\lambda), \tag{5.7}$$

and is illustrated in figure 5.12. Here V_0 is the height of the lattice potential and $\lambda/2$ is the periodicity of the lattice sites, where λ generally corresponds to the wavelength of the laser light λ_{laser}. However, if a relative angle θ exists between the two beams, the effective wavelength of optical lattice becomes $\lambda_{\text{laser}}/\sin\theta$. Assuming a laser wavelength $\lambda_{\text{laser}} \sim 0.8\ \mu$m (typically produced by a diode laser), then lattice wavelengths ranging from this value (which roughly corresponds to the size of the soliton) up to the order of $\lambda \sim 20\ \mu$m can be achieved. This is the range of lattice periodicities that we will consider here. The lattice depth V_0 is proportional to the laser intensity, and can be realistically varied from zero to values much larger than the chemical potential.

Kevrekidis *et al.* [168] and Theocharis *et al.* [234] have theoretically investigated the dynamics of dark solitons in optical lattices at slow speed, and observe sound emission. Scott *et al.* [133] have simulated the motion of a condensate through a 1D optical lattice and observe the disruption of the condensate with production of dark solitary waves and vortex rings. We will consider the soliton dynamics over the experimentally realistic range of lattice depths and periodicities. The

ambient harmonic trap is kept constant throughout this section, with frequency $\omega_z = \sqrt{2} \times 10^{-2}(c/\xi)$, while the initial soliton speed is $v_0 = 0.5c$.

5.3.1 Soliton dynamics and sound emission in an optical lattice

Figure 5.13 compares the evolution of a dark soliton in a harmonic trap to that in the same trap when additionally perturbed by an optical lattice. In the absence of the optical lattice (figure 5.13(a)) the soliton (dark line) oscillates in the trap at $\omega_s = \omega_z/\sqrt{2}$, emitting and reabsorbing sound waves (bright/dark regions). Overall, the soliton does not decay, but gets continuously perturbed by fluid motion generated by the soliton itself (light/dark regions). This sound field has a relatively large wavelength and an amplitude of the order of $0.01n_0$.

Application of an additional optical lattice potential, however, can greatly affect the soliton dynamics and stability. In figure 5.13(b) we show the evolution of the same system but now featuring an optical lattice with height $V_0 = 0.2\mu$ and wavelength $\lambda = 20\xi$. As the soliton oscillates in the trap due to the overall harmonic confinement, it is forced to traverse many lattice sites. This induces further instability in the soliton, in addition to the effect of the harmonic trap, and each interaction with a lattice site leads to the emission of counter-propagating sound waves of relatively short wavelength. The harmonic trap still contributes to the sound emission, as seen by the faint 'white' band of sound in figure 5.13(b), but this emission is heavily obscured (compared to figure 5.13(a)) by the lattice-generated sound waves. The subsequent re-interaction of these sound waves with the soliton does *not* lead to a full stabilisation of the decay, as it does in a pure harmonic trap. This is due to a modification, or dephasing, of the emitted sound as it propagates through the combined harmonic trap and optical lattice. This is similar to the effect observed for a dark soliton in the dimple trap of section 5.2. Indeed, it is known that the presence of an optical lattice can significantly modify the sound spectrum of a condensate [235]. The soliton undergoes relatively rapid decay, anti-damping to greater oscillation amplitudes, and by a time $t \approx 1400(\xi/c)$ is virtually indistinguishable from the sound field. Note that, at late times, this sound field is densely packed with many sound pulses of short extent, and has an amplitude of the order of $0.05n_0$.

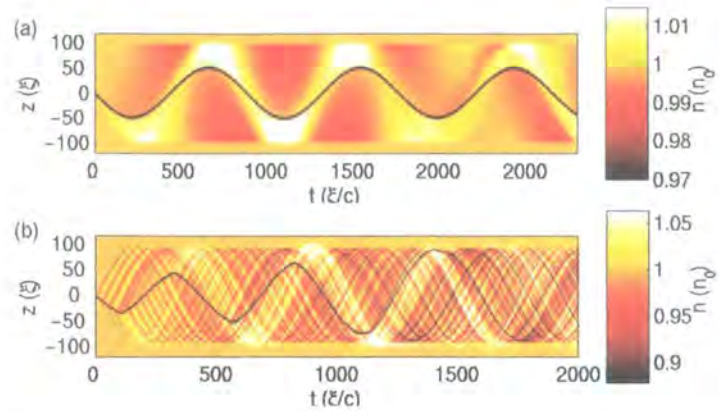

Figure 5.13: Space-time carpet plots of the renormalised condensate density for (a) harmonic confinement $\omega_z = \sqrt{2} \times 10^{-2}(c/\xi)$ only and (b) the same harmonic trap plus an optical lattice with $V_0 = 0.2\mu$ and $\lambda = 20\xi$. Both cases start with a dark soliton at the origin with speed $v_0 = 0.5c$. Sound waves are clearly emitted by the dynamically unstable soliton, not only as it climbs the trap walls, but also as it traverses the lattice sites. Note that the sound waves in (b) have a much greater amplitude (see the different density scales).

The short-term soliton dynamics for the case shown in figure 5.13, up until the time when the emitted sound reinteracts with the soliton, are shown in figure 5.14. The corresponding soliton dynamics in the absence of the optical lattice are also shown for comparison (grey lines). The lattice sites inhibit the soliton motion, causing the soliton to reverse direction earlier and at a lower amplitude, and therefore have a higher oscillation frequency (figure 5.14(a)), than the corresponding motion in the absence of the optical lattice. As the soliton traverses up and down the density modulations (figure 5.14(b)) it experiences a rapidly-varying acceleration (figure 5.14(c)). This is modulated by the relatively slow acceleration due to the soliton oscillation in the ambient harmonic trap, which is zero when at the trap centre and a maximum at its extremum.

The instability of the soliton to motion through an inhomogeneous density induces the soliton to radiate sound waves. As described in section 5.2.1, sound emission results in a shift of the soliton centre of mass from the density minimum. This shift, shown in figure 5.14(c)(right axis), oscillates in proportion to the soliton acceleration. The soliton decay is characterised by a periodic cascade of the soliton energy, as shown in figure 5.14(d). This cascade is more

evident when considering the power emitted by the soliton, shown in figure 5.14(e). The power consists of a series of regular peaks of various amplitudes, which clearly occur whenever the soliton traverses the side of a lattice site, i.e. where the density gradient is a local maximum. In addition, it features an overall modulation induced by the motion in the ambient harmonic trap, becoming a maximum when the soliton is at an extremum of the trap. The peaks are therefore greatest at around $t \sim 110(\xi/c)$, which corresponds to the point of maximum soliton acceleration.

The acceleration-squared model of equation (4.3) for the power emission is also plotted in figure 5.14(e)(dashed line). Despite the rapidly-varying soliton dynamics, this still represents a good model to the power emission, up to the point where sound returns to the soliton region at $t \approx 250(\xi/c)$. After this time, sound is partially reabsorbed by the soliton and the acceleration-squared law ceases to be valid. For the same reasons the proportionality between acceleration and the deformation parameter is no longer valid, as evident in figure 5.14(c).

5.3.2 Effect of varying the lattice height

In the previous section we studied the *short-term* dynamics of the soliton in the presence of a harmonic trap and optical lattice, up until the emitted sound reinteracts with the soliton. However, we have seen in figure 5.13 that this reinteraction does not fully stabilise the soliton decay, unlike in a pure harmonic trap. We now investigate the *long-term* stability of the soliton, which includes the effect of reinteraction with the emitted sound. First, we consider the effect on the soliton dynamics of varying the height of the optical lattice V_0. Throughout this section, the wavelength of the lattice is kept constant at $\lambda = 20\xi$.

Figure 5.15 shows the evolution of the soliton position and energy for various lattice heights. Increasing the lattice height leads to two distinct effects which modify the soliton dynamics in opposing manners. Firstly, the optical lattice modifies the condensate profile, periodically reducing the density. This inhibits the motion of the soliton and tends to shift its turning point towards the centre of the trap and *increase* its oscillation frequency. This effect can be seen by the dashed line ($V_0 = 0.1\mu$) in figure 5.15(a). Indeed, if the lattice height is

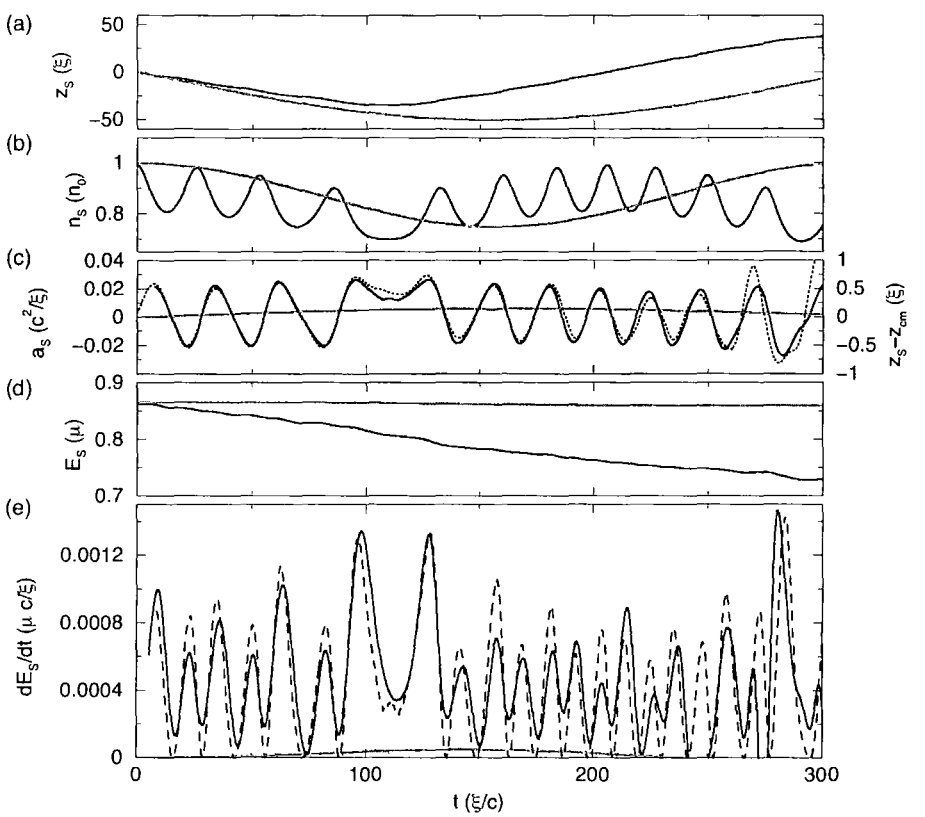

Figure 5.14: Comparison of dynamics of a soliton in a harmonic trap plus optical lattice with $V_0 = 0.2\mu$ and $\lambda = 20\xi$ (black lines) and corresponding dynamics only in the presence of the harmonic trap (grey lines). (a) Path of soliton z_s versus time. (b) Background density at the soliton position n_s . (c) Soliton acceleration a_s (solid line, left axis) and deformation parameter $(z_s - z_{cm})$ (dotted line, right axis). (d) Soliton energy E_s. (e) Power emitted by the soliton dE_s/dt as computed from the GP energy functional (solid line), compared with the acceleration squared law of equation (4.3) with $\kappa = 2.14(\mu\xi/c^3)$ (dashed line).

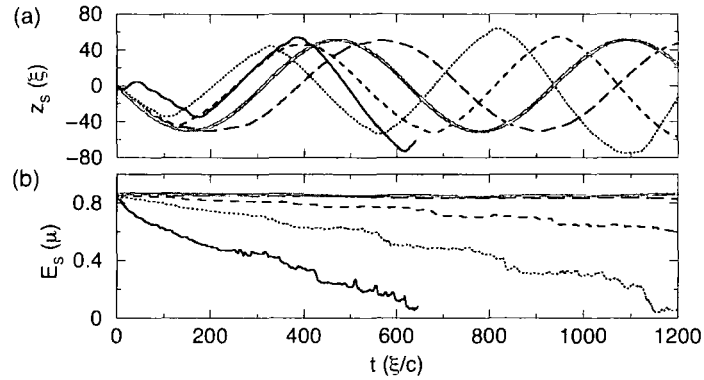

Figure 5.15: Effect of lattice height on the soliton dynamics. (a) Path and (b) energy of the soliton in a harmonic trap (grey lines), and a harmonic trap plus an optical lattice with $\lambda = 20\xi$ and lattice heights $V_0 = 0.05\mu$ (long-dashed line), $V_0 = 0.1\mu$ (dashed line), $V_0 = 0.2\mu$ (dotted line) and $V_0 = 0.4\mu$ (solid line). For the $V_0 = 0.4\mu$ case, the soliton decays rapidly and cannot be tracked numerically after $t \sim 650(\xi/c)$.

sufficiently large, the soliton will initially be trapped within a single lattice site. Secondly, the optical lattice induces sound emission from the soliton. The soliton energy decays essentially monotonically, with the average decay rate increasing with lattice height. This decay leads to a gradual *decrease* in the oscillation frequency and *increase* in the amplitude. For small lattice heights, e.g. $V_0 = 0.05\mu$ (long-dashed lines in figure 5.15), the optical lattice poses little resistance to the soliton motion, and the low level of sound emission it induces causes the main observable effects. These are a small decrease in the soliton oscillation frequency and a slow decay of the soliton energy. The competing effects are most clearly observed for $V_0 = 0.4\mu$ (solid line in figure 5.15(a)). The soliton is initially confined to a single lattice site, with a high oscillation frequency. Sound emission causes the soliton to gradually 'anti-damp' out of this site into adjacent sites, leading to a decrease in its oscillation frequency and an increase in its amplitude. This effect has been reported in [234]. The soliton rapidly accelerates towards the edge of the cloud where it ultimately merges into the sound field. However, in the limit $V_0 > \mu$, an array of mini-condensates is formed. Each lattice site becomes an effectively closed system, and the emitted sound cannot escape the site. In this limit the GP equation predicts that full

sound reabsorption by the soliton occurs, which stabilises it against decay, as in a pure harmonic trap. In the limit of very small lattice periodicities, the discrete nonlinear Schrodinger equation may be a more appropriate description, in which case additional oscillatory instabilities come into play [168, 169].

5.3.3 Effect of varying the lattice periodicity

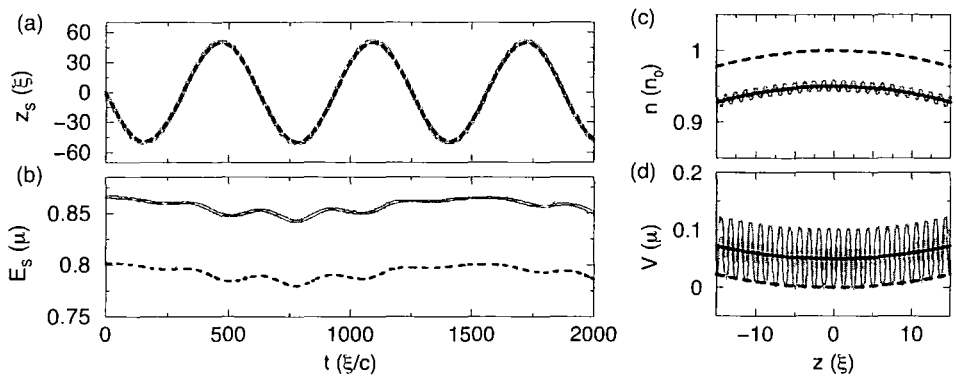

Figure 5.16: Effect of small lattice periodicity $\lambda/2 \sim \xi$ or less. (a) Path and (b) energy of a dark soliton in a tight optical lattice, $\lambda = 2.5\xi$, with height $V_0 = 0.1\mu$ (dashed line), compared to the absence of the optical lattice (grey line). (c) The density (grey line) for this tight lattice cannot fully heal, shifting the average density down (black line) in relation to the harmonic trap density (dashed line). (d) Since the fluid cannot heal fully to the tight lattice potential (grey line), the effective potential tends towards a harmonic trap shifted upwards (solid line) by the mean lattice potential $V_0/2$. The unperturbed harmonic potential is also shown (dashed line).

We now consider the long-term effect on the soliton dynamics of varying the lattice periodicity. This effect is also considered analytically and numerically in [234]. The soliton path and energy is shown in figure 5.15 for various lattice heights, while keeping the lattice height fixed at $V_0 = 0.1\mu$.

We start by discussing an anomalous regime, the tight lattice regime, where the lattice periodicity is of the order of, or less than, the soliton width. The path and energy of the dark soliton under the influence of a tight optical lattice ($\lambda = 2.5\xi$ and $V_0 = 0.1\mu$) are shown by the dashed line in figure 5.16(a) and 5.16(b)

respectively. The path of the soliton is identical to that in the absence of the optical lattice (solid grey line), while the energy has the same form but is shifted to a lower value. This effect can be explained by careful consideration of the density perturbations caused by the optical lattice. In the limit where the lattice wavelength is of the order of, or less than, the soliton width, the fluid cannot heal to the optical lattice, and the associated density modulations smear together. This is analogous to the healing of the condensate density for the narrow square potential barriers of Appendix B. The background density becomes reduced across the whole condensate, and in particular the peak density is suppressed $n_0 \rightarrow n_0'$. This is due to the fact that, in our simulations, the chemical potential μ is fixed. If, however, the peak density/number of particles were kept fixed, then the chemical potential would increase accordingly. The soliton essentially sees a constant effective optical lattice potential of height $V_0/2$, and overall it sees the ambient harmonic potential shifted upwards by this amount, an effect illustrated in figure 5.16(c) and 5.16(d). In both cases of a pure harmonic trap and a harmonic trap modified by a tight optical lattice, the initial soliton speed has been set to the same value $v = 0.5c$ (i.e. the dependence on peak density is removed), ensuring that the paths are identical. If we assume a Thomas-Fermi relationship between potential and density, then we would expect, to first order, the peak density to be decreased by $(V_0/2)n_0 = 0.05n_0$. According to equation (2.33) implies that the initial soliton energy will be rescaled by a factor of $(n_0'/n_0)^{\frac{3}{2}}$, i.e. $E_s^{\text{init}} \rightarrow 0.926 E_s^{\text{init}}$, and this is indeed the modified soliton energy observed.

We now investigate the general effect of lattice periodicity on the soliton dynamics. The soliton path and energy for various lattice wavelengths are shown in figure 5.17(a) and (b) respectively. In order to remove the effect of reduced peak density for sufficiently tight lattices (based on our fixed chemical potential simulations), the soliton energies in figure 5.17(b) have been rescaled in terms of the initial soliton energy. This effect is quantified in figure 5.17(c) which shows the variation in the initial soliton energy as a function of lattice wavelength.

Looking now at the decay of the (normalised) soliton energy as a function of time for various lattice wavelengths, we find that increasing the lattice wavelength (but still remaining far from the tight lattice regime considered earlier) leads to the decay of the soliton energy and an associated increase in the soliton

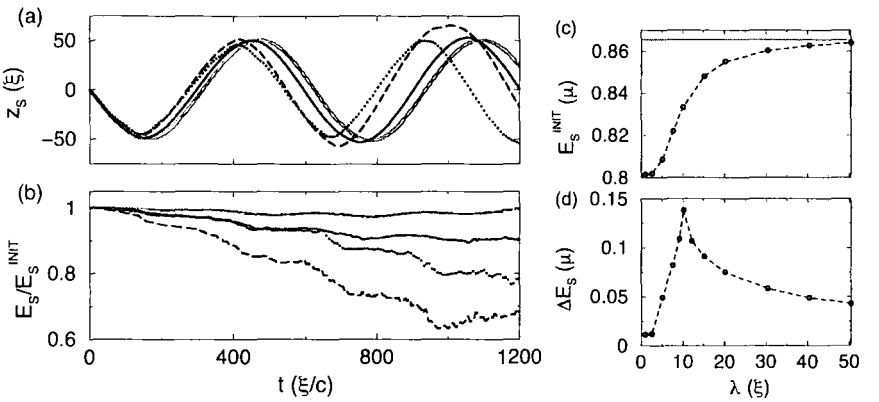

Figure 5.17: Effect of lattice periodicity on the soliton dynamics. (a) Path and (b) energy, rescaled by the initial soliton energy E_s^{init}, of a soliton in a harmonic trap (grey line), and an additional optical lattice with height $V_0 = 0.1\mu$ and various wavelengths: $\lambda = 5\xi$ (solid line), $\lambda = 10\xi$ (dashed), and $\lambda = 40\xi$ (dotted line). (c) Initial soliton energy E_s^{init} as a function of lattice wavelength, compared to the $V_0 = 0$ harmonic case (horizontal grey line). (d) Loss of soliton energy ΔE_s after one full oscillation, as a function of lattice wavelength.

amplitude and frequency (e.g. $\lambda = 5\xi$, solid line in figure 5.17(a) and(b)) in relation to the pure harmonic case (grey line). The rate of this decay increases up to some resonant wavelength ($\lambda = 10\xi$, dashed line). Any further increase in the wavelength leads to a slowing of the decay. This is illustrated in figure 5.17(b) by the reduced decay rate for $\lambda = 40\xi$ (dotted line) compared to $\lambda = 10\xi$ (dashed line).

The dependence of the soliton decay on the lattice periodicity can be explained in terms of the density inhomogeneity that the soliton experiences. To illustrate this analysis more quantitatively, figure 5.17(d) plots the loss in soliton energy after one full oscillation as a function of lattice wavelength. For tight lattices, where the lattice periodicity is of the order of, or less than, the soliton width, the soliton effectively sees a displaced harmonic trap, and so experiences no net decay, due to complete stabilisation by sound reabsorption. In this limit, the soliton energy oscillates periodically due to the continuous sound emission/reabsorption process. This takes the form a beating effect caused by the different oscillation frequencies of the soliton and sound (dipole mode). Therefore, one full oscillation of the soliton in the trap does not correspond to

one beat period, and hence the soliton energy has not yet returned to its initial value, explaining the small apparent energy loss.

For progressively weaker lattices, the density begins to heal to the optical lattice, thereby modifying the condensate density from the harmonic trap profile. This increases the density inhomogeneity that the soliton sees, and induces an increase in the rate of decay. Furthermore, the presence of these density modulations dephases the sound field such that the soliton is no longer fully stabilised by sound reabsorption.

Increasing the lattice periodicity further leads to some critical wavelength at which the condensate density can heal fully to the lattice potential. This represents the system with the maximum density inhomogeneity (for a fixed lattice height) and therefore features the most rapid soliton decay. This point is indicated by the resonance in figure 5.16(d) and occurs for $\lambda \sim 10\xi$. Further increase in the wavelength does not change the depth of the density modulations, but merely stretches them out. This now reduces the density gradient experienced by the soliton and causes a reduction in the decay rate. As $\lambda \to \infty$ the decay will asymptotically tend towards zero as the trap potential returns to becoming effectively harmonic.

We have shown that the application of an optical lattice in a harmonic trap tends to destabilise a moving dark soliton, leading to its decay via sound emission. The soliton is generally not stabilised by sound reabsorption, and the soliton ultimately decays completely away. This decay rate is a function of the lattice wavelength and height, as well as the trap frequency. Choosing the same experimental parameters as in section 5.2.2, the timescales presented in this section are within the expected lifetime of a dark soliton in a quasi-1D condensate of the order of 1 s [156]. The optical lattice geometry therefore provides a highly-controllable system in which to study the generation of sound from a soliton and the ensuing soliton-sound interactions, and is a convenient alternative to the double trap geometry of section 5.2.2.

5.4 Summary

In this chapter we have studied the longitudinal motion of dark solitons in confined BECs. In a harmonic trap, the soliton tends to oscillate in the trap at the predicted TF frequency of $\omega_s^0 = \omega_z/\sqrt{2}$. However, for fast solitons or away from the TF regime, we have observed that this frequency deviates by over 10%. As the soliton moves through the inhomogeneous density it continuously radiates sound waves due to its inherent instability under acceleration. In this confined system the emitted sound becomes reabsorbed, and the soliton is fully stabilised to this decay mechanism. In addition, the soliton motion induces a dipolar collective mode in the system.

By modifying the longitudinal harmonic trap geometry it is possible to induce soliton decay in a controllable manner. One method is to employ a dimple trap of finite depth, embedded in a weaker harmonic trap. For deep dimples, the emitted sound remains confined in the same region as the soliton and reinteracts with it, stabilising the soliton decay. However, for shallow dimples, the sound can escape to the outer region for a considerable time, during which the soliton dynamics can be observed in the limit of no reabsorption. This leads to soliton decay, with the power emission being consistent with the acceleration-squared laws of equations (4.3) and (4.4). Furthermore, the asymmetric sound emission leads to an apparent deformation of the soliton profile, causing a shift in the soliton centre of mass away from the density minimum. In the limit of no sound reinteraction, this shift is proportional to the soliton acceleration.

Another method to dissipate controllably the soliton in a harmonic trap is to add an optical lattice potential. This causes additional dynamical instability in the soliton and dephases the emitted sound such that it is not fully reabsorbed. Under appropriate parameters, both of these methods can result in rapid soliton decay, which is within the expected soliton thermodynamic lifetime of order 1 s. The decay is experimentally observable as an increase in the soliton oscillation amplitude and a change in the oscillation frequency. Ultimately the soliton disappears into the sound field.

Chapter 6

Parametric driving of dark solitons

In a real system solitary waves experience dissipation. A technique known as parametric driving can be employed to compensate for these dissipative losses, and has been demonstrated in various media. For example, parametric driving has led to the formation and/or stabilisation of solitary wave structures on the surface of shallow liquids [126, 236], at the interface between insoluble fluids [237], in 1D nonlinear lattices of coupled pendula [127] and granular materials [238]. In these cases, the parametric excitation takes the form of vertical oscillations of the system. In particular, some of these experiments led to the parametric stabilisation of non-propagating dark solitary wave structures [126, 127, 237]. Analogous driving techniques have also been suggested for spin waves (magnetisation solitons) in ferromagnets [239] and solitonic light pulses in optical fibres [240, 241, 242]. In general, the dynamics of the parametrically-excited solitary wave can be described by a perturbed nonlinear Schrödinger equation [243, 244, 245].

In dilute trapped BECs, dark solitary waves are prone to various dissipation mechanisms. In 3D geometries, a dynamical transverse instability dominates (see chapter 3) whereby the wave decays into vortex rings [76], but this effect is heavily suppressed in quasi-1D geometries [157, 203]. A further dynamical instability arises from motion through the inhomogeneous longitudinal density (see chapters 4 and 5), which induces sound emission from the soliton [157, 165, 166].

Interaction with the thermal cloud [156, 158], which has been neglected so far in this work, is expected to induce considerable dissipation in the solitary wave in a real environment. In this chapter we consider the possibility of parametrically driving a dark soliton in a trapped BEC, with the aim of stabilising it against realistic loss mechanisms. This work has been presented in [246].

6.1 Parametric driving technique

In chapter 5 we studied the longitudinal dynamics of a dark soliton in a harmonic trap in the limit of zero temperature. We observed that the soliton oscillates in the trap, emitting sound waves due to its acceleration through the inhomogeneous density. However, these sound waves have finite energy and are also confined to the condensate. The subsequent reinteraction of the soliton with the emitted sound leads to sound reabsorption, which completely stabilises the soliton (in the absence of other dissipative processes, e.g. snake instability and thermal dissipation). The ensuing dynamics in the trap can be resolved into two components: the stabilised soliton oscillating at $\omega_s \approx \omega_z/\sqrt{2}$, and a dipolar collective mode of the background fluid, set up by the soliton motion, oscillating at the trap frequency ω_z.

The equilibrium between the soliton and sound field in the harmonic trap is a delicate balance, and a perturbation to the harmonic trap can break this energy equilibrium. For example, certain perturbations can prevent full sound reabsorption and lead to a net soliton decay (see chapters 4 and 5).

Here we propose to pump energy into the dark soliton by a parametric driving technique. The basic idea is to enhance the sound field in the system by pumping energy into a dipolar motion of the background fluid. This will clearly break the energy balance between the soliton and sound field, and possibly lead to an energy transfer into the soliton node. To drive a dipolar condensate mode we employ two gaussian 'paddles', located symmetrically about the trap centre, which are made to oscillate in anti-phase. This drive potential has the form,

$$V_D(z) = \alpha \sin(\omega_D t) \left[\exp\left\{ \frac{-(z-z_0)^2}{w_0^2} \right\} - \exp\left\{ \frac{-(z+z_0)^2}{w_0^2} \right\} \right], \qquad (6.1)$$

where the gaussian bumps are located at $\pm z_0$, have amplitude α and width w_0,

and oscillate at frequency ω_D. This perturbation could be created experimentally by time-dependent red and blue detuned laser beams with beam waist w_0. The configuration is illustrated in figure 6.1. Note that the harmonic trap frequency is kept fixed to $\omega_z = \sqrt{2} \times 10^{-2}(c/\xi)$ throughout this chapter.

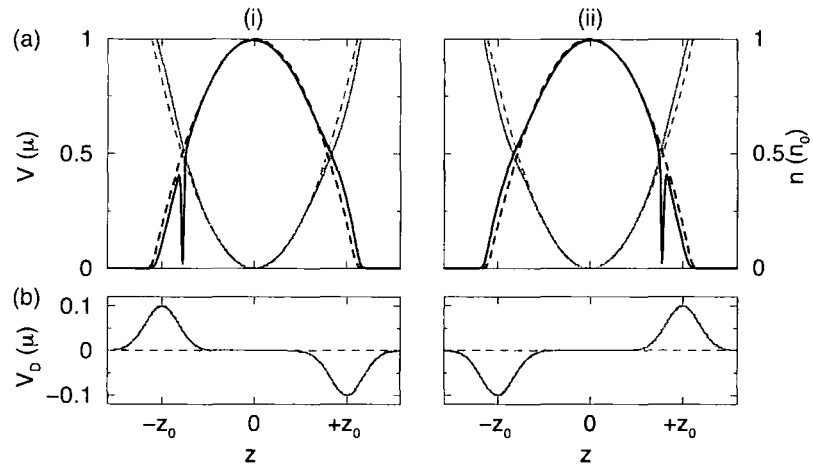

Figure 6.1: Schematic of the parametric driving of a dark soliton in a harmonic trap via two oscillating gaussian paddles. Two times are illustrated (left and right plots), corresponding to successive turning points in the soliton motion. (a) Combined longitudinal potential (grey solid line, left axis) and the perturbed condensate density featuring a dark soliton (black solid line, right axis). The unperturbed harmonic potential and corresponding unperturbed density are shown by dashed lines. (b) Drive potential V_D, given by equation (6.1) with amplitude $\alpha = 0.1\mu$.

6.2 Dissipationless regime

6.2.1 Continuous pumping

We consider first the case of driving the dark soliton in the absence of dissipative losses. In order to allow considerable energy to be pumped into the soliton, we choose to begin with a fast, low energy soliton, with an initial speed $v_0 = 0.75c$ (v_0 is the speed of the soliton at the trap centre) and energy $E_s = 0.386\mu$.

Figure 6.2 shows the energy and position of the dark soliton in the harmonic trap, with (solid lines) and without (dashed lines) the drive. These results are

presented for the 1D GPE (black lines) and the corresponding cylindrically-symmetric 3D GPE (grey lines). The results under both descriptions are essentially the same. There is a gradual phase drift between the dynamics in both cases due to the fact that the 3D system is not perfectly mapped onto the 1D system. Also, there is an additional oscillation of the soliton energy in the 3D case due to the coupling to transverse modes. This coupling, described in section 5.1.1, has no *net* effect on the soliton dynamics. We proceed to describe the dynamics in terms of the 1D description, i.e. ignoring the transverse-longitudinal coupling.

In the absence of the drive, the soliton dynamics take on the general form we have previously discussed in chapter 5. The soliton energy (figure 6.2(a), black dashed line) features small modulations due to the interaction with the dipolar fluid motion, but on average stays constant. We know from chapter 5 that the soliton oscillates in a sinusoidal manner at close to the predicted frequency $\omega_s^0 = \omega_z/\sqrt{2}$ [156, 157, 165, 166, 213, 222]. The oscillation amplitude remains approximately constant, and close to the TF prediction (equation (5.2), which corresponds to $z_s^{max} = 75\xi$ in this case. This average soliton oscillation amplitude indicated by the black dashed lines in figure 6.2(b).

We now consider the soliton dynamics in the presence of driving. The parameters of the drive potential used here are the optimised values that pump maximum energy into the soliton: $\omega_D = 0.98\omega_s^0$, $\alpha = 0.1\mu$, $w_0 = \sqrt{500}\xi$ and $z_0 = 90\xi$. At this early point we are aiming to give an initial demonstration of the driving effect - the discussion of the particular choice of the drive parameters will be presented in section 6.2.3.

In the presence of the drive the soliton dynamics become much more complex and, importantly, the soliton never reaches a steady state. The soliton energy undergoes large amplitude, low frequency oscillations between the initial soliton energy and some maximum energy E_s^{max}. These main energy oscillations are not smooth but feature considerable modulations of smaller wavelength and amplitude, indicating that a complex beating effect is occuring in the system.

The peak energy of these oscillations is $E_s^{max} \approx 1.3\mu$, which is almost equal to the maximum obtainable soliton energy corresponding to a black stationary soliton. Note that this peak value corresponds to a three-fold increase over the

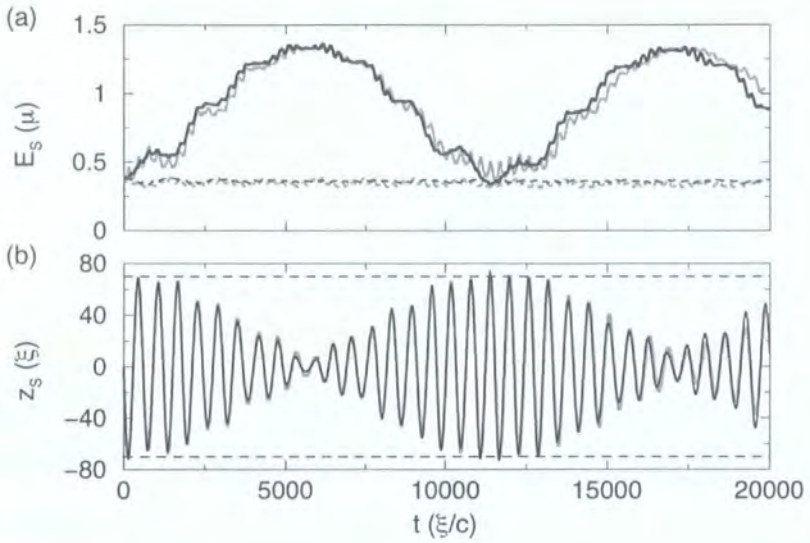

Figure 6.2: Dynamics of a dark soliton, with initial speed $v_0 = 0.75c$, in a harmonic trap with and without driving. (a) Soliton energy E_s in the absence (solid lines) and presence (dashed lines) of driving, with the results dervied from the 1D GPE (black) and cylindrically-symmetric 3D GPE (grey). (b) Soliton position z_s for the case of driving (solid lines), using the 1D GPE (black) and 3D GPE (grey). The average soliton amplitude in the absence of driving is indicated by the black dashed lines. The drive parameters are $\alpha = 0.1\mu$, $w_0 = \sqrt{500}\xi$, $z_0 = 90\xi$, and $\omega_D = 0.98\omega_{sol}$.

initial soliton energy. Accordingly, the amplitude of the soliton's oscillatory path decreases from the initial value of $z_s^{max} \approx 75\xi$ to an almost stationary soliton localised at the trap centre, and back again. The soliton oscillation frequency becomes slightly time-dependent and deviates from the unperturbed value ω_s^0, although this deviation is found to be less than 10%. We can consider the soliton as cycling between a fast, low energy state and an almost stationary soliton with close to maximum energy. This is somewhat analogous to the case of a stirred condensate which cycles between the 'no vortex' and 'single vortex' configurations [247], although here the vortex is not present initially but is created during the driving.

6.2.2 Interaction of soliton with driven dipole mode

We expect that the dominant excitation in the driven system, apart from the soliton, is a dipolar excitation of the background fluid. This is due in part to the dipolar nature of the drive potential, and also due to the oscillating soliton which is known to generate a dipolar fluid motion in an unperturbed harmonic trap. It is the interaction of the soliton with this driven dipolar fluid mode that leads to the complex cycling of the soliton dynamics. In order to gain insight into this process, we can follow the evolution of the condensate dipole mode D, defined by equation (5.3), and compare to the soliton trajectory. This was discussed for a soliton in an unperturbed harmonic trap in chapter 5, with the results shown in figure 5.1(c), albeit for a different initial soliton speed. The important features in the unperturbed trap are that the soliton and condensate dipole mode D oscillate sinusoidally at $\omega_z/\sqrt{2}$ and ω_z, respectively, with only minor modulations.

Figure 6.3(a) shows the evolution of the soliton energy, while figure 6.3b shows the soliton position (left axis, black line) and condensate dipole mode (right axis, grey line) for the driven system. The dipole mode oscillates in time but now with a heavily modulated amplitude. Additionally, the oscillation frequency now corresponds, on average, to the drive frequency ω_{D}, rather than the natural (unperturbed) dipole frequency ω_z. Note that in the absence of the soliton, the evolution of the dipole mode is practically unchanged. This implies that the dipole mode is now the dominant effect in the system.

Since the drive frequency employed here is almost equal to the soliton frequency in an unperturbed trap ω_{s}^0, we find that the soliton and dipole mode oscillate with *approximately* the same frequency. More specifically, the soliton and dipole mode frequencies have the same *average* value, but feature small individual time-dependent modulations, due to their mutual interaction. This leads to a time-dependent variation in the phase between the soliton and dipole mode oscillations, and this appears to be a key feature in the energy cycle. Consider the relative motion of the soliton and dipole mode in relation to the soliton energy. Initially the dipole mode and soliton are out of phase. Up to $t \sim 6000(\xi/c)$, which corresponds to energy being pumped into the soliton, the soliton and dipole mode come gradually into phase with each other, with the

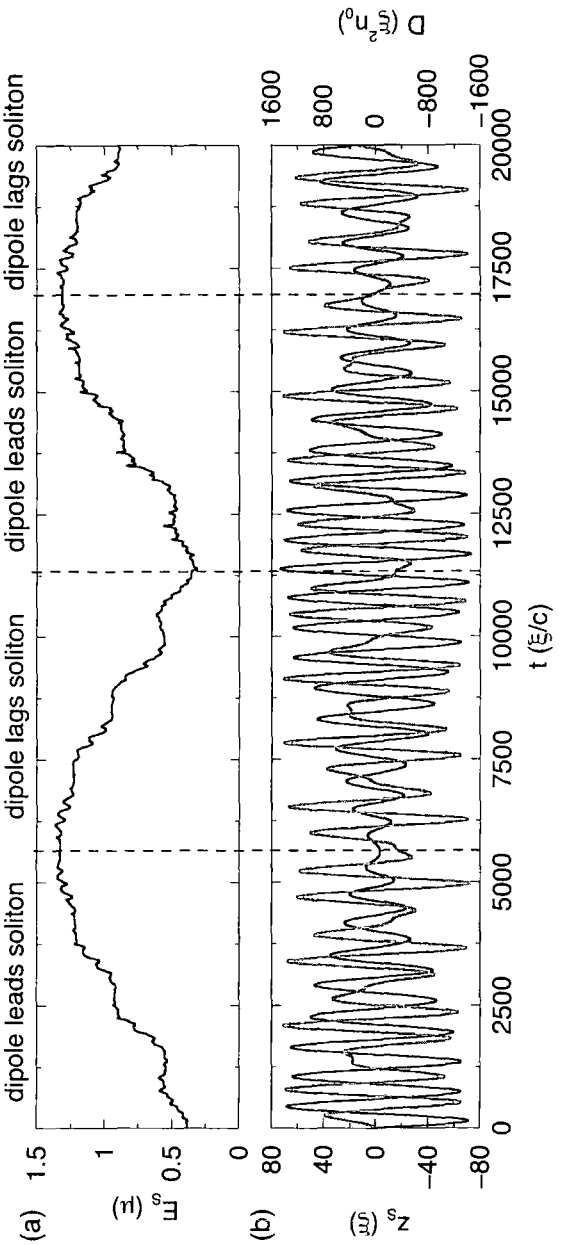

Figure 6.3: (a) Soliton energy for the case of continuous driving considered in figure 6.2. (b) Soliton position (left axis, black line) and condensate dipole moment (right axis, grey line). The regions where the soliton leads or lags the dipole mode are indicated by the vertical dashed lines.

dipole mode leading the soliton. At $t \sim 6000(\xi/c)$, which is the point of peak energy transfer into the soliton, the soliton and dipole mode are approximately in phase. Subsequently, the soliton and dipole mode move gradually out of phase, with the dipole mode now lagging behind the soliton. The soliton energy now decreases, with energy being transferred back into the dipole mode. By $t \sim 11000(\xi/c)$, the oscillations return to being completely out of phase. This corresponds to the point when the soliton energy returns to its initial (minimum) value. The soliton now begins to reabsorb energy, and the whole process repeats itself. We observe this to be a general phenomena in the driven system: as the soliton and dipole mode come into phase, energy is pumped from the dipole mode to the soliton, and when the two move out of phase, energy is transferred in the opposite direction.

6.2.3 Optimisation of drive parameters

The soliton dynamics depend sensitively on the soliton speed v_0 and the parameters of the driving potential: ω_D, α, w_0 and z_0. These drive parameters need to be optimised for a particular soliton speed in order to transfer a significant amount of energy between the soliton and sound field. Recall that the main idea is to use the drive potential to pump energy into the dipole mode. However, we want to avoid directly perturbing the soliton, as this tends to induce dynamical instability. We consider each of the drive parameters in turn, and indicate the qualitative ideas for their optimisation. As a quantitative illustration, figure 6.4(a)-(d) illustrates the efficiency of the energy pumping for each of the four drive parameters. These results apply for the particular values of the initial soliton speed, trap frequency, and remaining drive parameters that were employed in figure 6.2.

Drive frequency ω_D

Although the dipole mode naturally oscillates at the trap frequency, we consistently find that driving the dipole mode at close to the unperturbed soliton frequency ω_s^0 leads to optimum energy transfer. This trend is illustrated in figure 6.4(a), which maps the peak soliton energy E_s^{max} over a range of drive frequencies, while keeping the other parameters fixed to the values used in figure

6.2. There is a clear resonance located around $\omega_D \approx 0.98\omega_s^0$, where the soliton energy saturates to the maximum value corresponding to a black (stationary) soliton. The resonance is reasonably broad, with a width of the order of $10\%\omega_s^0$.

Paddle amplitude α

The amplitude of the paddles has a strong effect on the rate at which energy is pumped into the system, and therefore the peak energy obtained by the soliton. Figure 6.4(b) shows that the peak energy transfer to the soliton initially increases with α and saturates to the maximum value corresponding to a black soliton for $\alpha > 0.1\mu$. Further increases of α initially speed up the energy transfer process. However, for $\alpha > 0.26\mu$ we observe that the drive leads to the creation of additional dark solitons, which complicate the dynamics of the system. Although this is an interesting effect in its own right, we do not consider it further here since this chapter is concerned with driving the single original soliton. To have optimum energy transfer into the soliton but avoid the creation of additional solitons, we employ $\alpha = 0.1\mu$ in our simulations, which results in a density perturbation of the order of $0.1n_0$.

Width of the paddles w_0

The dipole mode in a harmonic trap, which we aim to drive, has a wavelength of the order of the size of the system, and is slowly varying on the lengthscale of the soliton. Therefore the extent of each paddle should lie in the region $\xi \ll w_0 < R_{TF}$. However, we do not want the oscillating paddle to have a significant direct perturbation on the soliton, since this induces a dynamical instability. An intermediate value is therefore a good choice. This behaviour is confirmed in figure 6.4(c). We observe that the regime for optimum energy transfer is $10\xi < w_0 < 40\xi$, while away from this region the energy transfer tails off. In our optimum drive parameters we employ $w_0 = \sqrt{500} \approx 22\xi$.

Position of the paddles z_0

The main condition for z_0 is that the paddles should be centred outside the region probed by the oscillating soliton (but within the radius of the conden-

sate). Otherwise the soliton will traverse the bumps, and this can lead to an additional dynamical instability in the soliton and a net soliton decay.

Figure 6.4(d) shows the peak energy pumped into the soliton as a function of the paddle position z_0. By equation (5.2), the $v_0 = 0.75c$ soliton probes up to $z \approx 75\xi$ in the system, which has a TF radius of $R_{\mathrm{TF}} = 100\xi$. For $z_0 < 75\xi$ the transfer of energy to the soliton is generally poor, since the soliton traverses the paddles in its motion. Indeed for $z_0 < 20\xi$, the soliton decays completely away. In the region $20\xi < z_0 < 60\xi$, we see an anomalous increase in the energy transfer, which must be due to some intricate effects between the soliton and dipole mode. As expected, optimum energy transfer (which reaches the maximum possible soliton energy) occurs for $75\xi < z_0 < 100\xi$. In our optimum set of drive parameters, we take $z_0 = 90\xi$.

6.2.4 Generating a higher energy soliton

While the drive is on, the soliton cycles continuously between a fast, low energy soliton and a slow, high energy soliton. We now ask the question of whether it is possible to generate a final soliton of higher energy. The obvious method is to turn the drive off at a time in the cycle when the soliton has gained energy.

Figure 6.5(a) shows the evolution of the soliton energy when the drive is turned off at various times (solid black lines). For comparison, the soliton energy in the absence of driving (dashed line) and under continuous driving (grey line) are indicated. Terminating the drive at a particular time leads to a breakdown of the energy cycle. Subsequently, the soliton stabilises to an energy around that point in the cycle. The soliton energy remains constant on average, but features modulations due to the interaction of the soliton with the dipole mode. The amplitude of these modulations varies depending on the point in the cycle at which the drive is terminated. In the limit where the drive is terminated at close to the initial soliton energy or the peak soliton energy, these energy modulations are minimal. For intermediate points in the cycle, the modulations are largest, with an amplitude of up to 0.2μ.

When the drive is terminated at the peak in the energy cycle (figure 6.5(a), topmost black line), the soliton stabilises to a soliton with very close to the maximum possible soliton energy. The corresponding soliton trajectory is shown

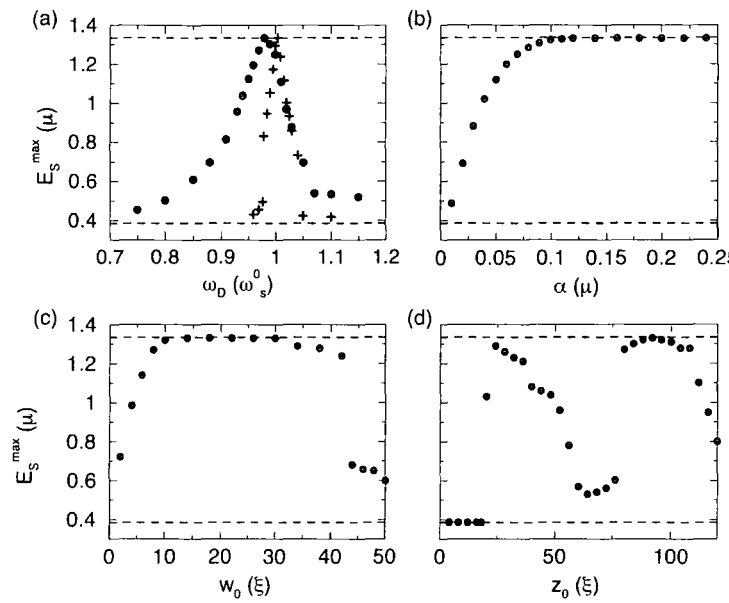

Figure 6.4: Peak energy E_s^{max} pumped into the soliton, with initial speed $v_0 = 0.75c$, as a function of each parameter of the drive potential. In each case, the remaining parameters are kept fixed, with the same values as in figure 6.2. Peak soliton energy as a function of (a) drive frequency ω_D, (b) paddle amplitude α, (c) paddle width w_0, and (d) paddle position z_0. The unperturbed initial soliton energy and maximum possible soliton energy are indicated by the lower and upper dashed lines. In (a), results are also presented in the presence of phenomenological dissipation $\gamma = 5 \times 10^{-4}$ (pluses). This value is chosen such that the lifetime of this undriven $v_0 = 0.75c$ soliton is of the order of 1 s (i.e. the predicted soliton lifetime in quasi-1D geometries [165, 157, 156]) for realistic trap parameters. Note that this is the same as the lifetime in figure 6.6 for the undriven $v_0 = 0.3c$ soliton.

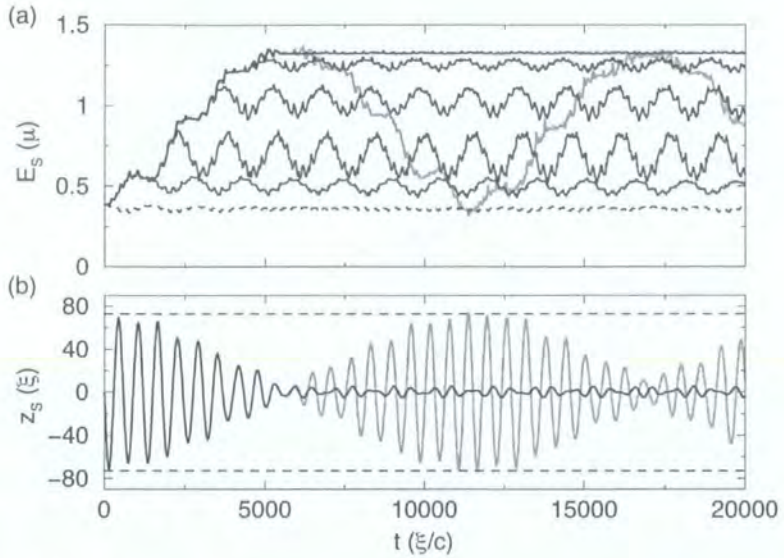

Figure 6.5: Effect of terminating the parametric driving after various evolution times. The system has the same trap and drive parameters as employed in figure 6.2. (a) Soliton energy under continuous driving (grey line), no driving (dashed black line), and driving which is terminated after various evolution times (black solid lines). These times are, from bottom to top, $t = 1280$, 1920, 3200, 4490 and $5770(\xi/c)$, which correspond to $2, 3, 5, 7$, and 9 full oscillations of the drive potential (and approximately of the soliton motion in the trap). (b) Soliton path for continuous driving (grey line) and the case where the driving is turned off at $5770(\xi/c)$ (black line), where the soliton reaches the peak in the energy cycle. The average soliton amplitude in the absence of driving is indicated by the horizontal dashed lines.

in figure 6.5(b) (solid black line), along with the continuously driven (grey line) and undriven (dashed black line) cases. Under the drive, the amplitude of the soliton oscillation decreases almost to zero. At this point, the drive is terminated and the soliton subsequently remains localised in the centre of the trap, making low amplitude oscillations ($z_s^{\max} \sim 5\xi$). The final speed of the soliton is around $v_0 \sim 0.05c$. In other words, the initially fast soliton has been almost stopped. Note that we cannot completely stop the soliton using this method because the considerable dipole mode present in the system will always modulate its position.

6.3 Dissipative regime

The results presented so far have been conducted in a non-dissipative system. In particular, they have illustrated how energy can be pumped into a dark soliton, even to the point where the soliton is essentially stopped. In a real environment however, dissipative losses are ever-present, for example, from interaction with the thermal component. These cause the gradual decay of the soliton, and its ultimate destruction [156, 158]. An important application of this parametric driving technique could therefore be to stabilise a dark soliton in an atomic BEC against dissipative losses. This is analogous to the parametric stabilisation of dark soliton structures against decay mechanisms in other media [126, 127, 237].

Generic dissipation in a condensate can be modelled by the inclusion of a phenomenological damping term γ into the GPE:

$$(i-\gamma)\frac{\partial\psi}{\partial t} = \left(-\frac{1}{2}\nabla^2 + V + |\psi|^2\right)\psi. \tag{6.2}$$

This leads to a dissipation of energy from the system, such that it transforms towards the ground state, but it preserves particle number. Any excitations in the system, e.g. soliton, sound, etc., become damped, with the rate being controlled by the value of the dimensionless parameter γ. The inclusion of this phenomenological damping has been considered in [96, 248].

In the presence of dissipation and driving, we discriminate two cases of stabilisation of the soliton. Firstly, it is possible to stabilise the soliton against decay, even for an apparently infinite time, although the initial soliton energy is *not* maintained. Secondly, the soliton can be stabilised at around its *initial* energy, but this has a limited lifetime. We will discuss these two regimes in turn.

6.3.1 Stabilisation against decay

Under the phenomenological damping, the soliton energy decays to zero, while the amplitude of the soliton oscillations tends towards the edge of the cloud, with the rate of the soliton decay depending crucially on γ. The soliton energy and path under dissipation *in the absence of driving* are shown in figure 6.6 (black dashed lines). Since the dissipation can rapidly anti-damp the soliton, we begin with a slow $v_0 = 0.3c$, high energy soliton. Figures 6.6(a) and (b)

show the initial soliton dynamics, whereas figures 6.6(c)-(d) show the long-term evolution. The soliton energy (figure 6.6(a), dashed line) decays in a roughly exponential manner, which is slightly modulated by the soliton motion. We choose γ such that the soliton lifetime is consistent with prediction of the order of 1 s for solitons in highly elongated, quasi-1D geometries [156, 157, 165]. In figure 6.6, we employ $\gamma = 10^{-3}$, leading to a soliton lifetime of the order of 5000 (ξ/c). According to the table 2.2, this corresponds to a real time in the region $0.3 - 1.5$ s, depending on the input parameters used.

The soliton dynamics under *continuous driving* are also shown in figure 6.6 (grey lines). The driving compensates for the dissipation up to a time $t \sim 7000(\xi/c)$, with the soliton energy increasing marginally during this time. However, at a time $t \sim 7000(\xi/c)$, the energy suddenly decreases, and the soliton amplitude increases. This loss in energy is associated with the soliton and dipole oscillations coming into phase, as described in section 6.2.2 for the dissipationless case. This phase relation continues to evolve, causing the decay to tail off at $t \sim 12000(\xi/c)$ and the soliton energy to undergo oscillations. These energy oscillations become damped over time, and the soliton equilibrates to a lower energy soliton, corresponding to a speed of $v_0 \approx 0.7c$. This remains stable for very long times, as indicated in figure 6.6(c)-(d) (grey lines). In other words, the dark soliton in the presence of dissipation can be stabilised against decay for long times, albeit at less than the initial energy.

These results are for optimised driving. If the driving is less optimised, or if γ is larger, the compensation against dissipation is only partial. The soliton lifetime becomes extended, but the soliton ultimately decays completely away.

6.3.2 Stabilisation at fixed energy

A potential application of this parametric technique is to maintain the soliton energy at a fixed value. This is demonstrated in figure 6.6(a)-(b) by solid black lines. Since the loss of energy from the soliton is associated with the soliton and dipole coming into phase, the idea is to *rephase* the system at appropriate times such that the relative phase does not become destructive. This is performed by pausing the drive at certain points, and restarting it after the soliton has evolved for a short period of time. For example, in the case of

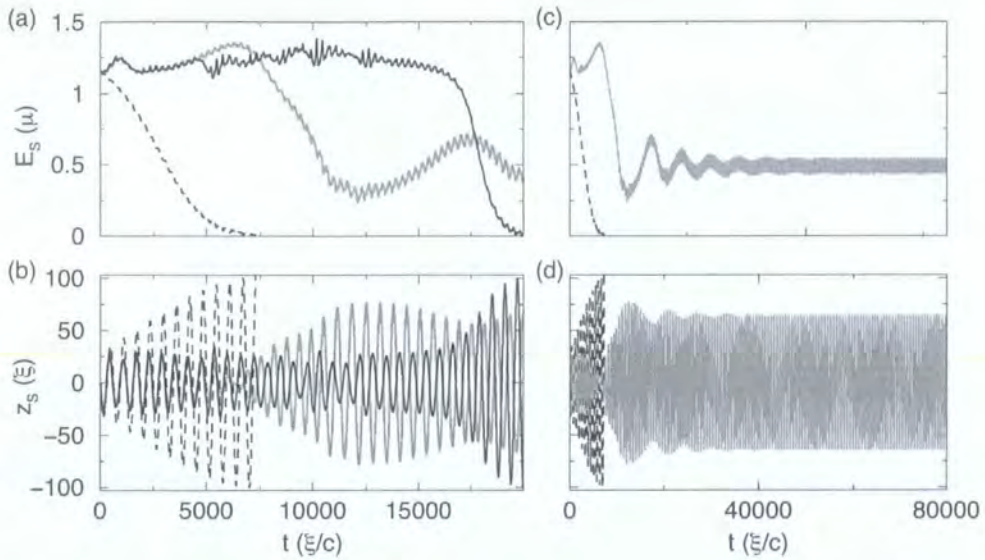

Figure 6.6: (a) Soliton energy and (b) position in the presence of dissipation $\gamma = 10^{-3}$ for a soliton with initial speed $v_0 = 0.3c$. The soliton dynamics under continuous driving and in the absence of driving are represented by grey lines and black dashed lines respectively. The solid black lines represent the soliton under driving which is turned on and off at times chosen to optimise the soliton stabilisation. The drive is turned off in the time ranges of $1400\pi < t < 1550\pi$, $2400\pi < t < 2500\pi$, $2900\pi < t < 3060\pi$, and $3600\pi < t < 3760\pi$. (c) and (d) show the long-term evolution of the soliton energy and position for the continuous driving (grey line) and undriven (dashed black line) cases.

continuous driving, the soliton undergoes a large energy drop at $t \sim 7000(\xi/c)$. We therefore rephase the soliton and drive before this can occur at $t \sim 4400(\xi/c)$ by switching the drive off for a fraction of a drive cycle. This process is also repeated at three further times $t \sim 7500$, 9100 and 11300 (ξ/c), although in each case the drive is terminated for different times. The resulting soliton energy (figure 6.6(a), solid black line) remains around the initial value for a time of over $17000(\xi/c)$. Similarly, the soliton oscillations (figure 6.6(b), solid black line) retain an approximately constant amplitude. These dynamics are vastly different from the undriven case (black dashed lines). They represent the soliton being stabilised at its initial energy for over three times the natural soliton lifetime. Following this, the soliton energy decays rapidly to zero, with the oscillations tending towards the condensate edge. With more rephasing

operations, it should be possible to extend this timescale further, or at least to enable the soliton to stabilise at a lower energy, as can be achieved in the absence of rephasing (figure 6.6, grey lines).

6.4 Summary

We have illustrated an analog of parametric driving for dark solitons in harmonically-confined BECs. Gaussian paddles are employed to pump energy into a dipolar motion of the condensate, leading to transfer of energy into the soliton. The direction of energy flow between soliton and dipole mode is related to the relative phase between their oscillations. In the absence of dissipation, a fast, low energy soliton can be converted into an almost stationary soliton with maximum energy. We indicate how to optimise the drive parameters to achieve efficient pumping. Under dissipative conditions, driving extends the soliton lifetime. Under continuous driving, the soliton can equilibrate to a lower energy soliton, which is stable for very long times. Furthermore, by rephasing the drive with respect to the soliton, the soliton energy can be maintained around its initial value for at least several times the natural soliton lifetime. We have performed the corresponding simulations in a highly-elongated, cylindrically-symmetric system (using the cylindrically-symmetric 3D GPE), and find essentially the same results. Under current experimental conditions it should be possible to realize and observe this parametric stabilisation of the soliton against dissipative losses.

Chapter 7

Single vortex in a confined Bose-Eintein condensate

Fundamental questions exist over the dynamical stability of quantized vorticity is superfluids. Experiments performed at very low temperature have observed dissipative effects in vortices, even though thermal dissipation at such temperatures is expected to be minimal. This suggests that dynamical dissipation processes are at work.

In the field of Helium II, Davis *et al.* [86] have observed the decay of vortex tangles at temperatures less than 70 mK, where dissipation due to mutual friction is expected to be negligible. Simulations using the GPE show that the reconnection of vortices induces a considerable burst of sound emission [87]. Similarly, oscillatory excitations of a vortex line, known as Kelvin waves, are expected to be generated in a reconnection [88] and following the interaction of a rarefaction pulse with a vortex [89], and are predicted to decay gradually via sound emission. These mechanisms are expected to give a significant contribution to the decay of vortex tangles in the limit of zero temperature, although they alone cannot account for the overall observed decay.

In the context of dilute BECs, Abo-Shaeer *et al.* [106] have investigated the crystallisation of vortex lattices, and observe that the process is temperature-independent at sufficiently low temperature. In contrast to vortex tangles, vortex experiments in dilute BECs generally feature an axis of rotation, with the vortices tending to align themselves parallel to this axis, such that the vortex

dynamics are dominantly two-dimensional. Reconnections and Kelvin wave excitations of the vortex lines are therefore suppressed. Initial attempts to model the vortex crystallisation with the GPE found it necessary to include an explicit damping term [96, 107, 108, 109, 110]. Recently, Lobo *et al.* successfully modelled the formation process using the basic zero-temperature 3D GPE [97]. As the system is rotated, condensate surface modes become excited. These fluid modes transfer energy and angular momentum to vortex structures, which enter from the edge of the condensate, and relax to a crystal structure. Not only does this process show the dynamical instability of vortices, but it also illustrates the important interactions that can take place between the vortices and fluid excitations, e.g. the sound field, in the condensate.

A possible dissipation mechanism is the dynamical instability of superfluid vortices to acceleration [64]. At zero temperature, a vortex can be set into motion by: the presence of a velocity field, e.g. from other vortices or fluid flow; or a locally inhomogeneous density, e.g. due to a confining potential. Indeed, corotating vortex pairs [149] and single vortices performing circular motion in 2D homogeneous superfluids [90, 152] are predicted to decay via the emission of sound waves. However, this decay mechanism is not expected to occur in finite-sized BECs due to the wavelength of the sound being larger than the system itself. In this chapter we probe the dynamical stability of an accelerating vortex within the framework of a single vortex precessing in a trapped quasi-two-dimensional BEC. This work has been partially presented in [224].

7.1 Vortex in a 2D BEC under harmonic confinement

7.1.1 Vortex in a quasi-2D BEC

We consider first the general dynamics of a vortex within a harmonically-confined condensate. The 3D trap geometry is cylindrically-symmetric about the z-axis, and given by,

$$V(r,z) = \frac{1}{2}(\omega_z^2 z^2 + \omega_r^2 r^2), \tag{7.1}$$

where ω_z and ω_r are the transverse and radial trap frequencies respectively, and $r = \sqrt{x^2 + y^2}$ is the radial coordinate. Figure 7.1 is a schematic illustration of a vortex line, oriented along the z-axis, in a slightly prolate ($\omega_z > \omega_r$) harmonically-confined condensate.

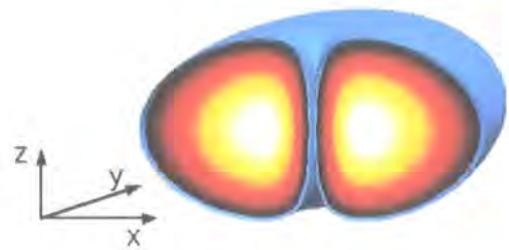

Figure 7.1: (a) Isosurface plot of the fluid density of a condensate under slightly prolate harmonic confinement, $\omega_z > \omega_r$. A rectilinear vortex line is present, oriented along the z-axis. In the x-z plane ($y = 0$), white and black correspond to maximum (n_0) and zero density, respectively.

If the system is 3D in nature, i.e. $\omega_z \sim \omega_r$, the vortex line is prone to excitation in the form of bending [249, 250] and long-wavelength travelling waves, known as Kelvin waves [154, 155], with both effects having been experimentally observed in dilute BECs [98, 101].

However, under tight transverse confinement the dynamics of the system become quasi-2D. The excitation of the vortex line is heavily suppressed and it becomes essentially rectilinear [251]. In this regime, the 2D GPE is expected to give a good description of the system.

7.1.2 Quasi-2D condensate and the 2D GPE

The quasi-2D regime is dynamically satisfied for $\hbar\omega_r > \mu$ and $\omega_z \gg \omega_r$. The former relation ensures that the transverse modes of excitation are of sufficiently high energy that they are strongly suppressed. The transverse condensate profile tends towards the harmonic oscillator ground state. (Note that at finite temperature the condition $\hbar\omega_r > k_B T$ must also be satisfied to ensure that transverse modes do not become thermally excited.) The latter relation implies that the radial modes of the system are preferentially excited over the transverse modes, such that the radial dynamics dominate the system. Under these

conditions the condensate becomes quasi-2D and pancake-shaped, and the 3D GPE describing the full system can be approximately reduced to a 2D GPE describing only the planar wavefunction.

Here we will consider the time-independent solution of the 2D GPE and then find its corresponding solution in the 3D GPE. Consider a 2D BEC confined by a radial harmonic trap with frequency $\omega_r = 0.5\sqrt{2} \times 10^{-1}(c/\xi)$ and featuring a vortex at $(x_0, y_0) = (5\xi, 0)$. We generate the vortex by propagating the 2D GPE in imaginary time subject to an enforced azimuthal 2π-phase slip, as outlined in appendix B. The black line in figure 7.2(a) shows a cross-section in the x-coordinate of the ground state density profile of this 2D system, solved using the 2D GPE. This 2D system has, in natural units, a peak density $n_{2D} = 1$, a scattering coefficient $g_{2D} = 1$, and chemical potential $\mu_{2D} = 1$. We now aim to identify the cylindrically-symmetric 3D system that this 2D GPE corresponds to. Essentially this means that the planar ($z = 0$) wavefunction of the quasi-2D system should match the pure 2D wavefunction. In order to achieve this mapping we expect from section 2.3 that:

- $\omega_z \gg \omega_r$;
- the radial component of the wavefunction resembles the harmonic oscillator ground state;
- the 3D scattering coefficient is related to the 2D value by $g = \sqrt{2\pi} l_z g_{2D}$, where $l_z = \sqrt{\hbar/m\omega_z}$;
- the 3D chemical potential is related to the 2D value by $\mu = \mu_{2D} + \hbar\omega_z/2$.

By varying the only remaining free parameter, ω_z, we find numerically that the respective ground state wavefunctions are matched closest when the transverse trap frequency is $\omega_z \approx 3.35(\xi/c)$. The grey line in figure 7.2(a) shows the corresponding density profile from the cylindrically-symmetric 3D GPE, and it is in excellent agreement with the 2D result. The transverse density profile of the quasi-2D system is shown in figure 7.2(b). The actual profile (solid line) is very close to the harmonic oscillator ground state (dotted line), and the transverse width is of the order of a healing length.

Figure 7.2 shows that the 3D GPE for a quasi-2D condensate and the 2D GPE give essentially identical time-*independent* results. We will show in the course

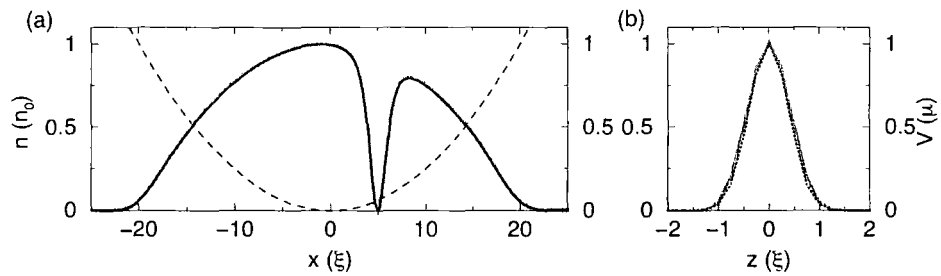

Figure 7.2: (a) Density profile along the x-axis for a harmonically-confined quasi-2D BEC under the cylindrically-symmetric 3D GPE (grey line) and the 2D GPE (black line). A vortex is located at $(x_0, y_0) = (5\xi, 0)$. (b) Transverse density profile (along the z-axis) for the quasi-2D system (grey line) and the harmonic oscillator ground state (dotted line). The trap frequencies are $\omega_r = 0.5\sqrt{2} \times 10^{-1}(c/\xi)$ and $\omega_z = 3.35(c/\xi)$.

of this chapter that the vortex dynamics are essentially identical under the two descriptions. However, due to its computational efficiency, we will proceed in general with 2D description.

7.1.3 Energetic stability of a vortex in a harmonic trap

The stability of a vortex in a harmonic trap can be investigated by considering the dependence of the vortex energy as a function of the radial position of the vortex. The vortex energy is evaluated numerically using the GP energy functional according to equation (2.31) (as described in appendix B).

In this work we are concerned with the dynamics of a vortex in a non-rotating trap. The radial dependence of the vortex energy E_V is shown in figure 7.3 for a fixed (non-rotating) trap $\omega_r = 0.5\sqrt{2} \times 10^{-1}(c/\xi)$. This system has a TF radius $R_{TF} = 20\xi$. Although this figure corresponds to a particular trap geometry, the qualitative features are generic for the non-rotating system. For a non-rotating system, a condensate featuring a vortex has a higher energy than the ground state condensate, and in this sense the vortex is thermodynamically unstable [144, 145, 146, 99].

A vortex at the centre of the trap has maximum energy. Since the density is locally homogeneous, the vortex represents a stationary solution, and will remain fixed at the centre. However, this vortex configuration is unstable to

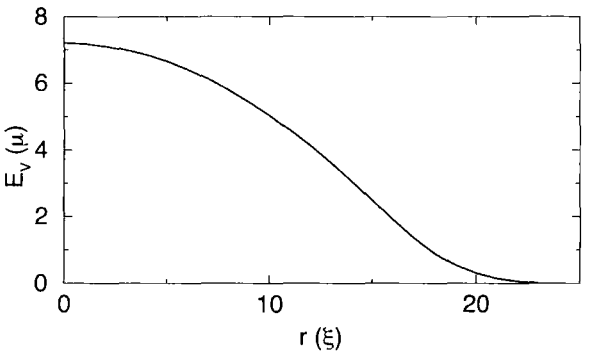

Figure 7.3: Vortex energy E_V as a function of the distance of the vortex from the trap centre. The trap frequency is $\omega_r = 0.5\sqrt{2} \times 10^{-1}(c/\xi)$, and the TF radius is $R_{TF} = 20\xi$.

infinitesimal displacements [144]. An off-centre vortex, however, is expected to follow a path of constant potential, i.e. precession of the vortex around the trap centre, and this has been observed experimentally [62]. At finite temperatures, thermal dissipation arises due to scattering of thermal excitations by the vortex, and transfers energy from the moving vortex to the thermal cloud [99]. The decay causes the vortex to move towards a local minimum, which amounts to a drift to lower densities and larger radii [145]. Since the vortex is topological it can only disappear at the egde of the condensate, where it is thought to decay into elementary excitations [99]. Furthermore, it has been modelled using the stochastic GPE that thermal fluctuations cause an uncertainty in the position of the vortex, such that even a vortex which is initially stationary at the trap centre will have a finite lifetime [147].

This discussion is for a non-rotating system. If the system is rotating, this modifies the energy-radius curve. In particular, above a certain rotation frequency, the presence of a vortex lowers the free energy of the system, signifying the stabilisation of the vortex within the system [64, 144].

7.1.4 Dynamics of a vortex in a harmonically-confined BEC

We now investigate the dynamics of an off-centre vortex in a harmonically-confined BEC. The radial trap frequency is taken to be $\omega_r = 0.5\sqrt{2} \times 10^{-1}$

(c/ξ), giving a TF radius of $R_{\rm TF} = 20\xi$, and the vortex is initially located at $(x_0, y_0) = (5\xi, 0)$. The evolution of the the system is shown in figure 7.4(a) in terms of snapshots of the condensate density. The vortex, seen as a node of zero density, precesses clockwise around the trap centre.

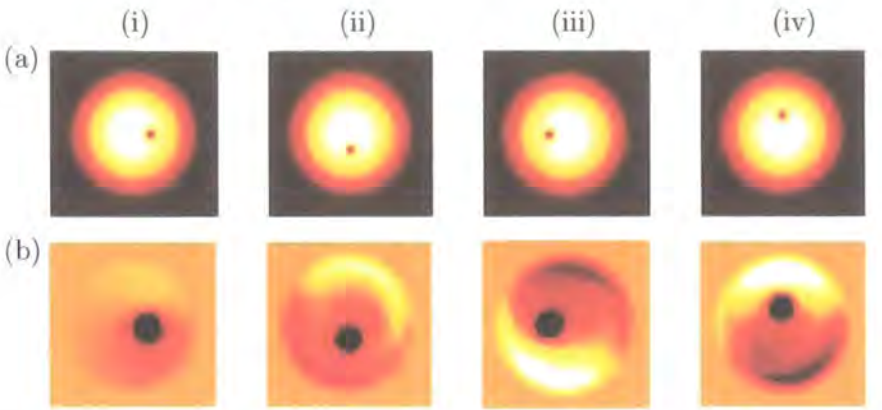

Figure 7.4: Snap-shots of an off-centre vortex precessing in a harmonic trap $\omega_r = 0.5\sqrt{2} \times 10^{-2}(c/\xi)$. The vortex is initially located at position $(x_0, y_0) = (5\xi, 0)$. (a) Condensate density, where black represents zero density and white maximum density n_0. (b) Renormalised density (actual density minus background density), where the density scale has an amplitude of $0.04n_0$. The snap-shots are taken at times (i) $t = 4$, (ii) 124, (iii) 248, and (iii) $372(\xi/c)$. Each box represents the region $[-25, 25]\xi \times [-25, 25]\xi$, .

The precessional motion of the vortex about the trap centre has been predicted [64, 144, 145] and experimentally observed [62]. It is analogous to the Magnus force effect, although here the system is inhomogeneous rather than homogeneous. The vortex represents an absence of fluid, i.e. has negative effective mass. It experiences a force towards regions of lower potential, i.e. radially outwards in the case of a harmonic trap. However, the vortex has circulation, and so the net effect is a drift perpendicular to the direction of the force. This amounts to the vortex following a path of constant potential, i.e. circular motion about the trap centre.

In weakly anisotropic 2D harmonic traps ($\omega_x \neq \omega_y$), the vortex precession occurs in an ellipse rather than a circle [252]. In the limit of strong anisotropy, however, deviations arise as the system tends towards the quasi-1D regime, where regular 2D vortices are not supported. This is the regime of solitonic

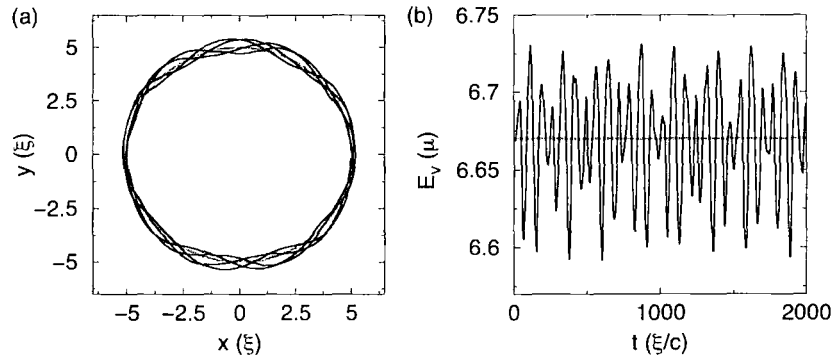

Figure 7.5: Dynamics of the off-centre vortex cosidered in figure 7.4. (a) Path of the vortex up to a time $t = 2000(\xi/c)$, corresponding to over 4 full precessions. (b) Corresponding vortex energy E_V. In (a) and (b) the constant radius/energy evolution is illustrated by grey lines.

vortices [163, 164] and dark solitary waves. This transition from 2D vortices to soliton-like structures is discussed in chapter 9.

Figure 7.5(a) shows the path of the vortex over a longer time corresponding to many precessions. The vortex tends to precess in a circular manner, but there are modulations from pure circular motion and the orbit of the vortex is not a closed path. The position modulations have an amplitude of around 10% of the initial radius. However, the *average* vortex radius and precession frequency remain essentially constant. Similarly, the vortex energy remains on average constant but features oscillations, as shown in figure 7.5(b). Similar modulations have been observed for vortices in a vortex lattice [97]. The angular frequency of the precession is $\omega_V \approx 0.0126(c/\xi)$, which corresponds to a fraction of the trap frequency $\omega_V \equiv 0.36\omega_r$.

In order to investigate the modulations of the vortex motion and energy in the harmonic trap, figure 7.4(b) shows corresponding snapshots of the renormalised condensate density (actual density minus the time-independent background density). This allows easy observation of the excitations on the background fluid. In addition to the precessing vortex, we observe the gradual generation of an oscillation of the background fluid, which is almost dipolar in character. This oscillation appears to rotate in the system, at a faster rate than the precessing vortex. The amplitude of this density oscillation is of the order of $0.04n_0$.

Furthermore, figure 7.6 plots the Fourier spectrum in frequency space of the

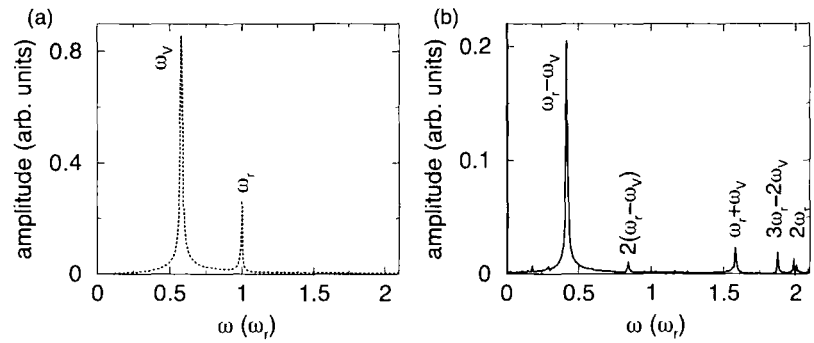

Figure 7.6: (a) Fourier spectrum in frequency space of the vortex radius from the trap centre, for the case considered in figures 7.4-7.5. (b) Spectrum of the vortex energy. Frequency is rescaled in terms of the trap frequency ω_r.

vortex radius and the vortex energy. This corresponds to the magnitude of the complex Fourier transform of equation (5.4). The spectrum of the vortex position (figure 7.6(a)) is composed of two fundamental frequencies, which relate to the harmonic trap frequency ω_r and vortex precession frequency ω_V. The energy spectrum (figure 7.6(b)) however is dominated by the corresponding beat frequencies, e.g. $(\omega_v - \omega_r)$, $(\omega_v + \omega_r)$, and harmonics, e.g. $2\omega_V$. These spectra are similar to the dark soliton spectrum in a harmonic trap (see chapter 5, figure 5.3). Beat effects have also been observed for a driven vortex in a trapped BEC [247].

From these results it becomes obvious that the precessing vortex disturbs the background fluid. This generates and drives a collective excitation which has a fundamental frequency corresponding to the trap frequency ω_r. We will see later that this fluid motion arises from sound emission from the vortex, which becomes focussed into a collective excitation. The subsequent back action of this fluid excitation leads to small perturbations on the vortex dynamics, and this results in the modulations in the vortex position and energy. This is analogous to interaction of a dark soliton with the dipole mode in a harmonic trap, described in chapter 5.

7.1.5 Precession frequency of a vortex in a harmonic trap

Using time-dependent variational analysis, and assuming a TF density profile, Svidzinsky and Fetter have derived the vortex precession frequency in an axisymmetric harmonic trap to be [64, 146, 252],

$$\omega_V = \frac{3\hbar\omega_r^2}{4\mu} \ln\left(\frac{R_{TF}}{\xi}\right) \frac{1}{1-(r/R_{TF})^2} \quad . \tag{7.2}$$

Note that in the limit of $r \to 0$ the predicted precession frequency tends towards a finite value. A similar equation has been derived by Jackson *et al.* based on a Magnus force argument [144].

We have calculated the vortex precession frequency by means of time-dependent simulations of the 2D GPE. Although there are small modulations of the vortex frequency in time due to the back action of the background fluid, we have taken the average precession frequency over many (typically over ten) precessions. Figure 7.7(a) plots the vortex precession frequency ω_V as a function of the radius from the trap centre (shown by symbols), with three trap frequencies being considered. All three cases show the same qualitative behaviour. In the limit of small displacements, the vortex precession frequency tends towards a finite value. As the vortex radius is increased, the precession frequency increases, and in the limit $r \to R_{TF}$, it diverges.

The predictions of equation (7.2) are plotted in figure 7.7(a) by lines for all three trap frequencies. The predictions have the same qualitative form as the numerical results, being finite at $r = 0$, increasing with r, and diverging as $r \to R_{TF}$. However, the quantitative agreement with the numerical results is variable, with the best agreement occurring for the weakest trap frequency (squares, solid line). For the two weaker traps, the prediction agrees well with the numerical data up to $r \sim 0.5R_{TF}$, while above this, the prediction increasingly over-estimates the numerical results. However, for the largest trap frequency (circles, dotted lines), the prediction does not match the numerical data well, although it still gives a reasonable estimate.

We attribute these deviations to the assumption of a TF density profile in the prediction of equation (7.2). The TF approximation is valid for a large number of atoms and/or strong interactions. In our case, where the peak density is fixed to unity, this corresponds to the limit of weak traps. The ground state density

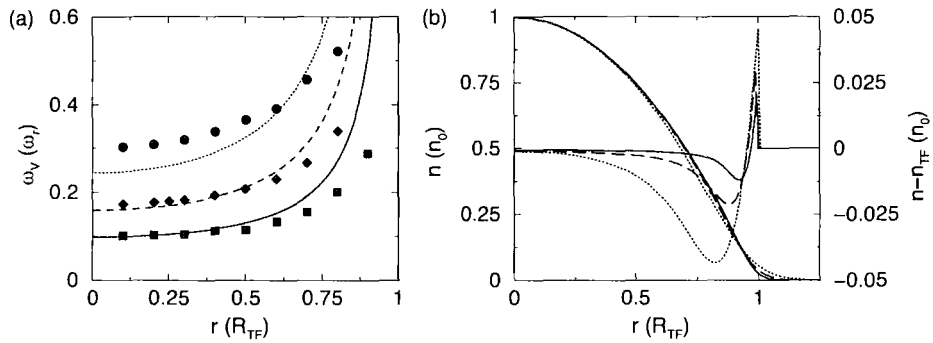

Figure 7.7: (a) Vortex precession frequency ω_V, scaled in terms of the trap frequency ω_r, as a function of radius r from the trap centre, scaled in terms of the Thomas-Fermi radius $R_{\rm TF}$. Three trap frequencies are considered: $\omega_r = 0.25\sqrt{2} \times 10^{-1}(c/\xi)$ (squares), $\omega_r = 0.5\sqrt{2} \times 10^{-1}(c/\xi)$ (diamonds), and $\omega_r = \sqrt{2} \times 10^{-1}(c/\xi)$ (circles). The corresponding predictions by Svidzinsky and Fetter [146], in the limit $r \to 0$, are shown by solid, dashed and dotted lines, respectively. (b) Radial density profile n (left axis) and deviation from TF profile $n - n_{\rm TF}$ (right axis) for the three trap frequencies: $\omega_r = 0.25\sqrt{2} \times 10^{-1}(\xi/c)$ (solid line), $\omega_r = 0.5\sqrt{2} \times 10^{-1}(\xi/c)$ (dashed line), and $\omega_r = \sqrt{2} \times 10^{-1}(\xi/c)$ (dotted line).

profiles of the three traps are shown in figure 7.7(b). As we would expect, the deviation from the TF profile of an inverted parabola gets larger as the trap frequency is increased. Due to the overall modulation of the density profile this deviation is hard to observe, and so to allow easier visualisation of this effect, figure 7.7(b) also plots the *deviation* in the density, i.e. actual density minus the TF density. In addition, the deviation of the density profile from the TF profile is most prominent towards the edge of the condensate, which is where equation (7.2) deviates most from the numerical data.

7.2 Vortex in a dimple trap

7.2.1 Dimple trap geometry

In the previous section we illustrated how a precessing vortex in a condensate under harmonic confinement sets up and then continuously re-interacts with

the background fluid mode, with no net vortex decay. In order to resolve these complicated dynamics, we will introduce a dimple trap geometry, with the aim of controlling the re-interaction of the vortex with the fluid excitations. A similar procedure was employed in chapter 5 to resolve the dynamics of a dark soliton in a trapped quasi-1D BEC.

The external confining potential $V_{\rm ext}$ in the radial plane is given by,

$$V_{\rm ext} = V_0 \left[1 - \exp\left(-\frac{2r^2}{{\rm w_0}^2}\right)\right] + \frac{1}{2}\omega_r^2 r^2, \tag{7.3}$$

and consists of a gaussian dimple trap with waist $\rm w_0$ and depth V_0 embedded within a weaker ambient harmonic trap of frequency ω_r. Note that, close to the centre of the dimple, the gaussian potential is approximately harmonic with frequency $\omega_{\rm d} = 2\sqrt{V_0}/{\rm w_0}$. This trap geometry can be realised experimentally by focussing a far-off-resonant red-detuned laser beam in the centre of a magnetic trap. The vortex is initially confined in the inner region, where it precesses. The configuration of the system in its full quasi-two-dimensional form is illustrated in figure 7.8.

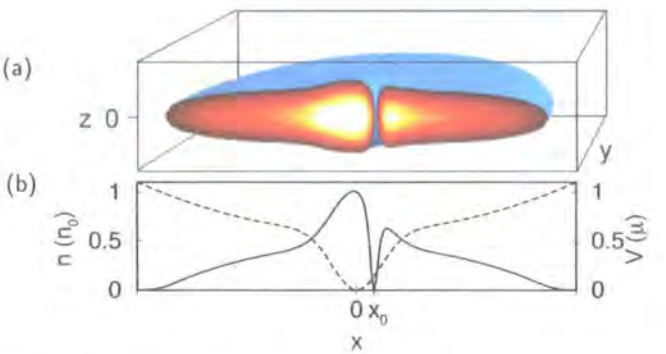

Figure 7.8: (a) Isosurface plot of the atomic density ($n = 0.1n_0$) of a quasi-2D BEC under the radial potential of equation (7.3) plus tight transverse confinement. A straight line vortex is located at $(x_0, 0)$ in the x-y plane. In the x-z plane (y=0), white and black correspond to maximum and zero density, respectively. (b) Density (solid line) and potential (dashed line) along the x-direction ($y = 0, z = 0$).

According to theoretical works by Lundh [152] and Vinen [153], a superfluid vortex undergoing circular motion radiates sound waves. However, in a confined BEC sound emission is expected to be prohibited due to the wavelength of the

sound being larger than the system itself. One interpretation of this is that sound waves *are* emitted, but are confined by the system and rapidly reinteract with, and stabilise, the vortex. This means that it is impossible to probe the effects if pure sound emission from a vortex in a standard harmonically-confined BEC.

The idea of the dimple trap geometry is that, depending on the depth of the dimple V_0, the interaction of the vortex with the sound field can be controlled. The energy of sound excitations is of the order of the chemical potential μ, and so there exist two dynamical regimes depending on the depth of the dimple in relation to μ:

- For deep dimples $V_0 > \mu$, the confinement appears as an effectively single trap. Any excitations generated by the precessing vortex rapidly reinteract with it.
- For $V_0 < \mu$, sound waves generated by the vortex can escape from the inner dimple to the outer region. The sound ultimately gets reflected from the edge of the condensate and returns back to the dimple. However, in the intervening time we can probe the dynamics of the vortex in the absence of reinteraction with the sound field.

We now consider each of these limiting cases in turn.

7.2.2 Deep dimple

For a deep $V_0 = 5\mu$ gaussian dimple, the potential seen by the condensate is almost harmonic, and the vortex dynamics are essentially identical to that in a single harmonic trap. The vortex precesses around the trap centre, generating excitations which remain within the dimple and re-interact with the vortex. There is no net decay, but both the vortex position (figure 7.9 and 7.10(a), dotted lines) and energy (figure 7.10(b), dotted line) become heavily modulated due to the back action of the fluid excitations. The results of the full 3D GPE for the quasi-2D system are also presented in figure 7.10 for comparison (dotted grey lines). We find good agreement with the results of the 2D GPE (dotted black lines), apart from a slight dephasing over time. This is due to the fact that we have not perfectly matched the 3D GPE to the 2D GPE.

7.2.3 Shallow dimple and homogeneous outer region

For the case of a shallow $V_0 < \mu$ dimple we will initially assume, for simplicity, that the outer region is homogeneous, i.e. $\omega_r = 0$. Any excitations generated by the vortex will have an energy of the order of the chemical potential μ and so can escape out of the dimple to the outer region, where they will propagate away to infinity. This allows us to probe the regime of pure vortex decay, where the vortex dynamics are not obscured by re-interaction with the radiation. We will consider the experimentally relevant case of $\omega_r \neq 0$ later.

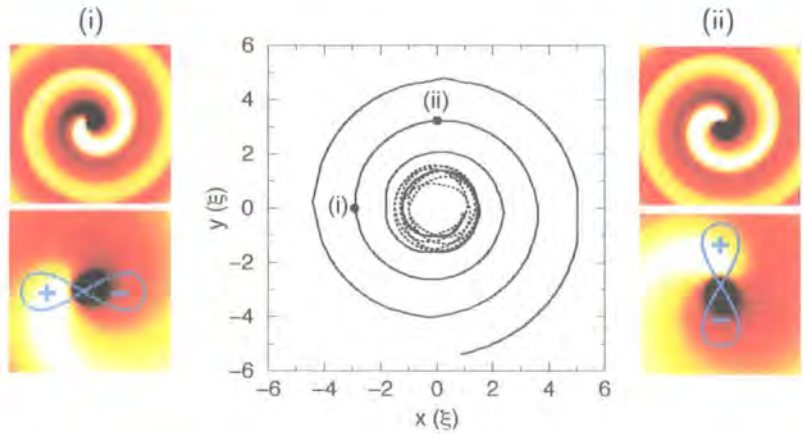

Figure 7.9: Path of a vortex, initially at $(1, 0)\xi$, in a gaussian dimple trap with effective frequency $\omega_d = 2\sqrt{2} \times 10^{-1}(c/\xi)$ for deep and shallow dimples. Deep $V_0 = 10\mu$ dimple (dotted line): mean radius is constant, but modulated by the sound field. Shallow $V_0 = 0.6\mu$ dimple, with homogeneous outer region $\omega_r = 0$ (dotted line): vortex spirals outwards. Insets: Density plots of renormalised density (actual minus background density) for $V_0 = 0.6\mu$ at times $t =$ (i) 220 and (ii) 226 (ξ/c), showing the emission of positive (light) and negative (dark) sound waves of amplitude $\sim 0.01 n_0$. Top: Far-field distribution in the region $[-90, 90]\xi \times [-90, 90]\xi$. Bottom: Near-field distribution in the region $[-25, 25]\xi \times [-25, 25]\xi$, with a schematic illustration of the dipolar radiation pattern.

The vortex dynamics in a shallow $V_0 = 0.6\mu$ gaussian dimple are significantly different from the case of a deep $V_0 > \mu$ dimple. The vortex precession is now accompanied by a drift outwards (figure 7.10(a), solid lines) to lower densities, resulting in a spiral motion of the vortex in the trap (figure 7.9, solid lines).

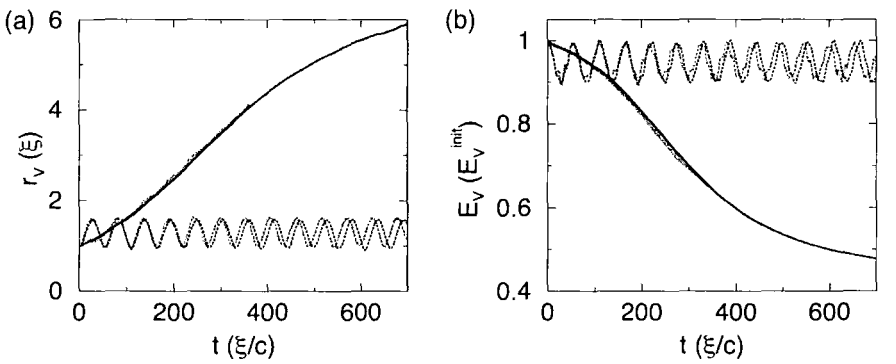

Figure 7.10: Evolution of the (a) vortex radius and (b) vortex energy (rescaled by the initial vortex energy E_V^{init}) for the cases considered in figure 7.9. Deep $V_0 = 10\mu$ dimple (dotted lines): vortex radius and energy oscillate about a mean value. Shallow $V_0 = 0.6\mu$ dimple and homogeneous outer region $\omega_r = 0$ (solid lines): vortex loses energy and drifts outwards. The results of the 2D GPE are indicated by black lines, while those of the 3D GPE with $\omega_z = 3.35(c/\xi)$ are shown by grey lines. Note that the 3D results for the shallow dimple terminate at $t \approx 350(\xi/c)$.

Accordingly, the vortex energy, shown in figure 7.10 (solid lines), decays monotonically. In figure 7.10 the results of the 3D GPE (grey lines) are in excellent agreement with the 2D results (black lines). However, due to the large computational demands of the 3D GPE, the simulations are only presented up to a time $t \approx 350(\xi/c)$.

A similar outward vortex motion has recently been predicted for a vortex precessing in a harmonic trap modulated by an optical lattice [253], where the sound excitations were numerically damped out.

Close inspection of the density in the region of the vortex during the precessional motion reveals the continuous emission of sound waves from the vortex. These sound excitations, shown in figure 7.9 (subplots), are emitted from the vortex core perpendicularly to the instantaneous direction of motion, in the form of a dipolar radiation pattern. The precessional motion of the vortex modifies this sound field into a swirling radiation pattern. This distribution is reminiscent of spiral waves often encountered elsewhere in nature [254]. The observed sound waves have amplitude $0.01n_0$ and wavelength $\lambda \sim 45\xi$, which agrees well with

the theoretical prediction of $\lambda \sim 2\pi c/\omega_V = 45\xi$ [64].

We can now interpret the vortex dynamics in a deep dimple/ single harmonic trap. The precessing vortex radiates sound waves which cannot escape the system and rapidly reinteract with the vortex. This leads to stabilisation of the vortex decay by reabsorption of the emitted energy. In addition, the vortex motion generates a collective mode in the condensate, which continuously perturbs the precessing vortex, leading to slight modulations in the vortex position and energy.

Power radiated from the vortex

The power radiated by the vortex, in the limit of no reinteraction with the emitted sound ($V_0 = 0.6\mu$) is shown in figure 7.11(a) as a function of time and radius from the trap centre. This curve was mapped out by one simulation in a large computational box with the vortex initially positioned slightly off-centre, and allowed to spiral out to much larger radii without the reinteraction of the emitted sound. The curve can also be obtained by running several simulations, with the vortex being started progressively further from the trap centre. This procedure could also be implemented experimentally in order to trace out the vortex decay.

The curve can be understood qualitatively by considering the density inhomogeneity that the spiralling vortex experiences. For this reason, the density distribution in the region of the dimple is shown in the inset of figure 7.11(a). The emitted power increases in line with the local radial density gradient up to $r \approx 2.8\xi$, where the gradient of the gaussian potential is a maximum, and subsequently tails off as the trap gradient decreases smoothly to zero. The precession frequency of the vortex during this evolution, shown in figure 7.11, features a similar dependence on the density distribution. At early times (and low radii), where the density gradient is weak, the precession frequency is slow to evolve and appears almost constant. As the vortex probes further outwards, the radial density gradient increases substantially, and the frequency rapidly decreases. Eventually, the density gradient tails off and accordingly the precession frequency tends slowly towards zero as $r \to 0$.

We have additionally considered the case where the dimple is harmonic instead

of gaussian, and find the same qualitative results, but with enhanced power emission for a particular ω_d due to the larger precession frequency (see figure 7.12, inset). For a harmonic trap with a cut-off ($V = V_0$ for $r > r_0$), the vortex frequency (figure 7.12 inset, crosses) agrees well with the prediction of equation (7.2). However, for a gaussian dimple of depth V_0, ω_V falls short of this prediction due to the tailing off of the gaussian potential with radius, as shown in figure 7.12 (inset, circles).

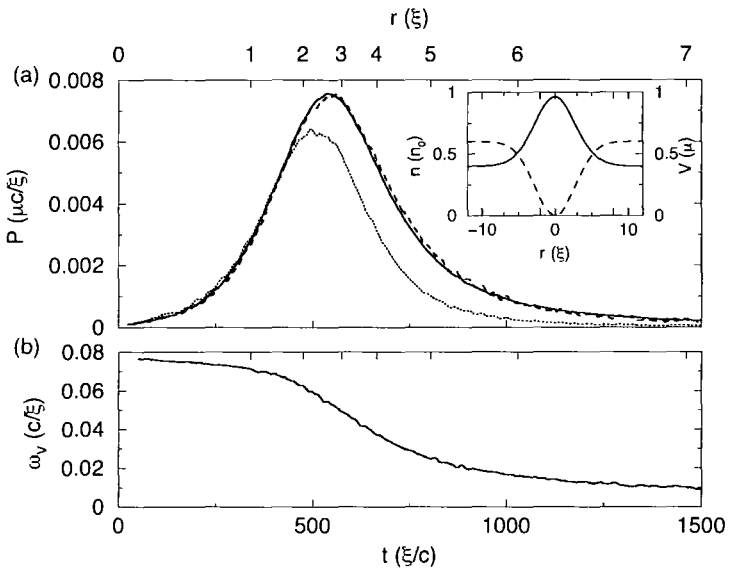

Figure 7.11: (a) Power radiated from the vortex as a function of radius from the trap centre (top axis) and time (bottom axis), as calculated from the GP energy functional (solid line), equation (7.4) with $\beta = 6.1$ (dashed line), and an acceleration-squared law with constant coefficient $94.4(\mu/c^2)$ (dotted line). Inset: radial density profile of the time-independent background (solid line) and potential (dashed line). (b) Vortex precession frequency ω_V as a function of radius (top axis) and time (bottom axis).

It is known from a mathematical perspective that a 2D homogeneous superfluid can be mapped on to a (2+1)D electrodynamic system, with vortices and phonons playing the role of charges and photons respectively [255]. By analogy to the Larmor radiation for an accelerating charge, and also the power emitted from an accelerating dark soliton in a quasi-1D BEC (see chapter 5) we assume the power radiated P by the spiralling vortex is proportional to the square of the local vortex acceleration a. The coefficient of this relation, P/a^2, is

mapped out in figure 7.12 over a range of dimple strengths ω_d. Each data point corresponds to the best-fit power coefficient and the average vortex precession frequency for that particular simulation. Note that there are limitations to the range of precession frequencies that we can probe, just as would be experienced experimentally. In the limit of very tight dimples the vortex escapes almost instantaneously, whereas for very weak dimples, the vortex motion is too slow for such effects to be systematically studied.

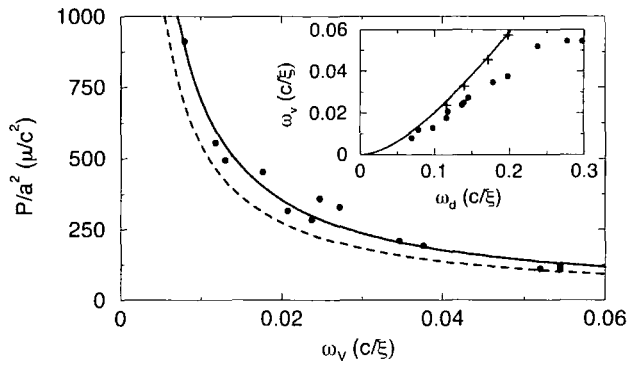

Figure 7.12: Coefficient of an acceleration squared power law, P/a^2, for a vortex, calculated over a variety of trap strengths ω_d, as a function of ω_V (circles), along with the analytical predictions [90, 152] (dashed line), and best fit line corresponding to equation (7.4) with $\beta = 6.3 \pm 0.9$ (solid line). Inset: Variation of ω_V with trap strength for a gaussian dimple (circles) and harmonic trap with a cut-off (crosses), along with the theoretical prediction for a harmonic trap of equation (7.2) (solid line).

The data in figure 7.12 for the power coefficient P/a^2 indicates a strong dependence on the inverse of the ω_V. For instance, when the data of figure 7.12 is plotted on a log-log plot, the best fit line is linear with a gradient of -1.04. For this reason, a best fit line is plotted in figure 7.12 which is proportional to $1/\omega_V$ (solid line). This best fit line (solid line) gives good agreement with the numerical data, and suggests a modified power law of the form

$$P = \beta m N \left(\frac{a^2}{\omega_V} \right), \tag{7.4}$$

where N is the number of atoms in the BEC and β is a dimensionless coefficient. An equation of this form has been derived by Vinen [90] and Lundh *et al.* [152] for the case of a vortex performing perfect circular motion in a homogeneous

2D fluid. The former approach was based on classical acoustics, while the latter derivation was obtained by mapping the superfluid hydrodynamic equations onto Maxwell's electrodynamic equations. Both approaches predict a rate of sound emission proportional to $\omega_{\rm v}^3 r_{\rm v}^2$, where $r_{\rm v}$ is the precession radius, and when put in the functional form of equation (7.4) yield a coefficient $\beta = \pi^2/2 \approx 4.935$. Our findings indicate that the coefficient is $\beta \sim 6.3 \pm 0.9$ (one standard deviation), with the variation due to a weak dependence on the geometry of the system. This is in remarkable agreement with these analytic predictions, despite their assumptions of perfect circular motion, a point vortex, and an infinite homogeneous system. We believe that the deviation from the predicted coefficient arises primarily due to the radial component of the vortex motion, which is ignored in the analytical derivations.

Also plotted in figure 7.11(a), alongside the power emission from the GP energy functional, are an acceleration-squared law (dotted line) and the modified acceleration-squared law of equation (7.4) (dashed line), with the coefficients being chosen to give a best fit. Both lines give excellent agreement until the vortex starts to escape the dimple region at $r \sim 2.8\xi$. Here the vortex precession frequency (figure 7.11(b)), which previously remained roughly constant, starts to decrease rapidly due to the form of the local density. This causes the acceleration-squared law to deviate, while the $1/\omega_{\rm V}$ term in equation (7.4) corrects for this deviation, giving excellent agreement throughout.

7.2.4 Shallow dimple and harmonic outer region

The results presented so far for a shallow dimple have assumed a homogeneous outer region $\omega_r = 0$. We now consider the experimentally relevant case where the inner dimple resides in an ambient harmonic trap $\omega_r \neq 0$, which ultimately confines the condensate. The inclusion of the ambient harmonic trap modifies the potential in the dimple region, making it more confining, i.e. larger potential gradient, than the $\omega_r = 0$ case. Provided $\omega_r \ll \omega_{\rm d}$, this modification will have a minor effect.

Figure 7.13 shows the evolution of the vortex radius and energy in a dimple plus ambient harmonic trap. Several trap strengths are considered $\omega_r = \omega_{\rm d}/10$ (dashed lines), $\omega_{\rm d}/20$ (dotted lines) and $\omega_{\rm d}/40$ (dot-dashed lines), with the

dimple strength being kept fixed to the value used previously of $\omega_d = 2\sqrt{2} \times 10^{-1}(c/\xi)$. The corresponding results for the case of a homogeneous outer region $\omega_r = 0$ are shown for comparison (solid lines).

The relatively weak ambient traps considered in figure 7.13 cause only a slight increase in the vortex precession frequency and rate of decay from the homogeneous results. Apart from this, the behaviour is identical up until the point when the sound, having reflected off the condensate edge, returns to the dimple. The time for this to occur depends crucially on the radius of the condensate and therefore on the frequency of the ambient harmonic trap. For the three traps of $\omega_r = \omega_d/10$ (dashed lines), $\omega_d/20$ (dotted lines) and $\omega_d/40$ (dot-dashed lines), sound reinteraction is apparent after times of $t \sim 100$, 300 and $600(\xi/c)$ respectively.

Following the interaction with the reflected sound, the vortex dynamics become more complicated, as both sound emission and reabsorption occur. We observe large oscillations of the vortex energy and radius, but overall the vortex continues to decay. Unlike in a single harmonic trap (or deep gaussian trap), where the vortex is fully stabilised by sound reabsorption, we observe no full stabilisation of the vortex. This is likely to be caused by a dephasing of the emitted sound modes in the outer trap. This decay under sound reinteraction is qualitatively analogous to the dynamics of a dark soliton in a dimple plus ambient harmonic trap and harmonic trap plus optical lattice (chapter 5).

The units employed here for a 2D BEC are related to real parameters for a quasi-2D BEC in table 2.3. Choosing the trap parameters to be $\omega_r = 2\pi \times 5$ Hz, $\omega_d = 20\omega_r$, and $\omega_z = 200\omega_r$, the time unit corresponds to $\xi/c \approx 2 \times 10^{-4}$ s for a ^{87}Rb condensate. In this case, the timescale of figure 7.13 is of the order of 0.3 s. This is much shorter than the expected thermodynamic vortex lifetime, which is of the order of seconds [99]. This dynamical decay of the vortex via sound emission should therefore be experimentally observable. In an experiment, one would track the position of the vortex over time, by repeated (destructive) absorption imaging of the cloud following expansion.

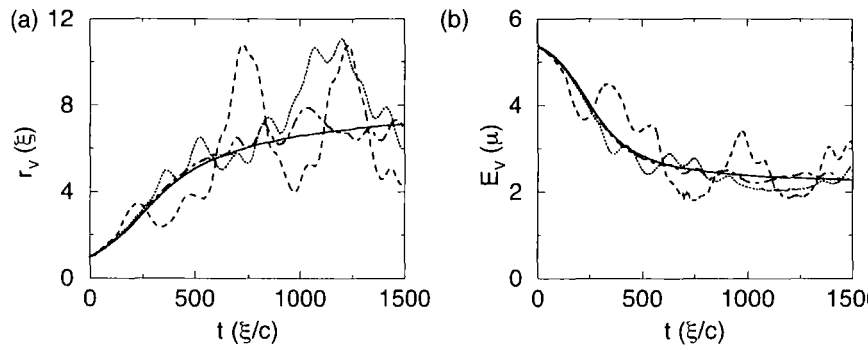

Figure 7.13: (a) Vortex radius and (b) energy for the case considered in figure 7.9 of a gaussian dimple with a low cutoff, but now featuring an outer harmonic trap of frequency $\omega_r = \omega_d/10$ (dashed lines), $\omega_d/20$ (dotted lines) and $\omega_d/40$ (dot-dashed lines). The case for a homogeneous outer region ($\omega_r = 0$) is shown for comparison (solid lines).

7.3 Application to vortex tangles in liquid Helium

Sound radiation due to the acceleration of a vortex may be an important effect in turbulent vortex tangles in liquid Helium. The decay of such tangles has been shown to occur at temperatures lower than 70 mK [86], where thermal dissipation is expected to be negligible, suggesting that dynamical dissipation mechanisms are at work. Reconnections and Kelvin wave excitations of vortex lines have been shown to contribute to the decay of vorticity via sound emission [87, 88, 89, 90, 153]. We now apply the acceleration-squared power law of equation (7.4) to the case of vortex tangles in liquid Helium, and present a derivation for the corresponding decay rate [256].

In a vortex tangle, the relevant measure of vorticity and energy is the vortex line density L, and evidence suggests that the rate of decay of vortex line density is given by Vinen's equation [90, 153],

$$\frac{\mathrm{d}L}{\mathrm{d}t} = -\zeta\kappa L^2, \tag{7.5}$$

where $\kappa = h/m$ is the quantum of circulation and ζ is a dimensionless coefficient. A value of $\zeta \sim 0.05$ is suggested by experiments on Helium II [257] and by vortex dynamics simulations [258] where an energy cutoff is assumed.

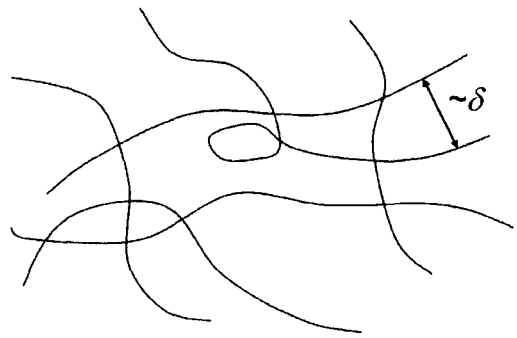

Figure 7.14: Schematic of a vortex tangle, with mean intervortex distance δ.

In such a system of many vortices, the acceleration of a vortex is induced by the surrounding vortex distribution. We assume that the sound emission observed in section 7.2 from a single precessing vortex is a generic feature of an accelerating superfluid vortex, independent of the nature of the acceleration.

A vortex tangle is a disordered array of vortex lines, as illustrated in figure 7.14. We consider a constant volume V of single-quantized vortices with average intervortex spacing δ. If we take the vortex line density to be $L = \Lambda/V$, where Λ is the total vortex line length, then $\mathrm{d}L/\mathrm{d}t = (1/V)\mathrm{d}\Lambda/\mathrm{d}t$. Furthermore, if we introduce the energy per unit length of vortex line $\varepsilon_0 = \mathrm{dE}/\mathrm{d}\Lambda$, then the rate of change of line density becomes related to the power emission by,

$$\frac{\mathrm{d}L}{\mathrm{d}t} = -\frac{1}{\varepsilon_0 V}P. \tag{7.6}$$

The kinetic energy per unit length of a singly-quantized vortex line is,

$$\varepsilon_0 = \int_0^\infty \frac{1}{2}mnv^2 d\mathbf{r}^2 = \frac{mn\kappa^2}{4\pi}\int_0^\infty \frac{dr}{r}, \tag{7.7}$$

where $v = \kappa/(2\pi r)$ is the velocity field about the vortex core. This integral diverges, and so we introduce lower and upper cutoffs, equivalent to the vortex core size ξ and the intervortex separation δ, respectively. The energy per unit length is then,

$$\varepsilon_0 = \frac{mn\kappa^2}{4\pi}\ln\left(\frac{\delta}{\xi}\right). \tag{7.8}$$

The vortex acceleration in a tangle arises primarily from the interaction with other vortices. We consider the most basic multi-vortex interaction, that of two vortices with the same charge of unity, known as a corotating (or vortex-vortex) pair. It is predicted that such a pair, when isolated, will corotate about

a central axis with an angular frequency $\omega_V = \kappa/(\pi\delta^2)$, where δ is the separation [27, 149, 153]. We will take this as the source of the vortex motion, and assume the vortex separation to be $\delta \sim L^{-1/2}$. This gives us an order of magnitude for the acceleration experienced by the vortices in the tangle. Substituting equations (7.4) and (7.8) into (7.6) leads to the expression,

$$\frac{\mathrm{d}L}{\mathrm{d}t} = -\frac{\beta\kappa}{\pi^2 \ln(\xi\sqrt{L})} L^2. \tag{7.9}$$

Remarkably, this expression, which is a generalisation of a numerically-obtained equation based on the GP model, yields the same L^2 form as Vinen's equation. The coefficient ζ in equation (7.5) corresponds to $\zeta = \beta/\pi^2 \ln[\xi\sqrt{L}]$. Taking typical Helium II parameters of $\xi = 0.18$ nm and $L = 10^{10}\mathrm{m}^{-2}$ [80], and the value $\beta = 6.3$ from our GP simulations, the coefficient corresponds to $\zeta \sim 0.06$. This is of the order of the experimentally obtained value for Helium II [90, 153].

Note that the prediction used here for the angular frequency of the corotating pair of $\omega_V = \kappa/(\pi d^2)$ is based on classical hydrodynamics, which ignores the core structure of the vortices. As we will show in chapter 8, this prediction over-estimates the angular frequency when the vortex cores are closely-situated. Therefore, equation (7.9) is only relevant when $\delta \gg \xi$.

7.4 Summary

In this chapter we have probed the dynamics of a single vortex in a quasi-2D condensate. The vortex motion is driven by the density inhomogeneity, and induces the vortex to precess about the trap centre. By considering a dimple trap embedded in a weaker harmonic trap, we have shown that the vortex is inherently unstable to acceleration, resulting in the emission of dipolar sound waves. In a deep dimple, or a single harmonic trap, the precessing vortex continuously reinteracts and maintains an equilibrium with the emitted sound, which fully stabilises the vortex against decay. A collective mode is set up in the system, oscillating at the trap frequency ω_r, which causes small-scale modulations of the vortex motion.

For a shallow dimple the sound escapes the dimple and the pure vortex decay is observed, with the vortex spiralling out to lower densities. We find that

the power emission from the vortex is proportional to the square of the vortex acceleration and inversely proportional to the vortex precession frequency, in good agreement with analytic predictions based on classical acoustics and electrodynamics. This emission is analogous to the Larmor radiation from an accelerating electron and the sound emission from an accelerating dark soliton described in chapters 4 and 5. When the ambient trap is explicitly included, we observe the same dynamics until the sound eventually reinteracts with the vortex. However, this does not fully stabilise the vortex against decay, and ultimately it disappears at the condensate boundary. In suitably engineered traps, the vortex decay is rapid, and can dominate over thermal dissipation. Indeed, the dynamical decay of a vortex is expected to be observable under current experimental conditions. By varying the depth of the cutoff between the two limiting regimes, it should be possible to control the degree of sound reinteraction with the vortex, and therefore the rate of vortex decay.

The energy loss from an accelerating vortex may be relevant to the problem of vortex tangles in superfluid Helium, which decay even at very low temperatures. We have related the power law for a single accelerating vortex in a BEC to a vortex tangle in Helium, and derive an expression which is consistent with Vinen's decay law.

This acceleration-induced vortex instability may also be relevant to the case of optical vortices, which have been shown to exhibit a fluid-like motion [85].

Chapter 8

Interaction of a vortex with other vortices

In a system of many vortices, such as a vortex tangle in Helium II or a vortex lattice in Helium II and dilute BECs, it is the interaction between vortices, rather than the density inhomogeneity, that dominates the dynamics of the system. At relatively large temperatures, thermal dissipation is the dominant dissipation mechanism of the vorticity. However, at very low temperature the observed temperature-independence of the crystallization of vortex lattices in BECs [106] and the decay of vortex tangles in Helium II [259, 86] has indicated that vortices are subject to a significant *dynamical* dissipation mechanism. Several theoretical works have suggested sound emission from the vortices as the decay process [87, 88, 90, 260, 261].

Due to the axis of rotation and well-ordered structure, the vortex dynamics in a lattice tend to be polarised in the direction of the axis, and dominated by rotational effects between vortices of the same topological charge. Vortex tangles, on the other hand, are disordered and have no preferred axis. As well as vortex lines, vortex rings are expected to form and play a major role in the dynamics [80]. The vortex dynamics in the tangle can take many forms; as well as rotational effects between adjacent vortex lines with the same topological charge, vortex lines and rings can collide and reconnect. Under reconnections, long-wavelength helical waves, known as Kelvin waves, can be excited along the vortex line. All of these dynamical effects are expected to induce decay in the

vortices via the emission of sound waves [87, 88, 149].

Due to its microscopic nature, the GPE is computationally demanding, and a full 3D description of a large system involving many vortices is currently unrealistic. One method of tackling the problem of many-vortex interactions on a microscopic level is to build up our understanding from cases involving a few vortices. In this chapter we consider the basic interactions between two and three vortices in a homogeneous system. We assume that the vortices are rectilinear and solve the 2D GPE. We show that, apart from the case of a vortex-antivortex pair, the vortex dynamics are generally accelerative, and lead to a decay in the vortex energy via sound emission. Some of this work has been presented in [262].

8.1 Corotating vortex pair

We consider first the case of two closely-positioned singly-charged vortices in a 2D homogeneous system, where the circulations are *parallel*. The density and phase profile of a pair with separation $d \approx 3.5\xi$ is illustrated in figure 8.1. Due to the mutual interaction of their circulating velocity fields, the vortices rotate about a point halfway between the cores. This excitation, known as a *corotating pair* (or vortex-vortex pair), can be regarded as the lowest order vortex lattice. Note that the far-field phase profile of the corotating pair resembles a double-charged vortex, and this implies that the pair is a topological excitation.

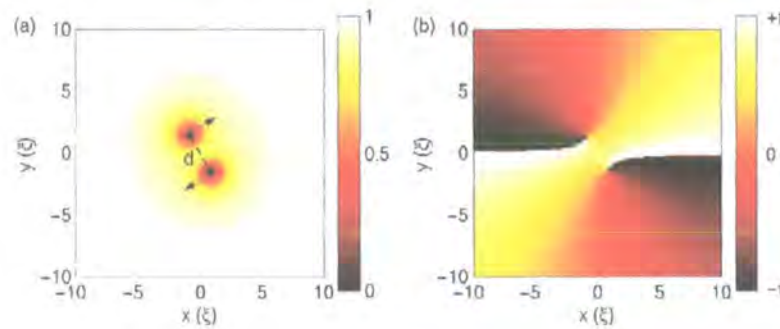

Figure 8.1: (a) Density and (b) phase of a corotating vortex pair in a 2D homogeneous system. The separation of the vortices is $d \approx 3.5\xi$.

8.1.1 Dynamical properties

The dynamical properties of the corotating vortex pair can be approximated using classical hydrodynamics [27, 149]. By assuming the vortices to be point-like, this approach ignores the core structure of the vortex, and so is only valid when the vortex cores are well separated. This approach predicts that the angular frequency of the corotating vortices is given by $\omega_V = \kappa/\pi d^2$ [27, 153, 149], where d is the separation of the vortices and $\kappa = h/m$ is the quantum of circulation.

We can map the dynamics of the pair numerically by performing repeated simulations of the pair at different separations using the time-dependent 2D GPE. The angular frequency and acceleration of the corotating vortices are shown in figure 8.2 as a function of the vortex separation d. Here, data obtained from simulations of the time-dependent 2D GPE (points with error bars) is compared to the prediction based on classical hydrodynamics (dashed lines). As would be expected, the prediction agrees well with the time-dependent numerical results when the vortices are well separated, which roughly corresponds to separations greater than $d \sim 5\xi$. However, for separations smaller than this value we observe a significant deviation. Under the hydrodynamic predictions, both the angular frequency and acceleration diverge to infinity as the separation tends to zero. The numerical results suggest that, as the vortex separation is decreased, the angular frequency (figure 8.2(a)) gradually levels out, and for separations of less than $d \sim 2\xi$, reaches an approximately constant value of $\omega_V \sim 0.25(c/\xi)$. Correspondingly, the numerically-obtained vortex acceleration (figure 8.2(b)) and speed (not shown) reach a peak at $d \sim 2\xi$ and decreases to zero as $d \to 0$. These effects at small separations are due to overlapping of the vortex cores. An important feature is that the numerical results suggest that there is a maximum acceleration and speed for an isolated corotating pair, approximately given by $a_V \sim 0.06(c^2/\xi)$ and $v_V \sim 0.25c$, respectively.

Also shown in figure 8.2 are numerical results based on the time-independent GPE in the rotating frame (solid lines)[263]. Despite the fact that the corotating pair is not a time-dependent solution to the GPE, the results are expected to be valid, and are found to be in reasonable agreement with the data obtained from the time-dependent 2D GPE.

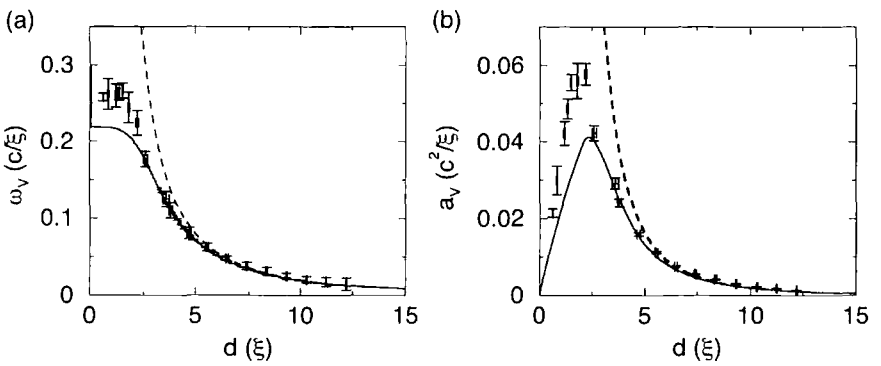

Figure 8.2: (a) Angular frequency ω_V and (b) acceleration a_V of a corotating pair as a function of the pair separation d. The results are derived from the (time-dependent) 2D GPE (points with error bars), a time-independent approach in the rotating frame (solid lines), and the hydrodynamical predictions corresponding to $\omega_V = \kappa/(\pi d^2)$ and $a_V = \kappa^2/(2\pi^2 d^3)$ [27, 149, 153] (dashed lines).

It has been predicted analytically that a superfluid corotating pair is dynamically unstable [149, 150, 151] and will decay via the continuous radiation of sound waves. The general form of the outgoing radiation is a summation over dipolar, quadrupolar, and higher order terms. Due to the symmetry of the corotating pair, the dipole fields from each vortex are expected to cancel such that the quadrupolar field dominates the radiation distribution [149, 150, 153].

Close examination of small-scale density perturbations in the region of the corotating pair during our time-dependent simulations reveals the continuous emission of sound waves from the vortices. This is illustrated in figure 8.3, which corresponds to figure 8.1(a) shown over a larger region and on a more sensitive density scale. As expected, the sound emission is clearly quadrupolar in nature. The rotation of the vortices modifies this quadrupolar emission into a swirling radiation pattern. We expect the quadrupolar radiation to have a frequency $2\omega_V$ [153]. For the pair considered here, with $d = 3.5\xi$, the angular frequency is $\omega_V \approx 0.14(c/\xi)$. We expect the wavelength of the emitted sound to be $\lambda = \pi c/\omega_V \approx 22\xi$, which is consistent with the appearance of the outgoing sound waves in figure 8.3. Note that the sound waves in figure 8.3 have a maximum amplitude of around $0.005n_0$, with the amplitude decreasing as the

waves spread radially outwards.

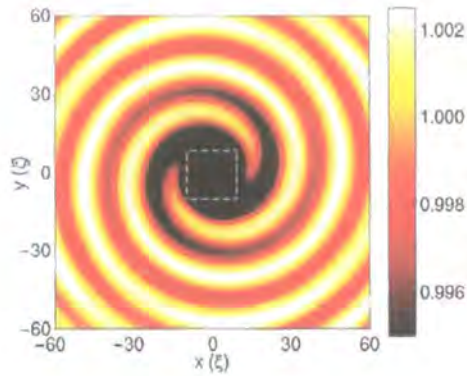

Figure 8.3: Density plot of the corotating pair considered in figure 8.1 showing small-scale density variations around the peak density. Sound waves of amplitude $\sim 0.5\%n_0$ are radiated from the pair in a quadrupolar manner, while the continuous rotation of the pair modifies the sound field into a swirling radiation pattern. Note that this figure is plotted on a larger length-scale than figure 8.1, the range of which corresponds to the white dashed box in this figure.

Since the system is homogeneous the core energy of the vortices cannot change, and so any energy loss must be at the expense of the interaction energy between the vortices. The interaction energy of the corotating pair depends on the vortex separation via $E_{\text{int}} = -2\pi\kappa^2 \ln(d)$ [149]. The sound emission from the pair leads to a decrease in this interaction energy, and therefore causes the vortex separation to grow. Indeed, we observe this in the numerical simulations.

It has been predicted [149, 150, 151] that the rate of change of the separation is proportional to $1/d^5$, and the power emission is proportional to $1/d^6$. Note that, within this framework, the power emission from the pair is consistent with being proportional to the acceleration-squared. This decay is slow. For example, the vortex separation is expected to grow in time in proportion to $t^{1/6}$. For this reason, it is not computationally viable to map the decay of the pair using the time-dependent 2D GPE.

For more than two vortices in a symmetric circular configuration around some central axis, the quadrupolar radiation term disappears, and higher order terms dominate the radiation distribution. This leads to even slower decay rates than for the corotating pair [149].

8.2 Vortex-antivortex pair

If the circulation of the two vortices is in the opposite direction, the pair propagates with a constant, self-induced speed. This vortex-antivortex pair represents a solution to the homogeneous 2D GPE in the moving frame [208, 209], analogous to the non-stationary dark soliton solutions of the homogeneous 1D GPE. The vortex-antivortex pair can also be considered as the cross-section of a 3D vortex ring. Here we present some of the basic properties of the vortex-antivortex pair.

8.2.1 Dynamical properties

The density and phase profile of a vortex-antivortex pair is illustrated in figure 8.4 for a separation $d = 5\xi$. On a large density scale (figure 8.4(a)), two density minima can be resolved corresponding to the vortex cores. Examination of small-scale density perturbations about the peak density (figure 8.4(b)) reveals lobes of perturbed density in the plane of the pair and perpendicular to this along the axis of the pair. In the plane of the pair, the lobes are of reduced density due to the presence of vortex cores, while along the axis of the pair, the lobes are of slightly raised density. In the latter case, the lobes have a peak amplitude of $0.01n_0$ and extend over 10 healing lengths away from the vortex cores. The phase profile of the vortex-antivortex pair (figure 8.4(c)) is dipolar and tends towards a constant homogeneous phase with distance from the pair. In this sense, the vortex-antivortex pair is not a topological excitation.

Under the classical hydrodynamics approach [27], which is valid providing the vortices are well-separated, the velocity of the pair is predicted to be,

$$v_{\mathrm{P}} = \frac{\kappa}{2\pi d}. \tag{8.1}$$

Similarly the energy of the pair is predicted to be,

$$E_{\mathrm{P}} = \frac{n\kappa^2}{2\pi} \ln\left(\frac{d}{\xi}\right) + E_{\mathrm{P}}^0, \tag{8.2}$$

where the first term is the vortex kinetic energy and the second term E_{P}^0 is a constant representing the (rest mass) energy of the vortex cores. Figure 8.5 shows the total energy and speed of the vortex-antivortex pair as a function of separation, as computed numerically using the homogeneous 2D GPE (solid lines)

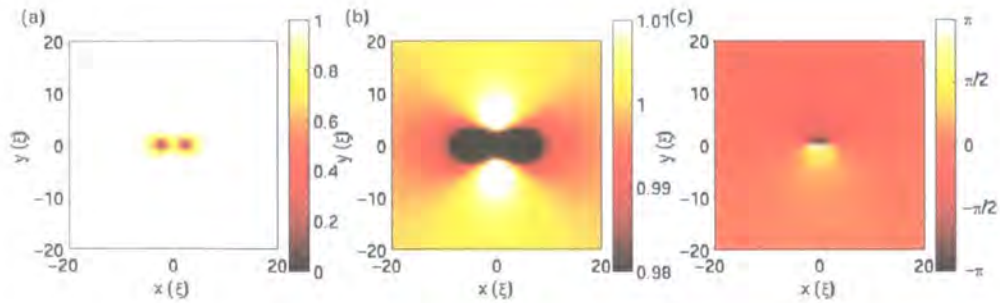

Figure 8.4: Density and phase profiles of a vortex-antivortex pair with separation $d = 5\xi$. (a) Large-scale density plot showing the two vortex cores. (b) Density plot on a small-scale revealing the quadrupolar lobe structure of the surrounding density, with amplitude $0.01n_0$. (c) Phase profile of the pair.

and the above predictions from classical hydrodynamics (dashed lines). As for the corotating pair, the hydrodynamical predictions agree well with the numerical data when the vortex separation is greater than $d \sim 5\xi$. For separations less than this, the predictions underestimate the numerically-obtained results. This is attributed to overlapping of the vortex cores, which is not described by classical hydrodynamics. Note that when the separation of the vortices is less than $d \sim 2\xi$, the pair is no longer stable and decays into a rarefaction pulse [208].

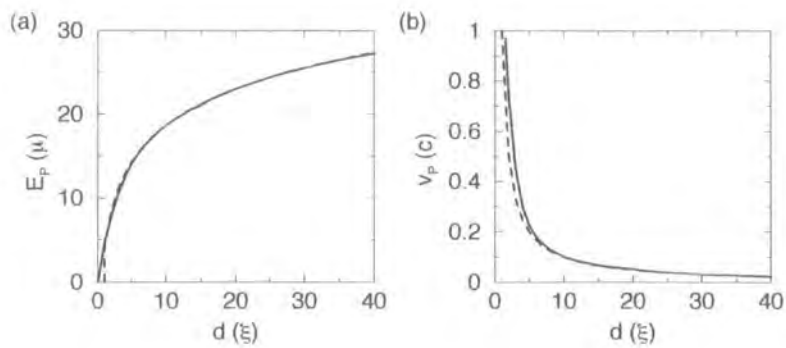

Figure 8.5: (a) Energy E_P and (b) speed v_P of the vortex-antivortex pair as a function of the separation d. The results obtained numerically from the 2D GPE are shown by solid lines, while the hydrodynamical predictions of equations (8.1)-(8.2) are shown by dashed lines. The energy term E_P^0 in equation (8.2) is found by fitting to be $E_P^0 \approx 4.25\mu$.

8.3 Interaction of a vortex-antivortex pair with a single vortex

As an example of a three-vortex interaction, we consider a vortex-antivortex pair incident on a single vortex in a 2D homogeneous system. The initial vortex configuration is illustrated schematically in figure 8.6(a). The vortex-antivortex pair, with vortices labelled 1 and 2, is created with its central point lying at the x-coordinate $x = h$. It is initially directed in the negative y-direction such that it approaches a single vortex, labelled 3, at the origin. Vortex 1 has clockwise circulation, while vortices 2 and 3 have anti-clockwise circulation. We investigate the dynamics of the three vortices during the ensuing interaction as a function of the initial offset h of the pair. The initial separation of the vortex-antivortex pair is $d = 5\xi$, while the initial y-coordinate of the pair is $y = 20\xi$.

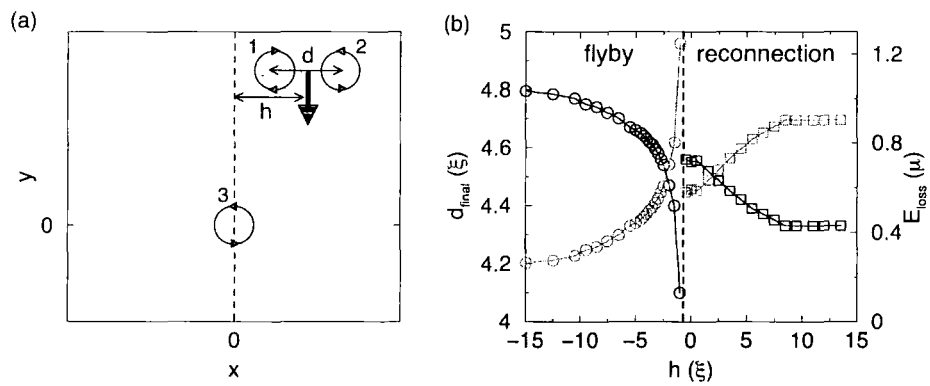

Figure 8.6: (a) Schematic of the three-body interaction. A vortex-antivortex pair, labelled 1 and 2, is incident on a single vortex, labelled 3, located at the origin. The initial offset of the pair from the $x = 0$ axis is h. (b) Final pair separation d_{final} (left axis, black data) and corresponding energy loss E_{loss} (right axis, grey data) for a pair with initial separation $d = 5\xi$ as a function of the offset distance h. The energy loss is inferred from the change in the pair separation, using equation (8.2), with the initial pair energy being $E_{\text{P}} = 14.4\mu$. Circles and squares denote the flyby and reconnection regimes, respectively.

We observe two regimes in the dynamics of the vortices: for $h \leq -\xi$, the vortex-antivortex travels past the single vortex with a deflected trajectory, while for $h \geq -0.5\xi$ a reconnection occurs whereby one of the vortices in the approaching

pair becomes swapped with the single vortex. We refer to these regimes as a *flyby* and a *reconnection*, respectively.

In a flyby interaction, vortex 2 in the pair is adjacent to vortex 3. These vortices have the same (anti-clockwise) circulation, and tend to repel each other. However, in the reconnective regime, the geometry of the interaction means that vortex 1 in the pair comes adjacent to vortex 3. These vortices have opposite charge, and can form a vortex-antivortex pair, leaving behind vortex 2. Note that we have simulated the reconnection events using smaller time/space steps, and can conclude that the reconnections are not numerical artifacts.

The decay of the vortex-antivortex pair during the interaction is mapped out in figure 8.6(b) by considering both the final pair radius (left axis, black data) and the corresponding energy loss (right axis, grey data). The left hand side of the plot ($h \leq \xi$) represents the flyby interaction, while the right hand side ($h \geq -0.5\xi$) represents the reconnection interaction. We will now make a detailed study of these two regimes in turn.

8.3.1 *Flyby* regime

The flyby regime occurs for $h \leq -\xi$. Figure 8.7(a) shows the trajectories of the vortices during the flyby interaction for several values of the offset distance h. The incoming pair, initially directed in the negative y-direction, becomes deflected by the velocity field of the single vortex. The single vortex makes slight deviations about its central position due to its interaction with the pair.

Dynamics of the vortices

The vortex pair tends to pass around the *far side* of the single vortex in an *anti-clockwise* sense. The amount of deflection depends heavily on how close the pair passes to the single vortex. For example, for the $h = -\xi$ case in figure 8.7(a) (blue lines), the pair experiences a strong circulating velocity field during the interaction due to its close proximity to the single vortex. This induces the pair to pass around the far side of the single vortex and almost reverse direction. Indeed, this pair becomes scattered by an angle $\sim 150^{\circ}$ in an anti-clockwise direction. As the initial offset h is increased in magnitude, the pair passes the

single vortex at a greater distance, reducing the velocity field it experiences, and therefore reducing the amount of deflection. For example, for $h = -4\xi$ in figure 8.7(a) (red case), the scattering angle is $\sim 30^{\circ}$ (anti-clockwise), while for $h = -12\xi$ (black case) the scattering is negligible.

During the flyby, the single central vortex makes small deviations about the origin due to its interaction with the pair. However it remains localised in the region of the origin at all times and returns to being stationary following the interaction.

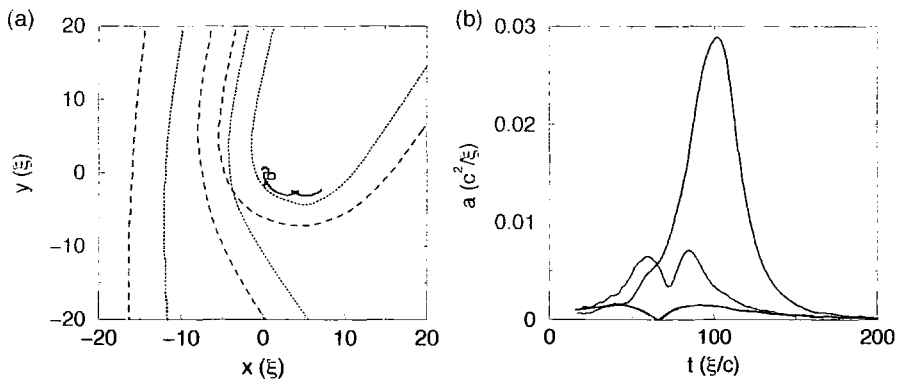

Figure 8.7: Dynamics of the vortices in the three-vortex interaction: flyby regime. (a) Path of the three vortices during their interaction, with vortices 1, 2 and 3 represented by dashed, dotted, and solid lines, respectively. Three values of the offset distance are considered: $h/\xi = -1$ (blue lines), -4 (red lines), and -12 (black lines). (b) Acceleration experienced by vortex 1 during the interactions considered in (a).

Energy loss during the flyby interaction

Since the system is homogeneous, the core energy of the vortices remains fixed, and the only energy contribution that can decay is the interaction energy of the vortex-antivortex pair. As evident from equation (8.2), the separation of the pair is a measure of its energy. In figure 8.6(b) we show the final separation of the pair (left axis, black data) following the interaction, as a function of the offset distance h. For the flyby regime (left side of figure8.6(b)), we observe that the *change* in separation is maximum for $h = -\xi$, and decreases asymptotically towards zero as $h \to \infty$. The maximum change in separation is almost 20% of

the original separation. Also plotted in figure 8.6(b) is the energy loss from the pair, derived from the change in the pair separation using equation (8.2). The maximum energy loss is $E_{\text{loss}} \sim 1.2\mu$, which corresponds to around 10% of the initial pair energy.

The amount of decay can be qualitatively understood in terms of the acceleration experienced by the pair. The pair acceleration is indicated in figure 8.7(b) for the three values of h considered in figure 8.7(a). Note that this acceleration corresponds to that of vortex 1, although this should have the same general form as the centre of mass acceleration of the pair. Due to the short-lived deflection of the pair by the single vortex, the acceleration consists of a peak, or double peak.

For $h = -\xi$ (blue data), where the deflection is considerable, the peak acceleration is of large amplitude. This corresponds to the case of maximum decay. For larger offsets, e.g. $h = -4\xi$ (red data) and $h = -12\xi$ (black data), the reduced deflections result in a much reduced peak acceleration. Correspondingly, the decay of the pair becomes reduced. In the limit $h \to \infty$, the acceleration and amount of decay both tend to zero.

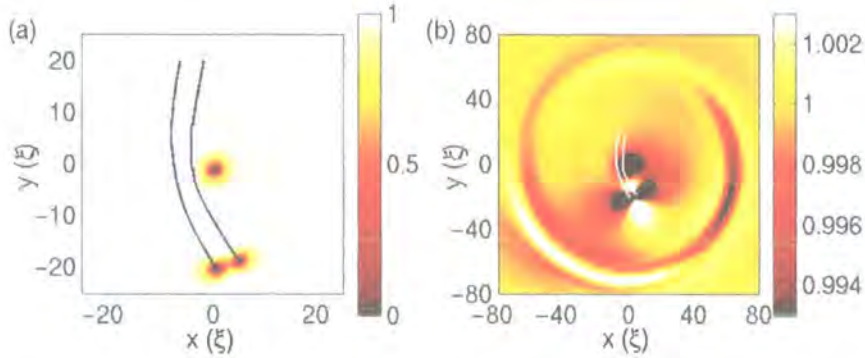

Figure 8.8: Density profile following the flyby interaction for initial offset $h = -4\xi$. (a) Density plot on a large density scale showing the position of the vortices at a time following the flyby interaction. (b) Density plot on a sensitive scale, revealing the emission of a burst of sound during the interaction. In both plots, the previous trajectory of the vortex-antivortex pair is indicated by solid lines. Note that (b) corresponds to a larger region than in (a).

We now address the question of what form the decay takes. We consider the case

for the offset $h = -4\xi$, corresponding to the red data in figure 8.7. Figure 8.8 shows the density profile in the region of the vortices following the interaction. In particular, figure 8.8(b) focusses on small-scale density perturbations. We observe the emission of a burst of sound from the interaction area, which propagates radially outwards. This sound pulse has an initial amplitude $\sim 0.5\% n_0$ and wavelength $\sim 20\xi$. The nature of this sharp (short wavelength) burst of sound is consistent with sharp acceleration experienced by the pair during the interaction (shown in figure 8.7(b), red line)).

8.3.2 *Reconnection* regime

For $h \geq -0.5\xi$, a vortex reconnection occurs. When the vortex-antivortex pair is in the vicinity of the central vortex, vortex 2 in the pair becomes replaced by the central vortex 3. This is possible since vortices 2 and 3 have the same circulation. Subsequently, vortex 2 becomes left behind in the region of the origin, and the new pair, consisting of vortices 1 and 3, propagates away.

Dynamics of the vortices

The paths of the vortices during the reconnective interaction are shown in figure 8.9(a) for several different initial offsets. The dynamics are more complicated than in the flyby regime, largely due to the effect of the reconnection.

For low h, e.g. $h = 0$ (blue lines), the outgoing pair becomes deflected anti-clockwise around the origin. Here, the swapping of vortex 2 and vortex 3 occurs over a short length-scale, and so the direction of motion of the pair just before and just after the reconnection is practically the same. In other words, the reconnection does not significantly affect the motion. The dominant effect on the motion of the pair is the velocity field of the central vortex - this induces an anti-clockwise motion of the pair around the single vortex, in a similar manner to that observed in the flyby regime.

As the offset h is increased, the anti-clockwise deflection of the pair decreases and eventually becomes clockwise, e.g. $h = 4\xi$ (red lines). This is due to the increasing effect of the reconnection on the pair dynamics. We find that the swapping of vortices 2 and 3 now occurs over a significant spatial extent. This

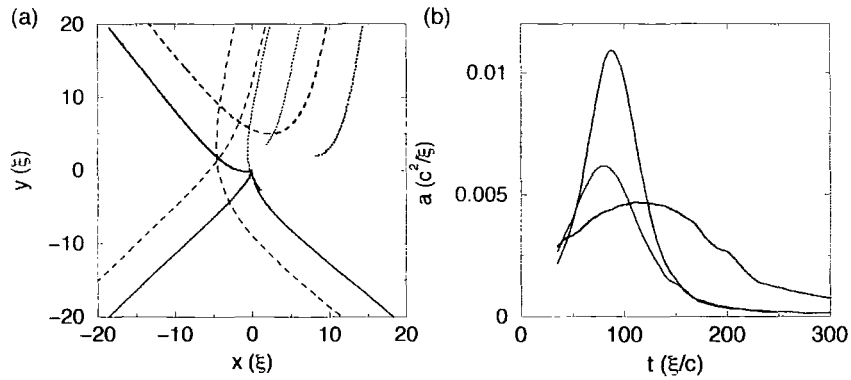

Figure 8.9: Dynamics of the vortices in the three-vortex interaction: reconnection regime. (a) Path of the vortices during the interaction, with vortices 1, 2 and 3 represented by dashed, dotted, and solid lines, respectively. Three values of the initial offset distance are considered: $h/\xi = 0$ (blue lines), 4 (red lines), and 12 (black lines). (b) Total acceleration experienced by all three vortices during the interactions considered in (a).

means that the orientation of the pair just before and just after the reconnection deviates, and induces a rapid *clockwise* change in the direction of motion.

For large offset, the spatial extent over which the vortices swap in the pair can be considerable. For $h = 12\xi$ (black lines in figure 8.9(a)), this distance is of the order of 10ξ. The corresponding scattering angle is $\sim 150^{\circ}$ in a clockwise manner.

Energy loss during the reconnection interaction

The decay of the vortex pair during the reconnective interaction is illustrated on the right side of figure 8.6(b). We find that the amount of decay in the pair increases with the initial offset distance h. However, for offsets greater than $h \sim 10\xi$, the decay appears to saturate. This maximum decay corresponds to a $\sim 14\%$ reduction in the pair separation and approximately 6% decay in the pair energy.

In order to investigate whether this decay trend is consistent with the acceleration experienced by the vortices, figure 8.9(b) shows the acceleration as a function of time, for offsets of $h/\xi = 0$ (blue line), 4 (red line), and 12 (black line). Due to the reconnection event, the acceleration of vortex 1 is not neces-

sarily a good indication of the overall vortex acceleration, so here we consider the summed acceleration of all three vortices.

Since the amount of pair decay increases with the offset h, we would expect to see a corresponding increase in the total acceleration experienced by the vortices. However, this is not the case. Firstly we note that the curves for $h = 0$ and $h = 4\xi$ are relatively sharp peaks, while for $h = 12\xi$ the acceleration is a broad peak due to the the relatively long-lived interaction. The area under the curves, representing the overall acceleration, is largest for $h = 0$ (blue line), smallest for $h = 4\xi$ (red line), while $h = 12\xi$ has an intermediate value. It is evident that the acceleration experienced by the vortices is not consistent with the decay of the pair.

These results are in contrast to the flyby regime, where the acceleration does give qualitative information about the decay. Therefore we expect that the process of reconnection must be responsible. It is known from studies of vortex rings that reconnections are accompanied by a substantial burst of sound emission [87]. Although a reconnection must involve some degree of accelerative motion, the amount of sound emitted is not necessarily directly dependent on it.

The form of the emitted energy from a reconnective interaction is illustrated in figure 8.10 by the density profile of the system following the interaction. We consider the case of $h = 0\xi$ (figure 8.9, red lines). Sound pulses are clearly radiated during the interaction, and appear to have a quadrupolar form. The sound pulse is broad, with a wavelength of around 60ξ, and of low initial amplitude $\sim 0.1\% n_0$. This is different to the sound emission observed in the flyby interaction of figure 8.8. There, the sound pulse appeared almost radial, with shorter wavelength and higher amplitude.

The flyby and reconnection regimes have distinct sound emission properties. In the former case, the accelerative motion induces the sound emission, whereas in the latter case, the reconnection is the dominant factor in generating sound. Importantly, when the acceleration of the vortices is large, e.g. in the regime $-2\xi < h < -0.5\xi$, the acceleration-induced sound emission can be significantly larger than that typically generated by a reconnection.

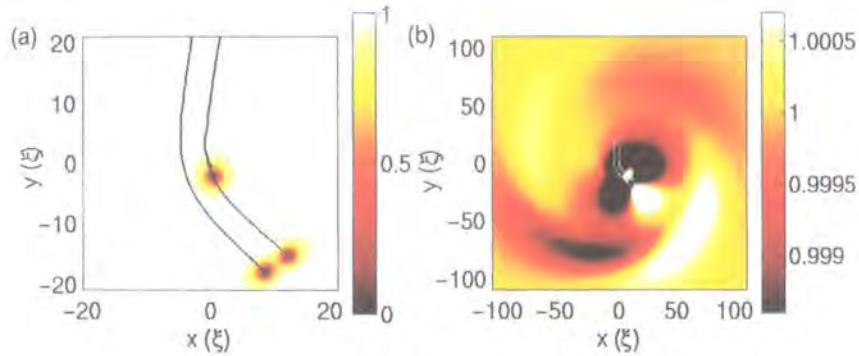

Figure 8.10: Density profile following the reconnective interaction for $h = 4\xi$. (a) Density plot on a large density scale, showing the position of the vortices at a time following the interaction. (b) Density plot on a senstive scale, revealing the emission of sound waves during the interaction. In both plots, lines indicate the previous trajectories of the vortices. Plot (b) corresponds to a larger region than plot (a).

8.4 Summary

In this chapter we have considered the interaction of two and three vortices in a 2D homogeneous system. Apart from the isolated vortex-antivortex pair, the dynamics of these vortex interactions are generally accelerative. We observe that this accelerative motion destabilises the vortices, and induces dissipation from the vortices via the radiation of sound waves. This is in qualitative agreement with the results of chapter 7 where we observed sound emission from a single accelerating vortex.

By considering the interaction of a vortex-antivortex pair with a single vortex, we have demonstrated reconnection events between vortices. A reconnection event results in a burst of sound waves from the vortices, in addition to the sound emission induced by the acceleration of the vortices.

Chapter 9

Vortices and svortices in non-axisymmetric geometries

In chapter 3 we investigated the dynamics of a dark solitary wave in a condensate as the transverse confinement of the system is relaxed. The solitary wave, which has a one-dimensional nature, is stable in quasi-1D geometries, but becomes unstable in 3D systems, where it is prone to decay into stable 3D excitations in the form of vortex rings. In the opposite sense, it is interesting to consider the stability of a vortex in a BEC as we move from 2D/3D systems towards the highly-restrictive geometries in the quasi-1D limit. In the former case, we know that vortex solutions exist, whereas in the latter case, one does not expect vortices to be supported. In the intermediate regime, squashed vortex structures with solitonic properties, known as solitonic vortices or svortices, are predicted to occur [163, 164].

In this chapter we investigate the dynamics of a single vortex in a condensate under non-axisymmetric harmonic trapping. In particular, we probe the regime of quasi-1D geometries, and show how vortex-like structures manifest themselves in these highly-restricted systems as svortices. Furthermore we draw links to dark solitary waves.

9.1 Vortex in a non-axisymmetric condensate

We consider a 2D condensate under harmonic confinement given by,

$$V_{\rm ext} = \frac{1}{2}\omega_x^2(x^2 + \gamma^2 y^2), \tag{9.1}$$

where $\gamma = \omega_y/\omega_x$ is the harmonic trap ratio. The trap is axisymmetric for $\gamma = 1$, and non-axisymmetric for other values. Note that the trap is non-rotating.

Throughout this chapter, the x-direction trap strength is taken to be $\omega_x = 0.5\sqrt{2} \times 10^{-1}(c/\xi)$, which corresponds to a TF radius $R_{\rm TF} = 20\xi$. We generate the initial vortex state by running the 2D GPE in imaginary time while enforcing the characteristic azimuthal 2π-phase slip about the point (x_0, y_0). In a fully 2D geometry, this numerical method generates the standard vortex density profile, while in restrictive quasi-1D geometries, we expect that the corresponding density profile will have a modified form. This will be discussed in due course. We initially create the vortex state at position $(x_0, y_0) = (5\xi, 0)$.

Figure 9.1 illustrates the evolution of the initial vortex structure in traps ranging from the axisymmetric case of $\gamma = 1$, through $\gamma = 2$ and $\gamma = 4$, to the strongly non-axisymmetric case of $\gamma = 8$. The plots show the density and phase profiles of the condensate when the excitation reaches the $x = 0$ axis. Note that the condensate becomes increasingly elongated as the trap ratio γ is increased. We find two regimes for the vortex state: the *weakly* and *strongly* non-axisymmetric cases.

9.1.1 Weakly non-axisymmetric regime

For $\gamma = 1$ (case (i)), the condensate is circular in shape. The dynamics of a vortex in an *axisymmetric* trap are discussed in detail in chapter 7. For $\gamma = 2$ (case(ii)) and $\gamma = 4$ (case(iii)), the condensate is elliptical in shape. In each of the cases (i)-(iii), the excitation clearly remains a vortex throughout its motion, as indicated by the node in the density and 2π phase profile.

A vortex in a trapped BEC (at zero temperature) tends to follow a path of constant energy [64, 144, 146], resulting in precession around the trap centre. This is due to a Magnus force effect, as outlined in chapter 7. In a weakly non-axisymmetric trap, where the geometry is elliptical in shape, the vortex is

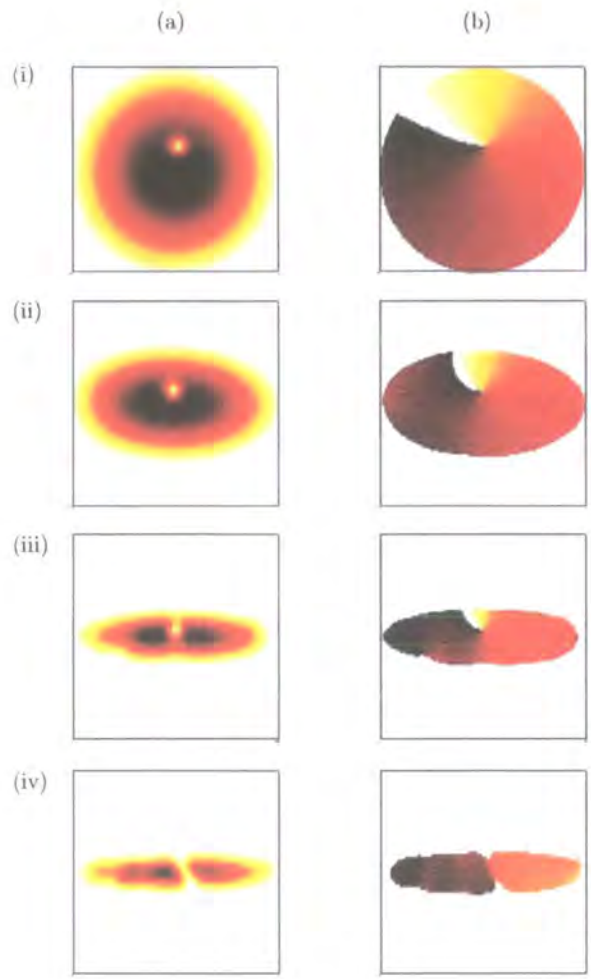

Figure 9.1: (a) Density and (b) phase profiles of a non-axisymmetric condensate containing a vortex. Four trap ratios are considered: $\gamma =$ (i) 1, (ii) 2, (iii) 4, and (iv) 8. The vortex is initially located at $(x_0, y_0) = (5\xi, 0)$, while the images correspond to when the vortex reaches the $x = 0$ axis. In the density (phase) plots, white corresponds to zero density ($-\pi$) and black to peak density ($+\pi$). Each box corresponds to the region $[-20\xi, +20\xi] \times [-20\xi, +20\xi]$. Note that in (b) the phase is set to zero in the region where the density is so low (less than $10^{-4} n_0$) that the phase cannot be interpreted.

predicted to follow an elliptical trajectory around the trap centre [252]. Figure 9.2 maps out the trajectory of the vortex in weakly non-axisymmetric traps for the cases (i)-(iii). For $\gamma = 1$ (figure 9.2(a)), the motion is approximately circular, while for $\gamma = 2$ and 3 (figure 9.2(b)-(c)) the trajectory tends to follow an elliptical path. However, in all these case, there is a visible modulation in the vortex path due to the interaction of the vortex with the fundamental fluid mode (oscillating at ω_x) set up by the vortex motion. This phenomenon is discussed for a vortex in an axisymmetric trap in chapter 7.

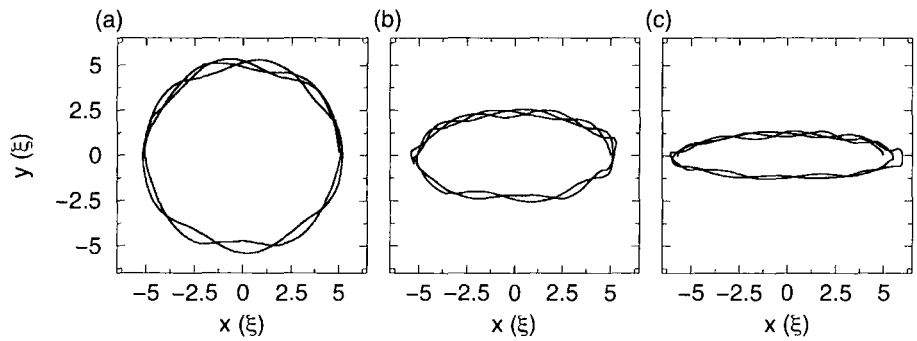

Figure 9.2: Trajectory of a vortex in a non-axisymmetric trapped BEC. Trap ratios of $\gamma =$ (a) 1, (b) 2, and (c) 4 are considered.

9.1.2 Strongly non-axisymmetric regime

For $\gamma = 8$ (case(iii)) the condensate is highly-elongated. The transverse density profile lies in between the harmonic oscillator ground state, with harmonic oscillator length $l_y = 1.3\xi$, and the TF profile, with radius $R_y = 2.5\xi$, such that the transverse width is now of the order of the size of the vortex core. By the time the excitation has reached the $x = 0$ axis, the excitation is centred on the origin, suggesting that the motion has changed from a precessional trajectory to a linear, 1D oscillation. We expect that this excitation corresponds to the solitonic vortex, or svortex, predicted by Brand *et al.* [163, 164] to occur in highly restricted geometries. From now on we will refer to this excitation as a svortex.

By the time it has reached the centre of the trap, the svortex does not have the appearance of a typical vortex. Instead of a node of zero density, it appears

in a transient form as an approximately linear stripe of low density, which is oriented at an angle to the x-axis. The phase of the excitation has the form of a linear phase slip, oriented in the same manner, in contrast to the initially-imprinted vortex 2π-phase profile. In these respects, the excitation resembles a dark solitary wave with its plane at an angle to the transverse direction. However, such a *tilted* dark solitary wave could not be dynamically stable: a dark solitary wave is a 1D object and not stable to rotational motion. We will discuss the nature and dynamics of the svortex later in this chapter.

9.1.3 Transition between the weakly and strongly non-axisymmetric regimes

Brand *et al.* [163] have considered the regimes of a dark solitary wave and a svortex, although their work concentrates on waveguides with hard wall boundaries in the transverse direction, rather than the harmonic confinement we employ. They observe that the transition between the two regimes is associated with the onset of quasi-1D behaviour. We therefore expect that the transition between our regimes of a vortex and svortex are associated with the reduction of the system from 2D (or 3D) to effectively 1D. We can give evidence to support this idea by studying the corresponding dynamics of a plane dark solitary wave. The stationary dark solitary wave is initially positioned at $x = 5\xi$, with its axis directed in the y-direction. For $\gamma < 5$, we observe the decay of the solitary wave into vortex rings, characteristic of the transverse snake instability in 3D geometries (see chapter 3). However, for $\gamma > 5$, the solitary wave oscillates in the trap as an effectively 1D object, with no indication of this transverse instability. We can therefore say, at least for the case of a plane dark solitary wave, that $\gamma \sim 5$ marks the critical point between 3D/2D and 1D dynamics. Note that this critical point varies slightly with the speed, and therefore the initial position, of the solitary wave.

So far we have assumed a fixed longitudinal trap frequency of $\omega_x = 0.5\sqrt{2} \times 10^{-1}(c/\xi)$. In general, we find that the critical point between these two vortex regimes occurs when the transverse size of the system is of the order of a healing length, which typically corresponds to when $\omega_y \sim 0.5(c/\xi)$. The critical trap ratio therefore depends on the value of ω_x (for fixed chemical potential μ). Note

that the critical point between these regimes also depends slightly on the initial longitudinal position of the vortex excitation in the trap.

We have therefore discriminated two regimes for a vortex in a non-axisymmetric trap. For sufficiently low trap ratios, the precessing vortex is stable and retains the characteristic vortex density/phase profile throughout its motion. For large trap ratios, the vortex cannot be supported and develops into an excitation with modified density and phase characteristics. Furthermore, it appears to undergo linear, soliton-like motion in the trap.

9.1.4 Oscillation frequency in a non-axisymmetric condensate

Using a variational Lagrangian method and assuming the Thomas-Fermi limit, Fetter [252] has predicted the precession frequency of a vortex in a non-axisymmetric 2D BEC to be,

$$\omega_{\mathrm{V}} = \frac{\hbar}{mR_xR_y} \ln\left(\frac{R_\perp}{\xi}\right) \frac{1}{1-r_0^2} \quad , \tag{9.2}$$

where $R_{x,y} = \sqrt{2\mu/m\omega_{x,y}^2}$ are the TF radii in the x,y-directions, $R_\perp^2 = 2R_x^2R_y^2/(R_x^2+R_y^2)$, and r_0 is the radius of the vortex scaled in terms of TF units.

By performing time-dependent simulations of the 2D GPE, we have calculated the frequency of the vortex motion in a non-axisymmetric trap for a range of trap ratios. Note that this is for a particular initial position of $(x_0, y_0) = (5\xi, 0)$. Since the 'vortex' motion becomes one-dimensional for high trap ratios, we consider the frequency of the vortex motion in the longitudinal (x-direction) ω_x^{V}, rather than the precession frequency. This allows us to compare the vortex motion in the weakly and strongly non-axisymmetric two regimes. In the weakly non-axisymmetric case, where the vortex precesses around the trap centre, this frequency coincides with the vortex precession frequency ω_{V}. The results are plotted in figure 9.3, with frequency scaled in terms of ω_x. The overall trend is that the vortex frequency ω_x^{V} increases with the trap ratio and eventually saturates to an approximately constant value.

Weakly non-axisymmetric regime

We consider first the regime up to $\gamma \approx 5.5$, which corresponds to what we would term the weakly non-axisymmetric regime. Here the vortex precesses around the trap centre. The precession frequency increases with γ mainly due to the decrease in the length of the elliptical path that the vortex traces out. Additionally, the modified curvature of the potential affects the Magnus force and therefore the precessional speed of the vortex. In this weakly non-axisymmetric regime, we expect the analytic prediction by Fetter *et al.* of equation (9.2) to be applicable. This prediction is plotted in figure 9.3 by the dashed line, and we find it to be in reasonable qualitative and quantitative agreement with our numerical results.

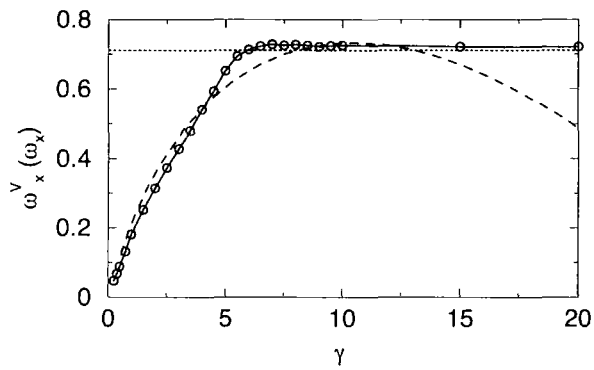

Figure 9.3: Longitudinal (x-direction) oscillation frequency ω_x^{V} of a vortex (or related excitation) in a non-axisymmetric harmonic trap as a function of the trap ratio γ. The results obtained from numerical simulation of the 2D GPE are shown (solid line, circles), along with the prediction according to equation (9.2) (dashed line). The vortex is initially located at $(x_0, y_0) = (5\xi, 0)$, and the x-direction trap frequency is $\omega_x = 0.5\sqrt{2} \times 10^{-1}(c/\xi)$. For comparison, the predicted dark soliton oscillation frequency of $\omega_x/\sqrt{2}$ is plotted (dotted line).

Strongly non-axisymmetric regime

For a trap ratio greater than $\gamma \approx 5.5$, the frequency in the x-direction saturates to an approximately constant value. This is the strongly non-axisymmetric regime, where the dynamics of the system become predominantly one-dimensional, and the vortex takes the form of an svortex. An important observation is that

the frequency of the excitation saturates to a value of $\omega_x^{\mathrm{V}} \approx 0.72\omega_x$. We have tested trap ratios up to $\gamma = 40$ and find the same oscillation frequency. This value is close to the predicted oscillation frequency of a dark soliton of $\omega_x/\sqrt{2}$ [156, 157, 165, 166, 213, 222] (figure 9.3, dotted line).

Even in this strongly non-axisymmetric regime, the Fetter prediction (equation (9.2)) initially gives reasonable agreement with the numerically-obtained oscillation frequencies. However, for $\gamma > 10$, this function decreases sharply.

9.2 Svortex in a strongly non-axisymmetric trap

We now investigate in more detail the nature of the svortex in the strongly non-axisymmetric regime. Brand *et al.* [163, 164] predict that a svortex has a vortex phase singularity and a squashed vortex density profile, and propagates in a soliton-like manner.

Figure 9.4 shows density and phase snapshots in the early evolution of the svortex, in a elongated system with a trap ratio of $\gamma = 8$. Firstly, we note that the svortex, which starts off-centre, accelerates along the x-direction towards the centre of the trap. This longitudinal motion is analogous to the evolution of an off-centre black (stationary) soliton in a harmonic trap (see chapter 3).

The initially-imprinted vortex soluition (case (i)) consists of the characteristic vortex density node and a 2π-phase slip. However, we clearly see that the transverse size of the condensate is barely wider than the vortex core, indicating the highly restrictive nature of the system. In the second snapshot (case(ii)) the initial vortex has evolved into a linear stripe of low density and an almost step-wise phase profile. Both the density stripe and phase slip are oriented at an angle of around -30^0 to the y-axis, where the negative sign denotes anti-clockwise rotation. This transient state resembles a dark solitary wave with its plane at an angle to the y-axis, i.e. a tilted dark solitary wave. In the third snapshot (case(iii)) a vortex-like state reappears but now with the opposite charge to the initial state. In the following frame (case (iv)), the linear stripe of low density and phase slip re-emerge, but now at a *positive* (clockwise) angle of similar magnitude. In the final snapshot (case (v)) we see the reappearance of the vortex-like state with the original charge. However, the phase profile of the

whole system does not return back to its initial state, due to the considerable fluid motion present.

This cycle repeats itself continuously, and this occurs at a much faster rate than the overall trajectory of the svortex in the trap: in the case examined here, the period of the cycle is approximately $20(\xi/c)$, whereas the period of the svortex trajectory is roughly $120(\xi/c)$. We have considered the frequency of this cycle over a range of trap ratios, and find it is is approximately proportional to the transverse trap frequency ω_y.

Note that other features, apart from the svortex, are present in the phase plots of figure 9.4(b). However, these generally occur outside the TF radius of the cloud, where the density is extremely low, and so do not have any physical interpretation.

We interpret the dynamics as follows. In this highly restricted geometry, the initially-imprinted vortex circulation is heavily suppressed in the y-direction, resulting in the vortex being unstable. The vortex tries to 'unravel' itself, transferring energy and angular momentum to the background fluid, and exciting large-scale rotational fluid modes. The vortex evolves into a transient state which resembles a tilted dark solitary wave. Subsequently the considerable rotational fluid modes in the system lead to the generation of a vortex state, and then another state which resembles a tilted dark solitary wave, both of which now occur with the opposite orientation. Since both the vortex and tilted dark solitary wave are unstable, the excitation exists as a hybrid of the two states, continuously cycling between them.

Note that the vortex state cannot evolve into a stable *plane* dark solitary wave because of the destabilising rotational effects in the system. However, if the angular momentum of the system is dissipated, e.g. by thermal or quantum effects, a plane dark solitary wave may emerge.

Although this complex phase and density cycle does not correspond to the appearance of the svortex predicted by Brand *et al.* we believe that this is the true time-dependent evolution of the svortex.

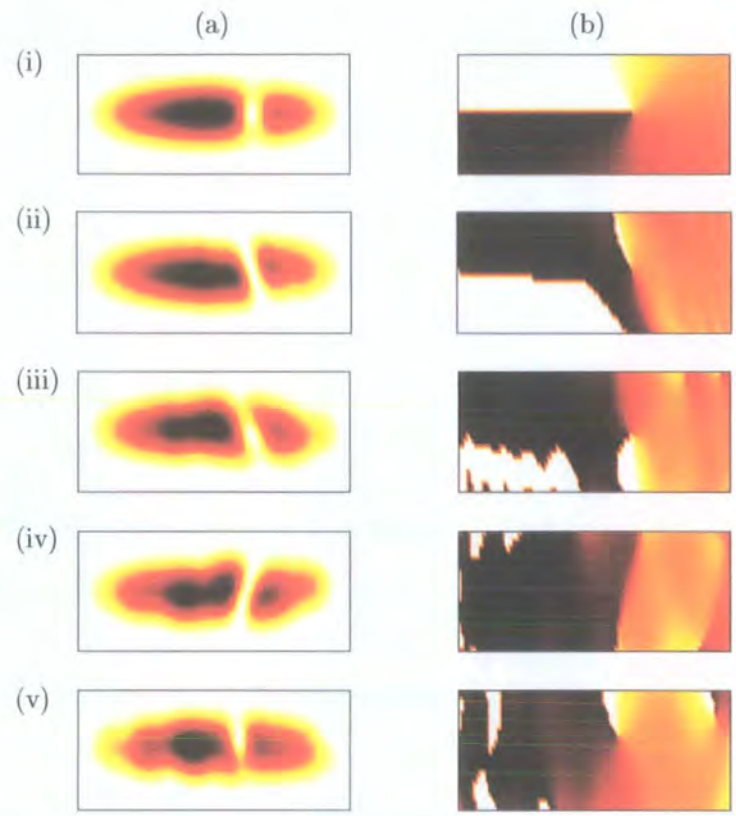

Figure 9.4: (a) Density and (b) phase snapshots of the evolution of a svortex in a strongly non-axisymmetric condensate. The system has a trap ratio of $\gamma = 8$, with $\omega_x = 0.5\sqrt{2} \times 10^{-1}(c/\xi)$, and the vortex state is initially located at $(x_0, y_0) = (5\xi, 0)$. The snapshots correspond to times of (i) $t = 0$, (ii) 4, (iii) 8, (iv) 14, and (v) $20(\xi/c)$. The boxes represent the region $[-20, 20]\xi \times [-2, 2]\xi$.

9.2.1 Analog with a tilted dark solitary wave

We have just illustrated how a svortex in a strongly non-axisymmetric, quasi-1D trap appears to cycle between a vortex state and a tilted dark solitary wave. In order to probe further this hybrid state, we will now consider the effect of starting with a tilted dark solitary wave. This tilt destabilises the dark solitary wave and allows it to couple to rotational fluid modes in the condensate.

Our initial configuration involves a black (stationary) solitary wave located off-centre in the trap, with its stripe oriented at an angle θ to the y-axis. This state is generated numerically by propagating the 2D GPE in imaginary time while enforcing a π-phase step at the desired angle (rather than the 2π-azimuthal

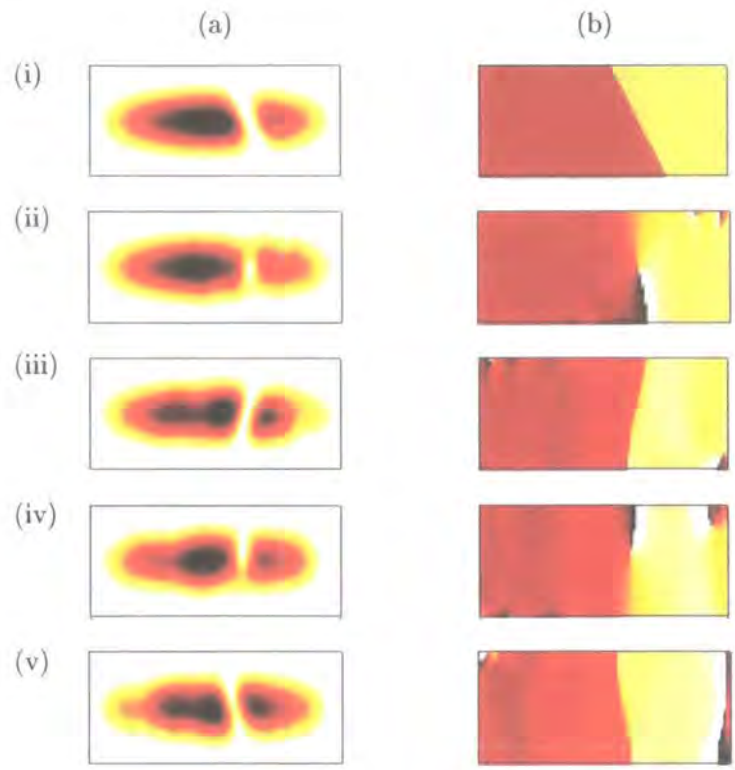

Figure 9.5: (a) Density and (b) phase snapshots following the evolution of a tilted dark solitary wave in a strongly non-axisymmetric trap. The system has a trap ratio of $\gamma = 8$, with $\omega_x = 0.5\sqrt{2} \times 10^{-1}(c/\xi)$. The solitary wave is initially stationary, oriented at an angle $\theta = -45^0$ to the y-axis, with its centre located at $(x_0, y_0) = (5\xi, 0)$. The snapshots correspond to times of (i) $t = 0$, (ii) 4, (iii) 8, (iv) 14, and (v) 20 (ξ/c). The boxes represent the region $[-20, 20]\xi \times [-2, 2]\xi$.

vortex phase profile we have generated so far).

Weakly non-axisymmetric regime

For weakly non-axisymmetric traps, i.e. away from the quasi-1D regime, we find that the wave undergoes the snake instability. For $\theta = 0$, the GPE predicts that a dark solitary wave can only decay into products which are symmetric about the x-axis, and so symmetric vortex rings (in 3D) or pairs (in 2D) and sound excitations are generated, as discussed in chapter 3. Note, however, that in a real environment effects exist which can break this symmetry, e.g. thermal and quantum fluctuations. We can dynamically break this symmetry

by introducing the dark solitary wave at an angle. For $\theta \neq 0$, we observe that the snake instability results in the generation of single vortices and/or vortex pairs (which are the 2D analogs of vortex rings), with no axis of symmetry in the 2D plane. Similar combinations have been considered in [163, 205]. Note that for a trap geometry which is close to the quasi-1D regime, we find that the snake instability of the tilted solitary wave leads to the generation of a single vortex.

Strongly non-axisymmetric regime

For the purpose of this discussion we are concerned with the dynamics in the opposite extreme of a condensate in the strongly non-axisymmetric, quasi-1D regime. Figure 9.5 illustrates the evolution of a dark solitary wave which is initialy tilted at an angle of $\theta = -45^0$, under a trap geometry which is the same as in figure 9.4. The key observation is that the solitary wave evolves in a similar manner to the vortex state in figure 9.5. The initial solitary wave (case(i)), tilted anti-clockwise, cycles to a state where the solitary wave is tilted in the opposite sense (case(iii)), and back again (case(v)). In between, vortex-like states of alternate charge appear (case(ii) and case(iv)). The period of this cycle is the same as for the vortex case in figure 9.4. Therefore, the tilted dark solitary wave also exists in the svortex state.

Although the initial angle of the solitary wave is $\theta = -45°$, the angle does not reach this magnitude again, and subsequently rotates with an amplitude of approximately 10°. This is a general feature when the tilt angle is greater than $\theta \sim 10°$, and suggests that there is a maximum tilt angle which can be excited. When the initial tilt angle is less than this, the amplitude of the tilt mode remains of the order of the initial tilt angle. Note that, following any initial decay, the tilt amplitude does not appear to decay over time.

9.3 Dynamics of svortices

We have so far demonstrated that a vortex and tilted black solitary wave in a quasi-1D condensate evolve into a hybrid excitation corresponding to a svortex, and have illustrated the appearance of this state in terms of its time-dependent

density and phase profile. We now briefly comment on the dynamics of svortices.

Strongly non-axisymmetric system

We first consider the behaviour of svortices in a strongly non-axisymmetric, quasi-1D condensate. Figure 9.6(a) shows the longitudinal path of two svortices corresponding to an initial vortex state (solid line) and initial tilted black solitary wave (dashed line). Both excitations are initially located at $(x_0, y_0) = (5\xi, 0)$. For comparison, the corresponding trajectory of an initially plane ($\theta = 0$) black solitary wave is also shown (dotted line). All three trajectories are similar, and consist of a sinusoidal oscillation in the trap, plus modulations due to interaction with excitations of the background fluid. It is likely that the three states have the same basic dynamics, but feature different modulations to the different levels to which the background fluid is excited. The modulation is largest for the initial vortex state since the decay of the initial vortex circulation transfers the most energy to the backgroud fluid modes. On the other hand, the plane ($\theta = 0$) dark solitary wave features the smallest modulation since it only excites and interacts with fluid modes which are symmetric about the $y = 0$ axis.

The Fourier spectra of the longitudinal trajectories are shown in figure 9.5(b). This corresponds to the magnitude of the complex Fourier transform of equation (5.4). The frequency components are virtually indistinguishable, with all three excitations oscillating in the trap at approximately $\omega_x/\sqrt{2}$ and interacting with the main fluid mode at a frequency ω_x. We have considered these dynamics for trap ratios as high as $\gamma = 40$. This restricts the excitation of rotational fluid modes, such that there is less back action on the svortex, and we observe that the trajectory of the svortex becomes even closer to that of the plane ($\theta = 0$) dark solitary wave.

If the vortex state/tilted black solitary wave is initially located at the centre ($x = 0$) of the trap, a svortex is generated which remains stationary at the trap centre.

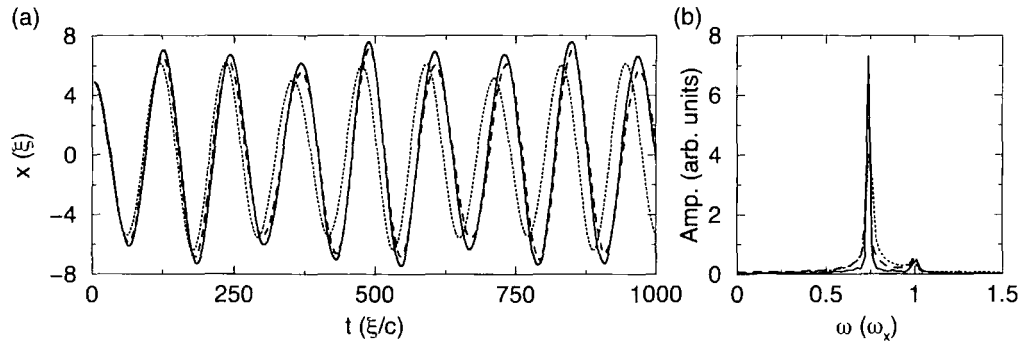

Figure 9.6: (a) Longitudinal trajectory of an initially imprinted vortex (solid line), tilted black solitary wave (dashed line), and untilted black solitary wave (dotted line) in a strongly non-axisymmetric harmonic trap. The excitations are created off-centre at $(x_0, y_0) = (5\xi, 0)$. The trap geometry is the same as in figures 9.4 and 9.5. (b) Fourier spectrum of the trajectories, with frequency rescaled in terms of the longitudinal trap frequency ω_x. This corresponds to the magnitude of the complex Fourier transform of equation (5.4).

Longitudinally homogeneous system

In addition to having harmonic confinement in the x-direction, we have also considered the longitudinally homogeneous system $\omega_x = 0$, and find consistent behaviour. The vortex/tilted black solitary wave evolves into a svortex which behaves dynamically as a black solitary wave, remaining stationary due to the absence of a longitudinal force. An interesting effect occurs if the tilted black solitary wave is almost, but not quite, aligned with the x-axis ($\theta \sim 90^0$). The wave then evolves into a central stationary svortex, and two fast counter-propagating ones.

If the initial tilted solitary wave is no longer black (stationary) but is a moving dark solitary wave solution, a moving svortex is generated which propagates with constant speed. Using this method, we have simulated the collisions of svortices. We observe that they propagate through each other with no change in shape or speed, just as occurs for plane ($\theta = 0$) dark solitary waves. Note that if a svortex and plane dark solitary wave collide, they also propagate through unaffacted; in particular the plane dark solitary wave does not appear to develop any rotational motion from the svortex.

9.4 Summary

In this chapter we have probed the motion of a single vortex in a quasi-2D non-axisymmetric condensate using the 2D GPE. For weakly non-axisymmetric geometries, the vortex precesses around the trap centre in an elliptical path, with the precession frequency increasing with the trap ratio. At some critical trap ratio, which is associated with the condensate becoming quasi-1D in nature, the 'vortex' undergoes longitudinal oscillations in the trap, with the oscillation frequency saturating to a value of around $\omega_x/\sqrt{2}$. In this regime, the vortex is no longer supported, and exists in the form of a solitonic vortex, or svortex. This excitation represents a hybrid vortex-soliton state, and we observe that the density and phase profile cycles continuously between a vortex (node in the density, azimuthal 2π-phase slip) and a tilted dark solitary wave (tilted stripe of low density and phase step). This state can also be generated from a dark solitary wave in a quasi-1D system, providing the wave is oriented at an angle to the longitudinal axis. This breaks the usual longitudinal symmetry axis of the solitary waves, and enables it to couple to rotational modes in the system.

It is important to point out that our proposed svortex state differs in several respects from that of Brand *et al.* [163, 164]. Whereas the svortex of Brand *et al.* has the phase profile of a vortex throughout, our state cycles between a vortex and tilted step-wise phase profile. Also, Brand *et al.* find no stationary svortex solution below a critical transverse width, whereas we observe that the svortex can exist up to very large transverse confinements. However, direct comparison between our results is perhaps limited. Brand *et al.* concentrate on a system with hard wall transverse confinement and seeded with white noise, whereas our system features harmonic transverse confinement and no added noise.

A further test could be to measure the phase-velocity relation of our svortex, and compare to Brand *et al.*'s findings. A dark solitary wave has a velocity given by $v = A\cos(S/2)$, where S is the longitudinal phase offset and the coefficient A is equal to the Bogoluibov speed of sound c. Brand *et al.* predict that a svortex obeys a similar phase-velocity relation, but where $A < c$.

The dynamical properties of our svortex are essentially identical to those of a plane dark solitary wave. In a harmonic trap, the svortex oscillates back and

forth at a close to the soliton frequency of $\omega_x/\sqrt{2}$. In a homogeneous system, a moving svortex propagates with constant speed, and, under the collision of svortices with each other or a dark solitary wave, the states emerge with unchanged form.

These dynamics should all be experimentally observable. To generate the initial vortex states, topological phase imprinting [94, 95] would seem the most relevant method. Not only is it the closest experimental match to our numerical phase imprinting method, but other methods, such as the rotation of the condensate, are not expected to work in strongly non-axisymmetric condensates [252]. Dark solitary waves have been produced in BEC by optically imprinting an axisymmetric step-like phase profile [74, 75, 76] and by the sudden removal of an axisymmetric disk-shaped region from the condensate [77]. Production of a tilted dark solitary wave would simply require the orientation of these methods to be non-axisymmetric. In order to distinguish a svortex from a dark solitary wave or a vortex, an experiment could look for the characteristic cycling of the density and phase profile between vortex and soliton states. The cycling of the density profile (from a node of zero density to a stripe of low density and back again) may not be large enough to detect. However, it should be possible to observe the evolving phase distribution (from 2π azimuthal vortex phase slip to a linear solitonic phase step) using an interferometric technique. In this method, the condensate is interfered with either an unperturbed condensate, or itself (after being separated into two parts), leading to an observable fringe pattern. A vortex appears as fringe dislocation [105, 264], with its form indicating the sign and magnitude of the vortex charge, while a linear phase slip would appear as a band of closely spaced fringes. Although this method is destructive, the experiment can be repeated with the interferometric technique employed at successive times in order to map out the time evolution of the phase profile.

An important point is that we have shown how a vortex can be reduced to soliton-like excitation. A dark soliton is indeed a 1D analog of a vortex, and they can be coupled together in a hybrid excitation known as a solitonic vortex.

Chapter 10

Future work

In this thesis we have considered the dynamical stability of vortices and dark solitary waves in dilute Bose-Einstein condensates. Both entities are inherently unstable to acceleration, leading to the emission of sound waves. Since confined BECs are finite-sized, the sound waves are forced to reinteract with the macroscopic excitation, such that sound reabsorption can occur. The interaction of the macroscopic excitation with the sound field of the condensate, both in emission and reabsorption, is therefore the key feature in the dynamics of vortices and dark solitary waves at zero temperature. Here we list some ideas for future work which could shed more light onto these effects. In sections 10.4 and 10.5 we present two ideas for future work in detail and present some preliminary results.

10.1 Dark solitons

Nature of sound reabsorption in confined systems

A dark soliton radiating sound waves in a finite-sized condensate is forced to reinteract with emitted sound. In the absence of other dissipation mechanisms, a soliton oscillating in a harmonic trap is completely stabilised by sound reabsorption. However, in a harmonic trap perturbed by an optical lattice, or a shallow dimple within an ambient harmonic trap, the reabsorption of the sound is only partial. We attribute this to the sound modes having become modified

by the additional features in the trap, such that it becomes partially 'invisible' to the soliton. We know, for instance, that the presence of an optical lattice can significantly modify the sound spectrum of a condensate [235].

In chapter 6 we pumped energy into a dipolar motion of the sound field, and observed periodic transfer of energy into the soliton, with the direction of transfer appearing to be linked to the relative phase of the soliton and the dipole mode in the trap. However, we do not understand the true mechanism of sound reabsorption by the dark soliton, and this requires further investigation. One could begin by studying the interaction of a dark soliton with an isolated sound pulse in an homogeneous system.

Interactions between solitons

This work has only considered systems featuring a single dark soliton. The head-on collisions of dark solitons have been investigated in an homogeneous system [220]: the solitons pass through each other in a non-dissipative manner, with the only effect being that the solitons experience a shift in their position. However, the interaction between solitons in a harmonically-confined condensate have, to our knowledge, not been considered, although the dynamics would seem, at first glance, to be rich. The oscillating solitons will collide not just once, as in the homogeneous case, but many times. The combined effect of many collisions may lead to the build up of significant effects, such as the shift in their position. The equilibrium that we have observed between a single soliton and the sound field in a harmonic trap must surely be modified by the presence of another soliton. Do the solitons only reinteract with their own emitted sound, or interact with each others? If the latter case is true, then it may be possible to couple two dark solitons together via their sound interactions.

Creation of dark solitons via parametric driving

In chapter 6 we considered the parametric driving of a soliton in a harmonically-confined condensate. Oscillating gaussian paddles were employed to pump energy into the system by driving a dipolar motion of the background fluid. Under suitable drive parameters, this process led to a significant amount of energy being transferred into the soliton. However, for vigorous pumping we observe an

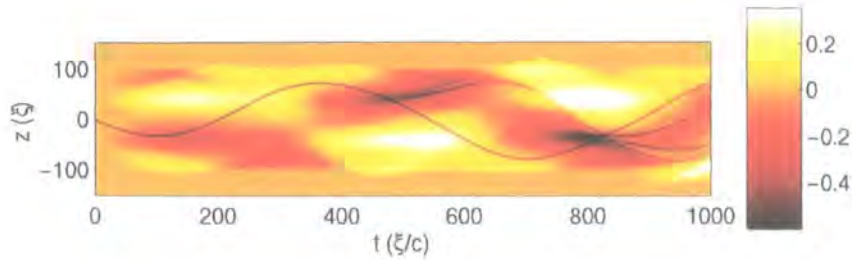

Figure 10.1: Space-time plot of renormalised density (actual density minus time-independent background density) for a $v_0 = 0.5c$ dark soliton in a harmonic trap under vigorous parametric driving according to equation 6.1. The trap frequency is $\omega_z = \sqrt{2} \times 10^{-2}(c/\xi)$ and the drive parameters are $\alpha = 0.3\mu$, $w_0 = \sqrt{500}\xi$, $z_0 = 90\xi$, and $\omega_D = 0.98\omega_{sol}$.

extra effect whereby the driven sound field generates additional moving dark solitons in the system. This effect was only briefly mentioned in the chapter 6 due to the lack of results. However, it is clearly an interesting effect and requires more investigation. Figure 10.1 shows a space-time density plot of the system. Two dark solitons are generated clearly, in addition to the initial soliton, during the evolution. The effect appears to be analogous to the creation of vortex rings when an obstacle is dragged through a superfluid above a critical velocity [60, 105]. This is due to a build up of a phase slip in the region of the obstacle, which is ultimately shed in the form of a vortex ring. In the soliton case, large phase slips may be set up by the large driven dipole mode, which then leads to the formation of dark solitons. Although our system initially contains a dark soliton, the spontaneous creation of dark solitons from an initial soliton-less condensate may be possible. Note that trains of dark solitons are predicted to form from a time-dependent obstacle in a condensate [134, 135, 136].

10.2 Vortices

Multiple vortices in a dimple trap

We have analysed the sound emission from a single vortex precessing in a dimple trap, where the acceleration is driven by the inhomogeneous density, and from a corotating pair in a homogeneous system, where the acceleration is driven by

the interacting velocity fields. One could consider a corotating pair located in a dimple trap, where the combined accelerative effects may lead to considerable sound emission. Indeed, the number of vortices could be further increased so as to probe the regime of vortex lattices. As more vortices are added, one could examine how the power emission from the structure scales with the number of vortices. For large numbers of vortices, one may be able to draw information on the crystallisation of vortex lattices.

Vortex tangles

In turbulent states of Helium II, the superfluid component is thought to take the form of a disordered array of vortices and vortex rings, known as a vortex tangle [27, 80]. Even at very low temperatures, where thermal friction is negligible, it is found that vortex tangles in Helium II decay rapidly [86]. Processes such as reconnections [87], vortex line excitations [88], and acceleration of the vortex lines [153] are predicted to lead to the dynamical (zero temperature) dissipation of the vorticity via sound emission. Although it cannot describe the full physics of strongly-interacting Helium II, the GPE describes such effects on a weakly-interacting level. In this thesis we have considered the radiative dynamics of up to three vortices in 2D system. Work is needed however to analyse and quantify the sound emission from a large number of disordered vortices. Although the GPE is computationally demanding, one could realistically consider the evolution of a system containing, say, tens of vortex lines and/or vortex rings. Although this is a very small-scale representation of a vortex tangle, it could still give useful information of the general behaviour of such states. Such mini-tangles are a realistic prospect in dilute BECs - single vortices can be created by phase imprinting, and vortex rings can be generated in the decay of a dark solitary wave and by dragging a laser obstacle through the condensate.

10.3 Vortex-antivortex pairs and rings

Vortex-antivortex pairs and vortex rings are solitary wave solutions to the homogeneous 2D and 3D GPE, respectively [208, 209]. They are solutions in the moving frame, and bear analogy to dark soliton solutions in 1D. We therefore

expect them to be unstable to acceleration, in a similar manner to dark solitons (see chapters 4 and 5). In chapter 8 we considered the interaction of a vortex-antivortex pair with a single vortex in a homogeneous 2D system. The acceleration of the vortices during the interaction, due to their mutual velocity fields, induced the emission of sound waves and the decay of the vortex-antivortex pair. The presence of the third vortex, however, limited the quantitative information we could derive about the decay of the vortex-antivortex pair. A better method of analysing the dynamical dissipation of the pair would be to accelerate it by means of an inhomogeneous local density, e.g. in the presence of a ramp potential, in an otherwise homogeneous system such that sound reinteraction is not a consideration. This would allow the power emission from the pair to be examined in terms of the acceleration of the pair. One could then compare results to the acceleration-squared laws for the power emission for an isolated dark soliton and vortex in an inhomogeneous system.

10.4 Dark solitons and vortices in anharmonic traps

In chapters 5 and 7 we have shown that a vortex/soliton accelerating in a harmonic trap radiates sound waves, which are subsequently focussed back into the vortex/soliton, such that the decay is stabilised (in the absence of other dissipation mechanisms). However, certain modifications to the pure harmonic trap, e.g. the presence of an inner dimple, or the addition of an optical lattice potential, can lead to only partial sound reabsorption, and therefore a net decay of the vortex/soliton. An additional feature of dark solitons is that they reflect elastically from hard walls (no sound emission), and so we can expect a dark soliton in a square-well trap to be stable. However, Radouani has investigated a dark soliton oscillating in a square-like trap with non-hard-walls, and observes sound emission and an overall decay of the soliton [265]. An obvious question is whether dynamical stabilisation of the soliton/vortex by sound reabsorption is particular to harmonic traps, and whether solitons/vortices are generically unstable in anharmonic traps geometries. In this chapter, we present some results which suggest that this is indeed the case. However, this topic requires

further investigation for a complete analysis.

10.4.1 Dark soliton in a gaussian trap

Gaussian traps are formed in the cross-section of an off-resonant laser beam and are now commonly used to confine atomic BECs. We consider the gaussian trap here since it allows control over the degree of anharmonicity in the system. For example, a 1D gaussian trap can be expressed as

$$V(z) = V_0\left[1-\exp\left(\frac{-\omega_z^2 z^2}{2V_0}\right)\right] \tag{10.1}$$

$$= \frac{1}{2}\omega_z^2 z^2 + V_0\left[\frac{1}{2}\left(\frac{\omega_z^2 z^2}{2V_0}\right)^2 - \frac{1}{3}\left(\frac{\omega_z^2 z^2}{2V_0}\right)^3 + ...\right], \tag{10.2}$$

where we have expanded the exponential term using the Taylor series. The leading term in the series is harmonic, with trap frequency ω_z, while the higher order terms are anharmonic. If ω_z is kept constant, then the depth of the trap V_0 controls the degree of anharmonicity experienced by the condensate. In the limit $V_0 \gg \mu$, the confinement seen by the condensate is effectively harmonic. Away from this regime the higher-order terms contribute and the trap becomes anharmonic. Note that the anharmonic terms give most contribution at the edge of the system.

Effect of trap depth

We first consider the dynamics of a soliton in a gaussian trap for various depths V_0. The effective harmonic frequency is constant throughout at $\omega_z = 2\sqrt{5} \times 10^{-2}(c/\xi)$, as is the initial soliton speed of $v = 0.5c$. Figure 10.2(a) shows the density profiles for the various values of the trap depth. For $V_0 = 5\mu$ (black lines), the trapping is effectively harmonic, while in the opposing limit, for $V_0 = 1.5\mu$ (blue lines), the trapping clearly deviates from harmonic. The path and energy of the soliton for the various trap depths are shown in figure 10.2(b) and (c). For $V_0 = 5\mu$ (black lines), the soliton oscillates with, on average, constant amplitude and energy, i.e. no net decay. This is the regime of the harmonic trap, where complete sound reabsorption stabilises the soliton decay (this regime is discussed in chapter 5).

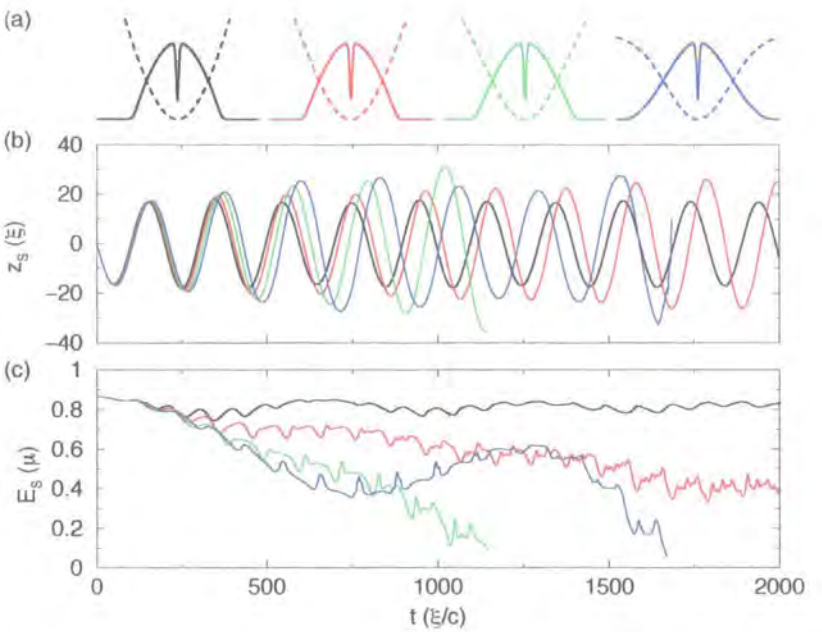

Figure 10.2: Dynamics of a dark soliton, with initial speed $v = 0.5c$, in a gaussian trap with effective harmonic frequency $\omega_z = 2\sqrt{5} \times 10^{-2}(c/\xi)$ and depths $V_0/\mu = 5$ (black lines), 3 (red lines), 2 (green lines), and 1.5 (blue lines). (a) Profiles of the initial density (solid lines) and potential (dashed lines). (b) Soliton path z_s. (c) Soliton energy E_s.

For $V_0 = 3\mu$ (red lines), we observe a slow increase in the soliton oscillation amplitude and decrease in the soliton energy. For $V_0 = 2\mu$ and 1.5μ, the soliton decay is more rapid. We attribute this to the increasingly anharmonic nature of the system. Here the ultimate fate of the soliton is complete dissipation, whereby it disappears into the sound field.

Note that for $V_0 \sim \mu$, sound waves can escape the gaussian trap, and so we only probe down to $V_0 = 1.5\mu$. For this trap depth, the decay features a slight revival at $t \sim 700(\xi/c)$, which is most evident in the evolution of the soliton energy (figure 10.2(c)). This is due to the complicated interaction of the soliton with the sound field, and indicates that sound reabsorption still occurs in the system. However, the reabsorption is, on average, only partial, and so the soliton ultimately decays completely away.

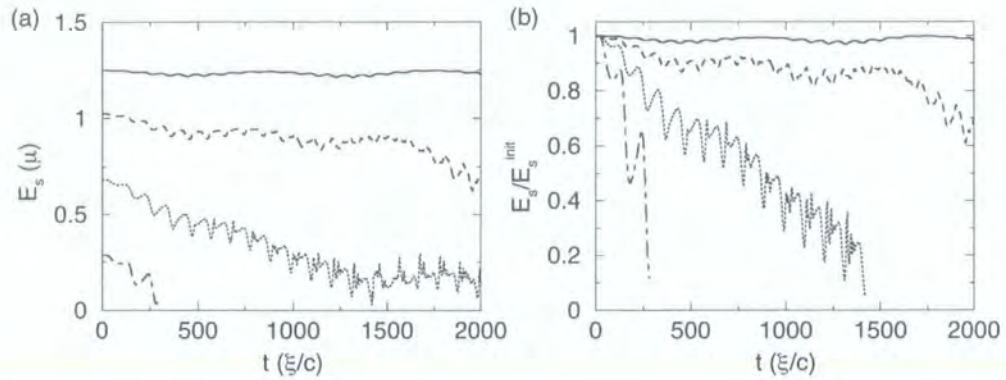

Figure 10.3: (a) Energy of a dark soliton in a gaussian trap with $\omega_z = 2\sqrt{5} \times 10^{-2}(c/\xi)$ and $V_0 = 3\mu$, for initial soliton speeds $v/c = 0.2$ (solid line), 0.4 (dashed line), 0.6 (dotted line), and 0.8 (dot-dashed line). (b) Same plot as (a) apart from the soliton energy E_s being rescaled in terms of the initial soliton energy E_s^{init}.

Effect of soliton speed

The anharmonicity in the gaussian trap has the greatest effect towards the edge of the condensate. Therefore, one would expect faster solitons to be more prone to these effects, since they probe further out from the trap centre. In order to investigate the speed dependence of this instability, figure 10.3 shows the evolution of the soliton energy in a fixed gaussian trap for various soliton speeds.

The slowest soliton, with initial speed $v = 0.2c$ (solid line), is localised in the central region of the trap which is dominantly harmonic. It features no decay. However, for initial speed $v = 0.4c$ (dashed line), we see a slow decay of the soliton due to the trap anharmonicity probed in its motion. For faster initial solitons, e.g. $v = 0.6c$ (dotted line) and $0.8c$ (dot-dashed line), the soliton decay becomes more rapid, as the soliton probes relatively strong anharmonic regions towards the edge of the trap.

10.4.2 Vortex in a gaussian trap

We consider a vortex in a 2D condensate confined by a gaussian trap. The trap is radially-symmetric and has the form of equation (10.2) under the substitutions

$z \to r$ and $\omega_z \to \omega_r$.

Effect of trap depth

Figure 10.4 shows the dynamics of a vortex in the gaussian trap for various trap depths. In each case, the vortex is initially off-centre at position $(x_0, y_0) = (6\xi, 0)$, and the effective trap frequency is kept fixed at $\omega_r = \sqrt{2} \times 10^{-1}(c/\xi)$. The initial density profiles (in the x-direction) are shown in figure 10.4(a). For $V_0 = 4\mu$ (black lines), the trapping is effectively harmonic, and as the trap depth is decreased through $V_0 = 2\mu$ (red lines), 1.5μ (green lines), and 1.3μ (blue lines), the confinement becomes increasingly anharmonic.

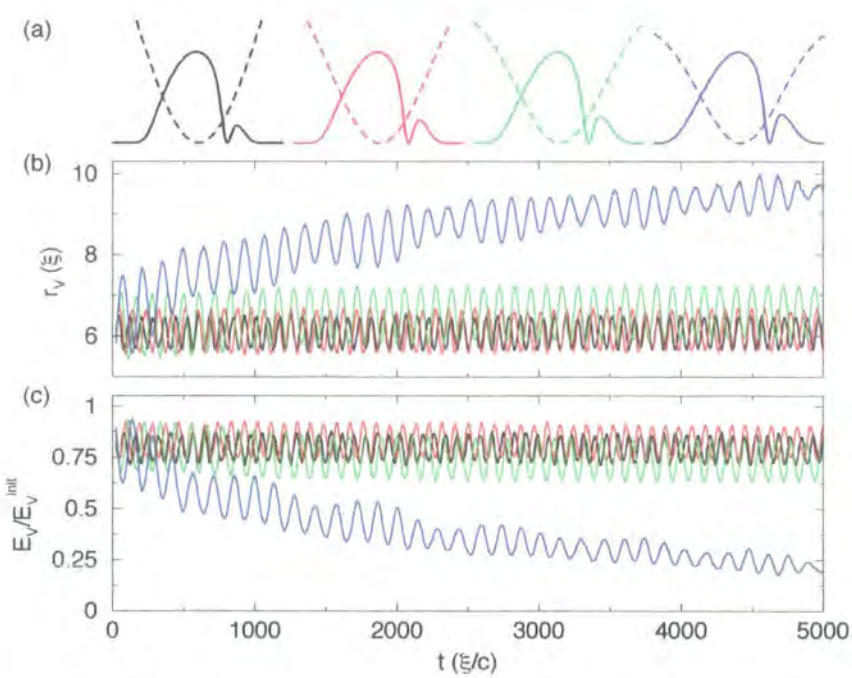

Figure 10.4: Dynamics of a vortex, with initial position $(x_0, y_0) = (6\xi, 0)$, in a gaussian trap with $\omega_z = \sqrt{2} \times 10^{-1}(c/\xi)$ and various depths $V_0/\mu = 4$ (black lines), 2 (red lines), 1.5 (green lines), and 1.3 (blue lines). (a) Profiles in the x-direction of the initial density (solid lines) and potential (dashed lines). (b) Vortex radius r_V. (c) Vortex energy E_V, rescaled in terms of the initial vortex energy E_V^{init}.

The evolution of the vortex radius and energy are shown in figure 10.4(b) and (c). For $V_0 = 4\mu$ (black lines) and $V_0 = 2\mu$ (red lines), the precessing vor-

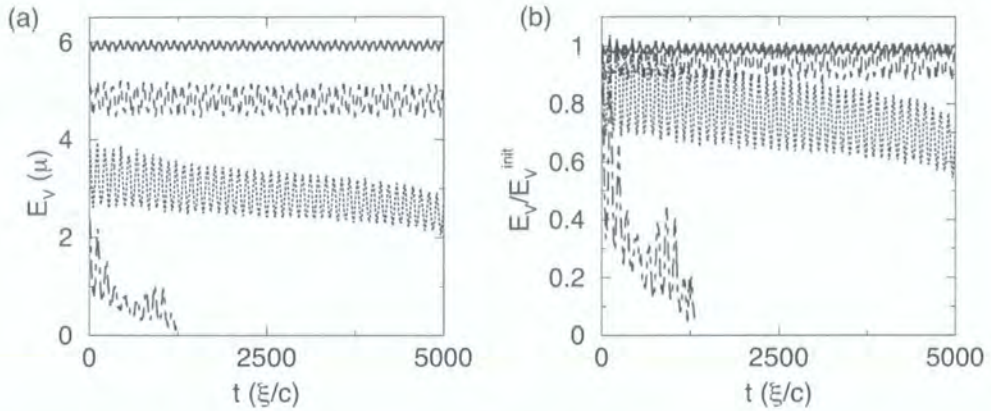

Figure 10.5: Evolution of the vortex energy in a gaussian trap with $\omega_z = \sqrt{2} \times 10^{-2}(c/\xi)$ and $V_0 = 2\mu$, for the vortex at initial radii $r_0/\xi = 2$ (solid line), 4 (dashed line), 6 (dotted line), and 8 (dot-dashed line). The TF radius of the condensate is $R_{\rm TF} = 10\xi$. The vortex energy $E_{\rm V}$ is rescaled in terms of the initial vortex energy $E_{\rm V}^{\rm init}$.

tex maintains, on average, the initial radius and energy, indicating no decay. Here the condensate experiences trapping which is effectively harmonic, and full sound reabsorption occurs. However, for $V_0 = 1.5\xi$ (green lines), the anharmonic terms start to have an effect and induce a very slight decay in the vortex, while for $V_0 = 1.3\mu$ (blue lines), the trap anharmonicity becomes significant and leads to a relatively rapid vortex decay.

Effect of vortex position

Since the trap anharmonicity has a greater effect towards the edge of the condensate, the vortex instability should be sensitive to the position of the vortex in the trap. Figure 10.5 shows the evolution of the vortex energy in a fixed gaussian trap for various initial radii of the vortex. When the vortex is initially located close to the centre of the trap, e.g. $r_0 = 2\xi$ (solid line) and 4ξ (dashed line), the vortex shows no signs of decay (or at least it is too slow to observe on these timescales). However, for $r_0 = 6\xi$, the vortex undergoes gradual decay, and for $r_0 = 8\xi$ the vortex rapidly decays completely away (disappears at the condensate edge into the sound field).

10.4.3 Dark solitons and vortices in other anharmonic traps

We have investigated the dynamics of dark solitons and vortices in other forms of anharmonic trapping, and this is summed up below.

Harmonic trap plus quartic term

Positive quartic contributions to a harmonic trap have been generated experimentally using a laser beam [266]. For weak perturbations to the harmonic trap we do not observe soliton/vortex decay. However, where the quartic term dominates, we find the same effect as in a pure quartic trap (see below).

Harmonic trap minus quartic term

These dynamics are similar to the case of a gaussian trap. When the perturbation affects the trapping potential in the region of the condensate, we observe soliton/vortex decay. The decay rate increases with the size of the perturbation, and the extent to which to soliton/vortex probes the trap anharmonicity. Note that when the quartic term becomes larger than some critical value, the condensate is no longer confined.

Pure quartic trap

Quartic traps can be generated by a combination of magnetic and optical traps [266]. We find that the soliton/vortex tends to undergo decay when it probes past some critical radius of the condensate, but does not decay otherwise.

Linear trap

We have simulated the dynamics of a dark soliton/vortex in a linear/cone-shaped trap, and generally observe complete decay of the soliton/vortex.

Preliminary results presented here suggest that the equilibrium between a dark soliton/vortex and the sound field in a confined system can become broken when the trap is anharmonic and the soliton/vortex probes the anharmonic re-

gion. The sound reabsorption then becomes only partial, and the soliton/vortex undergoes net decay, ultimately disappearing into the condensate sound field. This effect is most prevalent when the harmonic trap becomes *weakened* by the anharmonic perturbation. The physical mechanism that controls the level of sound reabsorption in the system is not clear, nor why harmonic traps are unique in focussing all the emitted energy back into the soliton/vortex. One possibility is that trap anharmonicities modify, or dephase, the emitted sound waves such that they are can not be fully reabsorbed. For example, in the parametric driving of a dark soliton in a harmonic trap (chapter 6) the relative phase between the soliton and dipole mode appears to play a crucial role in governing the loss or gain of sound energy by the soliton. The wavelength of the emitted sound in relation to the size of the system may also be a relevant consideration. For example, sound emission from a vortex in a purely harmonic trap has been predicted to be prohibited due to the wavelength of the sound being larger than the system itself [64, 152]. In order to understand fully the zero temperature dynamics of a dark soliton and vortex in a trapped condensate, this process has to be resolved.

10.5 Interaction of a vortex with plane sound waves

An important consideration is the interaction of a vortex with sound excitations which will typically be present in a confined BEC at zero temperature. We have demonstrated in the previous section that emitted sound can be reabsorbed to different degrees, but the mechanism of sound absorption is not clear. Here we present some qualitative findings on the interaction of a vortex with plane sound waves in a 2D homogeneous system.

Analog of the Aharonov-Bohm effect

This situation has interesting analogies with the Aharonov-Bohm effect, first proposed in 1959 [267]. They considered an electron beam incident normally on an impenetrable infinitely-long cylinder enclosing a magnetic field along its length, with no field existing outside the cylinder. Although the electron beam

experiences no magnetic force, the vector potential induces a dislocation in the electron wavefronts, although this cannot be observed. Berry showed that an analogous effect occurs in acoustics for water waves incident on an irrotational vortex [268], allowing easy observation of the wave dislocations.

Since the gradient of the phase in a fluid represents a momentum, the phase slip induced in a wavefront by a vortex will generate a force on the vortex, known as the Iordanskii force [269]. In Helium II, this force is expected to contribute substantially to the mutual friction between the superfluid and normal component [27].

Recently, Leonhardt and Öhberg predicted that the illumination of a vortex in a dilute BEC with slow light results in the optical analog of the Aharonov-Bohm effect [270, 271]. Furthermore, this is expected to generate an optical Iordanskii force on the vortex, causing it to to spiral towards the incident light in a manner which could be probed experimentally. This is in contrast to the magnetic Aharonov-Bohm effect, in which the magnetic vortex remains fixed.

Interaction of a vortex with plane sound waves

Here, we investigate the sonic analog of the Aharonov-Bohm effect by considering plane sound waves incident on a vortex in a 2D homogeneous condensate. This has also been considered by Pitaevskii [272] and Fetter [273].

The plane sound waves are generated by an oscillating one-dimensional gaussian paddle, with the form,

$$V_{\mathrm{P}} = A\left[1 - \cos\left(\omega_{\mathrm{p}} t\right)\right] \exp\left[\frac{-(y + y_{\mathrm{p}})^2}{\sigma^2}\right], \tag{10.3}$$

where A is the paddle amplitude, y_{p} is its y-coordinate, σ is its width, and ω_{p} is the frequency at which the paddle oscillates. We expect the vortex-sound interaction to be maximised when the lengthscales of the vortex and sound are comparable, i.e. when the wavelength of the sound is of the order of the size of the vortex. Here we take $A = 0.04\mu$, $\sigma = \sqrt{5}\xi$ and $\omega_{\mathrm{p}} = 0.2\pi(c/\xi)$. This drives a 1D oscillatory sound pulse, propagating in both the positive and negative y-directions, with amplitude $\sim 0.2n_0$ and wavelength $\sim 10\xi$. A singly-quantized vortex is located at the origin, while the paddle lies along the line $y_{\mathrm{p}} = -50\xi$.

We compare the interaction of the sound wave with the vortex to the interaction with a vortex-shaped obstacle. This allows us to resolve the effect of the circulating fluid on the interaction. We employ an obstacle potential of the form $V(r) = 1/2r^2$. The radial density profile induced by this obstacle potential is compared to that of a singly-quantized vortex in figure 10.6, and we find extremely good agreement.

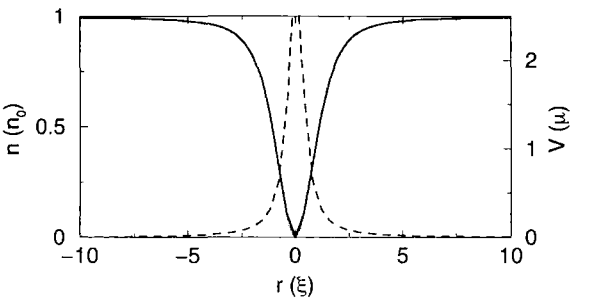

Figure 10.6: Radial density profile in the presence of a vortex (left axis, solid grey line) and an obstacle of the form $V(r) = 1/2r^2$ (left axis, solid black line). The potential of the obstacle is also shown (right axis, dashed line).

Continuous sound pulse

We first consider the case where the sound pulse is effectively continuous. From some initial time the paddle is set to oscillate continuously. This generates a train of plane oscillatory sound pulses incident on the vortex, with approximately constant amplitude and wavelength. At the front of the train, the sound waves tend to disperse slightly, although this has a negligible effect on the findings.

Figure 10.7(a) shows the density profile in the region of the vortex during the interaction with the continuous sound pulse. The pulse, travelling in the positive y-direction, propagates through the vortex. We see a clear dislocation, or phase shift, in the outcoming wave along the $x = 0$ axis. The dislocation induces a phase difference in the wavefronts of approximately half an oscillation. This is characteristic of the Aharonov-Bohm effect. A similar picture is observed experimentally in water for waves incident on an irrotational vortex [268, 274, 275]. Additionally, we see signs of a scattered sound wave propagating radially outwards from the vortex.

The interaction of a continuous sound pulse with a vortex-like obstacle is illustrated in figure 10.7(b). Here the sound waves propagate through the vortex with no phase dislocation. There is a scattered wave produced during the interaction, although it is too small in amplitude to be observed in this figure.

The creation of the phase dislocation when the plane sound waves interact with the vortex represents a momentum transfer. In order to conserve the momentum, one might expect the vortex to be set into motion. Such motion has been predicted for a vortex in a BEC incident with slow light [271], which is expected to spiral towards the incoming waves. However, we do not observe any motion of the vortex. We have varied the amplitude and wavelength of the incident sound, and illuminated the vortex for very long periods of time, yet the vortex remains fixed in position at all times.

Finite sound pulse

In order to observe clearly the outgoing waves following the vortex-sound interaction, we now consider a finite sound pulse, rather than a continuous one. We terminate the oscillating paddle after one full oscillation such that a short-length sound pulse is incident on the vortex. Figure 10.7(c) shows the density distribution following the interaction of the sound pulse with the vortex. Again, we see the dislocation of the transmitted plane waves. Importantly, we now clearly observe the scattering wave propagating on the unperturbed background. The scattered waves are not radially symmetric but have a spiral nature. This explains why we do not see a motion of the vortex: the phase dislocation of the transmitted wave is balanced by a phase shift in the scattered wave.

The interaction of the same sound pulse with the vortex-like obstacle is shown in figure 10.7(d). As would be expected we observe that the majority of the pulse transmits through the vortex, with a small component being scattered radially outwards. The amplitude and wavelength of this scattered wave is similar to that scattered by a vortex.

In this final section we have briefly investigated vortex-sound interactions by considering plane sound waves incident on a stationary vortex. This is the sonic analog of the Aharonov-Bohn effect. The sound wave becomes partially transmitted and partially scattered. The transmitted waves feature a dislocation in

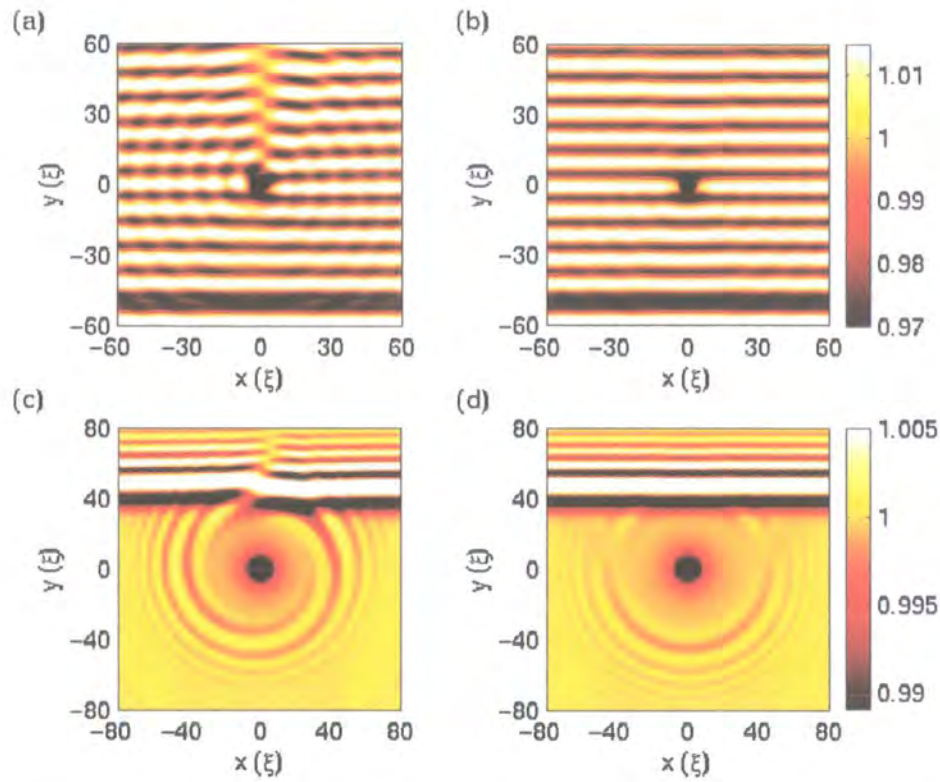

Figure 10.7: (a)-(b) A continuous train of plane sound waves interacting with (a) a vortex and (b) the potential $V = 1/2r^2$ which induces a vortex-like density profile, interacting in a 2D homogeneous system. (c)-(d) A burst of plane sound waves interacting with (c) a vortex and (d) the vortex-like potential. The plane sound waves propagate in the positive y-direction, and are produced by the oscillating paddle of equation (10.3) with $A = 0.04\mu$, $\sigma = \sqrt{5}\xi$, $\omega_P = 0.2\pi(c/\xi)$ and $y_P = -50\xi$. In (c)-(d) the paddle is terminated after one full oscillation.

the wavefronts, while the scattered wave is not radially symmetric but has a spiral appearance. The phase modifications serve to cancel each other out, and the vortex does not gain any momentum.

10.6 Summary

In this chapter, we have listed some ideas for future work. These ideas relate to the *creation* of sound waves by dark solitons and vortices, and the *interaction* of sound waves with dark solitary waves and vortices. In the final sections,

we presented some preliminary results on the dynamics of dark solitons and vortices in anharmonic traps and the interaction of a vortex with plane sound waves.

Chapter 11

Conclusions

In this thesis we have studied the zero-temperature dynamics of vortices and dark solitons in dilute atomic Bose-Einstein condensates. This has been performed by means of numerical simulation of the Gross-Pitaevskii equation. Even in the absence of external (e.g. thermal) dissipation these macroscopic excitations are prone to dynamical instabilities, which typically involve the emission of small-amplitude density perturbations in the form of sound waves.

A dark soliton is strictly a *one-dimensional* solution, and when embedded in a three-dimensional system as a dark solitary wave, is prone to a transverse dynamical instability whereby the soliton plane becomes bent and torn into vortex structures and sound. This is analogous to the snake instability of dark solitons in nonlinear optics. However, in quasi-one-dimensional geometries this decay mechanism is suppressed, and the soliton behaves as a one dimensional object.

A dark soliton is additionally a solution only in a *homogeneous* system. This renders the soliton unstable to longitudinal motion through the inhomogeneous density of trapped condensates. By considering the interaction of a dark soliton with various forms of potential, e.g. steps, ramps and harmonic traps, we have shown that the acceleration of the dark soliton results in decay via the emission of counter-propagating sound waves. In the absence of reinteraction of the soliton with the emitted sound, the power radiated is found to be proportional to the square of the local soliton acceleration. An analogous longitudinal instability arises in the context of nonlinear optics, where variations in the nonlinearity of

the optical medium destabilise the soliton and induce the emission of radiation. The emitted sound waves cause an apparent asymmetrical deformation of the soliton profile, such that the soliton centre of mass deviates from the density minimum, and this displacement is found to be proportional to the soliton acceleration.

In a real experiment, however, the condensate is confined and finite in size, such that the emitted sound must reinteract with the soliton. In harmonic traps, the emitted sound energy is refocussed back into the soliton, stabilising the dynamics. The soliton oscillates in the trap with on average constant amplitude and energy. However, the coupling of the soliton and the sound field leads to the generation of a dipolar fluid motion in the system, which induces slight modulations in these quantities. One way to control the soliton-sound interactions is to embed a dimple trapped within an ambient harmonic trap. For a deep dimple, the condensate sees an infinite trap, and rapid sound reinteraction stabilises the decay. However, for a shallow dimple, the emitted sound can escape to the outer trap and it is possible to observe pure soliton decay for a considerable time before sound reinteraction eventually occurs. This decay is marked by an increase in the soliton oscillation amplitude. Similarly, the addition of an optical lattice to a harmonic trap tends to dephase the emitted sound such that it is no longer fully reabsorbed, and this method can also be employed to manipulate the soliton-sound interaction. In suitable trap geometries, this longitudinal instability is predicted to be the dominant dissipation mechanism, and is expected to be experimentally observable under current experimental conditions.

We have further extended our control of the soliton-sound interactions in a trapped condensate to drive parametrically a dark soliton. Using gaussian paddles to generate a dipolar sound field can lead to significant energy transfer into the soliton. This process has important applications in stabilising a dark soliton against other dissipation mechanisms, e.g. thermal.

Superfluid vortices are also expected to be unstable to acceleration. Following from the investigation of dark solitons, we consider a single vortex in a two-dimensional dimple trap embedded in a weaker ambient harmonic trap. The inhomogeneous density drives the precession of the vortex about the trap centre and this acceleration induces the emission of dipolar sound waves from the

vortex core. For a deep inner dimple, i.e. an infinite harmonic trap, the sound waves reinteract with, and stabilise, the vortex, and this coupling sets up a collective motion of the background fluid. The vortex precesses with on average constant radius and energy, but this is modulated by the collective mode. For shallow dimples, the sound can escape to the outer region, allowing the pure decay of the vortex to be probed for a considerable time. From our numerical simulations, we obtain an expression for the power emission from the vortex. In particular, we find the power emission to be proportional to the vortex acceleration squared, and inversely proportional to the angular frequency of the precessional motion, in close agreement with analytic predictions. In suitable geometries, the vortex decay should be experimentally observable as a spiralling motion towards the condensate edge.

In vortex tangles in liquid Helium, the vortex motion is driven by the surrounding vortex distribution rather than an inhomogeneous density. By generalising our power emission formula to the case of a system of many vortices, we find that it is consistent with the experimentally-observed decay at very low temperature. To gain further insight into the problem of many interacting vortices, we consider the dynamics of two and three-body vortex interactions in a two-dimensional homogeneous system. Apart from the case of the vortex-antivortex pair, the vortex dynamics involve acceleration, and this induces vortex decay via sound emission, and supplements other instabilities such as vortex reconnections.

As a further illustration of the link between dark solitons and vortices, we consider the behaviour of vortices in non-axisymmetric systems. When the geometry of the system approaches the quasi-one-dimensional regime, a vortex can no longer be supported, and an intriguing state exists, known as a solitonic vortex. This state has a complex dynamical phase distribution which cycles between a vortex-like azimuthal phase profile to a soliton-like one-dimensional phase profile. However, the dynamics of the excitation resembles that of a dark soliton. This state can also be engineered by creating a dark solitary wave at an angle to the transverse direction.

In summary, we have shown that the zero temperature dynamics of dark solitons and vortices in atomic Bose-Einstein condensates is a rich and intriguing topic. Dynamical instabilities, in particular the instability to acceleration, lead

to dissipation of the excitation via sound emission. The coupling between the macroscopic excitation and the sound field plays a crucial role in the ensuing dynamics, and this can be engineered to induce decay, stabilise, or even drive energy into the vortex or soliton. All of these effects are expected to be observable under current experimental conditions.

Appendix A

Derivation of the Gross-Pitaevskii equation

In this Appendix we show in detail the derivation of the time-dependent Gross-Pitaevskii equation from the second quantized Hamiltonian under the approximations of the weakly-interacting Bose gas model.

We describe our system of N interacting bosons using the second quantized Hamiltonian in terms of the Bose field operator $\hat{\Psi}$. This operator is a function of space and time, although for convenience we will drop the time parameter. The second quantized Hamiltonian is then given by,

$$\hat{H} = \int \mathrm{d}^3\mathbf{r}\hat{\Psi}^\dagger(\mathbf{r})H_0\hat{\Psi}(\mathbf{r}) + \frac{1}{2}\int \mathrm{d}^3\mathbf{r}\int \mathrm{d}^3\mathbf{r}'\hat{\Psi}^\dagger(\mathbf{r})\hat{\Psi}^\dagger(\mathbf{r}')V_{\mathrm{int}}(\mathbf{r},\mathbf{r}')\hat{\Psi}(\mathbf{r}')\hat{\Psi}(\mathbf{r}), \quad \text{(A.1)}$$

where $V_{\mathrm{int}}(\mathbf{r},\mathbf{r}')$ is the interaction potential acting between the bosons and $H_0 = (\hbar^2/2m)\nabla^2 + V_{\mathrm{ext}}$ is the single particle hamiltonian, where m is the particle mass and V_{ext} is the external potential acting on the system. The operators $\hat{\Psi}^\dagger(\mathbf{r})$ and $\hat{\Psi}^\dagger(\mathbf{r})$ represent the creation and annihilation of a boson at position $\mathbf{r}$, and satisfy the crucial Bose commutation rules that will be given below.

The gas is sufficiently dilute that the atomic interactions are dominated by low energy, two-body s-wave collisions. These are essentially elastic, hard-sphere collisions between two atoms, and can be modelled in terms of the pseudo-potential,

$$V_{\mathrm{int}}(\mathbf{r},\mathbf{r}') = g\delta(\mathbf{r}'-\mathbf{r}), \quad \text{(A.2)}$$

where $g = 4\pi\hbar^2 Na/m$, with a the s-wave scattering length. Inserting this

potential into equation (A.1) and integrating over all $\mathbf{r}'$-space leads to,

$$\hat{H} = \int \mathrm{d}^3\mathbf{r}\hat{\Psi}^\dagger(\mathbf{r})H_0\hat{\Psi}(\mathbf{r}) + \frac{g}{2}\int \mathrm{d}^3\mathbf{r}\hat{\Psi}^\dagger(\mathbf{r})\hat{\Psi}^\dagger(\mathbf{r})\hat{\Psi}(\mathbf{r})\hat{\Psi}(\mathbf{r}), \tag{A.3}$$

where the dependence on $\mathbf{r}'$ has now been conveniently integrated out.

Using the Bose commutation relations,

$$\left[\hat{\Psi}(\mathbf{r}'), \hat{\Psi}^\dagger(\mathbf{r})\right] = \delta(\mathbf{r}' - \mathbf{r}), \qquad \left[\hat{\Psi}(\mathbf{r}'), \hat{\Psi}(\mathbf{r})\right] = \left[\hat{\Psi}^\dagger(\mathbf{r}'), \hat{\Psi}^\dagger(\mathbf{r})\right] = 0, \tag{A.4}$$

then Heisenberg's time evolution equation becomes,

$$\begin{aligned}
i\hbar\frac{\partial\hat{\Psi}(\mathbf{r}')}{\partial t} &= [\hat{\Psi}(\mathbf{r}'), \hat{H}] \\
&= \hat{\Psi}(\mathbf{r}')\hat{H} - \int \mathrm{d}^3\mathbf{r}\hat{\Psi}^\dagger(\mathbf{r})\hat{H}_0\hat{\Psi}(\mathbf{r})\hat{\Psi}(\mathbf{r}') - \frac{g}{2}\int \mathrm{d}^3\mathbf{r}\hat{\Psi}^\dagger(\mathbf{r})\hat{\Psi}^\dagger(\mathbf{r})\hat{\Psi}(\mathbf{r})\hat{\Psi}(\mathbf{r})\hat{\Psi}(\mathbf{r}') \\
&= \hat{\Psi}(\mathbf{r}')\hat{H} - \int \mathrm{d}^3\mathbf{r}\left[\hat{\Psi}(\mathbf{r}')\hat{\Psi}^\dagger(\mathbf{r}) - \delta(\mathbf{r}' - \mathbf{r})\right]\hat{H}_0\hat{\Psi}(\mathbf{r}) \\
&\quad -\frac{g}{2}\int \mathrm{d}^3\mathbf{r}\left[\hat{\Psi}(\mathbf{r}')\hat{\Psi}^\dagger(\mathbf{r})\hat{\Psi}^\dagger(\mathbf{r})\hat{\Psi}(\mathbf{r})\hat{\Psi}(\mathbf{r}) - 2\delta(\mathbf{r}' - \mathbf{r})\right]\hat{\Psi}^\dagger(\mathbf{r}\hat{\Psi}^\dagger(\mathbf{r}\hat{\Psi}^\dagger(\mathbf{r}) \\
&= \left[\hat{H}_0 + V_{\mathrm{ext}} + g\hat{\Psi}^\dagger(\mathbf{r}')\hat{\Psi}(\mathbf{r}')\right]\hat{\Psi}(\mathbf{r}').
\end{aligned} \tag{A.5}$$

Since the condensate state involves the macroscopic occupation of a single state it is appropriate to decompose the Bose field operator in terms of a macroscopically-populated mean field term $\psi(\mathbf{r}') \equiv < \hat{\Psi}(\mathbf{r}') >$ and a fluctuation term $\hat{\Psi}'(\mathbf{r}')$,

$$\hat{\Psi}(\mathbf{r}') = \psi(\mathbf{r}') + \hat{\Psi}'(\mathbf{r}'). \tag{A.6}$$

Then, taking only the leading order terms in ψ, equation (A.5) leads to the time-dependent Gross-Pitaevskii equation,

$$i\hbar\frac{\partial\psi}{\partial t} = \left(-\frac{\hbar^2}{2m} + V_{\mathrm{ext}} + g|\psi|^2\right)\psi. \tag{A.7}$$

Here $\psi \equiv \psi(\mathbf{r}, t)$ represents a function of space and time. Neglecting lower order terms involving the fluctuation operator $\hat{\Psi}'$ amounts to neglecting thermal and quantum depletion of the condensate. This is a valid approximation when (i) the temperature is much less than the transition temperature for the onset of condensation, and (ii) when the condensate is sufficiently weakly-interacting, which is true when $a \ll \lambda_{\mathrm{dB}}$, where λ_{dB} is the thermal de Broglie wavelength of the particles.

Appendix B

Numerical methods

This work is based on time-dependent simulations of the dimensionless Gross-Pitaevskii equation, performed using the Crank-Nicholson algorithm. This numerical method is outlined in section B.1. Furthermore, we illustrate how the initial ground state solution is localised using imaginary time propagation, and how to generate vortex and dark soliton solutions. In section B.2 we discuss the numerical evaluation of the vortex and dark soliton energy.

B.1 Crank-Nicholson method

The Crank-Nicholson method is a reliable and stable routine for numerically solving time-dependent Schrodinger-like equations [177]. Direct integration of the Schrodinger equation $i\partial\psi/\partial t = H\psi$ leads to the explicit time evolution of the wavefunction, which, after a time interval Δt, is formally given by,

$$\psi(\mathbf{r}, t + \Delta t) = \exp(-i\Delta t H)\psi(\mathbf{r}, t) + O(\Delta t^2). \tag{B.1}$$

This assumes that the hamiltonian H does not vary over this time interval. The time operator $\exp(-i\Delta t H)$ can be replaced by a finite difference representation known as Cayley's form

$$\exp(-iH\Delta t) = \frac{1 - \frac{i\Delta t}{2}H}{1 + \frac{i\Delta t}{2}H} + O(\Delta t^2). \tag{B.2}$$

Expressing the wavefunction after n time intervals as $\psi(\mathbf{r}, n\Delta t) \equiv \psi^n(\mathbf{r})$, the

time evolution step can be written as,

$$\left[1 - \frac{i\Delta t}{2} H^{n+1}(\mathbf{r})\right] \psi^{n+1}(\mathbf{r}) = \left[1 + \frac{i\Delta t}{2} H^{n}(\mathbf{r})\right] \psi^{n}(\mathbf{r}), \tag{B.3}$$

where $H^n(\mathbf{r})$ is the (dimensionless) GP hamiltonian at the n^{th} time step, $H^n(\mathbf{r}) = -(1/2)\nabla^2 + V_{\text{ext}}(\mathbf{r}) + |\psi^n(\mathbf{r})|^2$. The aim is then to solve this equation for $\psi^{n+1}(\mathbf{r})$. However, this requires knowledge of $H^{n+1}(\mathbf{r})$, which is not explicitly known (since it depends of $\psi^{n+1}(\mathbf{r})$). To overcome this, we calculate an intermediate solution by setting $H^{n+1}(\mathbf{r}) = H^n(\mathbf{r})$, and substitute this back into the original equation. This intermediate process can be iterated until convergence of the new wavefunction, although we find one iteration gives sufficient accuracy.

In order to numerically solve equation (B.3), we must discretise the wavefunction onto a spatial grid, characterised by grid spacing Δx, and proceed in calculating the Hamilitonian using finite differences. Note that equation (B.3) is second-order accurate in space and time, and stable provided $\Delta t < \Delta x^2/2$ [177]. Typical time and space steps used in this thesis are $\Delta t = 0.005$ and $\Delta x = 0.1$. In general we employ fixed boundary conditions whereby the wavefunction at the outer grid points is fixed to the initial values. The Crank-Nicholson method is unitary, i.e. preserves the norm of the wavefunction, and so it is not necessary to renormalise the wavefunction at each time step.

One-dimensional system

In one spatial dimension, the wavefunction is discretised onto a linear grid with separation Δx with index i, expressed as $\psi(x_i) \equiv \psi_i$. We define the forward time-difference operator δ_t via $\delta_t \psi_i^n = \psi_i^{n+1} - \psi_i^n$, and the central space-difference operator δ_x by $\delta_x \psi_i^n = \psi_{i+\frac{1}{2}}^n - \psi_{i-\frac{1}{2}}^n$. Then the double space derivative operator is given by $\delta_x^2 \psi_i^n = \psi_{i-1}^n - 2\psi_i^n + \psi_{i+1}^n$. In fully discretised form, equation (B.3) becomes,

$$\left[1 - \frac{i\Delta t}{2}\left(\frac{1}{2}\frac{\delta_x^2}{\Delta x^2} - V_i - |\psi_i^{n+1}|^2\right)\right] \psi_i^{n+1} = \left[1 + \frac{i\Delta t}{2}\left(\frac{1}{2}\frac{\delta_x^2}{\Delta x^2} - V_i - |\psi_i^{n}|^2\right)\right] \psi_i^{n}. \tag{B.4}$$

The right hand side of equation (B.4) represents a tridiagonal matrix and we may solve straight-forwardly for ψ^{n+1} using a Gaussian elimination algorithm tailored for a tridiagonal system [177]. Note that the LHS and RHS operators are complex conjugates.

Two-dimensional system

We now consider the case for a two-dimensional wavefunction $\psi(x,y)$. The box is discretised in the x and y directions, with steps Δx and Δy, and their respective indices i and j. In discretised form, equation (B.3) becomes,

$$\left[1-\frac{i\Delta t}{2}\left(\frac{1}{2}\frac{\delta_x^2}{\Delta x^2}+\frac{1}{2}\frac{\delta_y^2}{\Delta y^2}-V_{ij}-|\psi_{ij}^{n+1}|^2\right)\right]\psi_{ij}^{n+1}= \tag{B.5}$$
$$\left[1+\frac{i\Delta t}{2}\left(\frac{1}{2}\frac{\delta_x^2}{\Delta x^2}+\frac{1}{2}\frac{\delta_y^2}{\Delta y^2}-V_{ij}-|\psi_{ij}^{n}|^2\right)\right]\psi_{ij}^{n}$$

Each operator is now a function of x and y. Since we are only working to an accuracy of Δt^2 (see equation (B.2)) we can split the operators into the two separate directional components,

$$\left[1-\frac{i\Delta t}{2}\left(\frac{1}{2}\frac{\delta_x^2}{\Delta x^2}+\frac{1}{2}\frac{\delta_y^2}{\Delta y^2}-V_{ij}-|\psi_{ij}^{n+1}|^2\right)\right]\approx \tag{B.6}$$
$$\left[1-\frac{i\Delta t}{2}\left(\frac{1}{2}\frac{\delta_x^2}{\Delta x^2}-\frac{V_{ij}+|\psi_{ij}^{n+1}|^2}{2}\right)\right]\left[1-\frac{i\Delta t}{2}\left(\frac{1}{2}\frac{\delta_y^2}{\Delta y^2}-\frac{V_{ij}+|\psi_{ij}^{n+1}|^2}{2}\right)\right].$$

Crucially the x- and y-direction operators commute and the two-dimensional problem is reduced to an array of one-dimensional equations. The method is to evolve the wavefunction in one dimension and then switch to the other. This is the so-called Alternating Direction Implicit (ADI) approach. We can make one final modification to the time evolution operator. Again within the limit of Δt^2 accuracy it is feasible to drop the potential/nonlinear terms in all but one of the directional operators, say the x-direction, to give

$$\left[1-\frac{i\Delta t}{2}\left(\frac{1}{2}\frac{\delta_x^2}{\Delta x^2}+\frac{1}{2}\frac{\delta_y^2}{\Delta y^2}-V_{ij}-|\psi_{ij}^{n+1}|^2\right)\right]\approx \tag{B.7}$$
$$\left[1-\frac{i\Delta t}{2}\left(\frac{1}{2}\frac{\delta_x^2}{\Delta x^2}-V_{ij}-|\psi_{ij}^{n+1}|^2\right)\right]\left[1-\frac{i\Delta t}{4}\frac{\delta_y^2}{\Delta y^2}\right]. \tag{B.8}$$

We now only have to implement the iterative intermediate step in one direction. We have verified numerically that there is no discernable asymmetry in the hamiltonian due to this step. Extension of this method to three (cartesian) dimensions is straight forward.

Cylindrically-symmetric case

A full three-dimensional description of a condensate can be simplified by assuming a cylindrically-symmetric geometry. We employ cylindrical polar co-

ordinates in the longitudinal z-direction and transverse r-direction (with no dependence on the polar angle θ). The 3D system is then described by two coordinates, although the ensuing dynamics are not strictly 3D since they are constrained by the cylindrical symmetry. In these coordinates, the Laplacian terms in the Hamiltonian becomes,

$$\nabla^2\psi \rightarrow \frac{1}{r}\frac{\partial}{\partial r}\left(r\frac{\partial\psi}{\partial r}\right) + \frac{\partial^2\psi}{\partial z^2}. \tag{B.9}$$

In the transverse direction, the system is defined from $r = 0$ to some maximum radius $r = R$, with the $1/r$ term in the Laplacian leading to a singularity at $r = 0$. In order to overcome this, we shift the numerical grid such that the $r = 0$ point is not calculated: for example, if the radial space step is dr, we solve the radial direction from $r = dr/2$ to $r = R + dr/2$. Since this is no longer centred on the axis of cylindrical symmetry (i.e. $r = 0$ axis), we must enforce that $\partial\psi/\partial r = 0$ at the boundary to preserve the cylindrical symmetry.

B.1.1 Imaginary time propagation

A reliable and easily-implemented method of obtaining the ground state of the system is by propagation in imaginary time. Consider the wavefunction as a superposition of eigenstates $\phi_m(\mathbf{r})$ with time-dependent amplitudes $a_m(t)$ and eigenenergies $E_m(t)$, i.e. $\psi(\mathbf{r},t) = \sum_m a_m(t)\phi_m(\mathbf{r})$. By making the substitution $\Delta t \rightarrow -i\Delta t$, the time evolution equation (B.1) leads to an exponential decay of the wavefunction, and a corresponding decay of the eigenstates via,

$$\psi(\mathbf{r}, t + \Delta t) = \sum_m a_m(t)\phi_m(\mathbf{r})\exp(-E_m\Delta t). \tag{B.10}$$

Crucially, the eigenenergy governs the decay rate, and so the eigenstate with the lowest energy, i.e. the ground state of the system, decays slowest. From some trial wavefunction (which should ideally be a rough guess of the final solution), and by suitable renormalisation of the wavefunction (e.g. fixing the norm and/or the chemical potential) during the imaginary time propagation, the wavefunction will tend towards the ground state of the system.

B.1.2 Initial states involving a dark soliton or vortex

Dark soliton

In a one-dimensional system, with a time-independent background density $n(z)$, the initial solution involving a dark soliton is the product $\psi(z, t = 0) = \sqrt{n(z)}\psi_s(z, t = 0)$, where $\psi_s(z, t = 0)$ is the dark soliton solution of equation (2.33). Note that the analytic dark soliton solution is valid for a homogeneous background, whereas our density profile will in general be inhomogeneous. The dark soliton should therefore be initially placed at a locally homogeneous position in the background density, e.g. at the centre of a harmonic trap, to minimise the creation of transient sound waves.

In a multi-dimensional system, the time and length scales in the GPE will in general not coincide with the 1D scales, and so the 1D dark soliton solution of equation (2.33) is no longer the correct soliton solution. In this case, a stationary dark soliton solution can be generated by propagating the GPE in imaginary time, subject to a π-phase step. Here, the imaginary time method finds that stationary soliton solution at any position in the trap, and so this method is not limited to the trap centre.

Vortex

A vortex state in a 2D system, with rotational charge q, is generated by propagating the GPE in imaginary time, subject to a $2\pi q$ azimuthal phase slip. For example, to create a singly-charged vortex at the origin, the wavefunction should be modified at each time step via,

$$\psi \rightarrow |\psi| \exp[i \tan^{-1}(y/x)]. \tag{B.11}$$

To create a vortex line in 3D, the phase must be enforced along the desired axis. If the resulting vortex state is time-dependent, then, when run in real time, a small amount of transient sound will be released as the vortex initially accelerates to its moving state.

B.2 Numerical evaluation of the energy of a dark soliton and vortex

Since this work is concerned with the stability of dark solitons and vortices in dilute trapped BECs, the energy of the excitation is an important quantity. In particular we wish to compare the energies of the excitation and the background fluid, and investigate the transfer of energy between the two. This requires that we have a *local* definition of the soliton/vortex energy. However, the energy of a vortex technically extends up to the boundary of the system, and additionally there is no exact analytic form for the vortex energy. On the contrary, dark solitons do have a well-defined energy given by equation (2.33). However, this expression assumes homogeneous background density and does not hold in inhomogeneous systems, such as those considered here.

An alternative method is to derive the energy of the vortex/soliton numerically through integration of the GP energy functional (equation (2.12)). The essence of this approach is to integrate the energy functional locally about the excitation and subtract from this the corresponding value of the time-independent background density n_{TI}. The size of the integration region is the key parameter: it should be large enough to contain a significant proportion of the energy of the excitation, but small enough in relation to the overall system to act as a *local* indication of its energy.

In trapped BECs, the vortex/soliton will in general co-exist with other excitations within the system, e.g. sound waves. From the point of view of the numerically-integrated energy, any sound waves located in the soliton/vortex region will give a contribution to the energy. However, provided the energy of the vortex/soliton is not too small, this contribution will negligible.

Below we consider the case of a vortex and dark soliton in a 2D and 1D system respectively, and show how a local value of the vortex/soliton energy can be obtained numerically.

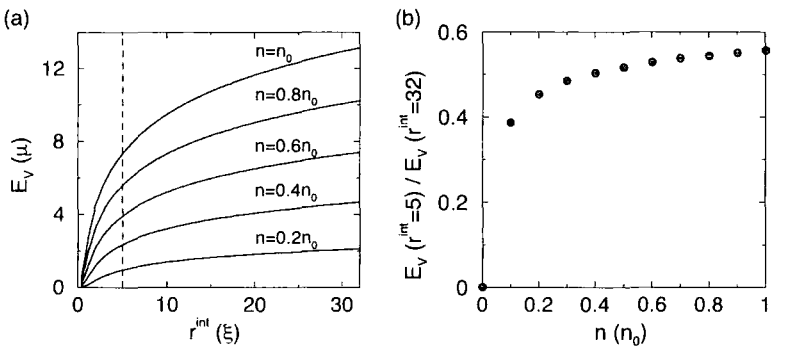

Figure B.1: (a) Integrated local energy of a vortex E_V in a 2D homogeneous system, according to equation (B.12), as a function of the radius of the integration region r^{int}. Five background densities are considered. In our numerics, we choose $r^{int} = 5\xi$, as shown by the dashed line. (b) The ratio of the local ($r^{int} = 5\xi$) integrated vortex energy to the non-local ($r^{int} = 32\xi$) integrated vortex energy, as a function of the background density.

B.2.1 Vortex energy

In the case of a 2D vortex, the integration region R is defined to be the area within a circle of radius r_{int} centred on the vortex core, such that the local vortex energy is defined as,

$$E_V = \int_0^{r^{int}} \varepsilon(\psi) 4\pi r^2 dr - \int_0^{r^{int}} \varepsilon(\sqrt{n_{TI}}) 4\pi r^2 dr, \tag{B.12}$$

where we employ cylindrical polar coordinates centred on the vortex core.

Figure B.1(a) shows the integrated vortex energy, according to equation (B.12), as a function of the integration radius, for a 2D homogeneous system. The integrated vortex energy increases indefinitely with the size of the integration region, with its magnitude being heavily dependent on the background density, as suggested by equation (2.30). Furthermore, the local healing length is proportional to $1/\sqrt{n}$, such that the size of the vortex core increases with decreasing density, and diverges in the limit $n \to 0$. This will additionally affect the proportion of the vortex energy contained within a certain radius.

In inhomogeneous BECs, the background density at the position of the vortex may in general be a time-dependent quantity. The strong density dependence on the integrated vortex energy therefore appears to be problematic. However, we require our numerically-obtained *local* vortex energy to be an accurate indication

of the actual (infinite) vortex energy over the course of a simulation. The important quantity is therefore the ratio of the *local* vortex energy to the *non-local* (infinite) vortex energy. We consider a trial integration radius of $r^{\rm int} = 5\xi$, and compare the resulting *local* vortex energy to the *non-local* vortex energy calculated over a much greater radius of $r^{\rm int} = 32\xi$. This proportion is shown in figure B.1(b) as a function of the background density. For small background densities $n < 0.3n_0$, the proportion is dependent on n, and tends to zero as $n \to 0$ due to the divergence of the vortex core size. However, for densities greater than $\sim 0.3n_0$, the proportion lies in the region of $\sim 0.5 - 0.55$. Over this range of densities the *local* vortex energy with $r^{\rm int} = 5\xi$ can be taken to be a good indication of the actual vortex energy. In this work, we will employ this integration radius $r^{\rm int} = 5\xi$ and only apply this method to vortices where the background density is greater than around $0.4n_0$.

B.2.2 Dark soliton energy

For a dark soliton in 1D, the integration region is taken to be the line extending a distance $z^{\rm int}$ either side of the dark soliton centre $z_{\rm S}$, such that the local soliton energy is given by,

$$E_{\rm S} = \int_{z_{\rm S}-z^{\rm int}}^{z_{\rm S}+z^{\rm int}} \varepsilon(\psi)\mathrm{d}z - \int_{z_{\rm S}-z^{\rm int}}^{z_{\rm S}+z^{\rm int}} \varepsilon(\sqrt{n_{\rm TI}})\mathrm{d}z. \tag{B.13}$$

Note that we define the soliton centre as the point of minimum density.

In contrast to a vortex, a dark soliton is not topological and has no energy contribution at large distances. We therefore expect the integrated energy to converge at a finite distance from its centre. This distance will be characterised by the soliton width, which depends on the background density (as for vortices) and the soliton speed. Figures B.2(a) and (b) illustrate the integrated soliton energy (solid lines) of equation (B.13) as a function of the size of the integration region, for various soliton speeds and background densities, respectively. We observe that the integrated soliton energy converges with the asymptotic prediction (dashed lines). The distance required for convergence is larger for faster solitons and/or lower densities, due to the increase in the soliton width. However, for the speeds and densities considered here, we observe that the integrated energy is virtually indistinguishable from the analytic prediction for

$z^{\mathrm{int}} > 5\xi$. We therefore choose our integration distance to be $z^{\mathrm{int}} = 5\xi$.

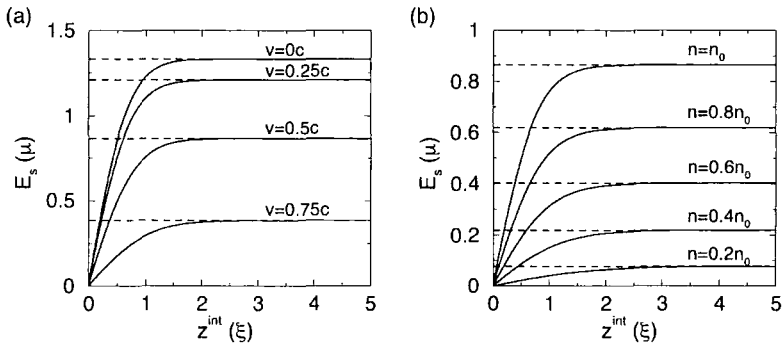

Figure B.2: Integrated local soliton energy E_{s}, according to equation (B.13), as a function of integration width z^{int}. (a) The background density is fixed to $n = n_0$, and various soliton speeds are considered. (b) The soliton speed is fixed at $v = 0.5c$ and various background densities are considered. In all cases, the analytic soliton energy is indicated by a dashed line.

Appendix C

Derivation of the Bogoliubov-de Gennes equations

Here we present a derivation of the Bogoliubov-de Gennes equations for the dilute Bose gas, describing the spectrum of small-scale excitations on the background state.

If $\phi_0(\mathbf{r})$ is the time-independent background state, then weak perturbations of the wavefunction can be expressed with the trial wavefunction,

$$\psi(\mathbf{r},t) = e^{-i\mu t/\hbar}\left[\phi_0(\mathbf{r}) + u(\mathbf{r})e^{-i\omega t} + v^* e^{i\omega t}\right], \tag{C.1}$$

where μ is the chemical potential of the system. The perturbation is time-dependent with characteristic frequency ω. The amplitude functions $u(\mathbf{r})$ and $v(\mathbf{r})$ are complex. For simplicity, we will drop the time and space notation in the parameters.

The time-dependent Gross-Pitaevskii equation is,

$$i\hbar\frac{\partial\psi}{\partial t} = \left[H_0 + g|\psi|^2\right]\psi, \tag{C.2}$$

where H_0 is the single particle hamiltonian $H_0 = -(\hbar^2/2m)\nabla^2 + V_{\text{ext}}$, with V_{ext} being the external potential acting on the system, and g is the nonlinear coefficient given by equation (2.7).

We proceed by evaluating the Gross-Pitaevskii equation for the trial wavefunction of equation (C.1) to first order in u and v. The left-hand side of the

Gross-Pitaevskii equation becomes,

$$i\hbar\frac{\partial\psi}{\partial t} = e^{-i\mu t/\hbar}\left[\mu\phi_0 + (\mu+\hbar\omega)ue^{-i\omega t)} + (\mu-\hbar\omega)v^*e^{i\omega t}\right]. \tag{C.3}$$

We now evaluate the right-hand side of the Gross-Pitaevskii equation. First we consider the term $\psi^*\psi\psi$. Keeping only the terms which are linear in u and v gives,

$$\begin{aligned}\psi^*\psi\psi &= e^{-i\mu t/\hbar}(\phi_0^* + u^*e^{i\omega t} + ve^{-i\omega t})(\phi_0 + ue^{-i\omega t} + v^*e^{i\omega t})^2 \qquad \text{(C.4)}\\ &= e^{-i\mu t/\hbar}\left[|\phi_0|^2\left(\phi_0 + 2ue^{-i\omega t} + 2v^*e^{i\omega t}\right) + \phi_0^2\left(u^*e^{i\omega t} + ve^{-i\omega t}\right)\right].\end{aligned}$$

Substituting all terms into the Gross-Pitaevskii equation and equating terms in $e^{-i\mu t/\hbar}$ leads to,

$$\mu\phi_0 = H_0\phi_0 + g|\phi_0|^2\phi_0. \tag{C.5}$$

Equating terms in $e^{-i(\mu+\hbar\omega)t/\hbar}$ gives,

$$(\mu+\hbar\omega)u = (H_0 + 2g|\phi_0|^2)u + g\phi_0^2 v, \tag{C.6}$$

and terms in $e^{-i(\mu-\hbar\omega)t/\hbar}$ gives,

$$(\mu-\hbar\omega)v^* = (H_0 + 2g|\phi_0|^2)v^* + g\phi^2u^*. \tag{C.7}$$

Taking the complex conjugate of equation (C.7) leads to,

$$(\mu-\hbar\omega)v = (H_0 + 2g|\phi_0|^2)v + g\phi^{*2}u. \tag{C.8}$$

Equations (C.5), (C.6) and (C.8) can be written in the form of a matrix equation in terms of u and v,

$$\begin{pmatrix} L & M \\ M^* & L \end{pmatrix}\begin{pmatrix} u \\ v \end{pmatrix} = \hbar\omega\begin{pmatrix} u \\ -v \end{pmatrix}, \tag{C.9}$$

where,

$$L = H_0 - \mu + 2g|\phi_0|^2, \tag{C.10}$$

and,

$$M = g\phi_0^2. \tag{C.11}$$

This is the Bogoliubov-de Gennes equation for the dilute Bose gas. Solutions to this matrix equation can be obtained by solving the eigenvalue equation,

$$\begin{vmatrix} L-\hbar\omega & M \\ M^* & L+\hbar\omega \end{vmatrix} = 0. \tag{C.12}$$

It follows that the energy of the excitations is given by,

$$\hbar\omega = \sqrt{L^2 - |M|^2}. \tag{C.13}$$

In particular, for a homogeneous system with background density n, $V_{\text{ext}} = 0$, $H_0 = \hbar^2 k^2/2m$, and $\mu = ng$, where k is the wavevector of the excitation. The energy spectrum is then given by,

$$\hbar\omega = \sqrt{\frac{\hbar^2 k^2}{2m}\left(\frac{\hbar^2 k^2}{2m} + 2ng\right)}. \tag{C.14}$$

This dispersion is particle-like ($\hbar\omega = \hbar^2 k^2/2m$) at high momenta, while at low momenta, the spectrum is linear ($\omega = ck$) and supports sound (phonon) waves with characteristic speed c.

Appendix D

Dark soliton interacting with gaussian bumps

Chapter 4 explores the stability of the dark soliton to motion through an inhomogeneous density in terms of its interaction with infinitely-long potential steps and ramps in an otherwise homogeneous system. Here we present some additional results which consider the interaction of a dark soliton with a square potential barrier of finite length, and gaussian-shaped potentials. Some of this work has been covered in [216].

D.1 Dark soliton incident on a finite potential barrier

In section 4.1 we explored the interaction of a dark soliton with an infinitely-long potential step. We now consider the more general case of a dark soliton incident on a potential barrier of *finite* length L, with the form,

$$V(z) = \begin{cases} V_0 & \text{for} \quad 0 < z \leq L \\ 0 & \quad\quad z \leq 0, z > L. \end{cases} \tag{D.1}$$

The barrier induces a density perturbation of positive (figure D.1) or negative amplitude (figure D.6), depending on whether the barrier is upward or downward, respectively. Such a potential can represent an artifically-induced barrier, e.g. by optical means, or the presence of a localised impurity.

D.1.1 Positive barrier ($V_0 > 0$)

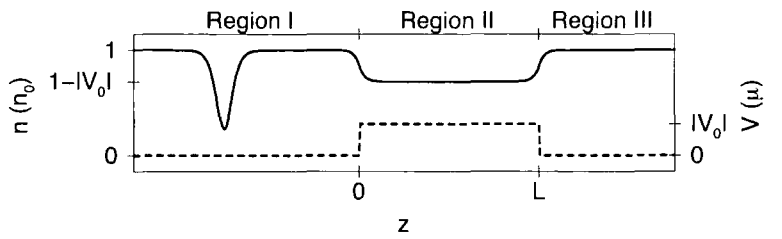

Figure D.1: Schematic of the atomic density (left axis, solid line) at a *positive* square barrier of height V_0, where $V_0 > 0$, and length L (right axis, dashed line), and an incident soliton.

For a positive barrier, as illustrated in figure D.1, the barrier induces a reduction in the ambient density and inhibits the transmission of the incident soliton. For sufficiently long barrier, the fluid can heal fully to the potential, and the density perturbation in region II reaches the TF amplitude of $n_{\rm II} = (1 - V_0)$, as illustrated in figure D.2(i)-(ii). Here the interaction of the soliton with the barrier can be considered as two separate processes: at the first boundary, a collision with a positive step; at the second boundary, a collision with a negative step. At the first boundary, the soliton can either transmit or reflect, depending critically on the speed/depth of the soliton and the barrier height, as described in section 4.1.1. Counter-propagating sound waves are emitted by the soliton during this interaction, apart from the limit of collision with a hard wall $V_0 \gg \mu$, where the soliton reflects elastically. In the case of transmission over the first upward boundary, the soliton will travel with reduced speed in region II due to the reduced local speed of sound. At the second boundary, the soliton will pass down and off the barrier, emitting sound waves and possibly generating additional dark solitons, as if it were interacting with an isolated negative step. Here the soliton speed will be increased again as it re-enters the $V = 0$ region (region II). However, its speed will be slightly higher than its initial value due to intervening soliton decay induced by its interaction with the barrier.

If the barrier is sufficiently narrow, the density cannot heal fully to the potential, as illustrated in figure D.2(iii). Then, the soliton dynamics cannot be understood in terms of separate interactions with a positive and negative step, and become more complicated. Since the density in region II does not reach

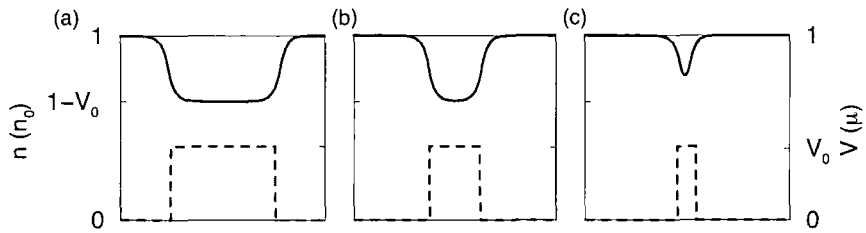

Figure D.2: Schematic of the density perturbation (solid line) and potential (dashed line) at a potential barrier of height V_0. (i) Sufficiently long barrier: density heals fully to the TF value of $(1 - V_0)$. (ii) Intermediate barrier length: density *just* heals to the TF value. (iii) Narrow barrier: density perturbation is restricted by its narrow spatial extent, and falls short of TF value. The resulting perturbation, with minimum density $n_{\rm min}$, is characterised by an effective potential $V_{\rm eff} = 1 - n_{\rm min}$.

the TF value, it is useful to characterise the density perturbation in terms of an *effective potential*. If the minimum of the density perturbation is $n_{\rm min}$, then the effective potential is defined as $V_{\rm eff} = (1 - n_{\rm min})$. This parameter is crucial in determining whether the soliton transmits or reflects at the barrier.

Figure D.3(a) maps the effective potential $V_{\rm eff}$ induced by the potential barrier for a range of heights V_0 and lengths L. For long barriers, where the density perturbation heals to the TF value, the effective barrier potential is identical to the actual potential. For narrow barriers, however, where the density perturbation is restricted, the effective potential that the soliton sees can be much less than the actual potential. Indeed, in the limit that the barrier width tends to zero, the effective potential also tends towards zero. In these cases, the soliton can tunnel through barriers for which the corresponding classical particle would be reflected. As outlined in section 4.1.1 for a positive step, the condition for soliton transmission is, to first order (ignoring sound emission), $v^2 > V_{\rm eff}$ (V_0 now replaced by $V_{\rm eff}$). For a soliton with initial speed $v_{\rm I} = 0.5c$, this approximate threshold between transmission and reflection corresponds to the $V_{\rm eff} = 0.25\mu$ contour in figure D.3(a). The actual threshold is slightly larger than this value due to the decay of the soliton by sound emission, and is illustrated by the dashed line in the same figure.

Figure D.3(b) shows the corresponding total sound emitted from the soliton,

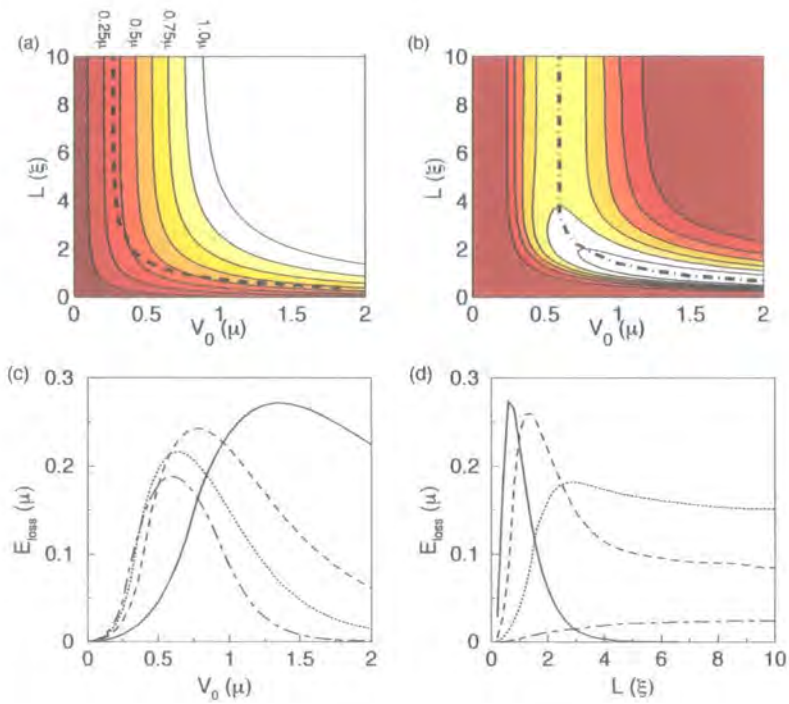

Figure D.3: (a) Effective potential $V_{\rm eff}$ imposed by the step as a function of length and height, with each contour representing an increment of 0.125μ. An effective potential of unity implies a pinning of the density to zero and although higher effective potentials exist, we do not show them here as, throughout this limit, the sound emission is essentially prohibited. Note that for effective potentials slightly greater than unity, the density is weakly pinned to zero and sound of positive amplitude can just propagate through. The dashed line indicates the transition between reflection/transmission for a soliton with initial speed $v_{\rm I} = 0.5c$ (the non-dissipative prediction would be the $V_{\rm eff} = 0.25\mu$ contour). (b) Total sound emitted from a dark soliton with inital speed $v_{\rm I} = 0.5c$ and energy $E_s = 0.866\mu$ incident on a step of height V_0 and length L. The emitted energy ranges from zero (darkest region) to maximum value in equal contour steps. Maximum sound emission occurs along the dot-dashed line $V_0 = V_0^m(L)$. (c) Cross-sections of (b) for constant step lengths of $L/\xi = 1$ (solid line), 2 (dashed line), 5 (dotted line) and 10 (dot-dashed line). (d) Cross-sections of c) for constant step heights of $V_0/\mu = 0.25$ (dot-dashed line), 0.5 (dotted line), 1 (dashed line) and 2 (solid line).

the magnitude of which is intimately related to the above-mentioned effective potential. Maximum sound emission occurs in the region of reflective quasi-trapping where the soliton is subject to its greatest time-integrated acceleration. The line of maximum sound emission, defined by $V_0 = V_0^m(L)$, is highlighted by the dot-dashed line in figure D.3(b). Note that $V_0^m(L)$ decreases with increasing length, and essentially saturates to the value of $V_0^m(L) \approx 0.6\mu$ for $L \geq 5\xi$. The maximum sound energy released in figure D.3(b) is approximately 0.27μ, which corresponds to 32% of the initial soliton energy. The sound emission tails off in the opposite limiting cases of $V_0 \to 0$, and $V_0 \to \infty$. To visualize the behaviour more clearly, figure D.3(c)-(d) plot, respectively, the total emitted sound energy as a function of step height V_0 (for various fixed step widths L) and as a function of L (for various fixed V_0).

Figure D.3(c) shows that, for fixed L, the total emitted sound increases abruptly with increasing step height, reaches a maximum at the point of reflective quasi-trapping, and decreases more slowly as $V_0 \to \infty$. This is similar to the behaviour encountered for an infinitely-long positive step, discussed in section 4.1.1. Here, however, the variation of the emitted energy with step height is smooth, and does not feature the discontinuity apparent in figure 4.4 for the infinitely-long step. This can be understood as follows: for a soliton transmitting over an *infinitely* long step, a single burst of energy is emitted before the soliton reaches its steady state on the step, whereas a soliton which is ultimately reflected interacts *twice* with the boundary, thus emitting two sound pulses. In the case of a *finite* length step, this distinction does not arise. For transmission, the soliton must ascend and descend the step before reaching its steady state on the far side of the step (where its final energy is to be computed). This clearly involves two bursts of energy being radiated. However, the case of reflection also features two bursts, occuring when the soliton ascends and descends the first boundary. Since the background fluid is symmetric around the centre of the step (as regions I and III have the same potentials), the net amount of sound emission in the two limiting cases of soliton marginally transmitting, or just reflecting, will be the same, and hence the discontinuity will be absent here.

To understand in more detail the features of figure D.3(c), it is instructive to consider the effective potential experienced by the soliton in the three cases of (i) transmission ($V_0 \ll V_0^m(L)$), (ii) reflection with maximum energy emission (oc-

curing at $V = V_0^m(L)$), and (iii) reflection with sound emission ($V_0 \gg V_0^m(L)$), but still far from the $V_0 \to \infty$ limit. These are shown in figure D.4 (a)-(c), respectively. Different lines in each of these figures correspond to different step widths ($L = \xi$, 2ξ, 5ξ and 10ξ). (Note that the step heights in figure D.4(b) differ from line to line.) For a constant step width L, the density depression becomes more pronounced with increasing step height (this can be visualized, e.g. by looking at the change of the solid line corresponding to $L = \xi$ from (a)-(c)).

Figure D.4(a) shows the background density at a low barrier, $V_0 = 0.25\mu$. The $v = 0.5c$ soliton can probe, to first order, densities down to $0.75n_0$, and so just transmits in this case. In the case of transmission, maximum sound emission occurs when the soliton experiences the greatest background density gradient. In figure D.4(a) this occurs for maximum step width $L = 10\xi$ (dot-dashed line).

Figure D.4(c) illustrates the background density in the opposite regime when the barrier is high, $V_0 = 2\mu$. In the case of a sufficiently long step, e.g. $L = 10\xi$ (dot-dashed line) in figure D.4(c), the fluid heals fully to the Thomas-Fermi limit, thus reaching zero density. The soliton effectively sees a hard wall and becomes reflected without any sound emission (see corresponding dot-dashed line in figure D.3(c) at $V_0 = 2\mu$). However, as the step width is decreased, the reflected soliton can emit increasing amounts of sound energy. This is because the finite density at the step now enables *sound propagation* into the second region, despite the fact that the *soliton* is reflected. Note that, despite appearing to do so, the dotted line of figure D.4(c) does *not* reach zero density (see figure D.4(e) showing enlarged version of figure D.4(c) near $n = 0$). This explains why there is some (albeit limited) sound emission for $L = 5\xi$ (dotted line) at $V_0 = 2\mu$ in figure D.3(c).

Although this accounts for the qualitative features of the lines in figure D.3(c), it still does not explain why the *maximum* emitted energy for narrow steps (e.g. solid line in figure D.3(c) at $V_0 = V_0^m(L = \xi) \approx 1.4\mu$ for which $E_{\rm loss}^m \approx 0.27\mu$) is larger than the *maximum* emitted energy for longer steps (e.g. dashed line of same figure for which$E_{\rm loss}^m \approx 0.24\mu$). To explain this, we must examine the background density profile for each of the lengths considered (i.e. $L/\xi = 1$, 2, 5 and 10) at the step height which corresponds to maximum sound emission. As evident from figure D.3 (b) and (c), this critical barrier height $V_0 = V_0^m$ depends

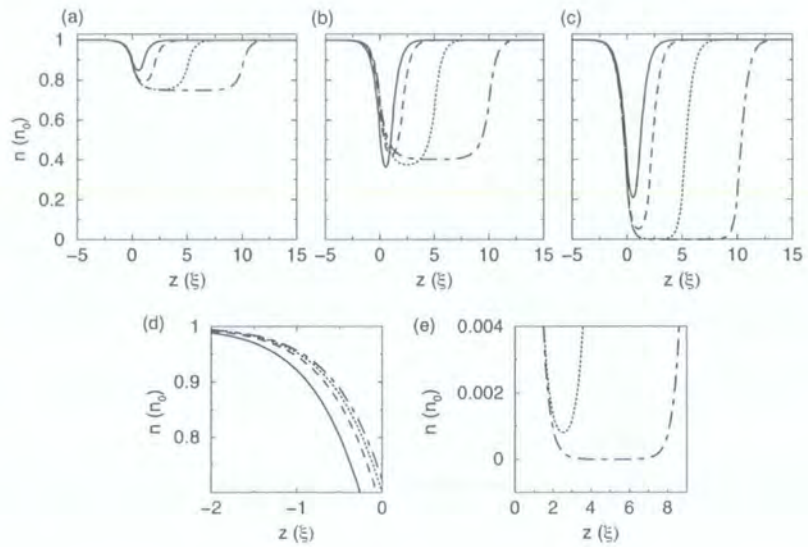

Figure D.4: Background density profiles due to fluid healing in the region of the barrier. Each sub-figure plots the cases of $L = \xi$ (solid line), 2ξ (dashed line), 5ξ (dotted line) and 10ξ (dot-dashed line) as in Fig. 2(d) for different potential heights V_0: (a) Transmitted soliton at $V_0 = 0.25\mu$, (b) Reflected soliton at $V_0 = V_0^m(L)$ corresponding to maximum sound emission for each L, i.e. at $V_0^m(\xi) = 1.36\mu$ (solid line), $V_0^m(2\xi) = 0.77\mu$ (dashed line), $V_0^m(5\xi) = 0.64\mu$ (dotted line) and $V_0^m(10\xi) = 0.60\mu$ (dot-dashed line). (c) Reflected soliton at $V_0 = 2\mu$. (d) Enlarged image of the background density inhomogeneity experienced by the soliton in (b), in the region $-2 < x < 0$ for $L = \xi$, 2ξ, 5ξ, and 10ξ. In this region, the density gradient is clearly maximized for the narrowest step ($L = \xi$, solid line), (e) Enlarged image of (c) showing the effective minimum density in the cases $L = 5\xi$ (dotted) and $L = 10\xi$ (dashed). For a width $L = 5\xi$ (dotted line), the density does not quite heal to zero, allowing a small amount of sound transmission through the barrier.

also on the step width (i.e. $V_0 = V_0^m(L)$). Therefore, to interpret the increase in the maximum emitted energy for narrower steps, we must compare the effective background densities for different widths L at their corresponding heights $V_0 = V_0^m(L)$. This is illustrated in figure D.4(b). Note that such density profiles, here obtained by imaginary time propagation of the GPE, can also be obtained by matching analytically known solutions of the GPE in finite and semi-infinite intervals (see, e.g. [124, 276]). To first approximation, in all these cases (i.e. all L), the soliton probes the step region down to a density of approximately $(1 - v_\mathrm{I}^2)$ (corresponding to $0.75n_0$ for the soliton under consideration) before being reflected. Consequently, the soliton is approximately limited to the $z < 0$ region. Therefore, the key parameter controlling the amount of sound radiation is the *gradient* of the background density probed by the soliton (which clearly depends on the step width). To see this gradient clearer, figure D.4(d) plots an enlarged version of the effective potentials of figure D.4(b) in the region $-2\xi < z < 0$. Hence, at the point of maximum emission for each L, it is actually the *narrower* step (solid line) which has the *steepest* gradient. As a result, the *maximum* sound emission occurs for narrower steps. We have hence accounted for the entire behaviour of the emitted sound energy as a function of step height.

From the above analysis, one can also understand the features of figure D.3(d) showing the dependence of emitted energy on step width. For small V_0 (e.g. $V_0 = 0.25\mu$, dot-dashed line) the soliton is transmitted, releasing maximum sound for longest steps, with the amount saturating for $L \to \infty$. Increasing V_0 (e.g. $V_0 = 0.5\mu$, dotted line) leads to larger density gradients and hence more sound emission as $L \to \infty$. The peak emitted energy at $L \approx 2.7\xi$ is due to a maximum time spent on the step in the regime of reflective quasi-trapping. Increasing V_0 further leads to the gradual suppression of sound transmission and hence a reduced total sound emission in the limit $L \to \infty$. Note that as V_0 is increased, the phenomenon of quasi-trapping appears at smaller L, leading to a shift of the peak emission to the left. The maximum sound emission occurs for large V_0 (and small enough L) since then the density gradient experienced by the soliton is maximised. This trend appears to be maintained with indefinite increase in V_0, although it requires smaller step widths, which will ultimately become unphysical. When $V_0 > \mu$, the soliton undergoes elastic reflection with

no sound emission, provided the step width L is sufficiently long to allow for complete fluid healing to the imposed potential V_0. This explains the tailing off of the sound energy for $V_0 = 2\mu$ (solid line) to zero as $L > 5\xi$.

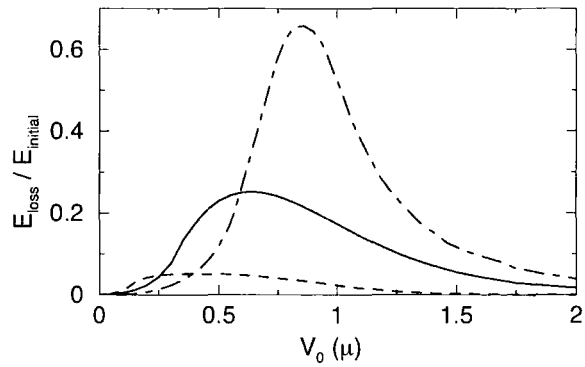

Figure D.5: Fraction of the initial soliton energy that is emitted for a soliton incident on a finite potential step of length $L = 5\xi$ as a function of step height V_0 for various initial soliton speeds: $v = 0.3c$ (solid line), $0.5c$ (dashed line - this corresponds to dashed line in figure D.3(c)), and $0.7c$ (dotted line). The initial soliton energies are 1.157μ, 0.866μ and 0.486μ respectively.

We have so far considered a soliton of fixed initial speed, and this has enabled us to map the entire dependence of emitted sound energy on L and V_0 for a particular soliton speed. We shall now briefly comment on the dependence of the emitted energy on initial soliton speed. Figure D.5 shows the energy radiated by a soliton incident on a finite potential step of fixed length $L = 5\xi$ and variable height V_0, for various initial soliton speeds, with the energies scaled in terms of the initial soliton energies. In the regime of transmission over the step (i.e. leftmost part of the figure), the slowest soliton emits the most sound energy. This can be attributed to the fact that, although all three solitons experience the same density gradient, the slowest soliton (solid line) spends the longest time at the step, thereby leading to the greatest time-integrated sound emission. However, a slower soliton features the deepest density profile. Its passage into the step region is therefore more restricted, causing it to reflect and reach the point of saturation of the sound emission (i.e. $V_0 = V_0^m(L)$) at an earlier point in space. Thus, increasing the initial soliton speed leads to a general shift of the emission curves to higher potentials. Faster solitons can

pass a greater distance into the step region, probing higher density gradients, and so have higher peak sound emission. However, faster dark solitons have lower energies. This means that, in addition to radiating more energy, faster solitons radiate a higher fraction of their total energy. For example, a soliton with initial speed $v_I = 0.7c$ can radiate as much as 65% of its initial energy. In all cases the sound emission eventually tends to zero as the step height V_0 becomes much greater than the chemical potential, although faster solitons still emit more energy in the limit of high barriers.

D.1.2 Negative barrier ($V_0 < 0$)

We now consider the case of a soliton incident on a barrier of *negative* amplitude, as illustrated in figure D.6. Here the impinging soliton always transmits across the well. In the region II it travels with increased speed due to the higher local density and speed of sound. As in section D.1.1, for long enough barriers, the density can heal fully to the barrier potential, while for narrow barriers, the density perturbation can be heavily suppressed in comparison to the TF prediction. The variation of the effective potential with barrier height and length, shown in figure D.7(a), is qualitatively similar to that for the $V_0 > 0$ case: for long barriers it is equivalent to the actual height, while for narrow barriers it becomes smaller in magnitude.

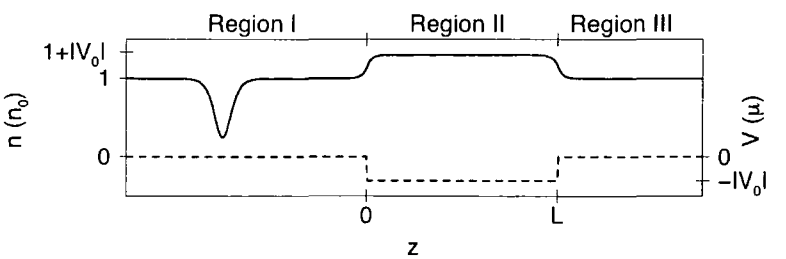

Figure D.6: Schematic of the atomic density (left axis, solid line), including an incident soliton, at a *negative* square barrier with height V_0 and length L (right axis, dashed line).

Figure D.8 illustrates the interaction of a dark soliton with a negative barrier of length $L = 40\xi$ for several barrier depths. For all cases, the soliton accelerates over the first boundary, propagates with increased speed in region II,

and decelerates into region III. For a shallow well, e.g. $V_0 = -0.25\mu$ (case(a)), the soliton radiates sound pulses at each boundary, with amplitude of around $0.02n_0$. For deeper well, e.g. $V_0 = -1\mu$ (case (b)) and $V_0 = -4\mu$ (case (c)), the radiated waves have greater amplitude $\sim 10\%n_0$. The waves radiated at both boundaries into region II become partially trapped in region II. They oscillate back and forth, becoming partially reflected and partially transmitted at each boundary. It appears that one dark soliton is created during the interaction with the first boundary, as most evident in figure D.8(c). At the first bound-

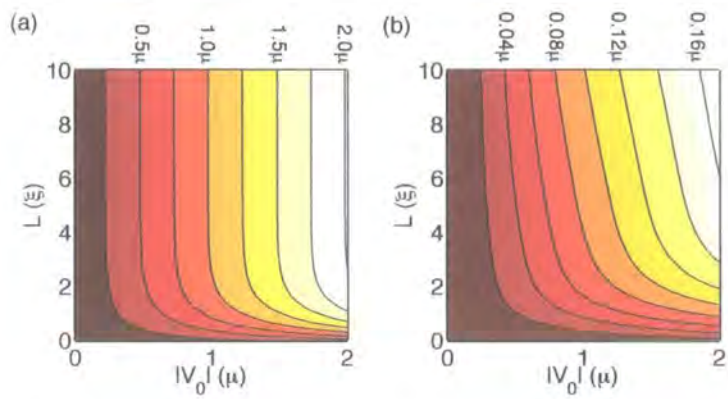

Figure D.7: (a) Magnitude of the effective potential $|V_{\text{eff}}|$ induced by a negative barrier of length L and depth $|V_0|$. (b) Energy emitted by a dark soliton, with initial speed $v_{\text{I}} = 0.5c$, incident on the barrier.

ary, a forward-propagating dark pulse is radiated which travels with the soliton and cannot be resolved from it. At the second boundary, where the original soliton is transmitted, this dark pulse becomes mostly reflected. It additionally includes sound radiated from the soliton as it transmits the second boundary. As this combined dark pulse interacts with the first boundary it becomes partially transmitted. In region I, the darkest component of this transmitted wave propagates at less than the speed of sound, at around $0.93c$, suggesting that it is a fast dark soliton.

The energy radiated by a dark soliton for a range of barrier lengths L and heights V_0 is shown in figure D.7(b). For fixed barrier length, the energy emitted increases monotonically with height V_0. For narrow barriers, the energy emission is suppressed, due to the reduction in the effective potential.

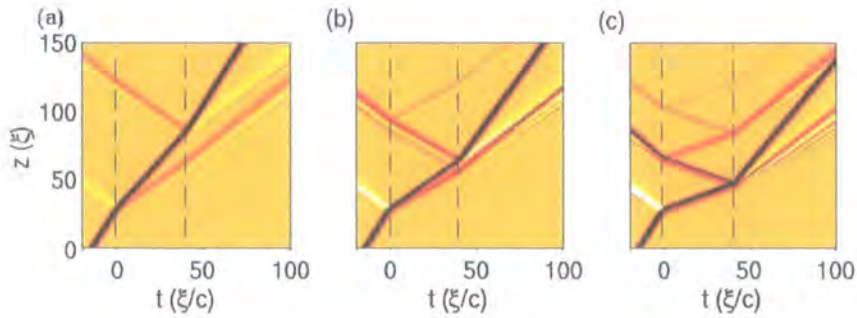

Figure D.8: Space-time carpet plots showing the interaction of a dark soliton, with initial speed $v_I = 0.5c$, with a negative barrier of length $L = 40\xi$, and height (a) $V_0/\mu = -0.25$, (b) -1, and (c) -4. The boundaries of the barrier are shown by dashed lines. The density scale has an amplitude of $10\%n_0$.

D.2 Dark soliton traversing a gaussian bump

We now investigate here the case of a dark soliton incident on a gaussian bump of the form,

$$V(z) = V_0 \exp(z^2/w^2), \tag{D.2}$$

in an otherwise homogeneous system. V_0 and w are the height and width of the bump, and the set-up is illustrated in figure D.9. Such a potential can be induced in a condensate by the presence of a focussed far-off-resonant laser beam. The gaussian potential can be considered as a smoothed-out version of the square potential barrier considered above: the height of the bump in relation to the soliton depth determines whether the soliton transmits or reflects. However, whereas the interaction of the soliton with a potential step is a sudden and short-lived effect, the interaction with the bump is more gradual. This makes it possible to resolve and analyse the soliton interaction in a more quantitative sense. The example we will consider here is that of a dark soliton, with initial speed $v = 0.5c$, incident upon a gaussian bump with height $V_0 = 0.25\mu$. For this height the soliton can just transmit over the bump. The soliton dynamics as it transmits over the step are shown in figure D.10. In the region of the bump the soliton experiences an inhomogeneous background density (figure D.10(b)), with the background density *gradient* causing the soliton to decelerate as it passes up the near-side of the bump, and accelerate down the far-side (figure D.10(c)). This induces the emission of two bursts of counter-propagating sound waves,

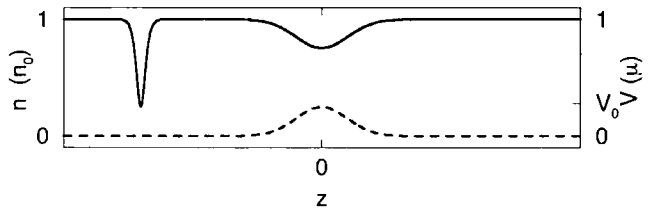

Figure D.9: Schematic of the gaussian bump (dashed line) in an otherwise homogeneous system, and the resulting fluid density (solid line). An incoming soliton is illustrated.

visible in figure D.10(a), which propagate off to infinity and do not reinteract with the soliton. The soliton energy (figure 8(c)) is intimately related to the instantaneous acceleration and background density. It decreases in a stepwise fashion during the interaction, with the energy instantaneously constant when the soliton is at the gaussian peak. Accordingly, the final soliton speed becomes slightly increased ($v = 0.5c \rightarrow v \approx 0.51c$). The power emission (figure D.10(e)) consists of two peaks, due to the two bursts of sound as the soliton climbs and descends the bump. At the peak of the bump, where the background density is locally homogeneous, both the acceleration and power emission are zero.

D.3 Dark soliton oscillating in a gaussian trap

The relation between emitted power and soliton acceleration can be put on firmer ground by considering the case of an oscillating soliton, since such a case includes a wide range of soliton speeds and background densities. The most lucid example is that of a symmetrical trap formed by two gaussian-shaped potentials,

$$V = V_0 \left[\exp\left\{ -\frac{(z - z_0)^2}{w^2} \right\} + \exp\left\{ -\frac{(z + z_0)^2}{w^2} \right\} \right], \tag{D.3}$$

within which the soliton is initially trapped, as illustrated in figure D.11. Here V_0 is the amplitude of the gaussians, z_0 the distance of the centres from the origin, and w the gaussian width. To monitor the effect of sound emission (without allowing for reabsorption of sound to complicate matters) we assume that the height of the gaussian bump is low enough ($V_0 < \mu$), such that the

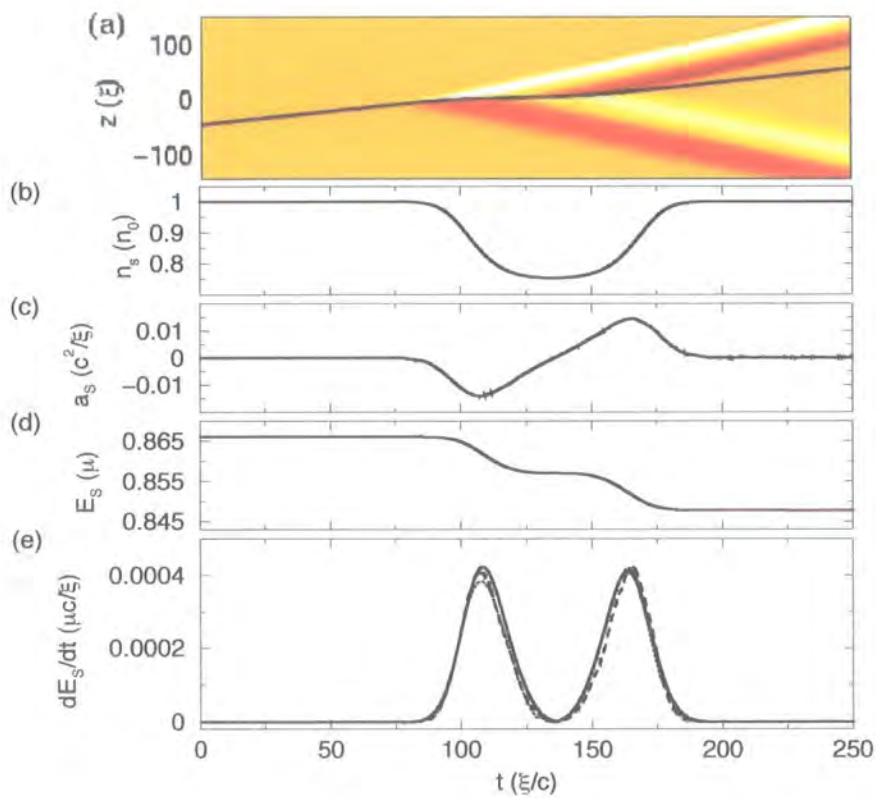

Figure D.10: Dynamics of a dark soliton, with initial speed $v = 0.5c$, incident on the gaussian potential with $V_0 = 0.25\mu$ and $w^2 = 50\xi^2$. (a) Space-time plot of renormalised density, showing the soliton (black line) and the bursts of sound (bright/dark bands) during the interaction. The density scale has an amplitude of $2\%n_0$. (b) Background density experienced by the soliton n_S. (b) Soliton acceleration a_S. (c) Soliton energy E_S. (d) Rate of energy loss, as evaluated by the GP energy functional (solid line), the acceleration-squared law of equation (4.3) with constant coefficient $\kappa = 2.28(\mu\xi/c^3)$ (dashed line) and the prediction from nonlinear optics of equation (4.4) (dotted line).

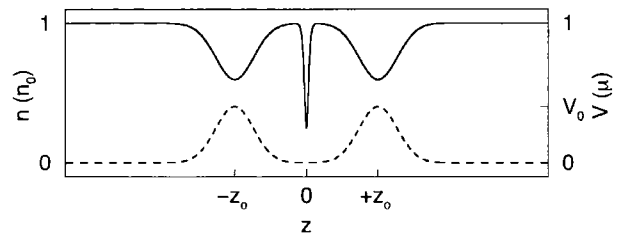

Figure D.11: A dark soliton (solid line) is confined to oscillate within a trap formed by two identical gaussian bumps (dashed line) of height V_0 centred at $-z_0$ and $+z_0$.

emitted sound escapes the mini-trap and propagates to infinity. This results in a drastic change in the soliton amplitude and frequency.

Figure D.12 considers the long term dynamics of a soliton with initial speed $v = 0.3c$ oscillating in a double gaussian trap. The bump amplitude is $V_0 = 0.3\mu$ which ensures that any sound emitted by the soliton will escape the trap and propagate to infinity. The dissipation of the oscillating soliton leads to an 'anti-damping' effect [165], whereby the soliton oscillates progressively faster and with greater amplitude (see figure D.12(a) for $t < 4000\ (\xi/c)$). This leads to an initial *decrease* in the oscillation period (figure D.12(b)) [213], and a significant deviation from the corresponding energy-conserving trajectory (dotted line in figure D.12(a)). However, as the soliton begins to probe the outer regions of the trap, where the potential gradient tails off, the period *increases*. Eventually, at $t \approx 6500\ (\xi/c)$ the soliton has lost sufficient energy, and anti-damped to such large amplitudes, that it can escape the trap [156, 165].

The periodic acceleration of the oscillating soliton, shown in figure D.12(c), is zero when the soliton passes through the minimum of the trap, where the background density is effectively homogeneous, and becomes maximum at the extremum of each oscillation. The energy of the soliton (figure D.12(d)) decreases in periodic steps, due to the periodic sound emission shown in figure D.12(e), with both of these (shown by solid lines) determined numerically from equation (2.12). The peak periodic values of both the power emission (figure D.12(e)) and soliton acceleration (figure D.12(c)) initially increase in time as the soliton probes further and further into the double gaussian trap, where the

background density gradient becomes *higher*. Later in the evolution, the peaks begin to decrease in amplitude and develop intermediate dips as the soliton probes the outer regions of the trap where the potential tails off and the density gradient *decreases*. Also plotted in figure D.12(e) is the power emission predicted by equation (4.3) (dotted line) with a suitably chosen value of κ, such that the initial peak emission rates match. The agreement is found to be very good, particularly at early times, when the soliton is localised within the central region of the trap. However, the non-uniformly increasing background density gradient in this trap causes a degraded agreement at later times. We attribute this to the fact that the coefficient κ, taken to be constant, will in general be time-dependent, depending on parameters such as the local density, soliton speed, etc.

To investigate the validity of equation (4.3) in more detail, we next investigate the two 'limiting' regimes of soliton motion arising in figure D.12. These correspond to (i) the soliton oscillating near the centre of the double gaussian trap (for which the density gradient increases monotonically as one moves away from the trap centre, roughly $t < 2000(\xi/c)$ in figure D.12), and (ii) the soliton oscillating essentially all the way to the edges of the trap, and thus probing both the initial monotonic increase of the background density to its maximum value, and its subsequent decrease (corresponding roughly to $t > 4000(\xi/c)$ in figure D.12). To look into these effects more clearly, we investigate respectively the cases of a slower and a faster soliton, compared to the initial soliton speed of figure D.12. This will also display more clearly the two competing mechanisms contributing to the change in the soliton oscillation frequency evident in figure D.12(a).

Figure D.12 considers a soliton with slow initial speed, $v = 0.2c$, oscillating in the double gaussian trap with the same parameters asfigure D.12. In particular, figure D.13(a) shows the deviation of the soliton oscillations from the corresponding non-dissipative predictions, with the soliton oscillating faster than the non-dissipative case, as a result of sound emission. Figure D.13(c) compares the power emission computed from the GP energy functional (solid line) to the prediction of equation (4.3) (dotted line), yielding excellent agreement.

The opposite regime of a sufficiently fast soliton probing the entire structure of the double gaussian trap is shown in figure D.14. In this regime, the soliton

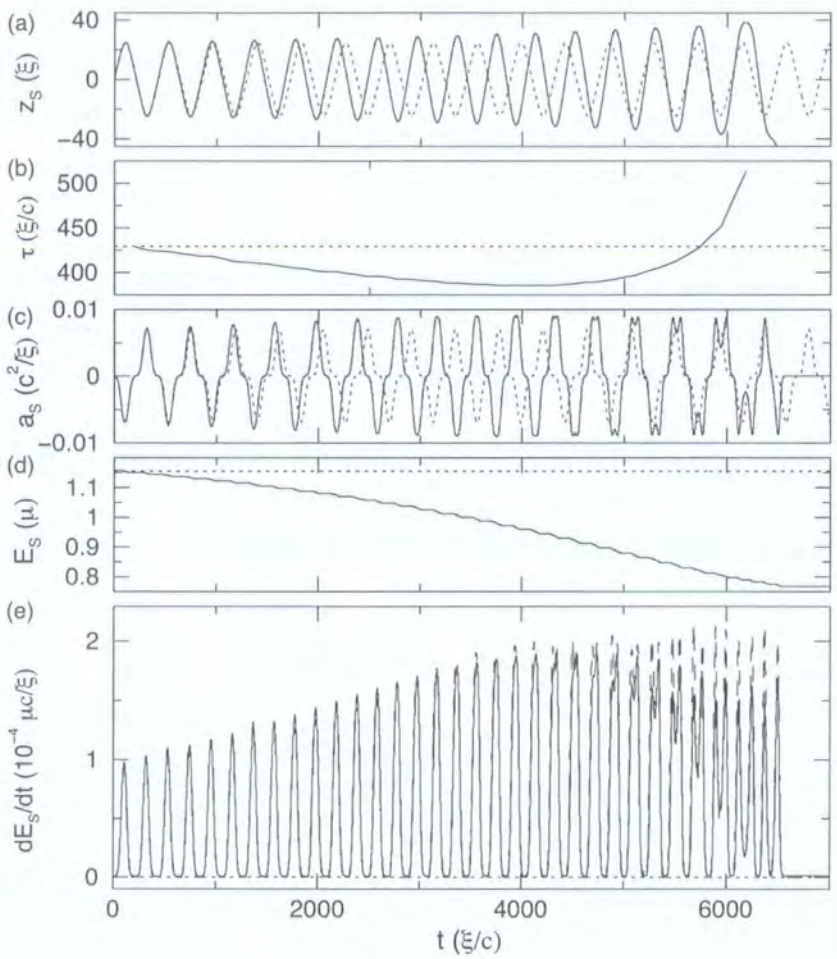

Figure D.12: Dynamics of a dark soliton (solid lines), with initial speed $v = 0.3c$, oscillating in the double gaussian trap with $V_0 = 0.3\mu$, $z_0 = 40\xi$, and $w^2 = 200\xi^2$, along with the corresponding non-dissipative dynamics (dotted lines). (a) Soliton trajectory z_S. (b) Soliton oscillation period τ. (c) Soliton acceleration a_S. (d) Soliton energy E_S. (e) Power emitted by the soliton computed from the GP energy functional (solid line) and the acceleration-squared law of equation (4.3) with $\kappa = 2.09(\mu\xi/c^3)$ (dashed line).

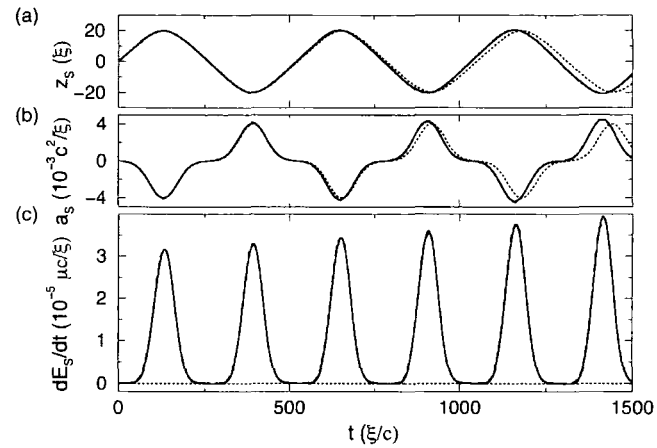

Figure D.13: Dynamics of a dark soliton (solid line), with initial speed $v = 0.2c$, oscillating in the same gaussian trap as figure D.12, along with the corresponding non-dissipative dynamics (dotted lines).(a) Soliton path. (b) Soliton acceleration. (c) Power emitted by the soliton from the GP energy functional (solid line) and equation (4.3) with $\kappa = 2.09(\mu\xi/c^3)$ (dashed line).

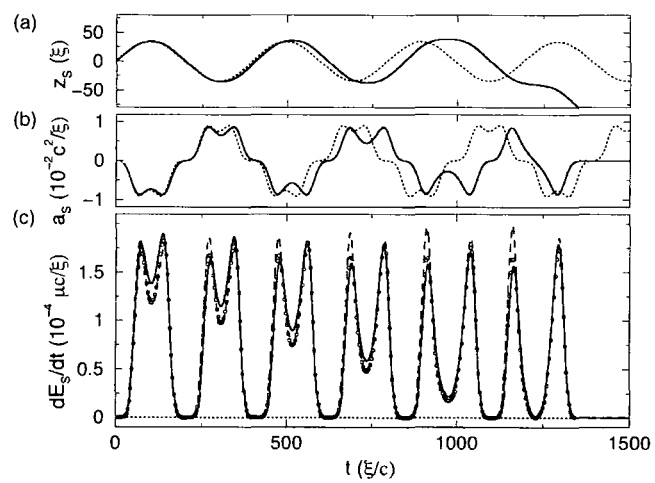

Figure D.14: Dynamics of a dark soliton (solid line), with initial speed $v = 0.5c$, oscillating in the same gaussian trap as figure D.12, along with the corresponding non-dissipative dynamics (dotted lines).(a) Soliton path. (b) Soliton acceleration. (c) Power emitted by the soliton from the GP energy functional (solid line), equation (4.3) with $\kappa = 2.09(\mu\xi/c^3)$ (dashed line), and the nonlinear optics prediction of equation (4.4) (circles).

experiences more complicated dynamics due to the tailing off of the gaussian potential. We see that, contrary to the case of a slow soliton (figure D.13(a)), the fast soliton (figure D.14(a)) oscillates *slower* than the corresponding non-dissipative trajectory. Note that the deviation from the non-dissipative trajectory is now more significant than for the case of the slower soliton (figure D.13(a)). Furthermore, the soliton acceleration (figure D.14(b)) develops intermediate dips at the extrema of each oscillation. Both of these effects are due to the nature of the changing background density in the double gaussian trap. Although this gradient initially increases with increasing deviation from the trap centre, it subsequently reaches a maximum and then starts decreasing again, such that the soliton period increases drastically as it spends more and more time at the edges of the trap. This also explains the intermediate dips in the rate of sound emissin (figure D.14(c)). Figure D.14(c) compares the rate of sound emission as computed from the GP energy functional (solid line), to the prediction of equation (4.3) based on a *constant* coefficient κ (dashed line). Although the intermediate dip is correctly accounted for by equation (4.3), the incorrect assumption of a constant κ leads to a slight overestimate of the peak energy emission, with the discrepancy increasing as the soliton probes the very edge of the trap. The acceleration-squared prediction from nonlinear optics, given by equation (4.4), which explicitly includes a time-dependent coefficient, is also shown in figure D.14(c) (dotted line). This yields near perfect agreement with the GP energy functional calculations. The peaks in power emission are now correctly accounted for, due to the constantly adjusting coefficient $L_s(v, n)$. Nonetheless, it is remarkable that even the oversimplified assumption of a *constant* κ yields reasonable values for the rate of sound emission.

Bibliography

[1] A. Einstein, Sitzber. Kgl. Preuss. Akad. Wiss. **23**, 3 (1925).

[2] S. N. Bose, Z. Phys **26**, 178 (1924).

[3] K. Huang, *Statistical Mechanics, 2nd edition* (John Wiley and Sons, New York, 1988).

[4] A. Griffin, D. W. Snoke, and S. Stringari (Eds.), *Bose-Einstein condensation* (Cambridge University Press, Campbridge, 1995).

[5] D. R. Tilley and J. Tilley, *Superfluidity and Superconductivity*, 3rd ed. (IOP, Bristol, 1990).

[6] P. Kapitza, Nature **141**, 74 (1938).

[7] J. F. Allen and A. D. Misener, Nature **141**, 75 (1938).

[8] F. London, Nature **141**, 643 (1938).

[9] L. D. Landau, J. Phys. (USSR) **5**, 71 (1941).

[10] N. N. Bogoliubov, J. Phys. (USSR) **11**, 23 (1947).

[11] L. Onsager, Nuovo Cimento **6**, 249/281 (1949).

[12] R. P. Feynman, *Progress in Low Temperature Physics, vol. 1* (North-Holland, Amsterdam, 1955).

[13] W. F. Vinen, Proc. R. Soc. London A **260**, 218 (1961).

[14] E. J. Yarmchuk and M. J. V. Gordon, Phys. Rev. Lett. **43**, 214 (1979).

[15] M. H. Anderson, J. R. Ensher, M. R. Matthews, C. E. Weiman, and E. A. Cornell, Science **269**, 198 (1995).

[16] K. B. Davis *et al.*, Phys. Rev. Lett. **75**, 3969 (1995).

[17] C. S. Adams and E. Riis, Prog. Quantum Elect. **21**, 1 (1997).

[18] S. Chu, C. Cohen-Tannoudji, and W. D. Phillips, *Nobel Lectures in Physics 1996-2000* (World Scientific, London, 2003).

[19] T. J. Greytak and D. Kleppner, *New Trends in Atomic Physics, Les Houches Summer School 1982* (North-Holland, Amsterdam, 1984), p. 1125.

[20] I. F. Silvera and J. T. M. Walraven, *Progress in Low Temperature Physics X* (Elsevier, Amsterdam, 1986), p. 139.

[21] D. Kleppner *et al.*, *Bose-Einstein Condensation in Atomic Gases* (IOS Press, Amsterdam, 1999), p. 177.

[22] D. G. Fried *et al.*, Phys. Rev. Lett. **81**, 3811 (1998).

[23] M. Inguscio, S. Stringari, and C. E. Wieman (Eds.), *Bose-Einstein condensation in atomic gases* (IOS Press, Amsterdam, 1999).

[24] C. J. Pethick and H. Smith, *Bose-Einstein Condensation in Dilute Gases* (Cambridge University Press, Cambridge, 2001).

[25] W. Ketterle, Rev. Mod. Phys. **74**, 001131 (2002).

[26] E. A. Cornell and C. E. Wieman, Rev. Mod. Phys. **74**, 875 (2002).

[27] R. J. Donnelly, *Quantized vortices in Helium II* (Cambridge University Press, Cambridge, 1991).

[28] E. W. Hagley *et al.*, Phys. Rev. Lett. **83**, 3112 (1999).

[29] C. C. Bradley, C. A. Sackett, J. J. Tollett, and R. G. Hulet, Phys. Rev. Lett. **75**, 1687 (1995).

[30] F. P. D. Santos *et al.*, Phys. Rev. Lett. **86**, 3459 (2001).

[31] G. Modugno *et al.*, Science **294**, 1320 (2001).

[32] T. Weber, J. Herbig, M. Mark, H. Nagerl, and R. Grimm, Science **299**, 232 (2003).

[33] Y. Takasu *et al.*, Phys. Rev. Lett. **91**, 040404 (2003).

[34] B. P. Anderson and M. A. Kasevich, Science **282**, 1686 (1998).

[35] I. Bloch, T. W. Hansch, and T. Esslinger, Phys. Rev. Lett. **82**, 3008 (1999).

[36] E. Hagley *et al.*, Science **283**, 1706 (1999).

[37] A. Gorlitz *et al.*, Phys. Rev. Lett. **87**, 130402 (2001).

[38] F. Schreck *et al.*, Phys. Rev. Lett. **87**, 080403 (2001).

[39] H. Moritz, T. Stoferle, M. Kohl, and T. Esslinger, Phys. Rev. Lett. **91**, 250402 (2003).

[40] D. Rychtarik, B. Engeser, H. C. Nagerl, and R. Grimm, Phys. Rev. Lett. **92**, 173003 (2004).

[41] S. L. Rolston and W. D. Phillips, Nature **416**, 219 (2002).

[42] H. Ott, J. Fortagh, G. Schlotterbeck, A. Grossmann, and C. Zimmermann, Phys. Rev. Lett. **87**, 230401 (2001).

[43] W. Hansel, P. Hommelhoff, T. W. Hansch, and J. Reichel, Nature **413**, 498 (2001).

[44] A. E. Leanhardt *et al.*, Phys. Rev. Lett. **89**, 040401 (2002).

[45] M. P. A. Jones, C. J. Vale, D. Sahagun, B. V. Hall, and E. A. Hinds, Phys. Rev. Lett. **91**, 080401 (2003).

[46] C. Orzel, A. K. Tuchman, M. L. Fenselau, M. Yasuda, and M. A. Kasevich, Science **291**, 2386 (2001).

[47] F. S. Cataliotti *et al.*, Science **293**, 843 (2001).

[48] O. Morsch, J. H. Muller, M. Cristiani, D. Ciampini, and E. Arimondo, Phys. Rev. Lett. **87**, 140402 (2001).

[49] M. Greiner, O. Mandel, T. Esslinger, T. Hansch, and I. Bloch, Nature **415**, 39 (2002).

[50] S. Inouye *et al.*, Nature **392**, 151 (1998).

[51] J. L. Roberts, N. R. Claussen, S. L. Cornish, and C. E. Wieman, Phys. Rev. Lett. **85**, 728 (2000).

[52] S. L. Cornish, N. R. Claussen, J. L. Roberts, E. A. Cornell, and C. E. Wieman, Phys. Rev. Lett. **85**, 1795 (2000).

[53] A. Roberts *et al.*, Science **292**, 461 (2001).

[54] M. Greiner, C. A. Regal, and D. S. Jin, Nature **426**, 537 (2003).

[55] S. Jochim *et al.*, Science **302**, 2101 (2003).

[56] M. W. Zwierlein *et al.*, Phys. Rev. Lett. **91**, 250401 (2003).

[57] C. A. Regal, M. Greiner, and D. S. Jin, Phys. Rev. Lett. **92**, 040403 (2004).

[58] M. Bartenstein *et al.*, Phys. Rev. Lett. **92**, 203201 (2004).

[59] C. Raman *et al.*, Phys. Rev. Lett. **83**, 2502 (1999).

[60] B. Jackson, J. F. McCann, and C. S. Adams, Phys. Rev. A **61**, 051603 (2000).

[61] M. R. Matthews *et al.*, Phys. Rev. Lett. **83**, 2498 (1999).

[62] K. W. Madison, F. Chevy, W. Wohlleben, and J. Dalibard, Phys. Rev. Lett. **84**, 806 (2000).

[63] E. Hodby *et al.*, Phys. Rev. Lett. **88**, 010405 (2002).

[64] A. L. Fetter and A. A. Svidzinsky, J. Phys. **13**, R135 (2001).

[65] D. Guery-Odelin and S. Stringari, Phys. Rev. Lett. **83**, 4452 (1999).

[66] O. M. Marago *et al.*, Phys. Rev. Lett. **84**, 2056 (2000).

[67] L. Deng *et al.*, Nature **398**, 218 (1999).

[68] S. Inouye *et al.*, Science **285**, 571 (1999).

[69] M. Kozuma *et al.*, Science **286**, 2309 (1999).

[70] D. Schneble *et al.*, Science **300**, 475 (2003).

[71] K. E. Strecker, G. B. Partridge, A. G. Truscott, and R. G. Hulet, Nature **417**, 150 (2002).

[72] L. Khaykovich *et al.*, Phys. Rev. Lett. **296**, 1290 (2002).

[73] B. Eiermann *et al.*, Phys. Rev. Lett. **92**, 230401 (2004).

[74] S. Burger *et al.*, Phys. Rev. Lett. **83**, 5198 (1999).

[75] J. Denschlag *et al.*, Science **287**, 97 (2000).

[76] B. P. Anderson *et al.*, Phys. Rev. Lett. **86**, 2926 (2001).

[77] Z. Dutton, M. Budde, C. Slowe, and L. V. Hau, Science **293**, 663 (2001).

[78] L. P. Pitaevskii, Zh. Eksp. Teor. Fiz. **40**, 646 (1961).

[79] F. Dalfovo, S. Giorgini, L. P. Pitaevskii, and S. Stringari, Rev. Mod. Phys. **71**, 463 (1999).

[80] C. F. Barenghi, R. J. Donnelly, and W. F. Vinen (Eds.), *Quantized Vortex Dynamics and Superfluid Turbulence* (Springer Verlag, Berlin, 2001).

[81] G. E. Volovik, *The Universe in a Helium Droplet* (Oxford University Press, Oxford, 2003).

[82] P. Nozieres and D. Pines, *The Theory of Quantum Liquids* (Perseus Publishing, New York, 1999).

[83] A. A. Abrikosov, Sov. Phys. JETP **22**, 1442 (1957).

[84] J. R. Abo-Shaeer, C. Raman, J. M. Vogels, and W. Ketterle, Science **292**, 476 (2001).

[85] D. Rozas, Z. S. Sacks, and G. A. Swartlander Jr., Phys. Rev. Lett. **79**, 3399 (1997).

[86] S. I. Davis, P. C. Hendry, and P. V. E. McClintock, Physica B **280**, 43 (2000).

[87] M. Leadbeater, T. Winiecki, D. C. Samuels, C. F. Barenghi, and C. S. Adams, Phys. Rev. Lett. **86**, 1410 (2001).

[88] M. Leadbeater, D. C. Samuels, C. F. Barenghi, and C. S. Adams, Phys. Rev. A **67**, 015601 (2003).

[89] N. G. Berloff, Phys. Rev. A **69**, 053601 (2004).

[90] W. F. Vinen, Phys. Rev. B **61**, 1410 (2000).

[91] J. Koplik and H. Levine, Phys. Rev. Lett. **71**, 1375 (1993).

[92] J. Koplik and H. Levine, Phys. Rev. Lett. **76**, 4745 (1996).

[93] P. C. Haljan, I. Coddington, P. Engels, and E. A. Cornell, Phys. Rev. Lett. **87**, 210403 (2001).

[94] A. E. Leanhardt *et al.*, Phys. Rev. Lett. **89**, 190403 (2002).

[95] Y. Shin *et al.*, cond-mat/0407045 (2004).

[96] M. Tsubota, K. Kasamatsu, and M. Ueda, Phys. Rev. A **65**, 023603 (2002).

[97] C. Lobo, A. Sinatra, and Y. Castin, Phys. Rev. Lett. **92**, 020403 (2004).

[98] P. Rosenbusch, V. Bretin, and J. Dalibard, Phys. Rev. Lett. **89**, 200403 (2002).

[99] P. O. Fedichev and G. V. Shylapnikov, Phys. Rev. A **60**, R1779 (1999).

[100] B. P. Anderson, P. C. Haljan, C. E. Wieman, and E. A. Cornell, Phys. Rev. Lett. **85**, 2857 (2000).

[101] V. Bretin, P. Rosenbusch, F. Chevy, G. V. Shlyapnikov, and J. Dalibard, Phys. Rev. Lett. **90**, 100403 (2003).

[102] E. Hodby, S. A. Hopkins, G. Hechenblaikner, N. L. Smith, and C. J. Foot, Phys. Rev. Lett. **91**, 090403 (2003).

[103] P. Engels, I. Coddington, P. C. Haljan, V. Schweikhard, and E. A. Cornell, Phys. Rev. Lett. **90**, 170405 (2003).

[104] I. Coddington, P. Engels, V. Schweikhard, and E. A. Cornell, Phys. Rev. Lett. **91**, 100402 (2003).

[105] S. Inouye *et al.*, Phys. Rev. Lett. **87**, 080402 (2001).

[106] J. R. Abo-Shaeer, C. Raman, and W. Ketterle, Phys. Rev. Lett. **88**, 070409.

[107] D. L. Feder, A. A. Svidzinsky, A. L. Fetter, and C. W. Clark, Phys. Rev. Lett. **86**, 564 (2001).

[108] K. Kasamatsu, M. Tsubota, and M. Ueda, Phys. Rev. A **67**, 033610 (2003).

[109] A. A. Penckwitt, R. J. Ballagh, and C. W. Gardiner, Phys. Rev. A **89**, 260402 (2002).

[110] E. Lundh, J. P. Martikainen, and K. A. Suominen, Phys. Rev. A **67**, 063604 (2003).

[111] P. G. Drazin and R. S. Johnson, *Solitons: an Introduction* (Cambridge University Press, Cambridge, 1989).

[112] M. Remoissenet, *Waves Called Solitons: Concepts and Experiments* (Springer Verlag, Berlin, 1996).

[113] J. L. Hammack and H. Segur, J. Fluid Mech. **65**, 289 (1974).

[114] J. S. Russell, Report of the fourteenth meeting of the British Association for the Advancement of Science, Plates XLVII-LVII , 311 (1845).

[115] F. Abdullaev, S. Darmanyan, and P. Khabibullaev, *Optical Solitons* (Springer Verlag, Berlin, 1993).

[116] G. P. Agrawal, *Nonlinear Fiber Optics* (Academic Press, Amsterdam, 1995).

[117] H. Kim, R. Stenzel, and A. Wong, Phys. Rev. Lett. **33**, 886 (1974).

[118] H. H. Chen and C. S. Liu, Phys. Rev. Lett. **37**, 693 (1976).

[119] M. Peyrard (Ed.), *Molecular Excitations in Biomolecules* (Springer Verlag, Berlin, 1995).

[120] K. A. Naugol'nykh and L. A. Ostrovsky, *Nonlinear Wave Processes in Acoustics* (Cambridge University Press, Cambridge, 1998).

[121] A. Hasegawa and Y. Kodami, *Solitons in Optical Communications* (Oxford University Press, Oxford, 1995).

[122] Y. S. Kivshar and G. P. Agrawal, *Optical Solitons: From Fibers to Photonic Crystals* (Academic Press, Amsterdam, 2003).

[123] L. D. Carr, C. W. Clark, and W. P. Reinhardt, Phys. Rev. A **62**, 063611 (2000).

[124] L. D. Carr, C. W. Clark, and W. P. Reinhardt, Phys. Rev. A **62**, 063610 (2000).

[125] P. Emplit, J. P. Hamaide, F. Reynaud, G. Froehly, and A. Barthelemy, Opt. Commun. **62**, 374 (1987).

[126] B. Denardo, W. W. S. Putterman, and A. Larraza, Phys. Rev. Lett. **64**, 1518 (1990).

[127] B. Denardo *et al.*, Phys. Rev. Lett. **68**, 1730 (1992).

[128] M. Chen, M. A. Tsankov, J. M. Nash, and C. E. Patton, Phys. Rev. Lett. **70**, 1707 (1993).

[129] Y. S. Kivshar and B. Luther-Davies, Phys. Rep. **298**, 81 (1998).

[130] P. D. Miller, Phys. Rev. E **53**, 4137 (1996).

[131] W. P. Reinhardt and C. W. Clark, J. Phys. B **30**, L785 (1997).

[132] T. F. Scott, R. J. Ballagh, and K. Burnett, J. Phys. B **31**, L329 (1998).

[133] A. M. Martin *et al.*, Phys. Rev. Lett. **90**, 110404 (2003).

[134] V. A. Brazhnyi and A. M. Kamchatnov, Phys. Rev. A **68**, 043614 (2003).

[135] A. M. Kamchatnov, A. Gammal, and R. A. Kraenkel, Phys. Rev. A **69**, 063605 (2004).

[136] A. Radouani, Phys. Rev. A **70**, 013602 (2004).

[137] R. Dum, J. I. Cirac, M. Lewenstein, and P. Zoller, Phys. Rev. Lett. **80**, 2972 (1998).

[138] B. Wu, J. Liu, and Q. Niu, Phys. Rev. Lett. **88**, 034101 (2002).

[139] L. D. Carr, J. Brand, S. Burger, and A. Sanpera, Phys. Rev. A **63**, 051601 (2001).

[140] S. Burger, L. D. Carr, P. Ohberg, K. Sengstock, and A. Sanpera, Phys. Rev. A **65**, 043611 (2002).

[141] P. Öhberg and L. Santos, Phys. Rev. Lett. **86**, 2918 (2001).

[142] P. G. Kevrekidis, D. J. Frantzeskakis, B. A. Malomed, A. R. Bishop, and I. G. Kevrekidis, New J. Phys. **5**, 64 (2003).

[143] A. A. Svidzinsky and A. L. Fetter, Phys. Rev. Lett. **84**, 5919 (2000).

[144] B. Jackson, J. F. McCann, and C. S. Adams, Phys. Rev. A **61**, 013604 (2000).

[145] D. S. Rokhsar, Phys. Rev. Lett. **79**, 2164 (1997).

[146] A. A. Svidzinsky and A. L. Fetter, Phys. Rev. A **62**, 063617 (2000).

[147] R. A. Duine, B. W. A. Leurs, and H. T. C. Stoof, Phys. Rev. A **69**, 053623 (2004).

[148] M. A. H. Ahsan *et al.*, Phys. Rev. A **64**, 013608 (2001).

[149] L. M. Pismen, *Vortices in Nonlinear Fields* (Clarendon Press, Oxford, 1999).

[150] Y. N. Ovchinnikov and I. M. Sigal, Nonlinearity **11**, 1295 (1998).

[151] V. I. Klyatskin, Izv. Akad. Nauk SSSR Mekh. Zhidk. Gaza **6**, 87 (1966).

[152] E. Lundh and P. Ao, Phys. Rev. A **61**, 063612 (2000).

[153] W. F. Vinen, Phys. Rev. B **64**, 134520 (2001).

[154] A. L. Fetter, Phys. Rev. A **69**, 043617 (2004).

[155] W. Thomson (Lord Kelvin), Philos. Mag. **10**, 155 (1880).

[156] P. O. Fedichev, A. E. Muryshev, and G. V. Shlyapnikov, Phys. Rev. A **60**, 3220 (1999).

[157] A. E. Muryshev, H. B. L. van den Heuvell, and G. V. Shlyapnikov, Phys. Rev. A **60**, R2665 (1999).

[158] A. Muryshev, G. V. Shylapnikov, W. Ertmer, K. Sengstock, and M. Lewenstein, Phys. Rev. Lett. **89**, 110401 (2002).

[159] J. Dziarmaga and K. Sacha, Phys. Rev. A **66**, 043620 (2002).

[160] V. Tikhonenko *et al.*, Opt. Lett. **21**, 1129 (1996).

[161] A. V. Mamaev, M. Saffman, and A. A. Zozulya, Phys. Rev. Lett. **76**, 2262 (1996).

[162] Y. S. Kivshar and D. E. Pelinovsky, Phys. Rep. **331**, 117 (2000).

[163] J. Brand and W. P. Reinhardt, Phys. Rev. A **65**, 043612 (2002).

[164] J. Brand and W. P. Reinhardt, J. Phys. B **34**, 113 (2001).

[165] T. Busch and J. R. Anglin, Phys. Rev. Lett. **84**, 2298 (1999).

[166] G. Huang, J. Szeftel, and S. Zhu, Phys. Rev. A **65**, 053605 (2002).

[167] D. E. Pelinovsky, Y. S. Kivshar, and V. V. Afanasjev, Phys. Rev. E **54**, 2015 (1996).

[168] P. G. Kevrekidis, R. Carretero-Gonzalez, G. Theocharis, D. J. Frantzeskakis, and B. A. Malomed, Phys. Rev. A **68**, 035602 (2003).

[169] M. Johansson and Y. S. Kivshar, Phys. Rev. Lett. **82**, 85 (1999).

[170] E. P. Gross, Phys. Rev. **106**, 161 (1957).

[171] V. L. Ginzburg and L. P. Pitaevskii, Sov. Phys. JETP **7**, 858 (1958).

[172] D. Schumayer and B. Apagyi, Phys. Rev. A **65**, 053614 (2002).

[173] U. A. Khawaja *et al.*, Phys. Rev. Lett. **89**, 200404 (2002).

[174] L. Salasnich, A. Parola, and L. Reatto, Phys. Rev. A **66**, 043603 (2002).

[175] L. Salasnich, A. Parola, and L. Reatto, Phys. Rev. Lett. **91**, 080405 (2003).

[176] L. D. Carr and J. Brand, Phys. Rev. Lett. **92**, 040401 (2004).

[177] W. H. Press, S. A. Teukolsky, W. T. Vetterling, and B. P. Flannery, *Numerical Recipes in Fortran: The Art of Scientific Computing*, 2 ed. (Cambridge University Press, Cambridge, 1992).

[178] E. Madelung, Zeit. fur Phys. **40**, 322 (1926).

[179] T. Winiecki, B. Jackson, J. F. McCann, and C. S. Adams, J. Phys. B **33**, 4069 (2000).

[180] E. A. Donley, N. R. Claussen, S. T. Thompson, and C. E. Wieman, Nature **417**, 529 (2002).

[181] J. M. Gerton *et al.*, Nature **408**, 692 (2000).

[182] S. Dettmer *et al.*, Phys. Rev. Lett. **87**, 160406 (2001).

[183] S. Richard *et al.*, Phys. Rev. Lett. **91**, 010405 (2003).

[184] D. S. Petrov, M. Holzman, and G. V. Shlyapnikov, Phys. Rev. Lett. **84**, 2551 (2000).

[185] U. A. Khawaja, J. O. Anderson, N. P. Proukakis, and H. T. C. Stoof, Phys. Rev. A **66**, 013615 (2002).

[186] M. Olshanii, Phys. Rev. Lett. **81**, 938 (1998).

[187] A. D. Jackson, G. M. Kavoulakis, and C. J. Pethick, Phys. Rev. A **58**, 2417 (1998).

[188] V. E. Zakharov and A. B. Shabat, Sov. Phys. JETP **34**, 62 (1972).

[189] V. E. Zakharov and A. B. Shabat, Sov. Phys. JETP **37**, 823 (1973).

[190] M. R. Andrews *et al.*, Phys. Rev. Lett. **79**, 553 (1997).

[191] S. Stringari, Phys. Rev. Lett. **77**, 2360 (1996).

[192] D. S. Jin *et al.*, Phys. Rev. Lett. **77**, 420 (1996).

[193] M. O. Mewes *et al.*, Phys. Rev. Lett. **77**, 988 (1996).

[194] R. Onofrio *et al.*, Phys. Rev. Lett. **84**, 810 (2000).

[195] M. A. de Moura, J. Phys. A **27**, 7157 (1994).

[196] M. A. de Moura, Phys. Rev. A **37**, 4998 (1988).

[197] S. A. Morgan, R. J. Ballagh, and K. Burnett, Phys. Rev. A **55**, 4338 (1997).

[198] M. J. Jamieson, A. Dalgarno, and M. Kimura, Phys. Rev. A **51**, 2626 (1995).

[199] T. C. Killian *et al.*, Phys. Rev. Lett. **81**, 3807 (1998).

[200] E. Tiesinga *et al.*, J. Res. Natl. Inst. Stand. Technol. **101**, 505 (1996).

[201] C. Samuelis *et al.*, Phys. Rev. A **63**, 012710 (2000).

[202] H. M. J. M. Boesten *et al.*, Phys. Rev. A **55**, 636 (1997).

[203] D. L. Feder, M. S. Pindzola, L. A. Collins, B. I. Schneider, and C. W. Clark, Phys. Rev. A **62**, 053606 (2000).

[204] S. Komineas and N. Papanicolaou, Phys. Rev. Lett. **89**, 070402 (2002).

[205] S. Komineas and N. Papanicolaou, Phys. Rev. A **68**, 043617 (2003).

[206] N. P. Proukakis, N. G. Parker, D. J. Frantzeskakis, and C. S. Adams, J. Opt. B **6**, S380 (2004).

[207] N. G. Parker, N. P. Proukakis, and C. S. Adams, *Progress in Soliton Research* (Nova Science, New York, due 2005), chap. Dark soliton dynamics in confined Bose-Einstein condensates.

[208] C. A. Jones and P. H. Roberts, J. Phys. A **15**, 2599 (1982).

[209] C. A. Jones, S. J. Putterman, and P. H. Roberts, J. Phys. A **19**, 2991 (1986).

[210] S. Komineas and N. Papanicolaou, Phys. Rev. A **67**, 023615 (2003).

[211] A. Dreischuh *et al.*, Phys. Rev. E **66**, 066611 (2002).

[212] G. Theocharis *et al.*, Phys. Rev. Lett. **90**, 120403 (2003).

[213] V. A. Brazhnyi and V. V. Konotop, Phys. Rev. A **68**, 043613 (2003).

[214] Y. S. Kivshar and X. Yang, Phys. Rev. E **49**, 1657.

[215] V. V. Konotop and V. E. Vekslerchik, Phys. Rev. E **49**, 2397 (1994).

[216] N. G. Parker, N. P. Proukakis, M. Leadbeater, and C. S. Adams, J. Phys. B **36**, 2891 (2003).

[217] A. B. Aceves, J. V. Moloney, and A. C. Newell, Phys. Rev. A **39**, 1828 (1989).

[218] Y. S. Kivshar, A. M. Kosevich, and O. A. Chubykalo, Phys. Rev. A **41**, 1677 (1990).

[219] Y. Nogami and F. M. Toyama, Phys. Lett. A **184**, 245 (1994).

[220] G. Huang, M. G. Velarde, and V. A. Makarov, Phys. Rev. A **64**, 013617 (2001).

[221] V. V. Konotop, V. M. Perez-Garcia, Y. F. Tang, and L. Vazquez, Phys. Lett. A **236**, 314 (1997).

[222] D. J. Frantzeskakis, G. Theocharis, F. K. Diakonos, P. Schmelcher, and Y. S. Kivshar, Phys. Rev. A **66**, 053608 (2002).

[223] J. D. Jackson, *Classical Electrodynamics* (John Wiley and Sons, New York, 1999).

[224] N. G. Parker, N. P. Proukakis, M. Leadbeater, and C. S. Adams, Phys. Rev. Lett. **90**, 220401 (2003).

[225] N. P. Proukakis, N. G. Parker, C. F. Barenghi, and C. S. Adams, Laser Physics **14**, 284 (2004).

[226] N. G. Parker, N. P. Proukakis, C. F. Barenghi, and C. S. Adams, J. Phys. B **37**, S175 (2004).

[227] S. Stringari, Phys. Rev. Lett. **58**, 2385 (1998).

[228] C. Menotti and S. Stringari, Phys. Rev. A **66**, 043610 (2002).

[229] M. D. Barrett, J. A. Sauer, and M. S. Chapman, Phys. Rev. Lett. **87**, 010404 (2001).

[230] K. M. Hilligsoe, M. K. Oberthaler, and K. P. Marzlin, Phys. Rev. A **66**, 063605 (2002).

[231] E. A. Ostrovskaya and Y. S. Kivshar, Phys. Rev. Lett. **90**, 160407 (2003).

[232] A. V. Yulin and D. V. Skryabin, Phys. Rev. A **67**, 023611 (2003).

[233] A. V. Yulin, D. V. Skryabin, and P. S. J. Russell, Phys. Rev. Lett. **91**, 260402 (2003).

[234] G. Theocharis, D. J. Frantzeskakis, P. G. Kevrekidis, R. Carretero-Gonzalez, and B. A. Malomed, preprint (2003).

[235] C. Menotti, M. Kramer, A. Smerzi, L. Pitaevskii, and S. Stringari, Phys. Rev. A **70**, 023609 (2004).

[236] J. Wu, R. Keolian, and I. Rudnick, Phys. Rev. Lett. **52**, 1421 (1984).

[237] W. Chen, R. Wei, and B. Wang, Phys. Lett. A **208**, 197 (1995).

[238] W. Chen, Phys. Lett. A **196**, 321 (1995).

[239] I. V. Barashenkov, M. M. Bogdan, and V. I. Korobov, Europhy. Lett. **15**, 113 (1991).

[240] J. N. Kutz *et al.*, Opt. Lett. **18**, 802 (1993).

[241] A. Mecozzi *et al.*, Opt. Lett. **19**, 2050 (1994).

[242] S. Longhi, Opt. Lett. **20**, 695 (1995).

[243] J. W. Miles, J. Fluid Mech. **148**, 451 (1984).

[244] C. Elphick and E. Meron, Phys. Rev. A **40**, 3226 (1989).

[245] I. V. Barashenkov, S. R. Woodford, and E. V. Zemlyanaya, Phys. Rev. Lett. **90**, 054103 (2003).

[246] N. P. Proukakis, N. G. Parker, C. F. Barenghi, and C. S. Adams, Phys. Rev. Lett. **93**, 130408 (2004).

[247] B. M. Caradoc-Davies, R. J. Ballagh, and K. Burnett, Phys. Rev. Lett. **83**, 895 (1999).

[248] S. Choi, S. A. Morgan, and K. Burnett, Phys. Rev. A **57**, 4057 (1998).

[249] J. J. Garcia-Ripoll and V. M. Perez-Garcia, Phys. Rev. A **63**, 041603 (2001).

[250] J. J. Garcia-Ripoll and V. M. Perez-Garcia, Phys. Rev. A **64**, 053611 (2001).

[251] A. A. Aftalion and R. L. Jerrard, Phys. Rev. A **66**, 023611 (2002).

[252] A. L. Fetter and J. K. Kim, **125**, 239 (2001).

[253] P. G. Kevrekidis *et al.*, J. Phys. B **36**, 3467 (2003).

[254] I. Biktasheva and V. N. Biktashev, Phys. Rev. E **67**, 026221 (2003).

[255] D. P. Arovas and J. A. Friere, Phys. Rev. B **55**, 1068 (1997).

[256] C. F. Barenghi, private communication.

[257] W. F. Vinen, Proc. R. Soc. A **242**, 493 (1957).

[258] M. Tsubota, T. Araki, and K. Nemirovskii, Phys. Rev. B **62**, 11751 (2000).

[259] P. C. Hendry, N. S. Lawson, R. A. M. Lee, and P. V. E. McClintock, Nature **368**, 315 (1994).

[260] C. Nore, M. Abid, and M. E. Brachet, Phys. Rev. Lett. **78**, 3896 (1997).

[261] D. C. Samuels and C. F. Barenghi, Phys. Rev. Lett. **81**, 4381 (1998).

[262] C. F. Barenghi, N. G. Parker, N. P. Proukakis, and C. S. Adams, cond-mat/0407045 (2004).

[263] Data supplied by Mark Leadbeater.

[264] F. Chevy, K. W. Madison, V. Bretin, and J. Dalibard, Phys. Rev. A **64**, 031601 (2001).

[265] A. Radouani, Phys. Rev. A **68**, 043620 (2003).

[266] V. Bretin, S. Stock, Y. Seurin, and J. Dalibard, Phys. Rev. Lett. **92**, 050403 (2004).

[267] Y. Aharonov and D. Bohm, Phys. Rep. **115**, 485 (1959).

[268] M. V. Berry *et al.*, Eur. J. Phys. **1**, 154 (1980).

[269] E. B. Sonin, Rev. Mod. Phys. **59**, 87 (1987).

[270] U. Leonhardt and P. Piwnicki, Phys. Rev. Lett. **84**, 822 (2000).

[271] U. Leonhardt and P. Öhberg, Phys. Rev. A **67**, 053616 (2003).

[272] L. P. Pitaevskii, Sov. Phys. JETP **8**, 888 (1959).

[273] A. Fetter, Phys. Rep. **136** (1964).

[274] P. Roux, J. de Rosny, M. Tanter, and M. Fink, Phys. Rev. Lett. **79**, 3170 (1997).

[275] F. Vivanco, F. Melo, C. Coste, and F. Lund, Phys. Rev. Lett. **83**, 1966 (1999).

[276] L. D. Carr, K. W. Mahmud, and W. P. Reinhardt, Phys. Rev. A **64**, 033603 (2001).